ISSN 1451 - 9372(Print)
ISSN 2217 - 7434(Online)
JULY-SEPTEMBER 2021
Vol.27, Number 4, 313-421

Chemical Industry & Chemical Engineering Quarterly

Belgrade SERBIA AChE

The AChE Journal for Chemical Engineering, Biochemical Engineering, Chemical Technology, New Materials, Renewable Energy and Chemistry

www.ache.org.rs/ciceq

Journal of the
Association of Chemical Engineers of
Serbia, Belgrade, Serbia

Chemical Industry & Chemical Engineering Quarterly

CI&CEQuarterly

Journal of the
Association of Chemical Engineers of
Serbia, Belgrade, Serbia

Chemical Industry & Chemical Engineering Quarterly

Vol. 26 | Belgrade, October-December 2020 | No. 4

Chemical Industry & Chemical Engineering Quarterly (ISSN 1451-9372) is published quarterly by the Association of Chemical Engineers of Serbia, Kneza Miloša 9/I, 11000 Belgrade, Serbia

Editor:
Vlada B. Veljković
veljkovic@yahoo.com

Editorial Office:
Kneza Miloša 9/I, 11000 Belgrade, Serbia
Phone/Fax: +381 (0)11 3240 018
E-mail: shi@yubc.net
www.ache.org.rs

For publisher:
Ivana T. Drvenica

Secretary of the Editorial Office:
Slavica Desnica

Marketing and advertising:
AChE Marketing Office
Kneza Miloša 9/I, 11000 Belgrade, Serbia
Phone/Fax: +381 (0)11 3240 018

Publication of this Journal is supported by the Ministry of Education, Science and Technological Development of the Republic of Serbia

Subscription and advertisements make payable to the account of the Association of Chemical Engineers of Serbia, Belgrade, No. 205-2172-71, Komercijalna banka a.d., Beograd

Computer typeface and paging:
Vladimir Panić

Printed by:
Faculty of Technology and Metallurgy, Research and Development Centre of Printing Technology, Karnegijeva 4, P.O. Box 3503, 11120 Belgrade, Serbia

Abstracting/Indexing:
Articles published in this Journal are indexed in *Thompson Reuters* products: *Science Citation Index - Expanded*™ - access *via Web of Science*®, part of *ISI Web of Knowledge*℠

CONTENTS

Activities of the Association of Chemical Engineers of Serbia are supported by:

- Ministry of Education, Science and Technological Development, Republic of Serbia
- Hemofarm Koncern AD, Vršac, Serbia
- Faculty of Technology and Metallurgy, University of Belgrade, Belgrade, Serbia
- Faculty of Technology, University of Novi Sad, Novi Sad, Serbia
- Faculty of Technology, University of Niš, Leskovac, Serbia
- Institute of Chemistry, Technology and Metallurgy, University of Belgrade, Belgrade, Serbia

CI&CEQ
Chemical Industry & Chemical Engineering Quarterly

Available on line at
Association of the Chemical Engineers of Serbia *AChE*
www.ache.org.rs/CICEQ

Chem. Ind. Chem. Eng. Q. 27 (4) 313–317 (2021) CI&CEQ

BOJANA R. DANILOVIĆ[1]
NATALIJA G. ĐORĐEVIĆ[1]
IVANA T. KARABEGOVIĆ[1]
DRAGAN Z. TROTER[1]
DRAGIŠA S. SAVIĆ[1]
VLADA B. VELJKOVIĆ[1,2]

[1]University of Niš, Faculty of Technology, Leskovac, Serbia
[2]The Serbian Academy of Sciences and Arts, Belgrade, Serbia

SHORT COMMUNICATION

UDC 577.115:66.061:58

ENHANCING LIPID EXTRACTION FROM GREEN MICROALGAE *Chlorella* SP. USING A DEEP EUTECTIC SOLVENT PRETREATMENT

Abstract

In recent years, many researchers have focused on microalgae as a potential source of lipids for various purposes. To improve the lipid yield, different biomass pretreatments have been investigated. The aim of this work was to determine the effect of an ultrasound and deep eutectic solvent (DES) pretreatment on lipid yield from green microalgae Chlorella sp. The chosen DESs were choline chloride:urea (ChCl:U), choline chloride:glycerol (ChCl:G) and choline chloride:acetic acid (ChCl:Aa), all in the mole ratio of 1:2. Lipids were extracted from the pretreated and untreated biomasses by Bligh and Dyer's method. The results showed that the lipid yields for the untreated and ultrasound-pretreated biomass were 39 and 48%, respectively. The pretreatments with ChCl:U, ChCl:G and ChCl:Aa resulted in lipid yields of 51, 46 and 40%, respectively. Therefore, the use of efficient and environmentally friendly DESs for the microalgae biomass pretreatment resulted in a higher lipid yield.

Keywords: Chlorella sp., deep eutectic solvents, lipid extraction.

Microorganisms such as yeasts, bacteria, and microalgae are often investigated as alternative sources of lipids due to their high productivity and rapid growth. Under specific conditions, some microalgae species can accumulate 30-70% of the lipids in dry biomass [1]. Among them, green microalgae *Chlorella* spp. and *Scenedesmus* spp. are considered potential feedstock for biodiesel production [2]. Also, due to its cell composition, this microalgae can be used for food and health products production. *Chlorella* spp. have the ability of fast growth on the commercial scale and great biomass and lipid accumulation. [3].

Classic extraction methods, which involve one or a mixture of different polar solvents, have been widely used for lipid extraction from microalgae biomass [4]. To improve lipid extraction efficiency, many studies have been directed towards the use of a combination of both mechanical and chemical extraction methods. Such processes involve the use of conventional solvents in combination with the various types of biomass pretreatment (ultrasound, microwave, enzymatic, ionic liquids, etc.) [5]. Methods used for cell disruption, including bead mill, microfluidization, microwave treatment, etc., are energy consuming, cannot be easily scaled up and often require extreme conditions of temperature and pressure. The small size of microalgae cells additionally aggravates the disruption process [6]. Thus, the use of new methods, including ultrasound, ionic liquids or integration of green solvents and mechanical treatments, is being extensively investigated [4].

The use of ultrasound is widely spread in the food industry. Originally, it was used as a control tool, but the interest increased as it has been proven to be an effective method for improving the extraction process due to the cell wall destruction by the cavitation mechanism [7]. The use of ultrasound as a biomass pretreatment in the process of lipid extraction from microalgae has been the subject of numerous studies [8,9,10]. Other pretreatments have also been used to obtain higher yields of microalgae lipids: microwave, bead milling, heat [9], chemical, and enzymatic pretreatments, as well as high-pressure homogenization [10]. Also, supercritical fluid extraction has gained much interest in the extraction of functional compounds from microalgae biomass [11].

Correspondence: B.R. Danilović, University of Niš, Faculty of Technology, Bulevar Oslobođenja 124, 16000 Leskovac, Serbia.
E-mail: bojana.danilovic@junis.ni.ac.rs
Paper received: 1 November, 2020
Paper revised: 6 December, 2020
Paper accepted: 10 December, 2021

https://doi.org/10.2298/CICEQ201101049D

Some ionic liquids, being safe and environmentally friendly solvents, are also used for lipid extraction from microalgae biomass. The mode of the action of ionic liquids includes the interaction between the specific functional groups of the cell wall and the charged particles of ionic liquids. Deep eutectic solvents (DESs) represent a new generation of ionic liquids, usually formed by mixing organic salts (such as choline chloride, ChCl) and hydrogen bond donors (amides, amines, alcohols, and carboxylic acids), resulting in a mixture with a lower melting point [12,13]. DES can form hydrogen bonds with biopolymers like cellulose which are present in the microalgae cell walls. Cellulose microfibrils are connected with hydrogen bonds which are being disrupted in the presence of DES. Thus, the cell wall structure becomes disrupted allowing more efficient extraction of lipids [14]. Simple preparation, low price, low toxicity, and high biodegradability are some of the advantages of DESs compared to classical ionic liquids [15]. In line with this, DESs pretreatment has a high potential for the green algae lipid extraction [16]. In addition, DESs can be used to extract various functional compounds from different plant materials [17].

The use of DESs for biomass pretreatment is an environmentally acceptable and safe process, which involves cheap, biodegradable, and non-toxic substances. Quaternary ammonium salt ChCl is included in the majority of DESs. The combination of ChCl with other compounds (carbohydrates, carboxylic and amino acids) is almost unlimited [18].

This work dealt with the use of several ChCl-based DESs, such as ChCl:urea (ChCl:U), ChCl:glycerol (ChCl:G), and ChCl:acetic acid (ChCl:Aa), and ultrasound for pretreating a freshwater green microalgae (*Chlorella* sp.) biomass to enhance lipid extraction The main goal was to compare the effect of the applied pretreatment methods of the lipid extraction efficiency

MATERIAL AND METHODS

Chemicals

ChCl (98.0%) was provided from Sigma Aldrich (St. Louis, USA), while glycerol (Ph. Eur. grade) was purchased from MeiLab (Belgrade, Serbia). Both urea (99.5%) and glacial acetic acid (>99.8%) were obtained from Zorka (Šabac, Serbia). All chemicals were used as received, without any purification.

Microalgae cultivation

Microalgae *Chlorella* sp. was isolated from standing water from Leskovac and identified [19]. The microalgae was cultivated in the BBM medium (g/dm^3): $NaNO_3$ 0.249; $CaCl_2{\cdot}2H_2O$ 0.0250; $MgSO_4{\cdot}7H_2O$ 0.075; K_2HPO_4 0.072; KH_2PO_4 0.175; NaCl 0.025; EDTA 0.16; KOH 0.077; $FeSO_4{\cdot}7H_2O$ 0.012; H_3BO_3 0.028; $ZnSO_4{\cdot}7H_2O$ 0.019; $MnCl_2{\cdot}4H_2O$ 0.004; MoO_3 0.002; $CuSO_4{\cdot}5H_2O$ 0.004; $Co(NO_3)_2{\cdot}6H_2O$ 0.001. Inoculum was prepared in 0.5 dm^3 BBM for 28 days at 27 °C. An appropriate volume of the inoculum was transferred to the 2 dm^3 sterile BBM medium (autoclaved for 15 min at 121 °C), to obtain an initial optical density of 0.05 at 680 nm. The microalgae cultivation flasks were fixed on a rotary shaker (PSU-20i, Biosan, Latvia, EU), 150 min^{-1}, at constant illumination (2000 lux) and 27 °C for 40 days.

Preparation of DESs

DESs were prepared as described elsewhere [20]. ChCl was mixed with the selected donors of hydrogen bonds (glycerol, urea, or acetic acid) in a 1:2 mole ratio in a round-bottomed flask placed on a rotary evaporator and held at 75 °C within 2 h (until the homogeneous, transparent liquid was formed). After preparation, the obtained DESs were kept in the well-closed glass bottles in a $CaCl_2$-containing desiccator. All DESs were viscous, homogeneous, and colorless. Only ChCl:U DES turned into a white semi-solid upon cooling.

Pretreatments

Algal biomass was first centrifuged (2-6E, Sigma, Germany) and then dried under vacuum at 40 °C (V50, Kambič Anton, Semič, Slovenia). The dried biomass (100 mg) was ultrasonically pretreated in an ultrasound water bath (ViMS electric, Sonic 4 GT, 250 W, 50 Hz) for 10 min at room temperature. The DES pretreatment was performed according to the method described by Tommasi *et al.* [15]. The DES (1 cm^3) was added to the pretreated dried biomass and stirred by a magnetic stirrer (MS-H280-Pro, China) for 24 h at room temperature. Then, distilled water (3 cm^3) was added and the biomass was separated by centrifugation at 3900 rpm for 12 min. The biomass was washed with distilled water three times and the collected aqua phase containing the DES (aDES phase) was collected to determine the lipid content.

Lipid extraction

Lipids were extracted from the untreated and pretreated biomass, as well as from the aDES phase. The extraction was performed in duplicate according to Bligh and Dyer's method [21] with a mixture of chloroform and methanol (2:1 volume ratio). After adding the solvent mixture (6 cm^3), the suspension of the biomass was stirred (MS-H280-Pro, Biobase,

China) for 2 h at room temperature. The lipid content in the aDES phase was determined in a similar way with the addition of 12 cm^3 of the solvent mixture. Then, the resulting suspension was transferred to a separation funnel and distilled water (6 cm^3) was added. The chloroform layer containing lipids was transferred to a pre-weighed flask and dried under a nitrogen stream. The lipid content was determined gravimetrically.

Statistical analysis

Statistical comparisons were carried out by one-way ANOVA followed by Tukey's multiple comparison test using the SPSS 26.0 (IBM, USA). Differences were considered significant when the *p*-value was lower than 0.05.

RESULTS AND DISCUSSION

The biomass of *Chlorella* sp. was pretreated by the ChCl-based DESs or ultrasound to enhance lipid yield. The lipid yields achieved from the treated and untreated biomass are compared in Figure 1. The total lipid yield in the samples treated with the DESs includes the sum of the lipid yields from both the biomass and the aDES phase.

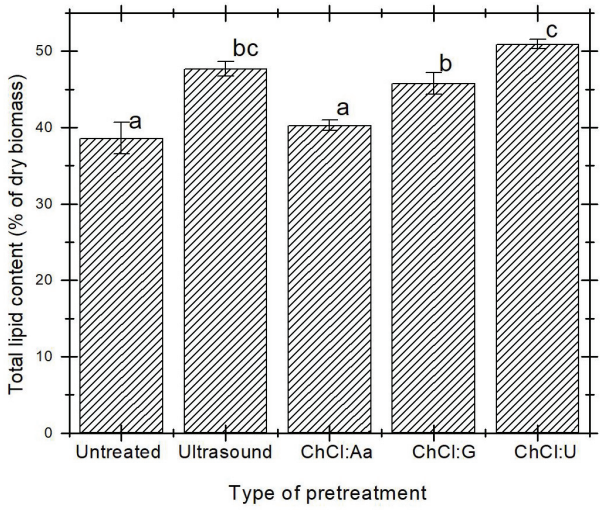

Figure 1. Total lipid yield from the untreated and Chlorella sp. biomass treated with ultrasound, ChCl:U, ChCl:G, and ChCl:Aa. Error bars represent standard deviation. Average values marked with different letters are significantly different according to one-way ANOVA ($p < 0.05$).

Statistical analysis of the results indicated significant difference between the untreated sample and samples treated with ChCl:U, ChCl:G and ultrasound. On the other hand, the lipid yield of the sample treated with ChCl:Aa was not significantly different compared to the untreated biomass. Based on the statistical analysis, the lipid yield of the samples treated with different DES was significantly different ($p < 0.05$) indicating the potential of the use of different DES pretreatments.

The extraction of lipids from the untreated biomass of *Chlorella* sp. resulted in a yield of 39%, which agreed with the results of Danilović *et al.* [19]. Under similar extraction conditions, a lower lipid yield of 26% was obtained from microalgae *C. vulgaris* [21]. A higher lipid yield from *Chlorella* sp. biomass (46%) was achieved with a mixture of chloroform and methanol (1:2) [22], while the same extracting agent applied to the *C. sorokiniana* biomass resulted in a lipid yield of only 19% [23].

The ultrasound pretreatment of the biomass of *Chlorella* sp. significantly increased lipid yield compared to the untreated biomass, with the final average value of 48%. Similar results were obtained by the ultrasound-assisted extraction of the wet *C. vulgaris* biomass (41%) [24] and a mixed microalgae culture (46%) [8]. In contrast, Lee *et al.* [25] obtained a lower lipid yield of only 6% from the phototrophically cultivated *C. vulgaris* in the BG11 medium despite the use of the ultrasound pretreatment. Another study has shown a lower efficiency of the combination of the ultrasound pretreatment and the Soxhlet method, applied to the microalgae *Nannochloropsis oculata*, with the lipid yield of 8% [26]. In the same research, a combination of ultrasound and the Folch method gave a higher lipid yield (24%). The use of ultrasound for pretreating of microalgae biomass increases the extracted lipid yield. However, the disadvantage of this mechanical pretreatment is reflected in their aggressive action to the cell wall, which accelerates the extraction of undesirable compounds (carbohydrates, protein, pigments) and reduces the purity of the final product [13].

Total lipid yields from the biomass of *Chlorella* sp. treated with ChCl:U, ChCl:G and ChCl:Aa were 51, 46 and 40%, respectively. The total lipid yield involved the sum of the lipid yields from the biomass and the aDES phase. The application of ChCl:U and ChCl:G resulted in a significantly higher yield compared to ChCl:Aa. Other studies showed that the combination of *Chlorella* sp. pretreatment with the ChCl:oxalic acid (ChCl:O) (mole ratio 3:2), ChCl:ethylene glycol (ChCl:EG) (mole ratio 6.5:2), and urea-acetamide (U>A) (mole ratio 5:1) DESs and the Bligh-Dyer extraction method (ethyl acetate:ethanol, molar ratio 1:1) gave total lipid yields of 15, 14 and 14%, respectively [16]. A significantly lower lipid yield of 0.9% was reported for the lipid extraction from the microalgae *Phaeodactylum tricornutum* treated with

ChCl:U (mole ratio 1:2). The same microalgae was treated with several other DESs, such as ChCl-O (mole ratio 1:2), ChCl:levulinic acid (ChCl:L, mole ratio 1:2), ChCl:EG (mole ratio 1:2), and ChCl:sorbitol (ChCl:S, mole ratio 1:1), where the lipid yields obtained by the dimethyl carbonate extraction were 14, 13.5, 12 and 11.5%, respectively [15].

A comparison of the lipid yields from the biomass treated with DESs and the aDES phase indicated that a small amount of the lipids remained in the aDES phase. The lipid content of the aDES phase after the application of ChCl:U was 1.6% of the total isolated lipid. When the ChCl:G and ChCl:Aa DESs were used, the lipid content in the aDES phase was 1.0 and 0.6% of the total lipids, respectively which agreed with the lipid yields from the aDES phase in the case of the microalgae *Phaeodactylum tricornutum* pretreated by the ChCl-O (3:2), ChCl-EG (6.5:2) and U-A (5:1) DESs (0.5, 1.75 and 1.0%, respectively) [15]. Therefore, the lipid content in the aDES phase had no significant effect on the total lipid yield of microalgae biomass treated with the DESs.

CONCLUSIONS

The lipid yield from the untreated biomass of *Chlorella* sp. was 39%. Compared to the untreated biomass, the use of ultrasound and ChCl:U and ChCl:G DES resulted in a significantly higher lipid yield. The highest lipid yield (51%) was obtained using a ChCl:U DES. The lipid yields obtained from the aDES phases made less than 2% of the total extracted lipids, thus not affecting the total lipid yield significantly. Although the application of ultrasound gave similar results, the use of DESs is more appropriate due to the possibility of high-purity lipids production, which can be further used for biodiesel production or animal feeding. Due to their low price and easy preparation, DESs have a promising commercial application for pretreating the microalgal biomass and obtaining a high yield of functional compounds from them. Due to the great variety of deep eutectic mixtures, their impact on lipid yield from different oleaginous microalgae should be further investigated.

Aknoledgements

This work was funded by the Ministry of Education, Science and Technological Development of the Republic of Serbia III45001 and the Faculty of Technology, University of Niš.

REFERENCES

[1] S. Bellou, M.N. Baeshen, A.M. Elazzazy, D. Aggeli, F. Sayegh, G. Aggelis, Biotechnol. Adv. 32 (2014) 1476-1493

[2] P. Feng, Z. Xu, L. Qin, M. Asraful Alam, Z. Wang, S. Zhu, Biores. Technol. 301 (2020) 122762

[3] X. Hu, B. Liu, Y. Deng, X. Bao, A. Yang, J. Zhou, Sep. Purif. Technol. 211 (2019) 816-822

[4] S. Vasistha, A. Khanra, M. Clifford, M.P. Rai, Renew. Sustain. Energy Rev. (2020), in press, 110498

[5] A. Patel, F. Mikes, L. Matsakas, Molecules 23 (2018) 1562

[6] S. Nagappan, S. Devendran, P.C. Tsai, S. Dinakaran, H.U. Dahms, V. Kumar Ponnusamy, Fuel 252 (2019) 699-709

[7] Z. Dong, C. Delacour, K. Mc Carogher, A.P. Udepurkar, S. Kuhn, Materials 13 (2020) 344

[8] U.D. Keris-Sen, U. Sen, G. Soydemir, M.D. Gurol, Bioresour. Technol. 152 (2014) 407-413

[9] A. Meullemiestre, C. Breil, M. Abert-Vian, F. Chemat, Bioresour. Technol. 211 (2016) 190-199

[10] C. Onumaegbu, J. Mooney, A. Alaswad, A.G. Olabi, J. Renewable Sustainable Energy 93 (2018) 16-26

[11] S.P. Jeevan Kumar, G. Vijay Kumar, A. Dash, P. Scholz, R. Banerjee, Algal Res. 21 (2017) 138-147

[12] S. S. de Jesus, R. Maciel Filho, Renew. Sustain. Energy Rev. 133 (2020) 110289

[13] D.Z. Troter, Z.B. Todorović, D.R. Đokić-Stojanović, O.S. Stamenković, V.B. Veljković, Renew. Sustain. Energy Rev. 61 (2016) 473-500

[14] Z. Chen, L. Wang, S. Qiu, S. Ge, S. Biomed. Res. Int. 2018 (2018)

[15] E. Tommasi, G. Cravotto, P. Galleti, G. Grillo, M. Mazzotti, G. Saccheti, C. Samori, S. Tabasso, M. Tacchini, E. Tagliavini, J. Am. Chem. Soc. 5 (2017) 8316-8322

[16] W. Lu, M.A. Alam, Y. Pan, J. Wu, Z. Wang, Z. Yuan, Bioresour. Technol. 218 (2016) 123-128

[17] Y. Dai., E. Rozema, R. Verpoorte, Y.H. Choi, J. Chromatogr., A 1434 (2016) 50-56

[18] H. Zhao, G.A. Baker, J. Chem. Technol. Biotechnol. 88 (2012) 3-12

[19] B.R. Danilović, J.M. Cvetković-Rakić, J. Ćirić, J.B. Simeunović, V.B. Veljković, D.S. Savić, Hem. Ind. 71 (2017) 69-74

[20] D.Z. Troter, Z.B. Todorović, D.R. Đokić-Stojanović, B.S. Đordević, V.M. Todorović, S.S. Konstantinović, V.B. Veljković, J. Serb. Chem. Soc. 82 (2017) 1039-1052

[21] R.A.I. Abou-Shanab, I.A. Matter, S.N. Kim, Y.K. Oh, J. Choi, B.H Jeon, Biomass Bioenergy 35 (2011) 3079-3085

[22] D. Savić, J. Ćirić, B. Danilović, V. Veljković, in Proceedings of 22th Congress of Chemists and Technologists of Macedonia, Ohrid, Macedonia, Book of Abstracts, 2012, p. 123

[23] J.L. Rodolfi, G. Chnini Zittelli, N. Bassi, G. Padovani, N. Biondi, G. Bonini, M.R. Tredici, Biotechnol. Bioengy 102 (2008) 100-112

[24] A. Widjaja, C.C. Chein, Y.H. Ju, J. Taiwan Inst. Chem. Eng. 40 (2009) 13-20

[25] Y.J. Lee, S.Y. Yoo, C.Y. Ahn, H.M. Oh, Bioresour. Technol. 101 (2010) 75-11

[26] A. Converti, A.A. Casazza, E.Y Ortiz., P. Perego, M. Del Borghi, Chem. Eng. Process. 48 (2009) 1146-1151.

BOJANA R. DANILOVIĆ[1]
NATALIJA G. ĐORĐEVIĆ[1]
IVANA T. KARABEGOVIĆ[1]
DRAGAN Z. TROTER[1]
DRAGIŠA S. SAVIĆ[1]
VLADA B. VELJKOVIĆ[1,2]

[1]Univerzitet u Nišu, Tehnološki fakultet u Leskovcu, Bulevar oslobođenja 124, 16000 Leskovac, Srbija
[2]Srpska akademija nauka i umetnosti, Kneza Mihaila 35, 11000 Beograd, Srbija

NAUČNI RAD

POBOLJŠANJE EKTRAKCIJE LIPIDA IZ ZELENIH MIKROALGI *Chlorella* SP. PREDTRETMANOM DUBOKIM EUTEKTIČKIM RASTVARAČIMA

Poslednjih godina, mnoga istraživanja su fokusirana na upotrebu mikroalgi kao potencijalnog izvora lipida za različite namene. Različiti predtretmani biomase se primenjuju kako bi se poboljšao prinos. Cilj ovog rada je utvrđivanje uticaja predtretmana ultrazvukom i dubokim eutektičkim rastvaračima na prinos lipida iz zelenih mikroalgi Chlorella sp. U tu svrhu korišćeni su eutektički rastvarači holin-hlorid: urea (ChCl:U), holin-hlorid:glicerol (ChCl:G) i holin-hlorid: sirćetna kiselina (ChCl: Aa) u molskom odnosu 1:2. Lipidi su ekstrahovani iz prethodno obrađene i neobrađene biomase Bligh-Dyer metodom. Rezultati su pokazali da je prinos lipida za netretiranu biomasu 39%, a za ultrazvučno tretiranu biomasu 48%. Predtretmani biomase sa ChCl:U, ChCl:G i ChCl:Aa dali su prinosa lipida od 51, 46 i 40%, redom. Može se zaključiti da upotreba efikasnih i ekološki prihvatljivih dubokih eutektičkih rastvarača u predtretmanu biomase mikroalgi rezultira većim prinosom lipida.

Ključne reči: Chlorella sp., duboki eutektički rastvarači, ekstrakcija lipida.

CI&CEQ
Chemical Industry & Chemical Engineering Quarterly

Available on line at
Association of the Chemical Engineers of Serbia *AChE*
www.ache.org.rs/CICEQ

Chem. Ind. Chem. Eng. Q. 27 (4) 319–328 (2021) CI&CEQ

ALI CAN ERSAN[1,2]
NURCAN TUGRUL[1]

[1]Yildiz Technical University, Faculty of Chemical and Metallurgical Engineering, Department of Chemical Engineering, Istanbul, Turkey
[2]Istanbul Esenyurt University, Vocational High School, Department of Occupational Health and Safety, Istanbul, Turkey

SCIENTIFIC PAPER

UDC 66.047:639.28

THE DRYING KINETICS AND CHARACTERISTICS OF SHRIMP DRIED BY CONVENTIONAL METHODS

Article Highlights

- Drying shrimp is very important in terms of increasing shelf life and not spoiling
- Increasing the drying temperature saves time by drying the shrimp in a shorter time
- The protein content of dried shrimp was higher than protein content of undried shrimp
- The heavy metal content of the dried shrimp was at acceptable levels for human health
- The rehydration ratio increased due to the increased drying temperature for both methods

Abstract

The main purpose of this study was to research the influence of different drying methods on the physical and qualitative properties of dried shrimps. Shrimps were dried with conventional methods at 60, 70 and 80 °C between 330 to 210 min and 190 to 110 min, in an oven and vacuum oven respectively. Drying time was shortened with the use of a vacuum pump. The drying kinetics of the shrimp were studied, and effective moisture diffusion and activation energy were calculated for both methods. The Alibas model and the Midilli and Kucuk model provided the best experimental data with a high coefficient of determination (R^2) for the oven and vacuum oven techniques, respectively. The final dried products were characterized by investigating the color characteristics, heavy metal content and by carrying out protein analyses. The rehydration ratio was also determined for the dehydrated shrimps. Drying conditions affected the color features so that shrimps dried in ovens and vacuum ovens showed an increase in brightness and yellowness values and a decrease in redness values. The concentration of As, Pb, Cd, Hg, Cu, Zn and Fe in the dried shrimp were within acceptable limits. The protein content of dried shrimp (~85%) is higher than that of undried shrimp (~20%).

Keywords: shrimp, drying kinetics, rehydration, protein content, color analysis, heavy metal.

Aquatic creatures like marine molluscs and insects have a high protein content and have been eaten for many years cooked or uncooked. Shrimps come from the family *Penaeidae* and are known as *Parapenaeus longirostris*. They are widely consumed in many countries of the world, especially in the Far East, with two thousand five hundred known species. Sixty-one species are found in the sea around Turkey and only seven of them are considered to be commercially viable. Shrimps are consumed a great deal in Turkey because the country is surrounded by the sea from three sides. Aquatic creatures can easily degrade due to microbiological activity; however, it can be reduced by decreasing their moisture content. There are many drying methods that can be found in published literature, including microwaves, hot air oven, vacuum-hot air oven, infrared drying, etc. The advantages of hot air drying are the equipment's simplicity, low cost, flexibility and easy control. However, low energy efficiency, long drying times and low thermal conductivity of foods are the disadvantages of hot air drying. The quality of the dried foods can be

Correspondence: N. Tugrul, Department of Chemical Engineering, Faculty of Chemical and Metallurgical Engineering, Yildiz Technical University, Davutpasa Campus, Davutpasa Street No. 127, Esenler, 34220 Istanbul, Turkey.
E-mail: ntugrul@yildiz.edu.tr
Paper received: 14 November, 2020
Paper revised: 23 December, 2020
Paper accepted: 25 December, 2020

https://doi.org/10.2298/CICEQ201114050E

improved by decreasing the drying temperature or the drying period. Therefore, instead of the hot air oven, vacuum-hot air oven drying is preferred [1-3]. In recent years, modern drying methods have become areas of interest in the dehydration of agricultural products like fruits and vegetables. This is because these drying techniques cause fast water evaporation and result in high drying ratios, thus they reduce the drying time and consume less energy [4,5]. Drying is a complex process, including simultaneous heat and mass transfer for the removal of moisture from the wet food and air. Food product behavior during drying is determined from the drying kinetics analyses. Mathematical models that characterize the drying process are employed to optimize drying systems working conditions [6-7].

There are many researches on drying food products. However, these studies are based on drying vegetables and fruits. There are fewer studies on meat and aquatic products. Humanity has to consume food products to survive. Food products, and especially aquatic products, deteriorate quickly. Drying methods are used to prevent this deterioration and increase the shelf life of foods. Examples of drying studies with different meat products include the following: Traffano-Schiffo *et al.* [8] studied the drying of meat with infrared thermography, Jangsawang [9] studied drying different meat products with a cabinet dryer and Corona *et al.* [10] studied ultrasonic characterization of dried meat products. Cantalejo *et al.* [11] studied freeze drying of chicken meat, while Dinçer and Erbaş [12] studied drying kinetics of vacuum-dried beef slices. Akhtar and More [13] studied the convective drying process of chicken meat.

There are very few studies about drying marine products. Tsuruta and Hayashi [14] practised the warm-air drying for seafood. Tirawanichakul *et al.* [15] studied hot air convection drying of shrimp, Zhang *et al.* [16] studied different drying methods of fruits, vegetables and aquatic products and Komolafe *et al.* [17] studied convective fish drying. Bai and Sun [18] studied electrohydrodynamic drying technique for shrimps. Bellagha *et al.* [19] studied drying of sardines. Jain and Pathare [20] studied the drying kinetics of fish dried via sun. Kipcak [21] studied microwave drying and Kipcak *et al.* [22] studied the infrared drying of the mussel.

There are many researches on drying meat, chicken and some on aquatic products in public literature, but there are a few studies conducted on the drying of shrimps by conventional drying methods. In this study, shrimps were dried with conventional methods (oven and vacuum oven drying). The drying rate, moisture ratio and moisture content of the shrimps were calculated, regression analyses were carried out, effective moisture diffusivity, activation energies and rehydration rates were also estimated. The color of dried products is one of the most important criteria for product quality, so color analysis was performed, as well as a heavy metal and protein content analysis. The scope of this study was to find out the effects of oven and vacuum oven drying methods on drying characteristics, color changes, heavy metal content and protein content of dried shrimp.

EXPERIMENTAL

Sample preparation

Fresh shrimps, caught in Turkish seas, were provided from a local store in İstanbul in February 2019 and were stored in a freezer at a temperature of 4 °C. Shrimp products were stored in the freezer for two days before drying experiments. The shrimp were taken out of the freezer 12 h before the experiment and kept at room temperature. In the experimental stage, shrimps of similar size were selected to have a mean length of 3.5±0.1 cm. The moisture content of the shrimps was obtained to be 4.8824 kg of water/kg of dry matter by using the AOAC method initially [23].

Drying experiments

Drying experiments of products were performed in a Nuve EV 018 model oven, working at ~220 V, 50 Hz, 3.5 A and an 800 W power output. The temperature setting was in increments of 1 °C and able to rise up to 250 °C if needed. The drying area was 30 cm L×20 cm H×25 cm W and vacuum conditions were produced by a laboratory type vacuum pump (KNF N026 1.2 AN 18, Turkey). The vacuum pump operated at 220 V, 50 Hz and a current of 0.85 A. The drying process was performed at 60, 70 and 80 °C with the oven and vacuum oven. When the moisture content of the shrimps decreased to 0.35±0.143 kg of water/kg of dry matter (dry basis), the drying process was terminated. Dried shrimps were cooled in a desiccator at room temperature when the drying process was completed. Afterwards, dried samples were stored in bags which are made of low-density polyethylene (LDPE). This procedure was repeated at different temperatures.

Modelling and regression analyses

The moisture content (M), moisture ratio (MR) and drying rate (DR) of shrimps were estimated by using Eqs. (1), (2) and (3) [4,5,22]:

$$M = \frac{m_w}{m_d} \quad (1)$$

where m_w, m_d and M are the water content (g), dry matter content (g) and moisture content (kg of water/kg dry matter), respectively.

$$DR = \frac{M_{t+dt} - M_t}{dt} \quad (2)$$

where t is the drying time in minutes, M_{t+dt} is the moisture content at $t+dt$ (kg water/kg dry matter), and DR is the drying rate (kg water/kg dry matter × min).

$$MR = \frac{M_t - M_e}{M_i - M_e} \quad (3)$$

where MR is the moisture ratio, M_t is the moisture content at the chosen time, M_e is the equilibrium value, and M_i is the initial value in kg water/kg dry matter. In the calculations, M_e is generally neglected due to its small number.

The drying curve data of each oven and vacuum oven method were fitted to 14 most widely used mathematical models: Aghbashlo *et al.*, Alibas, Henderson and Pabis, Jena and Das, Lewis, logarithmic, Midilli and Kucuk, Page, parabolic, Peleg, two-term exponential, Verma, and Wang and Weibull.

Regression analyses were practised *via* Statistica 8.0 software (StatSoft Inc., Tulsa, USA). Parameters for the model were calculated by applying a non-linear regression procedure using the Levenberg-Marquardt algorithm. To predict drying data, all of the models were used and were assessed by the coefficient of determination (R^2), root mean square error (*RMSE*) and reduced chi-square (χ^2) parameters. Higher R^2 values and lower χ^2 and *RMSE* values were accepted as better results in the literature [2,21-22]. R^2, χ^2 and *RMSE* are given in Eqs. (4)-(6), respectively:

$$R^2 \equiv 1 - \frac{\sum_{i=1}^{N}(MR_{exp,i} - MR_{pre,i})^2}{\sum_{i=1}^{n}(MR_{exp,i} - \left(\frac{1}{n}\right)\sum_{i=1}^{N}MR_{exp,i})} \quad (4)$$

$$\chi^2 = \frac{\sum_{i=1}^{N}\left(MR_{exp,i} - MR_{pre,i}\right)^2}{N - z} \quad (5)$$

$$RMSE = \left(\frac{1}{N}\sum_{i=1}^{N}(MR_{pre,i} - MR_{exp,i})^2\right)^{1/2} \quad (6)$$

In Eq. (6), predicted and experimental moisture ratio values are represented by MR_{pre} and $MR_{exp.}$ Z is a constant number and is the total number of experiments in the model.

Determination of the effective moisture diffusivity

The mass diffusion is based on Fick's second law. Furthermore, it can be used over a falling-rate period for agricultural drying [4,5]. The analytical solution of Fick's second law - assuming moisture migration because of diffusion, constant diffusion coefficients, negligible shrinkage and temperature while the process of drying is in a state of unsteady diffusion - is given using spherical coordinates in Eq. (7) [24]:

$$MR = \frac{8}{\pi^2} + \left[\sum_{n=1}^{\infty}\frac{4}{a^2\alpha_n^2}exp\frac{Ka^2\alpha_n^2 t}{\pi^2}\right] \times \times \left[\sum_{n=0}^{\infty}\frac{4}{(2n+1)^2}exp\left[-K(2n+1)^2 t\left(\frac{a}{l}\right)^2\right]\right] \quad (7)$$

where l is one-half the length of cylinder (m), and the value a is taken as the radius of the finite cylinder (m). K is the D_{eff} (effective moisture diffusivity, $m^2\ s^{-1}$)×π×a^{-2}. The complexity of Eq. (7) can be simplified as shown in Eq. (8):

$$MR = \frac{8}{\pi^2}exp\left[-Kt\left(\frac{a}{l}\right)^2\right] \quad (8)$$

By taking the *ln* of two sides and putting in the K value from Eq. (9), D_{eff} was estimated from the plot of ln *MR versus t*:

$$\ln MR = \ln\left(\frac{8}{\pi^2}\right) - \frac{D_{eff\times\pi^2}}{a^2}\left(\frac{a}{l}\right)^2 t \quad (9)$$

Determination of the activation energy

The Arrhenius equation describes the relationship of the effective moisture diffusivity to temperature, which is given in Eq. (10) [2,21-22]:

$$D_{eff} = D_0 exp\left(-\frac{E_a}{R(T+273.15)}\right) \quad (10)$$

where D_0 (m^2/s) is the pre-exponential factor of the Arrhenius equation, E_a (kJ/mol) is the activation energy, R (kJ/(mol K)) is the universal gas constant and T (°C) is the temperature.

Rehydration experiments

The experiments of rehydration were carried out in an oven at 20 °C for both drying methods. The dehydrated shrimps were placed in glass beakers including pure water with a mass ratio of 1:100. GFL 2004 (Gesellschaft für Labortechnik, Burgwedel, Ger-

many) was the system of water purification used to obtain pure water. The samples were weighed out at specific time intervals of 30 min after the subtraction of excess water from the surface. Eq. (11) was used to estimate the rehydration ratios (RR) [22]:

$$RR = \frac{W_t - W_{dry}}{W_{dry}} \quad (11)$$

where W_t (kg) and W_{dry} (kg) are the samples' weight at any time and the dry weight, respectively. The rehydration capacity values are means of three replicates.

Color measurement

The color of the dried product is the most significant criteria for product quality and consumers. In the Hunter color system, the *L* parameter represents the lightness or darkness value (100 for white, 0 for black), the *a* parameter represents the greenness and redness values, and the *b* parameter represents the blueness and yellowness values. Measurement was performed for these color parameters before and after the two different drying processes using a hand-held colorimeter (PCE-CSM 1; PCE Instruments UK Ltd., Southampton Hampshire, UK). The instrument was calibrated with the calibration kit in its packaging box before the measurement. Three measurements were recorded for each dried shrimp.

The total change in color (ΔE) of dried samples was estimated using Eq. (12) [25]:

$$E = \sqrt{(L_0 - L)^2 + (a_0 - a)^2 + (b_0 - b)^2} \quad (12)$$

where L_0, a_0 and b_0 are the color values of fresh samples before drying. *L*, *a* and *b* color parameters of samples were measured from five points of every sample just after the drying processes.

Determination of the heavy metal and protein contents

The concentration of heavy metals in dried shrimps was investigated with the Agilent 7700 Series ICP-MS analyzer. The protein content analysis was performed using the Leco FP-528 (3000 Lakeview Ave, USA) protein determinator. The heavy metal content and protein content values are means of three replicates.

RESULTS AND DISCUSSION

Drying curves

The influence of different drying methods and temperatures on the drying behaviour of shrimps is given in Figure 1. Initially, the average moisture content of the shrimp was approximately 4.8824 kg of water/kg of dry matter; for the oven, the moisture content in dried shrimps was reduced to 0.352±0.07 kg of water/kg of dry matter, and for the vacuum oven it was reduced to 0.355±0.143 kg water/kg dry matter. From the curves, it is seen that the increase in temperature decreased the drying times. This is due to the fact that the rate of mass transfer was higher at higher temperatures. The oven drying times were measured at 330, 240 and 210 min for 60, 70 and 80 °C, respectively. The vacuum oven drying times were measured at 190, 120 and 110 min for 60, 70 and 80 °C, respectively. The difference appearing between the drying times is due to the extraction of ambient air with the vacuum pump. Vacuum drying is a process in which materials are dried in a reduced pressure environment, which lowers the heat needed for rapid drying. Vacuum decreases the boiling point of water within foodstuffs and hence facilitates water removal.

In general, the drying process for food products happens in the falling-rate period [26]. The drying rate plots of the two methods related to the moisture content of the dried shrimps are shown in Figure 2. All the three periods of increasing-rate and decreasing-rate periods are seen on the graphs. The drying rate increased as the drying temperature rose.

The oven increasing-rate period is found at 60 °C resulting in 4.8824 to 3.4689 kg of water/kg dry matter, at 70 °C it results in 4.8824 to 3.8337 kg of water/kg dry matter, and at 80 °C it results in 4.8824 to 3.5706 kg of water/kg dry matter. At 60 °C from 3.4689 to 0.4497 kg of water/kg dry matter, at 70 °C from 3.8337 to 0.3210 kg of water/kg dry matter, and at 80 °C from 3.5706 to 0.2865 kg of water/kg dry matter, is calculated as the falling-rate period.

In the vacuum oven, the increasing-rate period is found at 60 °C from 4.8824 to 3.5069 kg water/kg dry matter, at 70 °C from 4.8824 to 3.1888 kg water/ /kg dry matter, and at 80 °C from 4.8824 to 2.9879 kg water/kg dry matter. At 60 °C from 3.5069 to 0.3997 kg water/kg dry matter, at 70 °C from 3.1888 to 0.3895 kg water/kg dry matter, and at 70 °C from 2.9879 to 0.2759 kg water/kg dry matter, is calculated as the falling-rate period.

In general, for the two drying methods, drying predominantly happens in the falling-rate period. Many studies show that in the drying of meat-type products that the major drying phase is during the falling-rate period [13].

Modeling and regression analyses results

For modeling and regression analyses, the experimental results of the two drying methods were

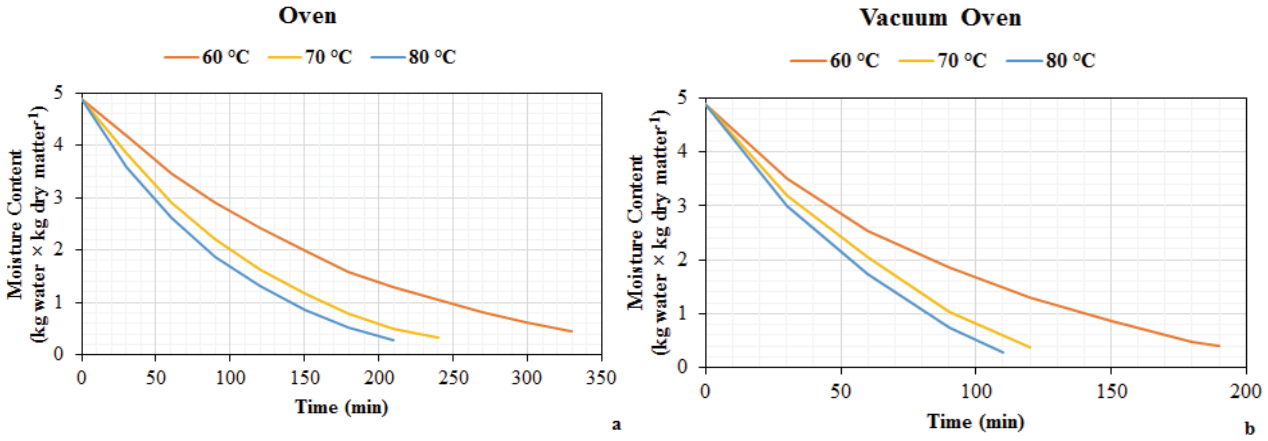

Figure 1. The drying curves of shrimps dried: a) in an oven, b) in a vacuum oven.

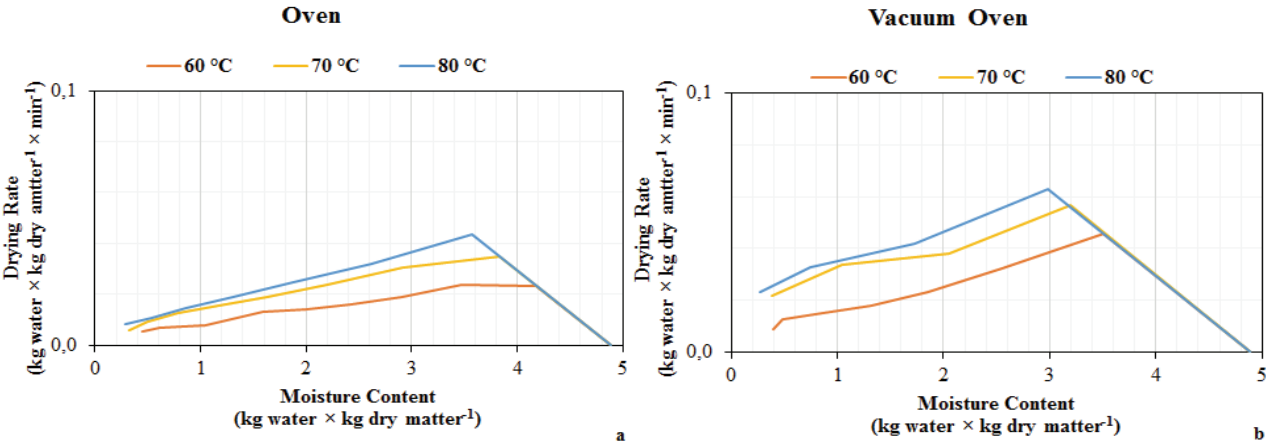

Figure 2. The drying rate curves of shrimps dried: a) in an oven, b) in a vacuum oven.

used with the mathematical models, using non-linear regression analysis. The optimum model was specified in terms of root mean square error (*RMSE*), the coefficient of determination (R^2) and the reduced chi-square error (χ^2), chosen by comparing the other values. R^2 values below 0.994 were not found in any of the drying methods.

In Table 1 it is seen that the Alibas and Midilli and Kucuk models produced the optimum experimental data for the oven and vacuum oven drying methods, respectively. R^2 values were found to be from 0.999834 to 0.999903, and from 0.999493 to 0.999956 for the oven and vacuum oven, respectively. The χ^2 values were found to be from 0.000012 to 0.000016 and from 0.000008 to 0.000144 for the oven and vacuum oven, respectively. *RMSE* values were found to be from 0.0002809 to 0.003673 and from 0.00206 to 0.010381 for the oven and vacuum oven, respectively.

Effective moisture diffusivity values

D_{eff} values were calculated from the equations below. For the oven, D_{eff} values were found to be 1.46×10^{-8}, 2.09×10^{-8} and 2.8×10^{-8} m^2/s for temperatures of 60, 70 and 80 °C, respectively. For the vacuum oven, D_{eff} values were found to be 3.68×10^{-8}, 5.24×10^{-8} and 5.49×10^{-8} m^2/s, for temperatures of 60, 70 and 80 °C, respectively. As seen from the obtained D_{eff} values, the vacuum oven drying had higher diffusion coefficient values than the oven drying. The diffusion coefficient values for the biological materials are within the general range of 10^{-8} to 10^{-12} m^2/s [27]. The temperature increase in meat-type products increases the vapour pressure [13,17,28]. The influence of temperature on the D_{eff} values can be estimated by using Eqs. (13) to (14):

$$\text{Oven} \rightarrow D_{eff} = 7\times10^{-10}T + 3\times10^{-8}\left(R^2 = 0.9985\right) \quad (13)$$

$$\text{Vacuum oven} \rightarrow D_{eff} = 9\times10^{-10}T + 2\times10^{-8}(R^2 = 0.8533) \quad (14)$$

Activation energy values

The estimated values for E_a were 31.65 and 19.72 kJ/mol for the oven and vacuum oven, respectively. Activation energy of oven drying was higher

Table 1. Oven and vacuum oven methods coefficients and statistical data (Avg. R^2>0.9996)

Method	Model	Parameter	Temperature, °C		
			60	70	80
Oven	Alibas	a	0.877978	1.703283	1.767061
		k	0.004299	0.005208	0.007785
		n	1.078032	1.015612	0.946261
		b	-0.000379	0.001377	0.001464
		g	0.122651	-0.702933	-0.767077
		χ^2	0.000014	0.000010	0.000001
		R^2	0.999903	0.999953	0.999997
		RMSE	0.002809	0.002091	0.000537
Oven	Midilli and Kucuk	a	1.000995	0.999681	0.999564
		k	0.004259	0.006041	0.009947
		n	1.058002	1.073694	0.997310
		b	-0.000142	-0.000218	-0.000337
		χ^2	0.000012	0.000013	0.000006
		R^2	0.999899	0.999919	0.999968
		RMSE	0.002862	0.002738	0.001718
Oven	Aghbashlo	k_1	0.005336	0.007812	0.009611
		k_2	-0.000752	-0.001288	-0.001190
		χ^2	0.000016	0.000008	0.000045
		R^2	0.999834	0.999929	0.999645
		RMSE	0.003673	0.002567	0.005793
Vacuum Oven	Aghbashlo	k_1	0.010026	0.011997	0.013738
		k_2	-0.001021	-0.003401	-0.003943
		χ^2	0.000144	0.000193	0.000203
		R^2	0.998826	0.998917	0.998949
		RMSE	0.010381	0.010767	0.011043
Vacuum Oven	Midilli and Kucuk	a	1.000271	0.999609	0.999879
		k	0.014127	0.013263	0.016015
		n	0.908217	0.963495	0.950995
		b	-0.000578	-0.001556	-0.001752
		χ^2	0.000008	0.000226	0.000046
		R^2	0.999956	0.999577	0.999920
		RMSE	0.002006	0.006728	0.003036
Vacuum Oven	Logarithmic	a	1.096500	1.340654	1.323021
		k	0.009246	0.009654	0.011297
		c	-0.102732	-0.342574	-0.324664
		χ^2	0.000074	0.000124	0.000047
		R^2	0.999493	0.999538	0.999839
		RMSE	0.006819	0.007031	0.004315

than vacuum oven drying. The activation energy is inversely related to moisture content, and vacuum drying facilitates moisture removal from food. The values for food product activation energy varied over a range from 12.7 to 110 kJ/mol [27].

Rehydration ratio values

Rehydration characteristic ability is an important feature of food products. It can be addressed as a measure of damage as a result of the drying process. The food product is structurally modified by the drying process and this modification changes water absorption [4,5]. Using Eq. (11), the rehydration ratio values are estimated with the increase in the temperature causing greater rehydration ratio, in that increasing temperature causes decreased drying time. Swelling ratios of oven-dried shrimps remained at 42.85±0.15, 47.19±0.35 and 50.75±0.17% for 60, 70 and 80 °C,

respectively, at 20 °C in 150 min. Swelling ratios of vacuum oven-dried shrimps remained at 32.13±0.12, 45.59±0.21 and 57.91±0.19% for 60, 70 and 80 °C, respectively, at 20 °C in 120 min. The ratio increased due to the increased drying temperature for both methods.

The porosity of the dried products decreased with the increase in drying time. The rehydration process occurs in a shorter time for the vacuum oven method than the oven method, due the more damage occurring in the oven to the pores. The swelling ratios are shown in Figure 3.

Color values

L, *a* and *b* values of the dried shrimps using different methods are shown in Table 2. *L* value changes relate to decreasing drying times for the two methods. *L* values change between 21.74 and 29.03 for the oven method and between 23.48 and 43.06 for the vacuum oven method. The highest and the lowest redness values for *a* were attained in the oven and vacuum oven, respectively. Redness values, *a,* for the oven method changed between 1.51 and 5.04 and for the vacuum oven method between 0.44 and 4.12. The highest and the lowest yellowness values for *b* were obtained in the oven dryer and vacuum oven dryer, respectively. Yellowness values, *b,* for the oven method changed between 3.13 and 7.14 and for the vacuum oven method between 1.58 and 4.75. Drying time and temperature affects the change in color and the highest *L, a* and *b* values of the dried shrimps were obtained from the oven-drying method. The drying temperature increases as the *L* and *b* values increase, but *a* value decreases for both methods.

For the comparison of the total color change, the highest color change is obtained in the oven due to the higher drying times and the lowest color change in the vacuum oven dryer due to the lower drying times.

Analyses of heavy metal content

The heavy metals investigated in the shrimp included arsenic, lead, cadmium, mercury, copper, zinc and iron. These metals can be divided into two classes: toxic (As, Pb, Cd, Hg) and essential elements (Cu, Zn, Fe) [29,30]. For both methods, the heavy metal content analyses were performed for each temperature. Permissible upper limits of heavy metals change according to national and international

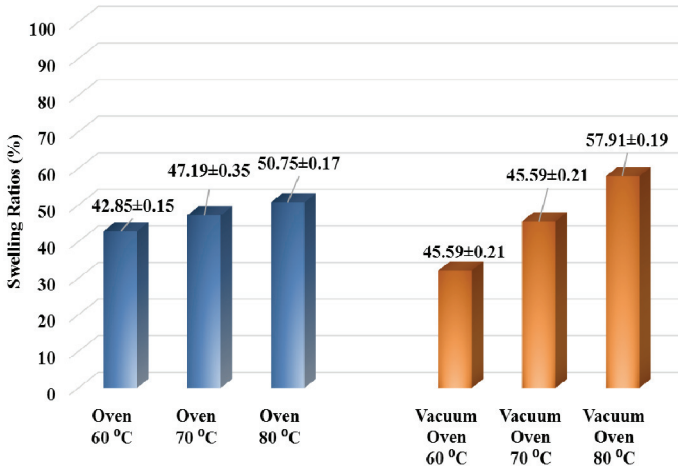

Figure 3. Comparison of swelling ratios between both methods (%).

Table 2. Color values of shrimp dried with oven and vacuum oven methods

Temperature, °C	*L*	*a*	*b*	*ΔE*
Fresh	60.18±0.42	5.36±0.09	1.42±0.01	-
		Oven		
60	21.74±0.18	5.04±0.09	3.13±0.02	38.48±0.24
70	27.59±0.15	3.56±0.10	5.81±0.04	32.93±0.27
80	29.03±0.11	1.51±0.11	7.14±0.06	31.90±0.31
		Vacuum Oven		
60	23.48±0.17	4.12±0.07	1.58±0.03	36.72±0.25
70	33.67±0.14	2.14±0.05	3.57±0.06	26.79±0.29
80	43.06±0.10	0.44±0.04	4.75±0.08	18.12±0.33

standards: FAO (Food and Agriculture Organization) (1983), WHO (World Health Organization, 1989), MAFF (Ministry of agriculture, fisheries and food in the UK, 1995), European Commission (2008, 2014) and Turkish Food Codex (2002) values are given in Table 3 [31-38].

Table 3. Maximum permissible limits (mg/kg) of heavy metal changes according to national and international standards

Standard	As	Pb	Cd	Cu	Zn	Fe	Hg
FAO (1983)	-	0.5	0.5	30	40	-	-
WHO (1989)	-	2	1	30	100	-	-
MAFF (1995)	-	2	0.2	20	50	-	0.5
EC (2008,2014)	-	0.3	0.5	-	30	-	1
Turkish Food Codex (2002)	1	0.5	0.5	20	50	-	0.5

The highest and lowest arsenic content in shrimp were found to be 133.8±5.5 to 99.9±4.1 μg/g, and 135.5±5.5 to 102.7±4.2 μg/g for the oven method and vacuum oven method, respectively. The quantity of Pb changed between 0.065±0.011 to 0.228± ±0.0033 μg/g, and between 0.228±0.0033 and 0.1156 μg/g for the oven method and vacuum oven method, respectively. The quantity of Cd changed between 0.0288±0.0014 and 0.0174±0.0005 μg/g, and between 0.0379±0.0011 and 0.03411±0.001 μg/g for the oven method and vacuum oven method, respectively. The quantity of Cu changed between 11.42±0.32 and 4.08±0.12 μg/g, and between 8.74± ±0.25 and 3.63±0.1 μg/g for the oven method and vacuum oven method, respectively. The quantity of Zn changed between 46.48±1.32 and 34.32± ±0.97 μg/g, and between 43.25±1.23 and 35.9±1.02 μg/g for the oven method and vacuum oven method, respectively. The quantity of Fe changed between 38.78±5.9 and 13.07±0.2 μg/g, and between 132.2±2 and 3.49±0.05 μg/g for the oven method and vacuum oven method, respectively. The quantity of Hg changed between 1.42±0.02 and 0.7±0.01 μg/g, and between 1.2±0.02 and 0.63±0.01 μg/g for the oven method and vacuum oven method, respectively. It was determined that the heavy metal levels of the dried shrimps were below the threshold values. No information could be found about maximum iron level in shrimp samples in any of the standards. The heavy metal content of dried shrimps is given in Table 4.

Protein content analyses

Shrimps have a high protein content like other aquatic creatures. The protein contents changed from 15 to 20%. In addition, the shrimps' protein content before drying was 19.57% [39]. After the drying process, for both methods, the protein ratio increased as the drying temperature increased. Protein rates changed between 83.413 and 85.986% and between 76.882 and 84.152% for the oven method and vacuum oven method, respectively. For both drying procedures, the protein content for dried shrimp is higher than for undried shrimp.

CONCLUSION

This study shows the influences of different drying methods on the quality and physical properties of dried shrimps. Oven and vacuum oven drying curves and the kinetics of shrimps were simultaneously studied at 60, 70 and 80 °C temperatures. Vacuum oven drying time was shorter than oven drying due to the extraction of ambient air with the vacuum pump. The Alibas model and Midilli and Kucuk model gave the best fit for the drying data for oven and vacuum oven drying methods, respectively. The D_{eff} values obtained for the vacuum oven and oven drying methods were found to be 5.49×10^{-8} and 2.8×10^{-8} m^2/s, respectively. The E_a values obtained for the vacuum oven and oven were found to be 19.72 and 31.65 kJ/mol, respectively. The rehydration ratio increased with increasing drying temperature in both methods. In both studied systems, the *L* and *b* values increased with increasing drying temperature while *a* values decreased. Heavy metal analysis showed that the metal content of the dried shrimps was acceptable for human consumption when considering nutritional and toxic levels. For both drying procedures, the protein content of dried shrimp (~85%) was significantly higher than of the undried (~20%). As a continuation of this research, we will study the drying of shrimp

Table 4. Heavy metal contents of dried shrimps (μg/g)

Sample name	As	Pb	Cd	Cu	Zn	Fe	Hg
Oven 60 °C	133.8±5.5	0.065±0.011	0.0288±0.014	11.42±0.32	46.48±1.32	38.78±5.9	1.42±0.02
Oven 70 °C	116.0±4.7	0.0427±0.006	0.0192±0.0006	5.480±0.16	36.16±1.03	13.28±0.2	1.16±0.02
Oven 80 °C	99.9±4.1	<0.011	0.0174±0.0005	4.08±0.12	34.32±0.97	13.07±0.2	0.7±0.01
Vacuum Oven 60 °C	135.5±5.5	0.228±0.0033	0.19±0.0059	3.63±0.1	35.9±1.02	132.2±2	0.63±0.01
Vacuum Oven 70 °C	128.7±5.3	0.380±0.055	0.0379±0.0011	8.74±0.25	43.25±1.23	16.71±0.25	0.68±0.01
Vacuum Oven 80 °C	102.7±4.2	0.116	0.03411±0.001	5.83±0.17	39.08±1.11	3.49±0.05	1.2±0.02

with modern methods and we will compare the advantage and disadvantages of modern and conventional methods.

Acknowledgement

This work was supported by the Yildiz Technical University Scientific Research Projects Coordination Department, Project Number: FDK-2019-3528".

REFERENCES

[1] S.H.M. Ashtiani, M. Rafiee, M.M. Morad, M. Khojastehpour, M.R. Khani, A. Rohani, B. Shokri, A. Martynenko, Innov. Food Sci. Emerg. Technol. 63 (2020) 102381

[2] A.S. Kipcak, İ. Doymaz, Chem. Ind. Chem. Eng. Q. 26 (2020) 203–212

[3] M. Başlar, M. Kılıçlı, O. S. Toker, O. Sağdıç, M. Arici, Innov. Food Sci. Emerg. Technol. 26 (2014) 182-190

[4] I. Doymaz, A.S. Kipcak, S. Piskin, Czech J. Food Sci. 33 (2015) 83-90

[5] I. Doymaz, A.S. Kipcak, S. Piskin, Czech J. Food Sci. 33 (2015) 367-376

[6] N.A. Latiff, L.C. Abdullah, P.Y. Ong, N.A.M. Amin, Chem. Ind. Chem. Eng. Q. 27 (2021)199-206

[7] S.H.M. Ashtiani, B. Sturm, A. Nasirahmadi, Heat Mass Transf. 54 (2018) 915-927

[8] M.V. Traffano-Schiffo, M. Castro-Giráldez, P.J. Fito, N. Balaguer, J. Food Eng. 128 (2014) 103-110

[9] W. Jangsawang, Energy Proc. 138 (2017) 1048-1054

[10] E. Corona, J.V. Garcia-Perez, T.E.G. Alvarez-Arenas, N. Watson, M.J.V. Povey, J. Benedito, J. Food Eng. 119 (2013) 464-470

[11] M.J. Cantalejo, F. Zouaghi, I. Perez-Arnedo, Food Sci. Technol. 68 (2016) 400-407

[12] E. Dinçer, M. Erbaş, Meat Sci. 145 (2018) 114-120

[13] J. Akhtar, P.K. More, Int. J. Chem. Stud. 6 (2018) 1590--1597

[14] T. Tsuruta, T. Hayashi, Dry. Technol. 25 (2007) 1393-1399

[15] S. Tirawanichakul, W.N. Phatthalung, Y. Tirawanichakul, J. Sci. Technol. 5 (2008) 77-100

[16] M. Zhang, H. Chen, A. S. Mujumdar, J. Tang, S. Miao, Y. Wang, Crit. Rev. Food Sci. 57 (2017) 1239-1255

[17] C. A. Komolafe, I. O. Oluwaleye, A. O. D. Adejumo, M. A. Waheed, S. I. Kuye, Int. J. Heat Technol. 36 (2018) 1262-1267

[18] Y. Bai, B. Sun, J. Food. Process. Pres. 35 (2011) 891-897

[19] S. Bellagha, E. Amami, A. Farhat, N. Kechaou, Dry. Technol. 20 (2002) 1527-1538

[20] D. Jain, P.B. Pathare, J. Food Eng. 78 (2007) 1315-1319

[21] A.S. Kipcak, Res. Chem. Intermed. 43 (2017) 1429-1445

[22] A.S. Kipcak, I. Doymaz, E.M. Derun, Chem. Ind. Chem. Eng. Q. 25 (2019) 1-10

[23] AOAC (Association of Official Analytical Chemists), Official Methods of Analysis of AOAC International, 16th ed., AOAC International, Rockville, MD, 1995

[24] A. Vega-Gálvez, I. Quispe-Fuentes, E. Uribe, J. Martinez-Monzo, A. Pasten, R. Lemus-Mondaca, J. Food. 17 (2019) 297-306

[25] A.S. Kipcak, O. İsmail J. Food Sci. Technol. (2020), DOI 10.1007/s13197-020-04540-0

[26] F. Sarpong, C. Zho, J. Bai, L.P. Amenorfe, M.K. Golly, H. Ma, Food Sci. Biotechnol. 28 (2019) 75-85

[27] N.P. Zogzas, Z.B. Maroulis, D. Marinos-Kouris, Food Sci. Biotechnol. 14 (1996) 2225-2253

[28] P. Saadchom, T. Swasdisevi, A. Nathakaranakule, S. Soponronnarit, Food Sci. Biotechnol. 104 (2011) 105-113

[29] Y.G. Gu, Q. Lin, X.H. Wang, F.Y. Du, Z.L. Yu, H. H. Huang, Mar. Pollut. Bull. 96 (2015) 508-512

[30] M. Tuzen, Food Chem. Toxicol. 47 (2009) 1785-1790

[31] Y. A. Candra, M. Syaifullah, B. Irawan, T.W.C. Putranto, D. Hidayati, A. Soegianto, Reg. Stud. Mar. Sci. 26 (2019) 100507

[32] A. Anandkumar, R. Nagarajan, K. Prabakaran, R. Rajaram, Reg. Stud. Mar. Sci. 16 (2017) 79-88

[33] FAO, Compilation of Legal Limits for Hazardous Substance in Fish and Fishery Products. Food and Agricultural Organization, Fishery circular No. 764, 1983

[34] WHO, Heavy Metals Environmental Aspects. Environmental Health Criteria, World Health Organization, Geneva, 1989

[35] MAFF, Monitoring and surveillance of non-radioactive contaminants in the aquatic environment and activities regulating the disposal of wastes at sea, 1993. Aquatic Environment Monitoring Report No. 44, Direcorate of Fisheries Research, Lowestoft, 1995

[36] EC, 2008. Commission Regulation. No 629/2008 of July 2008 amending Regulation (EC) No 1881/2006 setting maximum levels for certain contaminants in foodstuffs.

[37] EC, Commission Regulation No. 488/2014 of 12 May 2014 Amending Regulation (EC) No 1881/2006 as regards maximum levels of cadmium in foodstuffs, 2014

[38] Turkish Food Codex, Regulation of Setting Maximum Levels for Certain Contaminants in Foodstuffs, Official Gazette, 23 September 2002, Issue 24885

[39] S. Volker, E. Dana, World Euphausiacea database, World Register of Marine Species 67 (1852) 370-372.

ALI CAN ERSAN[1,2]
NURCAN TUGRUL[1]

[1]Yildiz Technical University, Faculty of Chemical and Metallurgical Engineering, Department of Chemical Engineering, Istanbul, Turkey
[2]Istanbul Esenyurt University, Vocational High School, Department of Occupational Health and Safety, Istanbul, Turkey

NAUČNI RAD

KINETIKA SUŠENJA I KARAKTERISTIKE ŠKAMPA SUŠENIH KONVENCIONALNIM METODAMA

Osnovna svrha ovog rada bila je istraživanje uticaja različitih metoda sušenja na fizička i svojstva kvaliteta sušenih škampa. Račići su sušeni konvencionalnim metodama na 60, 70 i 80 °C između 330 min do 210 min, odnosno 190 do 110 min, u rerni, odnosno u vakuumskoj peći. Vreme sušenja se skraćuje upotrebom vakuum pumpe. Proučavana je kinetika sušenja škampa i izračunata je efektivna difuzija vlage i energija aktivacije za obe metode. Alibasov model, odnosno Midilli-Kucuk model najbolje fituju eksperimentalne podatke sa visokim koeficijentom determinacije (R^2) za rernu, odnosno vakuum peći. Finalni osušeni proizvodi su okarakterisani ispitivanjem karakteristika boje, sadržaja teških metala i analizom proteina. Odnos rehidratacije je, takođe, određen za dehidrirane škampe. Uslovi sušenja su uticali na karakteristike boje, tako da su škampi sušeni u rerni i vakuum peći pokazivali povećanje vrednosti svetline i žute boje i smanjenje vrednosti crvenila. Koncentracije As, Pb, Cd, Hg, Cu, Zn i Fe u sušenim škampima bile su u prihvatljivim granicama. Sadržaj proteina u sušenim škampima (~85%) je veći od nesušenih škampa (~20%).

Ključne reči: škampi, kinetika sušenja, rehidratacija, sadržaj proteina, analiza boje, teški metal.

CI&CEQ
Chemical Industry & Chemical Engineering Quarterly

Available on line at
Association of the Chemical Engineers of Serbia *AChE*
www.ache.org.rs/CICEQ

Chem. Ind. Chem. Eng. Q. 27 (4) 329–340 (2021) CI&CEQ

J.N.M. BATISTA
R. BÉTTEGA

Federal University of São Carlos, Department of Chemical Engineering, SP, Brazil

SCIENTIFIC PAPER

UDC 633.17:66:544:519.87

EVALUATION OF DIFFERENT MATHEMATICAL MODELS IN THE CFD-DEM SIMULATION OF CONICAL SPOUTED BED FLUID DYNAMICS

Article Highlights

- A conical spouted bed, applied to drying operations, was simulated by CFD-DEM
- Different particle rotation conditions, turbulence, and drag models are evaluated
- Analysis of particle rotation indicates its importance in CFD-DEM simulation
- Koch-Hill and Gidaspow drag models showed better agreement with the experimental data
- The standard *k-ε* turbulence model showed a greater agreement with experimental data

Abstract

The input parameters, empirical, and semi-empirical models significantly influence the responses obtained by CFD-DEM simulations. In this work, the effects of three turbulence models, three conditions of the particle rotation, and five drag models, on the fluid dynamic behavior of a conical spout bed applied to the drying of sorghum grains were evaluated. Experimental data on the solids pressure drop, height, and shape of the fountain were used to validate the simulations. Results showed the importance of including the particle rotation in the model to approximate the results simulated with the experimental behavior. Compared with experimental data, considering the particle rotation by the Dennis et al. model, the deviation was 2% for the fountain height and 9.18% for the pressure drop. Whereas, for the model without the particle rotation, the deviations were 106.33 and 42.31% for the fountain height and pressure drop, respectively. For the analyzed case, the standard k-ε turbulence model showed a greater agreement with the experimental data. For the drag models evaluated, the best fit with the experimental data was obtained by the Koch-Hill drag model, followed by the Gidaspow model, with deviations less than 10%.

Keywords: drag model, particle rotation, turbulence model, sorghum grains.

The mathematical modeling of the fluid dynamic behavior in spouted beds follows two main methods. The first, known as two-fluid model (TFM), considers the solid and fluid phases as continuous and interpenetrating, and the properties of the solid phase can be described by the kinetic theory of granular flow (KTGF). This approach is widely used [1-4]. The second, called computational fluid dynamics/discrete element method coupled (CFD-DEM), considers the fluid phase as continuous, while the solid phase is treated as discrete from the modeling of the individual motion of each particle present in the system. Studies that employ CFD-DEM are being conducted mainly to evaluate fluid dynamics characteristics [5-8]. Through this method, it is possible to obtain information on the particle scale, such as the forces acting between particle-particle, particle-wall, as well as track the particle individually. For the success of simulations applying this approach, it is essential to determine the DEM input parameters, which are divided into: material properties (average equivalent diameter, sphericity and specific mass) and interaction

Correspondence: R. Béttega, Federal University of São Carlos, Department of Chemical Engineering, SP, Brazil.
E-mail: bettega@ufscar.br
Paper received: 15 September, 2020
Paper revised: 18 December, 2020
Paper accepted: 8 January, 2021

https://doi.org/10.2298/CICEQ110707002B

properties (restitution coefficient, static friction coefficient, and rolling friction coefficient).

In the CFD-DEM coupled, many parameters and models are applied to describe the behavior of the solid and fluid phases, and these have a great influence on the simulated response. Rotation is a natural feature of particle motion. Marchelli *et al.* [9] mention the importance of considering its effect, mainly in gas--solid flows involving particles with larger diameters. The authors analyzed the influence of the rotational drag force and the effect of neglecting the particle rotation on the dynamics of glass spheres in a pseudo-2D spouted bed. The simulated results showed that in neglecting the particle rotation, there was an imprecise prediction of the particle motion, though this consideration did not affect the formation of a central and linear spout channel, and oscillations could be observed. Although its effect is important, in many studies it is neglected.

Turbulence is an important point in CFD simulations and can have a strong influence on the simulated results. Turbulence models can be grouped into three classes: direct numerical simulation (DNS), large Eddy simulation (LES), and Reynolds-average Navier-Stokes (RANS). Within the RANS modeling, with regard to the two equation turbulence models, the standad k-ε model is widely used, due to its robustness, lower computational cost and reasonable precision for a wide range of turbulent flows. Proposed by Launder and Spalding [10], the k-ε model describes the freestream flow regions. The SST k-ω model includes both a model for addressing the wall regions and another for the regions with greater turbulence, interspersing the standard model k-ω and the model k-ε, respectively. This model was developed by Menter [11]. Regarding the use of turbulence models in CFD-DEM simulations applied to spouted beds, the most applied are: standard k-ε [5,12,13], RNG k-ε [14], realizable k-ε [15], and SST k-ω [16]. In some studies, turbulence is not considered in CFD--DEM simulations [17,18]. Marchelli *et al.* [9] investigated the effect of four turbulence models (standard k-ε model, standard k-ε model with an enhanced wall treatment (EWT), realizable k-ε model, standard k-ω model) and lack of a turbulence model (laminar case) in spouted bed by CFD-DEM simulations. The standard k-ε and k-ω models produce almost identical results. Accord to Yang *et al.* [19], an appropriate turbulence model is necessary to predict the central jet that penetrates the bed materials, since the lack of knowledge of the turbulence results in the difficulty to model the spout-annulus interface in the spouted bed. However, it should be noted that there is no consensus on the most appropriate model to describe the turbulence in spouted beds using CFD-DEM simulations.

The drag is mainly responsible for the momentum exchange between the phases in a gas-solid flow. The literature reports several models to obtain the drag coefficient. In TFM simulations, the Gidaspow drag model [20] is widely used in spouted bed simulations [3,4,21-23]. However, there is no such agreement for CFD-DEM simulations. The drag models most used in CFD-DEM simulations are: Wen and Yu [24], Gidaspow [20] and Di Felice [25], developed through classical approaches (*e.g.*, empirical methods), and models proposed by means of Lattice-Boltzmann simulations: Rong, Dong, Yu [26], Beetstra, Van Der Hoef, Kuipers [27], Koch and Hill [28]. In order to evaluate the effect of these models in CFD--DEM simulations, several studies have been developed to identify the influence of the drag model in the simulations. He *et al.* [29] evaluated the influence of Gidaspow [20], and Koch and Hill [28] drag models in a rectangular fluidized bed with dry and wet granular systems. The authors found better results simulated by the drag model by Koch and Hill [28]. Zhang *et al.* [30] analyzed the binary mixture segregation of glass spheres (2.5 and 1.5 mm) in a rectangular fluidized spouted bed evaluating different drag models [20,26,31,32]. The results predicted by Rong, Dong, Yu [26] presented smaller deviations (5.3%) compared to the experimental. Pietsch *et al.* [15] analyzed the particle dynamics of a three-dimensional prismatic spouted bed using the drag models of Beetstra, Van Der Hoef, Kuipers [27], Di Felice [25], Gidaspow [20], and Koch and Hill [28]. The drag models of Beetstra, Van Der Hoef, Kuipers [27] and Koch and Hill [28] predicted with greater precision the expansion of the bed and the establishment of the spout regime. Furthermore, Marchelli *et al.* [13] employed the four drag models described above, added to the Rong, Dong, Yu [26], Tenneti, Garg, Subramaniam [33] and Wen and Yu [24] to evaluate the fluid dynamics of two spouted beds in different configurations (pseudo-2D and 3D cylindrical). The authors observed that in the simulations where the minimum fluidization flow was applied, only the Gidaspow model [20] can predict the fluidization, but for low air flow rates, the Beetstra, Van Der Hoef, Kuipers [27] model was more suitable for predicting the characteristic behavior of the spouted bed.

The simulated results vary significantly with the models used to calculate the drag force, turbulence, and particle rotation, among others. In many cases, models are used without justification. Generally, the

simulated data is not validated with experimental data, only a qualitative analysis is performed. Thus, due to lack of agreement on which drag model is more effective for the experimental data reproducibility, we assessed the influence of drag models of Beetstra, Van Der Hoef, Kuipers [27], Di Felice [25], Gidaspow [20], Koch and Hill [28] and Rong, Dong, Yu [26]. In addition to the drag models, the effect of standard k-ε, realizable k-ε, and SST k-ω turbulence models were also analyzed, and the influence of the particle rotation condition, considering the torque equal to zero, calculating the rotational drag coefficient by the model of Dennis *et al.* [34], and neglecting the particle rotation, on the fluid dynamic behavior of the conical spouted bed applied to drying operations, operating with sorghum grains through CFD--DEM simulations. Experiments were carried out to validate the models analyzed.

EXPERIMENTAL METHODOLOGY

Experimental unit

The spouted bed used in the experiments was constructed in acrylic, with a cylindrical column with a height of 30 cm and a diameter of 14.2 cm, with a 60° conical base with a height of 11 cm and a lower diameter of 2.5 cm. A Venturi-type air distributor was attached to the bottom of the conical base. Figure 1a shows the dimensions of the equipment.

Experimental procedure

Fluid dynamic tests were performed according to the methodology proposed by Mathur and Epstein [35]. The tests were carried out in triplicate, for 500 g of sorghum grains. This method consists of obtaining pressure drop curves as a function of air velocity for increasing velocities (fixed bed to stable spout regime) and decreasing velocities (stable spout regime to fixed bed).

Sorghum grains characterization

In this work, sorghum grains were used as particulate material. The characterization of this material was carried out in a previous work [5]. Therefore, the physical and particle-particle interaction properties were the same as in this work. To obtain the particle-wall interactions, the methodology described in this work was used, using an acrylic surface with the same characteristics as the spouted bed wall (thickness of 3 mm).

MATHEMATICAL METHODOLOGY

Mathematical modeling

Simulations were performed using the CFD--DEM coupled. The fluid phase was assumed to be continuous, with its motion described by the Navier-Stokes equations, since air is considered a Newtonian fluid. The particulate phase was treated as a discrete phase and the particle motion was evaluated using Newton's second law.

Equations of governing fluid phase

The mass and momentum conservation equations for the fluid phase are presented in Eqs. (1) and (2), respectively:

$$\frac{\partial}{\partial t}\left(\alpha_f \rho_f\right) + \nabla \cdot \left(\alpha_f \rho_f \vec{v}_f\right) = 0 \quad (1)$$

$$\frac{\partial}{\partial t}\left(\alpha_f \rho_f \vec{v}_f\right) + \nabla \cdot \left(\alpha_f \rho_f \vec{v}_f \vec{v}_f\right) = \alpha_f \nabla p + \nabla . \bar{\bar{\tau}}_f - \vec{F} + \alpha_f \rho_f \vec{g} \quad (2)$$

where α_f, ρ_f, $\vec{v}_f$, ∇p, and $\bar{\bar{\tau}}_f$ are the volume fraction, density, velocity, pressure, and shear stress of the

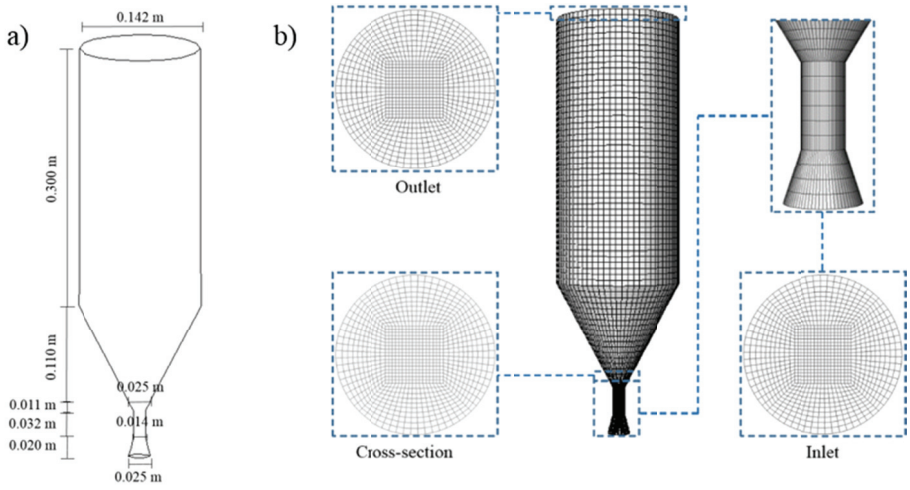

Figure 1. a) schematic illustration of the spouted bed; b) representation of the computational grid.

fluid phase, respectively, and $\vec{g}$ is the gravitational acceleration.

The fluid volume fraction (α_f) in a computational cell (V_{cel}) can be estimated by Eq. (3) [36]:

$$\alpha_f = 1 - \frac{1}{V_{cel}} \sum_{i=1}^{k_v} \sigma_i V_{s,i} \quad (3)$$

where σ_i is the volume fraction of particle *i* in the fluid cell.

Drag force. The volumetric fluid-particle interaction force ($\vec{F}$) can be obtained using the drag force, according to Eq. (4):

$$\vec{F} = \frac{1}{V_{cel}} \sum_{i=1}^{k_v} \vec{f}_i^{\,d} \quad (4)$$

where V_{cel} is the volume of the computational cell and k_v is the number of particles in the cell.

The drag force ($\vec{f}_i^{\,d}$) can be calculated using Eq. (5):

$$\vec{f}_i^{\,d} = \frac{V_{s,i}\beta_{fs}}{1-\alpha_f}\left(\vec{v}_f - \vec{v}_s\right) \quad (5)$$

where $V_{s,i}$ and $\vec{v}_s$ are the volume and velocity of the particle, respectively. β_{fs} is the interphase momentum exchange coefficient, obtained by:

$$\beta_{fs} = \frac{\alpha_s \mu_f}{d_s^2} D \quad (6)$$

where α_s and d_s are the volume fraction and diameter of the particles, respectively, μ_f is the fluid viscosity. D is the drag function; it can be calculated with different drag models. Most of these models are of empirical or half-empirical nature. In this study, different drag models were investigated.

Gidaspow drag model

Through the Gidaspow model [20], D is calculated by:

$$D = 18\alpha_f{}^{-3.65}\left[1 + 0.15\left(\alpha_f Re_s\right)^{0.687}\right], \quad \alpha_f > 0.8 \quad (7)$$

$$D = 150\frac{\alpha_s}{\alpha_f{}^2} + 1.75\frac{Re_s}{\alpha_f}, \quad \alpha_f \le 0.8 \quad (8)$$

$$Re_s = \frac{\rho_f d_s |\vec{v}_s - \vec{v}_f|}{\mu_f} \quad (9)$$

Di Felice drag model

For the Di Felice model [25], D is obtained as:

$$D = 0.75 C_D Re_s \alpha_f{}^{2-\chi} \quad (10)$$

$$C_D = \left(0.63 + \frac{4.8}{\sqrt{\alpha_f Re_s}}\right)^2 \quad (11)$$

$$\chi_{Di\ Felice} = 3.7 - 0.65 e^{\left\{-\frac{\left[1.5 - log_{10}\left(\alpha_f Re_s\right)\right]^2}{2}\right\}} \quad (12)$$

where C_D is the drag force coefficient, and Re_s is the particle Reynolds number.

Rong, Dong, Yu drag model

The Rong, Dong, Yu [26] model can be considered an enhancement of the Di Felice drag model [25]; it uses the same drag function, and only varies in the definition of χ:

$$\chi_{Rong} = 2.65\left(\alpha_f + 1\right) - (5.3 - 3.5\alpha_f)\alpha_f^2 e^{\left\{-\frac{\left[1.5 - log_{10}\left(\alpha_f Re_s\right)\right]^2}{2}\right\}} \quad (13)$$

Koch and Hill drag model

In the Koch and Hill model [28], the drag function (D) is calculated by:

$$D = 18\alpha_f(F_0 + 0.5F_1\alpha_f Re_s) \quad (14)$$

$$F_0 = \frac{1+3\sqrt{\frac{\alpha_s}{2}}+\frac{135}{64}\alpha_s \ln(\alpha_s)+16.14\alpha_s}{1+0.681\alpha_s-8.48\alpha_s^2+8.16\alpha_s^3}, \quad \alpha_s \le 0.4 \quad (15)$$

$$F_0 = \frac{10\alpha_s}{\alpha_s^3}, \quad \alpha_s > 0.4 \quad (16)$$

$$F_1 = 0.0673 + 0.212\alpha_s + 0.0232\alpha_f^{-5} \quad (17)$$

Beetstra, Van Der Hoef, Kuipers drag model

For the Beetstra, Van Der Hoef, Kuipers model [27], the drag function (D) is obtained by the equation:

$$D = 18\alpha_f F_B \quad (18)$$

$$F_B = 10\frac{\alpha_s}{\alpha_s^2} + \alpha_s^2\left(1 + 1.5\sqrt{\alpha_s}\right) + \frac{\left(\frac{0.413 Re_s}{24\alpha_s^2}\right)\left(\frac{1}{\alpha_s}+3\alpha_f\alpha_s+8.4Re_s^{-0.343}\right)}{1+10^{3\alpha_s}Re_s^{-0.5-2\alpha_s}} \quad (19)$$

Turbulence. The Reynolds stress tensor of the fluid phase ($\bar{\bar{\tau}}_f$) is expressed as follows:

$$\bar{\bar{\tau}}_f = -\frac{2}{3}\left(\alpha_f\rho_f k + \alpha_f\rho_f\mu_{f,t}\nabla\cdot\vec{v}_f\right)\bar{\bar{I}} + \alpha_f\rho_f\mu_{f,t}\left(\nabla\vec{v}_f + \nabla\vec{v}_f^{\,T}\right) \quad (20)$$

For modeling the turbulence, two-equation models are historically the most widely used turbulence models in industrial CFD. Examples of such models are the *k-ε* and *k-ω* models in their different forms. They solve two transport equations and model the Reynolds stresses using the turbulent viscosity approach.

Standard k-ε model

The standard *k-ε* model for the dispersed phase was used to simulate the turbulent nature of the bed flow. The turbulent viscosity ($\mu_{f,t}$) is computed as:

$$\mu_{f,t} = \rho_f C_\mu \frac{k^2}{\varepsilon} \quad (21)$$

where C_μ is a constant that was set to 0.09 in all simulations. The parameters k and ε are the turbulence kinetic energy and turbulence energy dissipation

rate, respectively, which are governed by the following transport equations:

$$\frac{\partial}{\partial t}\left(\alpha_f \rho_f k\right) + \nabla \cdot \left(\alpha_f \rho_f \vec{v}_f k\right) = \nabla \cdot \left(\alpha_f \frac{\mu_{t,f}}{\sigma_k} \nabla k\right) + \alpha_f G_k - \alpha_f \rho_f \varepsilon \quad (22)$$

$$\frac{\partial}{\partial t}\left(\alpha_f \rho_f \varepsilon\right) + \nabla \cdot \left(\alpha_f \rho_f \vec{v}_f \varepsilon\right) = \nabla \cdot \left(\alpha_f \frac{\mu_{t,f}}{\sigma_\varepsilon} \nabla \varepsilon\right) + \alpha_f \frac{\varepsilon}{k}\left(C_1 G_k - C_2 \rho_f \varepsilon\right) \quad (23)$$

where σ_k=1 and σ_ε=1.3 are the turbulent Prandtl numbers for k and ε, respectively. C_1=1.44 and C_2=1.92 are model constants. G_k denotes the generation of turbulence kinetic energy by the mean velocity gradient and is given by:

$$G_k = \mu_{f,t}\left(\nabla \vec{v}_f + \left(\nabla \vec{v}_f\right)^{\mathrm{T}}\right) : \nabla \vec{v}_f \quad (24)$$

Realizable k-ε model

The turbulent viscosity ($\mu_{f,t}$) is calculated in the same form as the standard k-ε model. But, in the realizable k-ε model, C_μ is not constant. It is computed from:

$$C_\mu = \frac{1}{4.04 + A_s \frac{kU^*}{\varepsilon}} \quad (25)$$

$$U^* \equiv \sqrt{S_{ij} S_{ij} + \widetilde{\Omega}_{ij} \Omega_{ij}} \quad (26)$$

$$\widetilde{\Omega}_{ij} = \Omega_{ij} - 2\varepsilon_{ijk}\omega_k \quad (27)$$

$$\Omega_{ij} = \overline{\Omega_{ij}} - \varepsilon_{ijk}\omega_k \quad (28)$$

where $\overline{\Omega_{ij}}$ is the mean rate-of-rotation tensor viewed in a moving reference frame with the angular velocity ω_k. The constant A_s is given by:

$$\mathrm{A}_s = \sqrt{6} cos\varphi \quad (29)$$

$$\varphi = \frac{1}{3} cos^{-1}\left(\sqrt{6} W\right) \quad (30)$$

$$W = \frac{S_{ij} S_{jk} S_{ki}}{\tilde{S}^3} \quad (31)$$

$$\tilde{S}^3 = \sqrt{S_{ij} S_{ij}} \quad (32)$$

$$S_{ij} = \frac{1}{2}\left(\nabla \vec{v}_f\right) \quad (33)$$

The modeled transport equations for k and ε in the k-ε realizable model are:

$$\frac{\partial}{\partial t}\left(\alpha_f \rho_f k\right) + \nabla \cdot \left(\alpha_f \rho_f \vec{v}_f k\right) = \nabla \cdot \left(\alpha_f \frac{\mu_{t,f}}{\sigma_k} \nabla k\right) + \alpha_f G_k - \alpha_f \rho_f \varepsilon \quad (34)$$

$$\frac{\partial}{\partial t}\left(\alpha_f \rho_f \varepsilon\right) + \nabla \cdot \left(\alpha_f \rho_f \vec{v}_f \varepsilon\right) = \nabla \cdot \left(\alpha_f \frac{\mu_{t,f}}{\sigma_\varepsilon} \nabla \varepsilon\right) + \alpha_f \varepsilon C_1 S - \alpha_f C_2 \rho_f \frac{\varepsilon^2}{k + \sqrt{\nu\varepsilon}} \quad (35)$$

$$C_1 = max\left[0.43, \frac{\eta}{\eta + 5}\right] \quad (36)$$

$$\eta = S\frac{k}{\varepsilon} \quad (37)$$

$$S = \sqrt{2 S_{ij} S_{ij}} \quad (38)$$

where σ_ε=1.2.

SST k-ω model

For the SST k-ω model, the turbulent viscosity ($\mu_{f,t}$) is computed as:

$$\mu_{f,t} = \frac{\rho_f k}{\omega} \frac{1}{max\left[\frac{1}{\alpha^*}, \frac{SF_1}{\alpha_1 \omega}\right]} \quad (39)$$

$$F_1 = tanh(\phi_1^2) \quad (40)$$

$$\phi_1 = max\left[2\frac{\sqrt{k}}{0.09\omega y}, \frac{500\mu_f}{\rho_f y^2 \omega}\right] \quad (41)$$

where S is the strain rate magnitude, and where y is the distance to the next surface.

The turbulence kinetic energy, k, and the specific dissipation rate, ω, are obtained from the following transport equations:

$$\frac{\partial}{\partial t}\left(\alpha_f \rho_f k\right) + \nabla \cdot \left(\alpha_f \rho_f \vec{v}_f k\right) = \nabla \cdot \left[\alpha_f \left(\mu_f + \frac{\mu_{f,t}}{\frac{1}{\frac{F_2}{\sigma_{k,1}} + \frac{1 - F_2}{\sigma_{k,2}}}}\right) \nabla k\right] + \alpha_f G_k \quad (42)$$

$$\frac{\partial}{\partial t}\left(\alpha_f \rho_f \omega\right) + \nabla \cdot \left(\alpha_f \rho_f \vec{v}_f \omega\right) = \nabla \cdot \left[\alpha_f \left(\mu_f + \frac{\mu_{t,f}}{\frac{1}{\frac{F_2}{\sigma_{\omega,1}} + \frac{1 - F_2}{\sigma_{\omega,2}}}}\right) \nabla \omega\right] + \alpha_f G_\omega \quad (43)$$

where:

$$F_2 = tanh(\phi_2^4) \quad (44)$$

$$\phi_2 = min\left[max\left(\frac{\sqrt{k}}{0.09\omega y}, \frac{500\mu_f}{\rho_f y^2 \omega}, \frac{4\rho_f k}{\sigma_{\omega,2} D_\omega^+ y^2}\right)\right] \quad (45)$$

$$D_\omega^+ = max\left(2\rho_f \frac{1}{\sigma_{\omega,2}} \frac{1}{\omega} \nabla k \nabla \omega, 10^{-10}\right) \quad (46)$$

$\sigma_{k,1}$=1.176, $\sigma_{\omega,1}$=2.0, $\sigma_{k,2}$=1.0, $\sigma_{\omega,2}$=1.168 and α_1=0.32 are model constants. G_ω represents the generation of ω and is given by:

$$G_\omega = \frac{\rho_f \alpha \alpha^*}{\mu_{f,t}} G_k \quad (47)$$

where:

$$\alpha^* = \alpha_\infty \left(\frac{0.24 + \frac{\rho_f k}{6\mu_f \omega}}{1 + \frac{\rho_f k}{6\mu_f \omega}}\right) \quad (48)$$

$$\alpha_\infty = 0.55 F_2 + 0.44(1 - F_2) \quad (49)$$

More details about the turbulence models can be seen in [37].

Equations of particle motion

A particle with mass m_i and moment of inertia I_i has translational and rotational motions, described by Eqs. (50) and (51), respectively:

$$m_i \frac{d\vec{v}_{si}}{dt} = \vec{f}_i^{\,d} + \vec{f}_{ij}^{\,c} + \vec{f}_i^{\,g} \tag{50}$$

$$I_i \frac{d\vec{\omega}_i}{dt} = \vec{T} = \frac{\rho_f}{2}\left(\frac{d_p}{2}\right)^5 C_\omega |\vec{\Omega}|.\vec{\Omega} \tag{51}$$

where $\vec{v}_{si}$ and $\vec{\omega}_i$ are the translational and angular velocities of particle *i*, respectively, $\vec{f}_i^{\,g}$ is the gravitational force, $\vec{f}_{ij}^{\,c}$ is the contact force acting on particle *i* by particle *j* or the wall, $\vec{T}$ is the torque, C_ω is the rotational drag coefficient, and $\vec{\Omega}$ is the relative particle-fluid angular velocity.

Rotation is a natural characteristic of particle motion. To evaluate the effect of the particle rotation in the fluid dynamics of the spouted bed, simulations were performed neglecting the particle rotation (where Eq. (51) is neglected), considering the torque equal to zero ($\vec{T} = 0$), and calculating the rotational drag coefficient by Eq. (52), developed by Dennis *et al.* [34]:

$$C_\omega = \frac{6{,}45}{\sqrt{Re_\omega}} + \frac{32{,}1}{Re_\omega} \tag{52}$$

$$Re_\omega = \frac{\rho_f |\vec{\Omega}| d_s^2}{4\mu_f} \tag{53}$$

where Re_ω is the rotational Reynolds number.

In the soft-sphere approach, the particles slightly overlap during collisions, considering the unit vector $\vec{e}_{12}$ and the overlap (δ) of two colliding particles 1 and 2, defined by Eqs. (54) and (55), respectively:

$$\vec{e}_{12} = \frac{(\vec{x}_2 - \vec{x}_1)}{\|\vec{x}_2 - \vec{x}_1\|} \tag{54}$$

where $\vec{x}_1$ and $\vec{x}_2$ represent the particle position vectors 1 and 2, respectively.

$$\delta = \|\vec{x}_2 - \vec{x}_1\| - (r_1 - r_2) \tag{55}$$

where r_1 and r_2 represent the radii of particles 1 and 2, respectively.

The spring-dashpot collision law requires the definition of a spring constant (K), as in the spring collision law, along with a coefficient of restitution (η) for the dashpot term:

$$\vec{F}_1 = -\vec{F}_2 = (K\delta + \gamma(\vec{v}_{12}.\vec{e}_{12}))\vec{e}_{12} \tag{56}$$

in which:

$$f_{loss} = \sqrt{\pi^2 + ln^2\eta} \tag{57}$$

$$m_{12} = \frac{m_1 m_2}{m_1 + m_2} \tag{58}$$

$$t_{coll} = f_{loss}\sqrt{\frac{m_{12}}{K}} \tag{59}$$

$$\gamma = -2\frac{m_{12} ln\eta}{t_{coll}} \tag{60}$$

$$\vec{v}_{12} = \vec{v}_2 - \vec{v}_1 \tag{61}$$

where f_{loss} is a loss factor, m_1 and m_2 are the masses of particles 1 and 2, respectively, m_{12} is the so-called "reduced mass", t_{coll} is the collision time scale, $\vec{v}_1$ and $\vec{v}_2$ are the velocities of particles 1 and 2, respectively, $\vec{v}_{12}$ is the relative velocity, and γ is the damping coefficient.

The friction force between the particles was based on the Coulomb friction law:

$$\vec{F}_{friction} = (\mu_s + \mu_R)\vec{F}_{normal} \tag{62}$$

where μ_s is the static friction coefficient, μ_R is the rolling friction coefficient, and $\vec{F}_{normal}$ is the magnitude of the force normal to the surface.

Simulation setup and computational grid

To evaluate the models, CFD-DEM simulations were performed for the air inlet velocity of 22 m/s and a mass of 500 g of sorghum grains, which corresponds to 21,300 particles. The simulations were performed using the Fluent® software. The geometries were constructed in Design Modeler and the grids were generated using Meshing, which is available in Ansys® Student version 19.1. The 3D computational grid was constructed in accordance with the spacing between nodes determined in the grid independence test performed in our previous work [5]. The computational grid showed spacing between the nodes of $1d_s$ in the Venturi air distributor. On the conical base, the spacing between nodes was $1.35d_s$ at the entrance of the cone, and $8d_s$ at the intersection with the cylinder, and $8d_s$ in the cylindrical region, totaling 1.680 cells. Figure 1b shows the computational grid used in the CFD-DEM simulations.

The particle-particle and particle-wall interaction properties employed in the CFD-DEM simulations are shown in Table 1.

Table 1. Interaction properties

Interaction	η	μ_S	μ_R
Particle-particle	0.46±0.02	0.79±0.09	0.70±0.10
Particle-wall	0.53±0.04	0.65±0.05	0.33±0.06

Table 2 shows the models and parameters of the numerical solution used in the CFD-DEM simulations.

In CFD-DEM simulations, some considerations were made. The modeling assumes an isothermal

condition, with the physical properties of the solid phase constant ($\rho_s = 1300\,\frac{kg}{m^3}, d_s = 0{,}0032\,m, \varphi = 1$), and the air properties were also constant.

Table 2. Boundary conditions, models and numerical solution parameters adopted in CFD-DEM simulations

Boundary conditions	Inlet: inlet velocity
	Outlet: outlet pressure
	Wall: no-slip for the fluid phase
Solution methods	Pressure-velocity coupling was obtained using the SIMPLE algorithm
	Spatial discretization:
	Momentum: QUICK
	Volume fraction: QUICK
	Turbulence: First order upwind
	Transient formulation: First order implicit
Turbulence	Turbulent intensity: 5%
	Turbulent viscosity ratio: 10
Spring constant (*K*)	1000 N/m
Convergence criterion	$1x10^{-3}$
Time step	Fluid phase: $1x10^{-4}$
	Solid phase: $2x10^{-5}$
Time step number	100,000
Max. iterations/time step	200
Under-relaxation factors	Momentum: 0.2
	Volume fraction: 0.5
	Discrete phase: 0.5

Drag models from Beetstra, Van Der Hoef, Kuipers [27], Di Felice [25], Koch and Hill [28] and Rong, Dong, Yu [26] were implemented to Fluent® through UDF (user defined function). The Gidaspow model [20] is available on Fluent®.

RESULTS AND DISCUSSION

Fluid dynamics analysis

Figure 2 shows the fluid dynamics curves obtained experimentally for the 500 g of sorghum grains; the results show a satisfactory reproducibility between the curves. Through a qualitative analysis, the typical spouted bed behavior is observed. For low air velocities, the fluid just percolates through the bed, without particle motion, as shown in Figure 3i. With the increase in air velocity, the pressure drop also increases, reaching a maximum value with the formation of the internal jet and an increase in the arc of solids (Figure 3ii). Then, with an additional increase in air velocity, the internal jet becomes extended in relation to the compact arc of solids, reducing the pressure drop, and the downward motion of the solids in the annular region begins. Subsequently, the solids are dragged into the central region, the bed expands, further reducing the pressure drop. With an increase in air velocity, the incipient spout is observed and then the minimum spout condition is observed (Figure 3iii). After the minimum spout condition, the spout becomes stable. The minimum spouting velocity is an important operational parameter, the value measured for the mass of 500 g was 17.10±0.20 m/s.

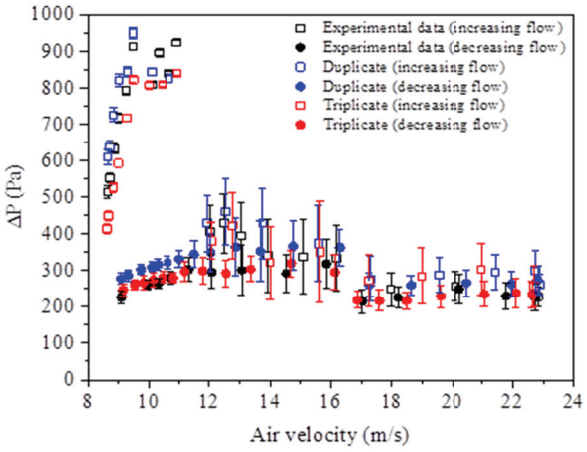

Figure 2. Experimental fluid dynamic curves for the 500 g mass.

After carrying out the experiments, simulations were conducted at an air velocity of 22 m/s, corresponding to the stable spout regime.

Effect of particle rotation

The results were obtained considering an average of 6 s of simulated real time. Figure 4 shows the experimental flow pattern, simulated by CFD-DEM using the Dennis *et al.* [34] model to calculate the rotational drag coefficient (Eq. (52)), considering the torque equal to zero, and neglecting the particle rotation. Similar behavior can be seen when the Dennis *et al.* [34] model was used to calculate the rotational drag coefficient and considering the torque equal to zero; the behavior was similar to the experimental behavior. When the particle rotation was neglected, a flow pattern different from the experimental can be observed, with a high and diluted fountain.

To quantify these observations, it was based on fountain height and pressure drop, parameters characteristic of the spouted bed. Table 3 presents the simulated results for the different conditions of particle rotation and experimental results for the fountain height and pressure drop.

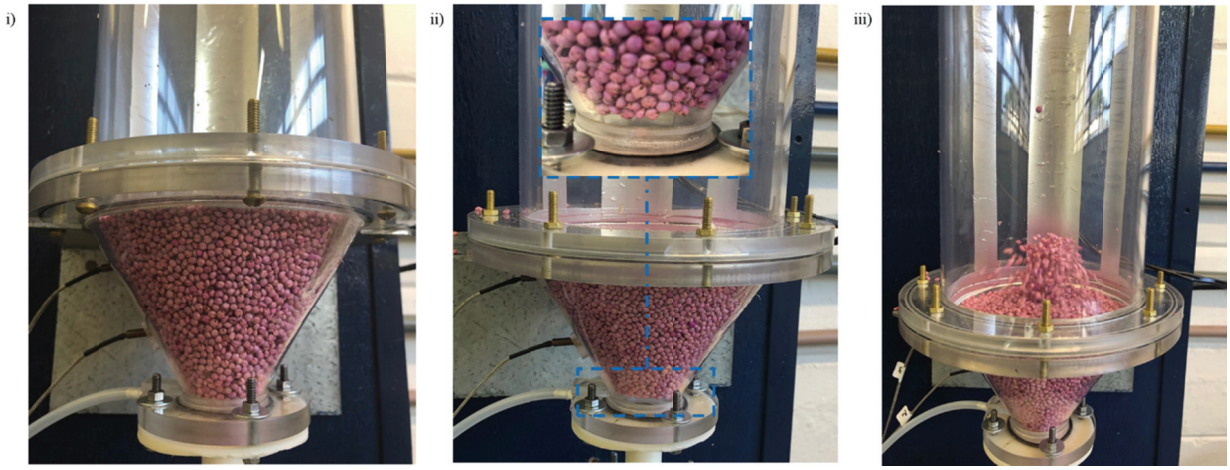

Figure 3. Development of a spouted regime: i) fixed bed; ii) internal jet (arc of solids); iii) minimum spout.

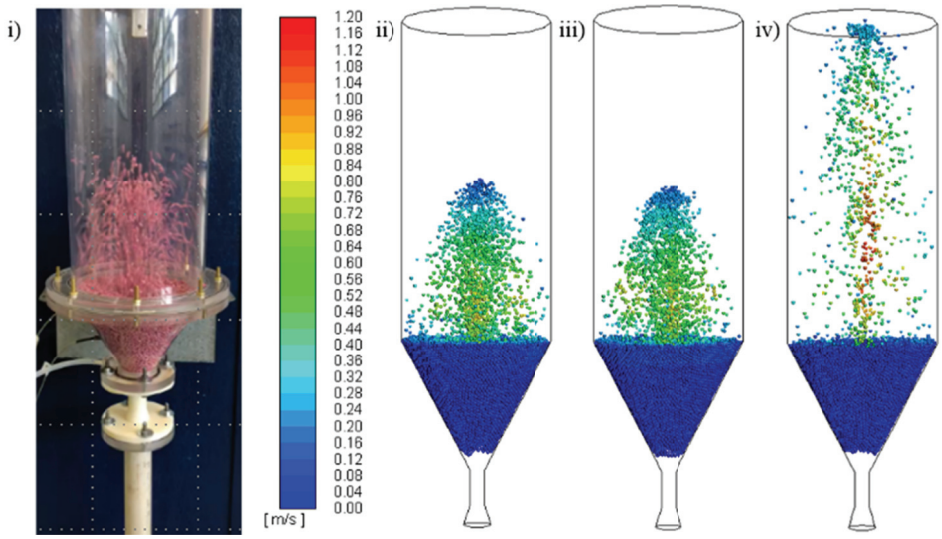

Figure 4. Solids flow pattern: i) experimental; ii) Dennis et al. [34] model; iii) $\vec{T} = 0$; iv) without particle rotation.

Table 3. Comparison between experimental data of fountain height and pressure drop, and simulated by different rotation conditions

Condition	H_f (m)	Deviation (%)	ΔP (Pa)	Deviation (%)
Experimental	14.54		238.27	
Dennis *et al.* [34]	14.83	-2.00	216.40	9.18
$\vec{T} = 0$	13.80	5.08	206.90	13.16
Without particle rotation	30	106.33	137.45	42.31

For both parameters, the deviations between the experimental data and data simulated by the Dennis *et al.* [34] model were lower than 10%. Although the case in which the torque was equal to zero showed a low deviation from the experimental value, this hypothesis is less realistic, since the angular velocity is assumed constant. The highest deviation observed when neglecting the particle rotation is coherent, since the particle rotation is a phenomenon observed experimentally. The deviations between experimental and simulated data can be related to some simplification by the model used, as the angular velocity calculation. For the simulations to evaluate the turbulence models, the Dennis *et al.* [34] model was chosen, because this model had better agreement with the experimental data.

Effect of the turbulence models

There are several turbulence models reported in the literature. The *k-ω* model is known to provide better results in the wall regions. However, for the spouted bed simulated in this work, it can be seen in Figure 5a that results for the standard *k-ε* and SST *k-ω* models are similar in the region close to the wall. This result may be related to the fact that the computational grid employed in CFD-DEM simulations shows

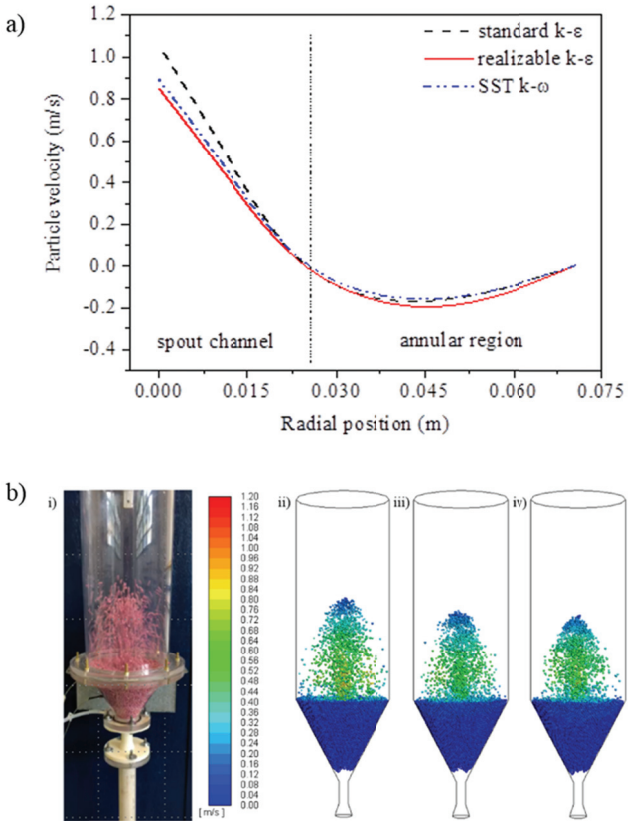

Figure 5. a) particle velocity for different turbulence models at the position of 0.173 m; b) solids flow pattern for different turbulence models: i) experimental; ii) standard k-ε; iii) realizable k-ε; iv) SST k-ω.

high spacing between nodes, which may have minimized the effects of the SST *k-ω* model in the wall region; a similar observation was found in [9]. Figure 5b shows the fountain shape obtained experimentally, simulated by CFD-DEM using the standard turbulence *k-ε*, realizable *k-ε* and SST *k-ω* models. Table 4 shows the fountain height and pressure drop, experimental and simulated, for different turbulence models. Qualitatively, these parameters showed that the best fit was obtained for the standard *k-ε* model. Thus, for the conditions simulated in this work, the standard *k-ε* model was the most adequate.

Table 4. Comparison between experimental data of fountain height and pressure drop, and data simulated by the different turbulence models

Model	H_f (m)	Deviation (%)	ΔP (Pa)	Deviation (%)
Experimental	14.54		238.27	
Standard *k-ε*	14.83	-2.00	216.40	9.18
Realizable *k-ε*	13.26	8.80	209.70	11.99
SST *k-ω*	12.56	13.62	207.46	12.93

CFD-DEM simulations carried out with the objective of evaluating the drag models were performed using the standard *k-ε*, and the Dennis *et al.* [34] model, since these models showed better agreement with the experimental data.

Effect of the drag models

Figure 6a shows the experimental flow pattern obtained by the different drag models for the inlet air velocity of 22 m/s. It can be observed that there was no particle drag for the models of Di Felice [25], and Rong, Dong, Yu [26]; the bed of solids remained static for both models. According to Marchelli *et al.* [13], Di Felice [25] and Rong, Dong, Yu [26] models produce similar values for the drag force. Greater fountain heights and a very similar behavior between the models of Gidaspow [20], and Koch and Hill [28] can be verified, which are in accordance with the experimental flow pattern. Although the equations for calculating the drag coefficient are different, the two models present different equations for the different fluid volumetric fraction ranges (porosity). The Beetstra, Van Der Hoef, Kuipers [27] model underestimated the solid drag, with a small and narrow fountain.

To quantify the simulated results, Table 5 presents a comparison between the fountain height and pressure drop data, experimental and simulated, with the different drag models. Both for the fountain height

and for the pressure drop, it can be verified that the Gidaspow [20], and Koch and Hill [28] models presented low deviations in relation to the experimental value. As for the pressure drop, there is a smaller deviation for the Beetstra, Van Der Hoef, Kuipers [27] model, however, this model showed a high deviation for the fountain height. High deviations were observed for Di Felice [25], and Rong, Dong, Yu [26] models for both evaluated properties.

Table 5. Comparison between experimental data of fountain height and pressure drop, and data simulated by different drag models

Model	H_f (m)	Deviation (%)	ΔP (Pa)	Deviation (%)
Experimental	14.54		238.27	
Beetstra [21]	9.43	35.14	236.24	0.85
Di Felice [19]	0	100.00	368.94	54.84
Gidaspow [12]	14.83	-2.00	216.40	9.18
Koch and Hill [22]	14.55	0.07	224.46	5.80
Rong [20]	0	100.00	354.04	48.59

Figure 6b shows the axial solid velocity as a function of the radial position for the five drag models analyzed. The data were obtained at the position of 0.173 m (referring to the static bed height, positioned at the intersection between the cone and the cylinder). It can be seen that the solids reach higher velocities in the spout channel for the models of Gidaspow [20], Koch and Hill [28], and Beetstra, Van Der Hoef, Kuipers [27] models, respectively, causing the larger fountain heights. This behavior is related to the higher drag force values obtained by these models. In spouted beds, drag is predominant in the spout channel, justifying the observed profiles. Zero velocity was observed for the models of Di Felice [25], and Rong, Dong, Yu [26].

CONCLUSIONS

The simulations showed the influence of the turbulence, drag, and particle rotation models on the results obtained, highlighting the importance of the appropriate choice of models for agreement with the experimental data. For the evaluated properties (solid flow pattern, fountain height, and pressure drop), the results obtained through the drag model of Koch and Hill [28], followed by the Gidaspow [20], were those that presented the best agreement with experimental data; deviations lower than 10% were obtained for these models. For the drag models of Di Felice [25], and Rong, Dong, Yu [26] there was no particle drag. For the case presented in this study, the standard k-ε turbulence model and the Dennis *et al.* [34] model were the most appropriate for calculating the rotational drag coefficient. The importance of considering

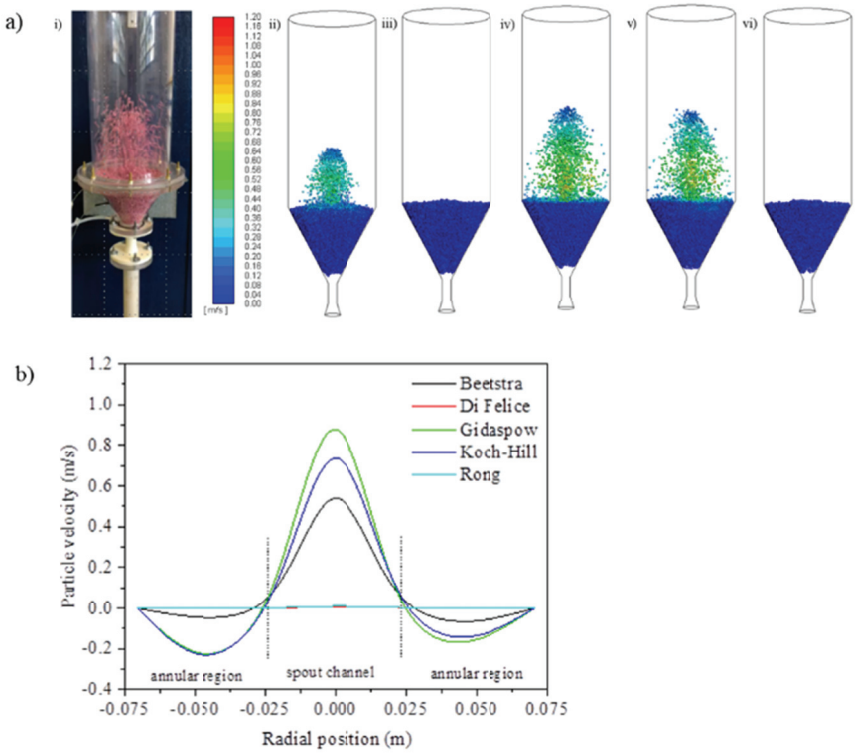

Figure 6. a) solids flow pattern for different drag models: i) experimental; ii) Beetstra, Van Der Hoef, Kuipers [21]; iii) Di Felice [19]; iv) Gidaspow [12]; v) Koch and Hill [22]; vi) Rong, Dong, Yu [20]; b) axial solid velocity for different drag models.

particle rotation to obtain a realistic behavior was also observed.

Acknowledgement

Authors appreciate the financial support from Coordenação de Aperfeiçoamento de Pessoal de Nível Superior - Brasil (CAPES) - Finance Code 001 and Conselho Nacional de Desenvolvimento Científico e Tecnológico - Brasil (CNPq).

Nomenclature

C_1, C_2, C_μ	Coefficients in turbulence model
C_D	Drag force coefficient
C_ω	Rotational drag coefficient
D	Drag function
d_s	Particle diameter, m
$\vec{f}_i^d$	Drag force on particle *i*, N
$\vec{f}_i^g$	Gravitational force on particle *i*, N
$\vec{f}_{ij}^c$	Contact force between particles *i* and *j*, N
$\vec{F}$	Volumetric force acting on particles by the surrounding fluid, N/m^3
G_k	Production of turbulent kinetic energy, J/(m^3·s)
$\vec{g}$	Gravitational acceleration, m/s^2
H_f	Fountain height, m
h_0	Static bed height, m
$\bar{\bar{I}}$	Unit tensor
I_i	Moment of inertia of particle *i*, kg/m^2
K	Spring stiffness, N/m
k_v	Number of particles in the cell
m_i	Mass of particle *i*, kg
p	Pressure, N/m^2
Re_s	Particle Reynolds number
Re_ω	Rotational Reynolds number
$\vec{T}$	Torque, N·m
t	Time, s
t_{coll}	Collision time, s
$\vec{v}$	Velocity, m/s
V	Volume, m³
V_{cell}	Volume of computational cell, m^3
$V_{s,i}$	Volume of particle *i*, m^3

Greek symbols

α	Volume fraction
β	Interphase momentum exchange coefficient
γ	Damping coefficient, kg/s
ε	Turbulence energy dissipation rate, m^2/s^3
ΔP	Pressure drop, Pa
δ	Overlap, m
η	Restitution coefficient
k	Turbulence kinetic energy, m^2/s^2
μ_f	Fluid viscosity, Pa·s
μ_s	Static friction coefficient
μ_R	Rolling friction coefficient
ρ	Density, kg/m^3
σ_i	Fraction of volume of particle *i* that is in the fluid cell
$\vec{\tau}_f$	Shear stress of fluid, N/m^2
φ	Sphericity
χ	Function of α_f and Re_s in the Di Felice and Rong models
Ψ	Asymptotic range
$\vec{\omega}_i$	Rotational velocity of particle *i*, rad/s
ω	Specific dissipation rate, m^2/s^3

Subscripts

f	Fluid
i	Particle *i*
j	Particle *j*
s	Solid/particle
w	Wall

Abbreviations

CFD	Computational fluid dynamics
DEM	Discrete element method
2D	Bidimensional
UDF	User defined function

REFERENCES

[1] B. Hooshdaran, S.H. Hosseini, M. Haghshenasfard, M.N. Esfahany, M. Olazar, CAppl. Therm. Eng. 127 (2017) 224-232

[2] E.F. Ahmadabadi, M. Haghshenasfard, M.N. Esfahany, Chem. Eng. Res. Des. 160 (2020) 476-485

[3] J.N.M. Batista, R.C. Brito, R. Béttega, Chem. Ind. Chem. Eng. Q. 24 (2018) 369-378

[4] A.S. Souza, J.T. Freire, R. Béttega, Ind. Eng. Chem. Res. 57 (2018) 13876-13888

[5] J.N.M. Batista, D.A. Santos, R. Béttega, Particuology (2020)

[6] F. Marchelli, D. Bove, C. Moliner, B. Bosio, E. Arato, Powder Technol. 321 (2017) 119-131

[7] H. Zhang, M. Liu, T. Li, Z. Huang, X. Sun, H. Bo, Y. Dong, Powder Technol. 307 (2017) 175-183

[8] S. Golshan, R. Zarghami, N. Mostoufi, Chem. Eng. Res. Des. 121 (2017) 315-328

[9] F. Marchelli, C. Moliner, B. Bosio, E. Arato, Powder Technol. 353 (2019) 409-425

[10] B. Launder, D.B. Spalding, Lectures in mathematical models of turbulence, Academic Press Inc, London, 1972

[11] F.R. Menter, in Proceedings of 24th Fluid Dynamics Conference, July 6-9, 1993, Orlando, FL

[12] B. Mahmoodi, S.H. Hosseini, G. Ahmadi, Particuology. 43 (2019) 171-180

[13] F. Marchelli, Q.F. Hou, B. Bosio, E. Arato, A.B. Yu, Powder Technol. 360 (2020) 1253-1270

[14] V. Salikov, S. Antonyuk, S. Heinrich, V.S. Sutkar, N.G. Deen, J.A.M. Kuipers, Powder Technol. 270 (2015) 622–636

[15] S. Pietsch, S. Heinrich, K. Karpinski, M. Müller, M. Schönherr, F. Kleine, C Powder Technol. 316 (2017) 245–255

[16] P. Breuninger, D. Weis, I. Behrendt, P. Grohn, F. Krull, S. Antonyuk, Particuology 42 (2019) 114-125

[17] Y. Yue, T. Wang, Y. Shen, Powder Technol. 366 (2020) 736-746

[18] M. Ebrahimi, E. Siegmann, D. Prieling, B.J. Glasser, J.G. Khinast, Adv. Powder Technol. (2017)

[19] S. Yang, K. Luo, K. Zhang, K. Qiu, J. Fan, Powder Technol. 272 (2015) 85-99

[20] D. Gidaspow, Multiphase flow and fluidization: Continuum and kinetic theory descriptions, Academic Press, New York, 1994

[21] R. Béttega, C.A. da Rosa, R.G. Corrêa, J.T. Freire, Ind. Eng. Chem. Res. 48 (2009) 11181–11188

[22] C.A. Da Rosa, J.T. Freire, Ind. Eng. Chem. Res. 48 (2009) 7813–7820

[23] F. Wu, J. Zhang, X. Ma, W. Zhou, Adv. Powder Technol. 29 (2018) 1848-1858

[24] C.Y. Wen, Y.H. Yu, Mechanics of Fluidization, Chem. Eng. Prog. Symp. Ser. 62 (1966) 100-111

[25] R. Di Felice, Int. J. Multihase Flow 20 (1994) 153-159

[26] L.W. Rong, K.J. Dong, A.B. Yu, Chem. Eng. Sci. 116 (2014) 508-523

[27] R. Beetstra, M.A. van der Hoef, J.A.M. Kuipers, Fluid Mech. Transp. Phenom. 5 (2007) 489-501

[28] D.L. Koch, R.J. Hill, Anu. Rev. Fluid Mech. 33 (2001) 619–647

[29] Y. He, W. Peng, T. Tang, S. Yan, Y. Zhao, Adv. Powder Technol. 27 (2016) 93-104

[30] Y. Zhang, Y. Zhao, L. Lu, W. Ge, J. Wang, C. Duan, Chem. Eng. Sci. 160 (2017) 106-112

[31] S. Sarkar, M.A. Van Der Hoef, J.A.M. Kuipers, Chem. Eng. Sci. 64 (2009) 2683–2669

[32] F. Cello, A. Di Renzo, F.P. Di Maio, Chem. Eng. Sci. 65 (2010) 3128-3139

[33] S. Tenneti, R. Garg, S. Subramaniam, Int. J. Multiphase Flow 37 (2011) 1072-1092

[34] S.C.R. Dennis, S.N. Singh, D.B. Ingham, J. Fluid Mech. 101 (1980) 257-279

[35] K.B. Mathur, N. Epstein, Spouted Beds, Academic Press, New York, 1974

[36] B.P.B. Hoomans, J.A.M. Kuipers, W.J. Briels, W.P.M. Van Swaaij, Chem. Eng. Sci. 51 (1996) 99-118

[37] Ansys, Chapter 4: Turbulence, ANSYS FLUENT Theory Guid, ANSYS, 2020.

J.N.M. BATISTA
R. BÉTTEGA

Federal University of São Carlos, Department of Chemical Engineering, SP, Brazil

NAUČNI RAD

VREDNOVANJE RAZLIČITIH MATEMATIČKIH MODELA U CFD-DEM SIMULACIJI DINAMIKE KONUSNOG FONTANSKOG SLOJA

Ulazni parametri, empirijski i poluempirijski modeli značajno utiču na odgovore dobijene CFD-DEM simulacijama. U ovom radu je procenjen uticaj tri modela turbulencije, tri uslova rotacije čestica i pet modela otpora na dinamičko ponašanje fluida konusnog fontanskog sloja korišćenog za sušenje zrna sirka. Eksperimentalni podaci o padu pritiska čvrstih materija, visini i obliku fontane korišćeni su za validaciju simulacija. Rezultati su pokazali važnost uključivanja rotacije čestica u model radi aproksimiranja rezultata simuliranih eksperimentalnim ponašanjem. U poređenju sa eksperimentalnim podacima, uzimajući u obzir rotaciju čestica po modelu Denisa i saradnika, odstupanje je bilo 2% za visinu fontane i 9,18% za pad pritiska. Za model bez rotacije čestica odstupanja su iznosila 106,33% i 42,31% za visinu fontane i pad pritiska, redom. Za analizirani slučaj, standardni k-ε model turbulencije pokazao je veće slaganje sa eksperimentalnim podacima. Za procenjene modele otpora, najbolje uklapanje sa eksperimentalnim podacima je dobijen Koh-Hilovim modelom otpora, a zatim modelom Gidaspaua, sa odstupanjima manjim od 10%.

Ključne reči: model otpora, rotacija čestica, model turbulencije, zrna sirka.

CI&CEQ
Chemical Industry & Chemical Engineering Quarterly

Available on line at
Association of the Chemical Engineers of Serbia AChE
www.ache.org.rs/CICEQ

Chem. Ind. Chem. Eng. Q. 27 (4) 341–354 (2021) CI&CEQ

REDOUANE OUAFI[1]
ANASS OMOR[1]
YOUNES GAGA[2]
MOHAMED AKHAZZANE[1]
MUSTAPHA TALEB[1]
ZAKIA RAIS[1]

[1]Engineering Laboratory of Organometallic, Molecular Materials and Environment, Faculty of Science Dhar El Mahraz, Sidi Mohamed Ben Abdellah University, Route d'immouzer, Fez, Morocco
[2]Laboratory of Biotechnology, Ecology and Preservation of Natural Resources, Faculty of Science, Dhar El Mahraz, Sidi Mohamed Ben Abdellah University, Route d'immouzer, Fez, Morocco

SCIENTIFIC PAPER

UDC 544.723:58:66

PINE CONE POWDER FOR THE ADSORPTIVE REMOVAL OF COPPER IONS FROM WATER

Article Highlights

- Valorisation of a natural waste in the treatment of copper ions from aqueous solutions
- The adsorption process was successfully represented by pseudo-second-order kinetic model
- Langmuir isotherm model describes the adsorption of Cu(II) ions onto pine cone powder
- The functional group study set the role of hydroxyl, carboxyl and phenolic groups in metal binding
- Pine cone powder can be used as adsorbent for the removal of copper ions from aqueous solution

Abstract

This research investigates the adsorption potential of pine cone powder (PCP) for the removal of copper ions (Cu(II)) from aqueous solutions. The process of adsorption was reasonably fast, completed within a time of 60 min. The pseudo-second order kinetic model describes properly the Cu(II) adsorption by PCP. The adsorbent was characterised by various instrumental techniques and batch experiments were conducted to investigate the effect of PCP dose, solution pH, particle size and initial Cu(II) concentration on adsorption efficiency. Optimum Cu(II) removal occurred at a slightly acidic pH, with a particle size less than 100 μm. The effective PCP dose was estimated to be 36 g L^{-1}. The increase in the initial concentration of Cu (II) was accompanied by a reduction in the rate of its reduction by almost half. The Langmuir model was the best fitting isotherm with a maximum adsorption capacity of 9.08 mg g^{-1}. The thermodynamic parameters values showed that the Cu(II) adsorption was a spontaneous and endothermic process. The results of this research suggest that Cu(II) could be removed through an environmentally friendly process using PCP as low-cost natural waste.

Keywords: copper ion removal, isotherms, kinetic, natural waste, pine cone powder, water treatment.

The growth of industrial activity has resulted in the discharge of large quantities of pollutants including dyes, phenols, oil, toxic salts and heavy metals. The toxic nature of these contaminants constitutes a severe threat to human health and the whole biological system. Consequently, their treatment remains a topic of scientific interest [1]. Among these pollutants, copper is one of the most prevalent heavy metal pollutants in the environment because of its extensive use in many industries. It is used in electronics, construction, electroplating, surface treatment and brass industry. At high levels, chronic overexposure to copper can lead to various health effects on human beings, including liver and kidney damage, Wilson's disease and carcinogenicity [2,3]. Thus, because of its toxic properties at high levels, copper-contaminated water should be treated before its discharge in the environment.

In recent decades, a growing interest in natural, available and low-cost adsorbents has been observed, and they have been extensively used for heavy metal and other pollutant removal [4]. Therefore, various materials have been investigated as adsorbents

Correspondence: R. Ouafi, Sidi Mohamed Ben Abdellah University, Route d'immouzer, B.P 2626, Fez, Morocco.
E-mail: redouane.ouafi@usmba.ac.ma
Paper received: 1 January, 2020
Paper revised: 4 December, 2020
Paper accepted: 12 January, 2021

https://doi.org/10.2298/CICEQ200101001O

to remove different types of pollutants from wastewater. These materials include mineral materials, synthetic organic materials, agriculture wastes, industrial by-products and natural residues [5-7].

One of the most important challenges that face researchers in adsorption investigations is the selection of favourable types of biomass among numerous materials. Sawdust has been widely studied for its property to remove pollutants from wastewater. It is considered as an economic, efficient, sustainable and green process. It was hence extensively reported as a low-cost potent remedial tool [8].

In parallel with the ongoing research for cheaper, viable and probable adsorbents, the efficiency of pine cones for Cu(II) removal has been investigated. Further, it will be a step forward in exploring the possibility of using waste biomass to remove pollutants from wastewater. Pine cone is abundant in nature, requires little processing and represents an unused resource. It contains various organic compounds such as cellulose, hemicellulose and lignin, which contain several groups that would attach compounds through different mechanisms [9-12]. Preliminary research have previously shown the potential use of pine cones in the treatment of various compounds [13-15]. However, very few works have reported its applicability for Cu(II) removal [16-18]. The aim of this work was to deepen the studies of different depollution parameters influencing the use of this natural waste in the treatment of wastewater. Thus, a local pine cone, collected from the peri-urban forests in Fez, Morocco, was investigated for its application for the treatment of Cu(II) from aqueous solutions. The kinetics were studied by applying pseudo-first order, pseudo-second order, intraparticle diffusion and Elovich kinetics models. The effect of the experimental parameters such as pH of solutions, adsorbent dose, initial metal concentration, and contact time on the adsorption efficiency were inspected. The characterisation of the products before and after the reaction was carried out by using physicochemical technique. Langmuir, Freundlich, Redlich-Peterson and Dubinin-Radushkevich isotherm models were used to analyse experimental data of Cu(II) adsorption by PCP. Thermodynamic analysis was used to describe the nature of the process.

MATERIALS AND METHODS

Adsorbent material preparation

The pine cones (*Pinus halepensis*) were collected from the peri-urban forests in Fez, Morocco. The cone scales were removed and then rinsed extensively with distilled water. The materials were oven-dried at 60 °C for 48 h. The above dried natural waste was ground to a fine powder. The resulting pine cone powder (PCP) was sieved and stored for experimental purposes.

Preparation of aqueous metal ions solutions

The solutions of Cu(II) were prepared by dissolving 3.927 g of $CuSO_4{\cdot}5H_2O$ in deionised water obtained by Barnstead EASYpure II system to achieve a concentration of 1000 mg L^{-1}. Experimental solutions of the desired concentrations of metal ions were prepared by diluting the stock solution in deionised water. The pH of the solutions was adjusted using 0.1 N HCl and 0.1 N NaOH to achieve the desired values. The pH measurements were performed using a Hanna pH-meter model HI 2221.

Metal concentration analysis

The metal concentration analysis was determined using inductively coupled plasma atomic emission spectroscopy (ICP-AES) model Activa from Horiba Jobin-Yvon, equipped with an argon plasma, cyclonic chamber and concentric nebuliser.

Physicochemical characterisation

The pH and the electrical conductivity (EC) were determined by placing 1 g of PCP in contact with 100 mL of distilled water and then shaken for 24 h. After filtering the suspension, the pH and EC values of the filtrate were measured using a Hanna pH-meter model HI 2221. The point of zero charge of PCP (pH_{pzc}) was determined by solid addition method in our previous research [19].

The specific surface area (S_{BET}) was measured using a Gemini VII 2390t surface area analyser (Micromeritics Instruments Corp.) The value of S_{BET} was determined from the N_2 adsorption isotherms by applying the Brunaeur-Emmett-Teller (BET) equation at a relative pressure range of 0.05-0.30 and an average area per molecule of N_2 in a completed monolayer (σ_m) of 0.162 nm².

Scanning electron microscopy (SEM) was carried out by a FEI-Quanta 200 environmental scanning electron microscope under a vacuum of 90 Pa, an accelerating voltage (*HV*) of 15 kV and a working distance (*WD*) of 9.8 mm.

The Fourier-transform infrared spectroscopy (FTIR) was recorded using Bruker FTIR spectrophotometer model Vertex 70, in the range of 400–4000 cm^{-1}, using ATR mode; 16 scans were accumulated at a resolution of 4 cm^{-1}.

The X-ray diffraction pattern (XRD) of the sample was obtained using a Panalytical X'Pert Pro

X-ray diffractometer equipped with a CuKα monochromatic source (1.54 Å), operating at a voltage of 40 kV and a filament current of 40 mA. The diffraction pattern was recorded from 5 to 40° (2θ) at a scan step time of 90.17 s.

The thermal gravimetric analysis (TGA) and the differential thermal analysis (DTA) were performed using a Shimadzu DTG-60H instrument under air atmosphere, with a heating rate of 20 °C/min from 27 to 1000 °C. The sample mass introduced was 11.16 mg.

Kinetic study

The adsorption kinetic was conducted using the batch method. The experiments were carried out in 100 mL Erlenmeyer flasks containing 1.8 g of adsorbent mixed with 50 mL of Cu(II) solution at an initial concentration of 100 mg L^{-1}, a pH of 5.3 and a temperature equal to 25 °C. The flasks were agitated at a constant speed of 200 rpm in a shaker incubator (Cleaver Scientific Ltd). After specified intervals of time from 5 to 180 min, the solutions were collected and filtered using a 0.22 μm filter paper. The Cu(II) concentrations were determined using ICP-AES.

The amounts of metal ions adsorbed on the adsorbent phase q_t (mg g^{-1}) were calculated from the following expression:

$$q_t = \frac{(C_0 - C_t)V}{m} \tag{1}$$

where C_0 and C_t are the initial metal ions concentration and concentration at a defined time (mg L^{-1}), V is the solution volume (L) and m is the mass of the adsorbent (g).

Pseudo-first-order (PFO) [20], pseudo-second-order (PSO) [21], the intraparticle diffusion [22] and Elovich [23] model, in linearised form, were selected to examine the ability of these types of kinetic models to describe adsorption of Cu(II) by PCP.

Batch adsorption experiments

The adsorption experiments in batch modes were carried out by bringing into contact in 100 ml flasks a determined quantity of adsorbents, with 50 mL of a synthetic solution of Cu(II) at the desired concentration. The flasks were stirred in a shaker incubator (Cleaver Scientific Ltd.) at the required temperature and time. After sufficient contact time, allowing the adsorption to reach equilibrium, the solutions were collected and filtered. Afterwards, the Cu(II) concentrations in the filtrate were determined.

The amount of adsorbate per gram of adsorbent denoted q_e (mg/g) was calculated from the following expression:

$$q_e = \frac{(C_0 - C_e)V}{m} \tag{2}$$

The Cu(II) elimination rate R (%) was defined by:

$$R = 100\frac{C_0 - C_e}{C_0} \tag{3}$$

where C_e is the residual metal ions concentration measured at equilibrium (mg L^{-1}).

Effect of adsorption parameters

The effect of adsorbent dose was determined by varying the amount of PCP from 0.1 to 2.8 mg, the measured amount of PCP was stirred in a 100 mL Erlenmeyer flask with 50 mL of 100 mg L^{-1} Cu(II) at 25 °C.

The effect of pH on the adsorption process was examined maintaining the described batch experiments and varying the pH of the solution from 2 to 8 in a solution of initial Cu(II) concentration of 100 mg L^{-1} with adsorbents mass of 1.8 g at 25 °C.

The effect of particle size of PCP was examined through different particle size powders (50, 100, 200, 300 and 800 μm) with a solution of initial Cu(II) concentration equal to 100 mg L^{-1}, an adsorbent mass of 1.8 g, temperature of 25 °C and a solution pH of 5.3.

The effect of metal concentration on Cu(II) elimination rate was examined by varying the Cu(II) concentration from 20 to 500 mg L^{-1} with an adsorbent mass of 1.8 g, particle size powder of 50 μm and temperature equal to 25 °C. The pH of the solution remained at 5.3.

Equilibrium isotherm models

Langmuir [24], Freundlich [25], Dubinin-Radushkevich [26] and Redlich-Peterson [27] models were used to describe the distribution of metal ions between liquid and solid phases. To calculate the parameters of isotherm models accurately in batch experiments, the use of the nonlinear method rather than the linear method has been advised by numerous researchers [28]. Nonlinear optimisation is a mathematically rigorous method to determine the parameters of the adsorption model using the original form of the equation. Accordingly, the isotherm models were fitted through the Levenberg-Marquardt algorithm using OriginPro software.

Thermodynamic study

The thermodynamic parameters were investigated at 298, 313, 323 and 333 K. The standard free energy changes (ΔG), standard enthalpy change (ΔH) and standard entropy change (ΔS) were calculated according to the following equations [29]:

$$\Delta G = -RT \ln K_c \quad (4)$$

$$\Delta G = \Delta H - T\Delta S \quad (5)$$

$$\ln K_c = -\frac{\Delta H}{R}\frac{1}{T} + \frac{\Delta S}{R} \quad (6)$$

where R is the universal gas constant (8.3144 J mol^{-1} K^{-1}), T is the absolute temperature (K), and K_c the equilibrium constant.

According to previous research [30-32], the equilibrium constant K_c could be derived from the Langmuir constant using the following equation:

$$K_c = 63.54 \times 55.5 \times 1000 K_L \quad (7)$$

where the 55.5 (mol L^{-1}) is the number of moles of pure water per litre, 63.54 (g mol^{-1}) is the molecular weight of adsorbate (copper), 1000 (g L^{-1}) is the value for the density of water and K_L is the Langmuir constant (L mg^{-1}).

Error functions

The goodness of the experimental data fit to the proposed kinetic and isotherm models was evaluated by the coefficient of determination, which is also known as R-squared (R^2) and by Adj. R-squared (R_{adj}^2). In general, the closer R^2 and R_{adj}^2 to 1, the better the fitted line fits the data. Their values are between 0 and 1.

RESULTS AND DISCUSSION

Characteristics of PCP

SEM analysis

The irregularity, roughness and heterogeneous texture characterised the raw PCP surface (Figure 1a). These surface distortion gives a favourable condition for the retention of Cu(II) between the interstices. These characteristics were also reported by other research [33,34]. The inspection of SEM images after Cu(II)-loaded PCP (Figure 1b) revealed no obvious difference compared to the raw PCP material.

FTIR analysis

The FTIR spectra of both raw PCP and PCP after metal adsorption given in Figure 2 present various bands characteristic of the chemical structure of cellulose. The FTIR spectral analysis of raw PCP was interpreted in a detailed manner in our previous investigation [19]. Compared to raw PCP spectrum, spectrum of Cu(II)-loaded PCP shows a decrease in the intensity of the major infrared bands.

The band intensity of the OH groups decreased significantly and shifted from 3301 to 3350 cm^{-1} after Cu (II) adsorption suggesting the possible formation of complexes between OH groups and metal loaded. The shift in the bands from 1718 to 1734 cm^{-1} was probably due to Cu(II) and carboxylic groups bonding.

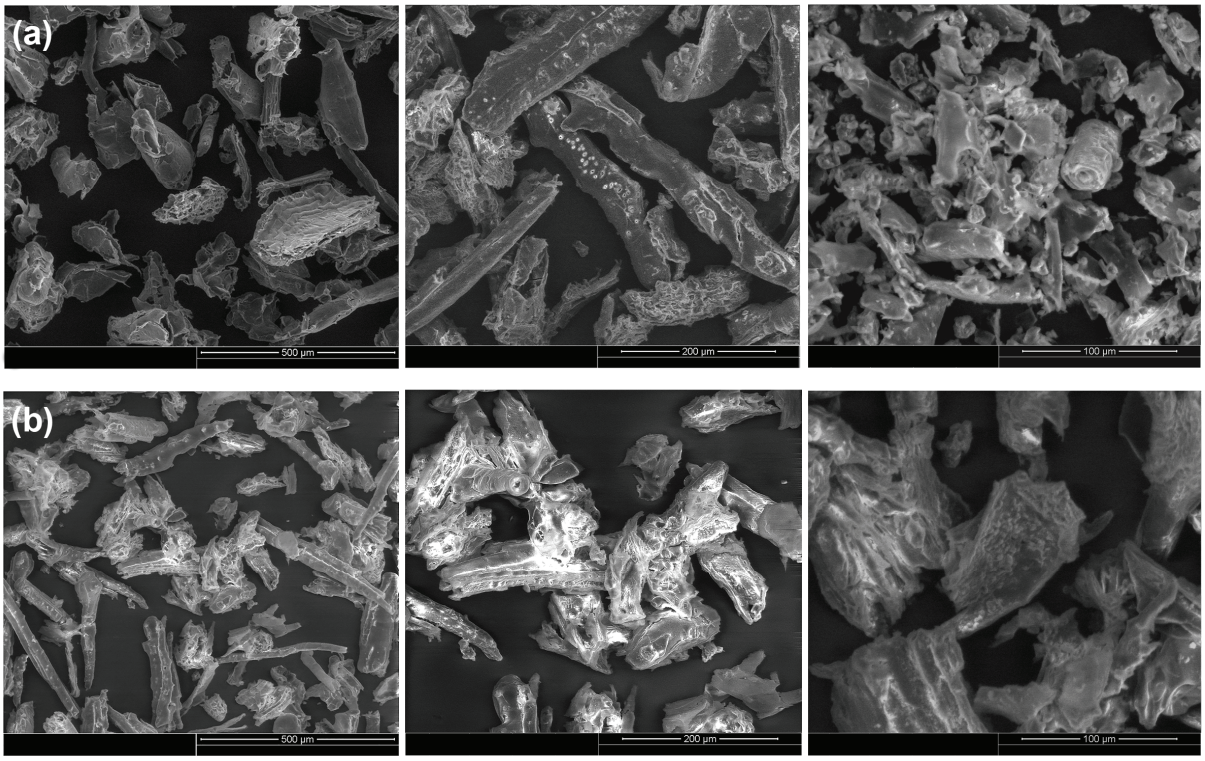

Figure 1. Images of PCP visualised by SEM: (a) Raw PCP; (b) PCP after Cu(II) adsorption.

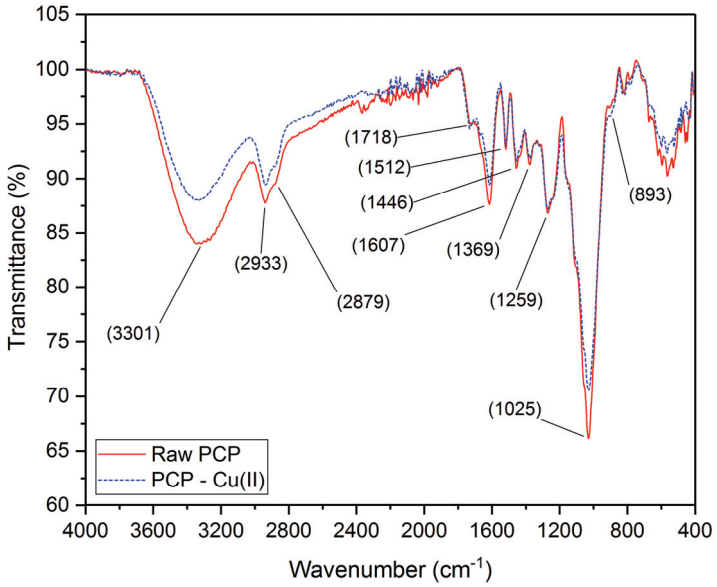

Figure 2. FTIR spectra of raw PCP and PCP after Cu(II) adsorption.

The alteration of the IR bands can be interpreted by their involvement in Cu(II) adsorption. This change is probably due to the interaction between these groups and Cu(II). The participation of the hydroxyl, carboxyl and phenolic groups in metal ions binding was reported in several studies [34-37].

XRD analysis

Figure 3 shows the diffractograms of raw PCP and PCP after Cu(II) adsorption. X-ray diffraction was used to study the effect of Cu(II) adsorption on the PCP cellulose crystallinity. The four peaks located at 2θ angles of 15.09, 16.25, 22.21 and 34.47° are characteristic of cellulose I [38,39].

The empirical crystallinity index (*CrI*) was estimated using the Segal equation [40] :

$$CrI\,(\%) = 100\,\frac{I_c - I_{am}}{I_c} \tag{8}$$

where *CrI* expresses the relative degree of crystallinity, I_c is the intensity of the diffraction at 2θ = 22.21° and I_{am} referring to the intensity at 2θ = 18.28° assigned to the amorphous cellulose phase which corresponds to the minimum position of the diffraction profile.

The calculated crystallinity index of the cellulose shows a slight decrease in crystallinity from approx-

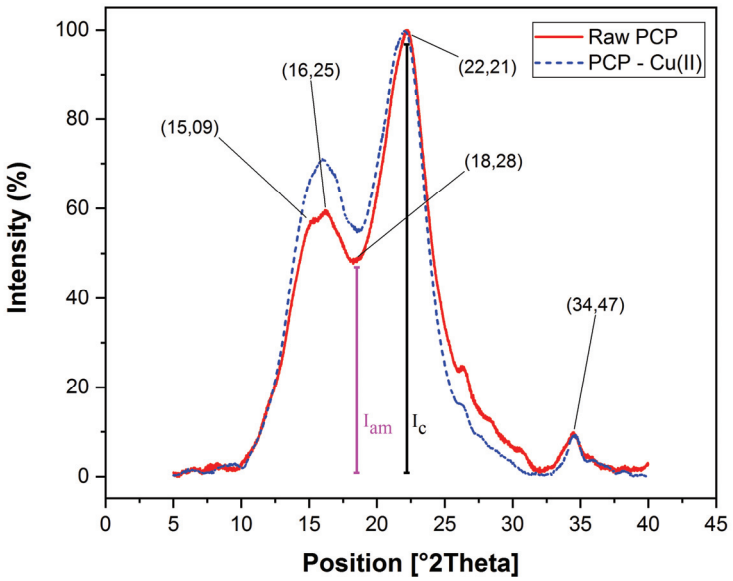

Figure 3. XRD of raw PCP and PCP after Cu(II) adsorption.

imately 51.32 to 45.10% when the adsorption of Cu(II) occurs. The results of XRD analysis suggest that the cellulose is involved in the adsorption of Cu(II) on the PCP.

Thermogravimetric analysis

Figure 4 presents the TGA and DTG profiles of PCP, the TGA measurements revealed three stages of the decomposition process: water evaporation (40-175 °C), removal of volatile organic matters (175-400 °C), and combustion of carbonaceous matter (400-645 °C). The temperature of the maximum mass loss rate can be determined by DTG, they are 79, 342 and 456 °C for the first, the second and the third stage, respectively. The processes of thermal destruction of PCP proceeded with maximum rate at 342 °C under air atmosphere.

The specific surface area of the material was found to be 0.76 $m^2\ g^{-1}$ (Table 1), it's similar to that of sawdust of walnut 0.72 $m^2\ g^{-1}$ [41] and peanut hulls 0.57-0.01 $m^2\ g^{-1}$ [42]. The latter has a maximum adsorption capacity equal to 14.13 mg g^{-1} for Cu(II).

Table 1. Some characteristic properties of PCP

Sample	pH_{pzc}	S_{BET} ($m^2\ g^{-1}$)	$pH_{adsorbent}$	*EC* (µS cm^{-1})
PCP	5.62	0.76	5.30	441

Adsorption kinetics study

The effect of contact time on the adsorption of Cu(II) by PCP was shown in Figure 5. Evidently, the Cu(II) adsorption capacity increased with contact time until it reached a maximum value of 2.53 mg g^{-1} at 60 min and remained constant over time. Contact time of 60 min was assumed appropriate for subsequent experiments, in which case the adsorption equilibrium could be reached. Similar results were reported using spruce sawdust [44].

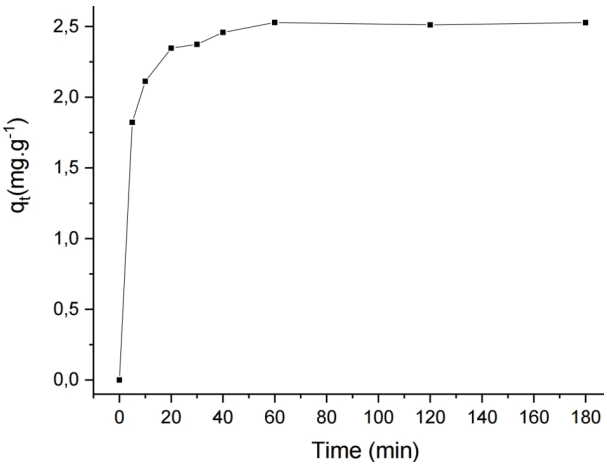

Figure 5. Effect of time on Cu(II) adsorption by PCP.

Due to the large number of active adsorbent sites accessible for metal adsorption, the rate of Cu(II) removal was higher at the beginning. As the competition for the availability of active sites intensifies by the metal ions remaining in the solution, the metal uptake by the PCP surface slowed down. After 60 min, the surface pores of adsorbents may be covered and it becomes difficult for Cu(II) to enter into the interior of the pores. Ofomaja *et al.* [39] reported that Cu(II) adsorption by cone powder became almost constant after 15 min. On the other hand, Değirmen *et al.* [18] reported an equilibrium time about 120 min.

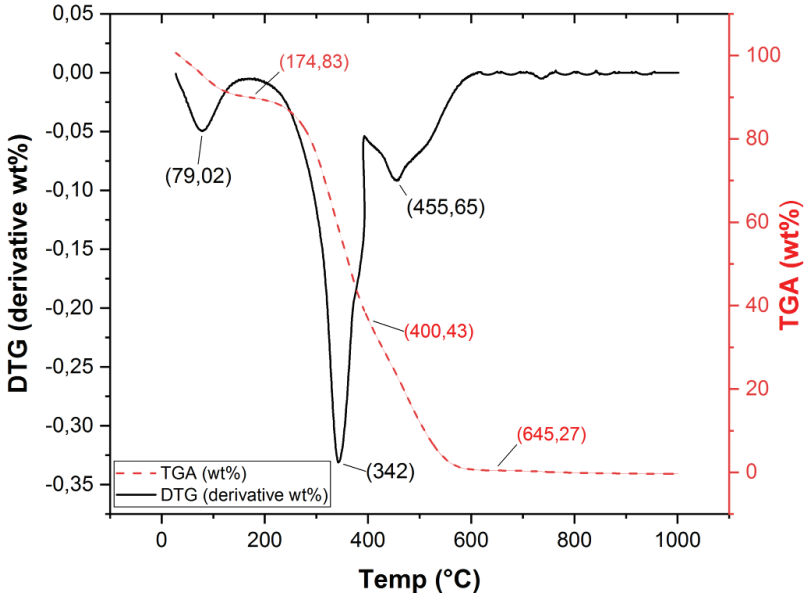

Figure 4. Thermogravimetric analysis (TGA) and derivative thermogravimetry (DTG) profiles of PCP.

Kinetic adsorption models

The study of adsorption kinetic describes the solute uptake rate, which controls the residence time of adsorbate uptake at the solid-solution interface including the diffusion process.

The pseudo-first order equation (Eq. (9)) can be expressed in nonlinear (Eq. (10)) and linear forms (Eq. (11) or Eq. (12)):

$$\frac{\mathrm{d}q_t}{\mathrm{d}t} = k_1\left(q_e - q_t\right) \tag{9}$$

$$q_t = q_e\left(1 - e^{-k_1 t}\right) \tag{10}$$

$$\log\left(q_e - q_t\right) = \log q_e - \frac{k_1}{2.303}t \tag{11}$$

$$\ln\left(q_e - q_t\right) = \ln q_e - k_1 t \tag{12}$$

Eq. (10) is known as PFO kinetic adsorption model, where q_t is the amount of adsorbate adsorbed at time t (mg g^{-1}) and can be calculated using Eq. (1), q_e is the equilibrium adsorption capacity (mg g^{-1}), k_1 is the PFO rate constant (min^{-1}), and t is the contact time (min).

The integration of PSO equation (Eq. (13)) with initial conditions leads to Eq. (14), which is known as PSO kinetic adsorption model:

$$\frac{\mathrm{d}q_t}{\mathrm{d}t} = k_2\left(q_e - q_t\right)^2 \tag{13}$$

$$q_t = \frac{q_e^2 k_2 t}{1 + k_2 q_e t} \tag{14}$$

PSO kinetic adsorption model can be expressed in the following linear form:

$$\frac{t}{q_t} = \frac{1}{k_2 q_e^2} + \left(\frac{1}{q_e}\right)t \tag{15}$$

where k_2 (g mg^{-1} min^{-1}) is the PSO rate constant.

The plot of ln (q_e-q_t) *versus* t gives a straight line for the pseudo-first adsorption kinetic, which allows the determination of k_1 from the slope and q_e from y--intercept. For the second order adsorption kinetic, q_e and k_2 can be determined from the intercept of the linearised plot of $1/q_t$ *versus* t.

The Elovich equation can be expressed mathematically as follows:

$$q_t = \frac{1}{\beta}\ln\left(1 + \alpha\beta t\right) \tag{16}$$

where α is the initial rate constant (mg g^{-1} min^{-1}) and β (mg g^{-1}) is the desorption constant at time.

The intraparticle diffusion model can be described by the following equation:

$$q_t = K_{int}t^{\frac{1}{2}} + C \tag{17}$$

where K_{int} is the intraparticle diffusion model rate constant (mg g^{-1} min$^{1/2}$), which can be evaluated from the slope of the linear plot of q_t *versus* $t^{1/2}$. C (mg g^{-1}) is the constant related to the thickness of the boundary layer. Extrapolation of the linear portions of the plots back to the y-axis gives the intercepts, which provide the measure of the boundary layer. A higher value of C corresponds to a greater boundary layer effect.

The kinetic parameters in Eqs. (12) and (15) could be derived from the slopes and intercepts of the fitted curves shown in Figure 6b and a, respectively.

The calculated kinetic constants and their corresponding error function values are given in Table 2. Figure 6b shows the experimental data fitted to the linear PFO kinetic model; poor linearity was perceived for the PFO linear model with R^2 = 0.89 and R_{adj}^2 = = 0.87. Additionally, the calculated adsorption at equilibrium ($q_{e,cal}$ = 1.32 mg g^{-1}) is underestimated when compared to the experimental equilibrium adsorption capacity ($q_{e,exp}$ = 2.53 mg g^{-1}). Accordingly, the linear PFO model was inadequate to describe the kinetic behaviour of Cu(II) adsorption by PCP.

The PSO kinetic model presented in Figure 6a gives a value of R^2 = 1 and R_{adj}^2 = 1. The calculated adsorption at equilibrium (2.55 mg g^{-1}) is much closer to the experimental value. These results indicate that the adsorption process was successfully represented by PSO model. Such findings support the assumption that the rate-limiting step of Cu(II) adsorption by PCP could be chemisorption involving valence forces through sharing or exchange of electrons between adsorbate and adsorbents [45]. According to the literature data, the PSO model was well applied to the adsorption of metal ions, dyes, and organic substances from aqueous solutions onto a wide range of adsorbents [18,46,47].

The intraparticle diffusion model is presented in Figure 6d. The plot of q_t *versus* $t^{1/2}$ gives multiple linear regions indicating that the adsorption process is governed by a multistep mechanism.

The first stage, with a higher slope, represents the transport in the solution phase, known as bulk transport, which takes place instantaneously after the adsorbent is transferred into the adsorbate solution; usually, this stage is too fast for agitated systems.

Then follows the second gradual adsorption stage, due to the film diffusion effects. In this stage,

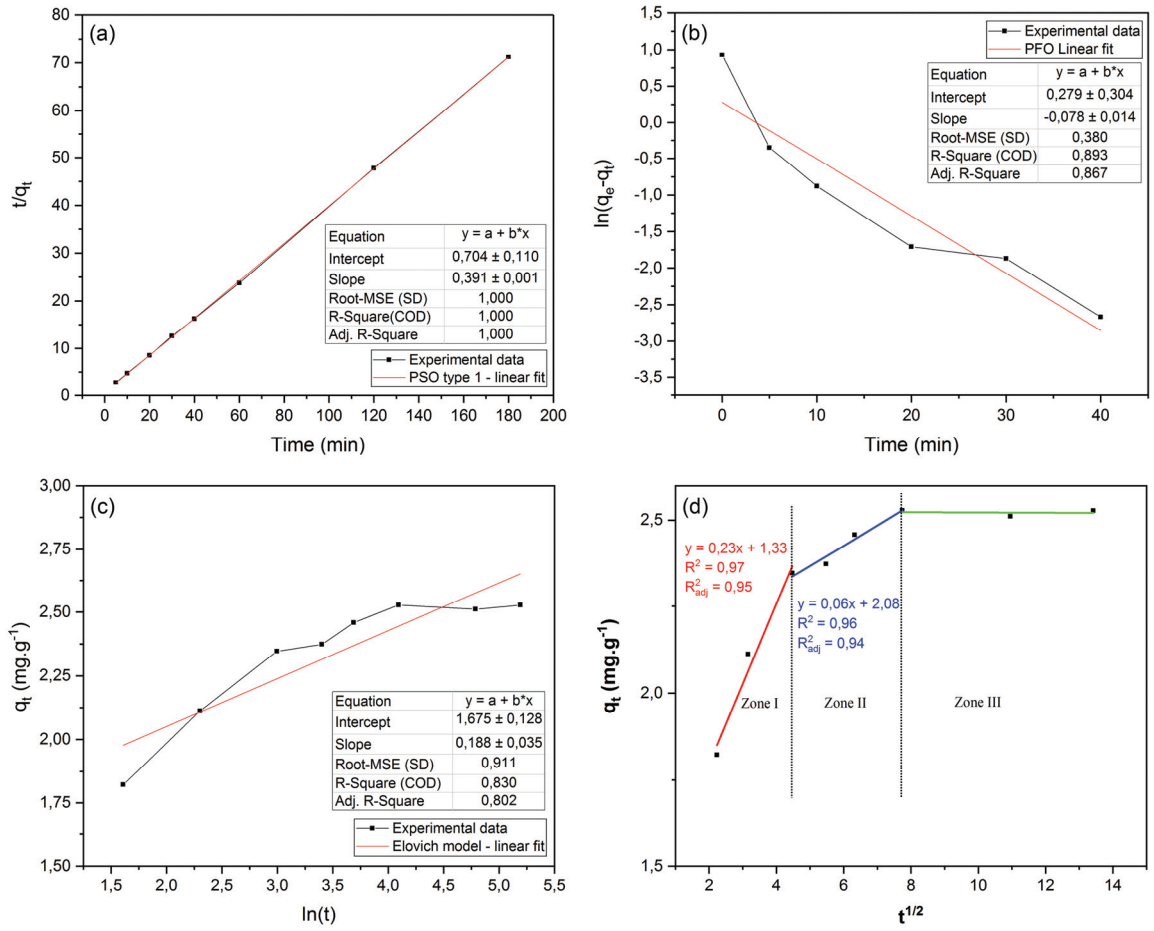

Figure 6. Kinetic model plots for Cu(II) adsorption by PCP: a) pseudo-second order; b) pseudo-first order; c) Elovich; d) intraparticle diffusion.

Table 2. Pseudo-first order, pseudo-second order and Elovich kinetics parameters for the adsorption of Cu(II) by PCP

Pseudo-first-order				
k_1 (min^{-1})	$q_{e,cal}$ (mg g^{-1})	$q_{e,exp}$ (mg g^{-1})	R^2	R_{adj}^2
0.078	1.322	2.528	0.893	0.867
Pseudo-second-order				
k_2 (g mg^{-1} min^{-1})	$q_{e,cal}$ (mg g^{-1})	$q_{e,exp}$ (mg g^{-1})	R^2	R_{adj}^2
0.218	2.555	2.528	1.000	1.000
Elovich				
β (mg g^{-1})	α (mg g^{-1} min^{-1})	R^2	R_{adj}^2	β (mg g^{-1})
5.315	1380.467	0.830	0.802	5.315

the heavy metals are transported from the solution to the adsorbent's external surface.

After saturation of the surface, the third straight stage involves the intraparticle diffusion through pore and interior surface of the PCP until the equilibrium between the metal ions in the solution and on the adsorbent surface is reached. Several previous investigations have reported a similar type of pattern [31,41,47].

According to this model, if only intraparticle scattering is involved in the process, the line passes through the origin, which is not the case in this study implying that intraparticle scattering is not the only one that controls the rate of adsorption of Cu(II) by PCP. From the slope of the linear portion of the second zone it was possible to determine k_{id} which is 0.06 mg g^{-1} min$^{-0.5}$ [28].

The Elovich kinetic model presented in Figure 6c gives a value of R^2 = 0.83 and R_{adj}^2 = 0.80, which

is lower than PSO and PFO models. The Elovich equation describes mainly chemisorption kinetic on systems with heterogeneous adsorbent surfaces [31].

Effects of adsorption parameters

Effect of pH

The effect of the pH solution was carried out by varying the initial pH of solutions from 2 to 8 (Figure 7a). A low adsorption capacity was observed at strong acidic medium. Also, it is remarkable that the adsorption capacity of PCP tends to increase with increasing pH value. The effect of pH can be interpreted by a decrease in the competition of positively charged species including H^+, H_3O^+ and Cu^{2+} for the same adsorption sites. As the pH value was increased, more active sites were exposed and the number of negatively charged groups on the adsorbent matrix probably increased, enhancing the Cu(II) removal. In addition, it was observed that the optimum Cu(II) removal occurred between the pH values of 5 and 6. At pH solution higher than 6, precipitation of Cu(II) as copper hydroxides $Cu(OH)_2$ begins taking place, restricting the adsorption study. These findings are in agreement with results reported in the previous studies [49,50].

The effect of pH could also be explained by considering pH_{pzc} presented in Table 1. It was observed a rise and fall of % of Cu(II) removal at pH > > pH_{pzc} and pH < pH_{pzc}, respectively. These observations could be explained by the fact that the adsorbent surface is positively charged for pH < 5.62 and it becomes negatively charged for pH > 5.62. At pH below 5.62, the adsorption is unfavourable because of repulsive electrostatic interactions between metal ions and positively charged functional groups. The maximum adsorption of Cu(II) occurs at pH values between 5 and 6 when the adsorbent surface is negatively highly charged.

It is noteworthy that Cu^{2+}, $Cu(OH)^+$ and $Cu(OH)_2$ are the dominant species involved in the adsorption below pH 5.3. Thus, Cu^{2+} and $Cu(OH)^+$ species may be adsorbed at the surface of PCP by ion exchange mechanism, while $Cu(OH)_2$ are accounted in the formation of hydrogen bonding with the -COOH and -OH functional groups present in PCP [48,50].

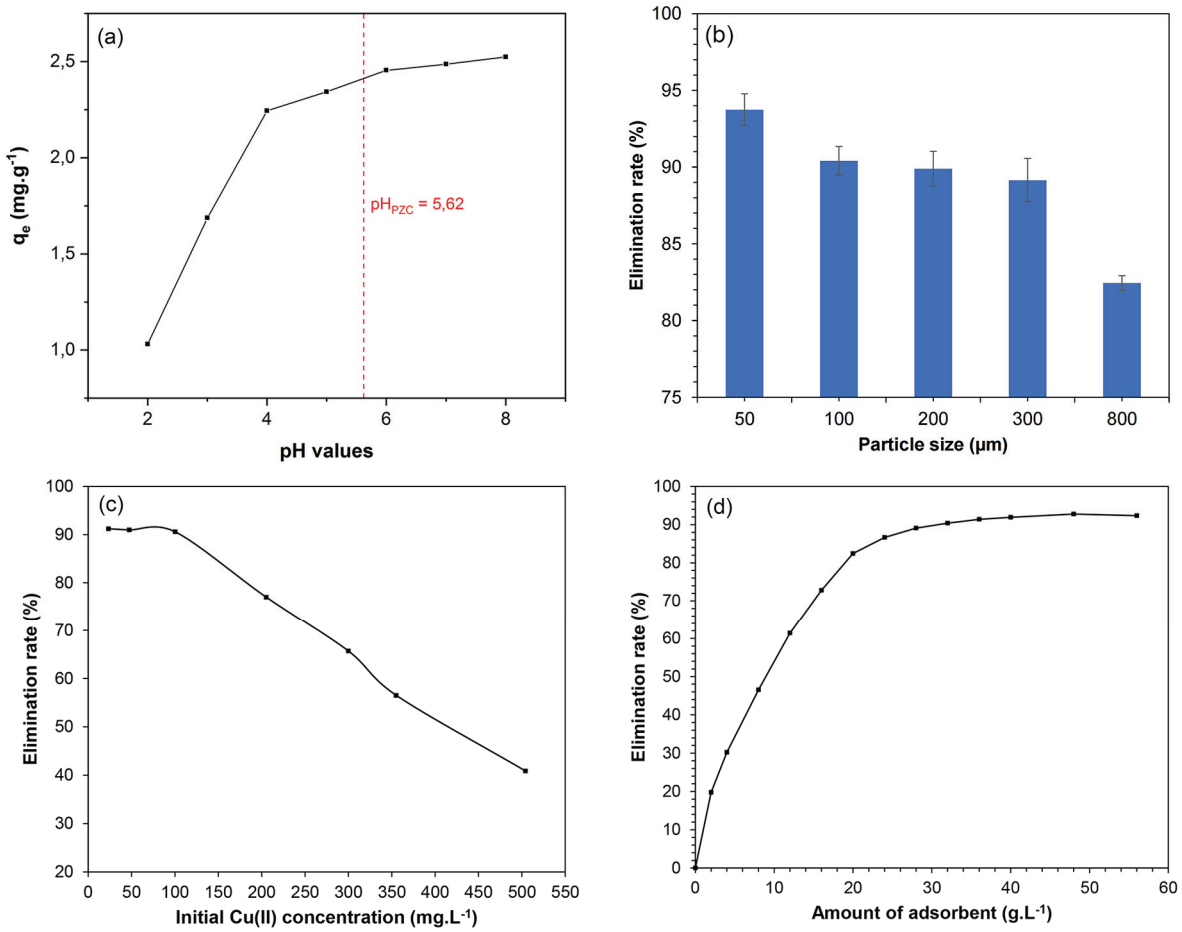

Figure 7. Effect of Cu(II) adsorption parameters by PCP: a) pH; b) particle size; c) initial Cu(II) concentration; d) adsorbent dose.

Ion exchange mechanism:

$R\text{-}OH + Cu^{2+} \leftrightarrow R\text{-}OCu^{+} + H^{+}$

$R\text{-}COOH + Cu^{2+} \leftrightarrow R\text{-}COOCu^{+} + H^{+}$

$R\text{-}OH + Cu(OH)^{+} \leftrightarrow R\text{-}OCu(OH) + H^{+}$

$R\text{-}COOH + Cu(OH)^{+} \leftrightarrow R\text{-}COOCuOH + H^{+}$

Hydrogen bonding mechanism:

$R\text{-}OH + Cu(OH)_2 \leftrightarrow (R\text{-}OH)_2Cu(OH)_2$

$R\text{-}COOH + Cu(OH)_2 \leftrightarrow (R\text{-}COOH)_2Cu(OH)_2$

The pH of the solution is one of the most critical parameters governing the metal adsorption process. It is correlated with the competition ability of hydrogen ions with metal ions to active sites on the PCP surface [48]. The FTIR spectroscopic analysis showed that the PCP has a variety of functional groups such as carboxyl, hydroxyl and amine. These groups are involved in almost all potential binding mechanisms.

Effect of adsorbent dose

Figure 7d shows that the percentage removal of Cu(II) increases with the increase in the adsorbent dose from 2 to 36 g L^{-1}; further increase of the adsorbent dose did not provide a significant rise in the percentage of the metal ion removed. Such behaviour was expected due to the saturation level attained during the adsorption process. The maximum elimination rate of Cu(II) was found to be 91% at PCP concentration of 36 g L^{-1}.

This result can be explained by the fact that the increase of the PCP dose provides more binding sites. Thus, leading to the enhancement of Cu(II) uptake. A similar effect of adsorbent dose was reported in the previous studies [17,18].

Effect of adsorbent particle size

The percentage removal of Cu(II) at different particle size presented in Figure 7a showed that a decreasing in the particle size leads to an increase in the adsorption efficiency. Particle sizes smaller than 100 μm were found to yield highest percentage removal of Cu(II). The higher adsorption level achieved by smaller particle sizes of the adsorbent may be related to the fact that smaller particles give large surface areas. Indeed, there is a tendency that smaller particles have more accessible surface for metal ions uptake [42].

Effect of initial Cu(II) concentration

The effect of metal concentration on the percent removal of Cu(II) shown in Figure 7c, revealed that the percentage of metal removal decreased with the increase of the initial Cu(II) concentration. At lower Cu(II) concentrations, the elimination rate was higher due to the large number of active sites available for Cu(II) adsorption. While at a higher initial Cu(II) concentration, the active sites are saturated and the ratio of the initial number of Cu(II) to the available adsorption surface area was higher. As a result, the Cu(II) elimination percentage decreases. The lower adsorption percentages at higher Cu(II) concentrations might be associated with insufficient binding sites for adsorption or to the saturation of the binding sites. A similar effect of the initial metal ions concentration on the adsorption of Cu(II) by pine cone shells was found by Değirmen *et al.* [18].

Adsorption isotherms

Langmuir model

The Langmuir isotherm was developed by assuming that the adsorption happens at a specific number of accessible sites on the adsorbent surface. All adsorption sites involved have the same energy. The adsorption is monolayer, reversible and maximum adsorption occurs when adsorbed molecules form a saturated layer on the surface of adsorbent [51].

The nonlinear expression of the Langmuir isotherm model is given as:

$$q_e = \frac{q_{\max} K_L C_e}{1 + K_L C_e} \tag{18}$$

where q_{max} is the maximum saturated monolayer adsorption capacity (mg g^{-1}) and K_L is the Langmuir constant (L mg^{-1}) related to energy of adsorption which quantitatively reflects the affinity of binding sites.

The Langmuir model can be expressed in terms of a constant known as separation factor or equilibrium parameter (R_L) given by the following equation [52]:

$$R_L = \frac{1}{1 + K_L C_0} \tag{19}$$

R_L value indicates the adsorption nature to be either unfavourable ($R_L > 1$), linear ($R_L = 1$), favourable ($0 < R_L < 1$) or irreversible ($R_L = 0$) [31,53].

Freundlich model

The Freundlich isotherm model suggests that molecules are adsorbed as a monomolecular layer or multilayer on heterogeneous adsorbent surfaces and there is an interaction between the adsorbed molecules. Freundlich isotherm is suitable in treating metal ions adsorption at high concentrations. The non-linear expression of the Freundlich isotherm model is given as [25]:

$$q_e = K_F C_e^{\frac{1}{n}} \tag{20}$$

where K_F (mg g^{-1})(L mg^{-1})$^{1/n}$ is the Freundlich constant and n (dimensionless) is the Freundlich intensity parameter, which indicates the magnitude of the adsorption driving force or the surface heterogeneity [54].

Redlich-Peterson model

The Redlich-Peterson isotherm was proposed upon considering the limitations of the Freundlich and Langmuir isotherms. This model incorporates the features of the Freundlich and Langmuir models, and it might be applicable for demonstrating adsorption equilibrium over a wide range of adsorbate concentrations. The nonlinear form of this empirical model is given as follows:

$$q_e = \frac{K_{RP} C_e}{1 + a_{RP} C_e^g} \tag{21}$$

where K_{RP} (L g^{-1}) and a_{RP} (mg L^{-1})$^{-g}$ are the Redlich-Peterson constants and g (dimensionless) is an exponent whose value is limited to ≤1.

Eq. (21) reduces to the Langmuir isotherm when g = 1, and transforms into the Freundlich isotherm when a_{RP} >> 1 and g = 1.

Dubinin-Radushkevich model

The Dubinin-Radushkevich equation was developed to express the adsorption isotherms in micropores. It is expressed as follows [31]:

$$q_e = q_{DR} e^{-K_{RD}\varepsilon^2} \tag{22}$$

ε is the Polanyi potential expressed as follows:

$$\varepsilon = RT \ln\left(1 + \frac{1}{C_e}\right) \tag{23}$$

where q_{DR} (mg g^{-1}) is the adsorption capacity, K_{DR} (mol^2 kJ^{-2}) is a constant related to the sorption energy, R is the gas constant, T is the temperature in K, and q_e and C_e are obtained from Eq. (2).

The mean adsorption energy E (kJ mol^{-1}) can be obtained using:

$$E = \frac{1}{\sqrt{2K_{DR}}} \tag{24}$$

The isotherms using Langmuir, Freundlich, Redlich-Peterson and Dubinin-Radushkevich models are presented in Figure 8. The parameters of the models are listed in Table 3. The values of R^2 = 0.98 and R_{adj}^2 = 0.97 indicated that the Langmuir model yielded better fits compared to the other models. Therefore, Cu(II) bonding may occurs on a homogenous surface under monolayer adsorption by energetically identical sites. In addition, the R_L values obtained using Eq. (19) are greater than zero and smaller than unity, indicating favourable adsorption of Cu(II) by PCP.

The value of adsorption energy obtained using Dubinin-Radushkevich Eq. (24) gives the nature of the adsorption of Cu(II) by PCP. A physical adsorption is obtained for E < 8 kJ mol^{-1} and chemical adsorption for E > 8-16 kJ mol^{-1} [30,55]. The E value (20.31 kJ mol^{-1}) indicates that the removal of Cu(II) may occurs through chemisorption uptake based on the ion exchange mechanism.

Table 4 presents the comparison of adsorption capacities of various adsorbents for Cu(II). The maximum adsorption capacity of Cu(II) by PCP reached a value of 9.08 mg g^{-1}, higher than that used by Blázquez *et al.* [17] and lower than that used by Değirmen *et al.* [18]. When it is opposed to other investigated raw waste materials, it is clearly visible that the PCP has a good adsorbent characteristic. These findings show that PCP may be used successfully for the removal of Cu(II) from aqueous solution.

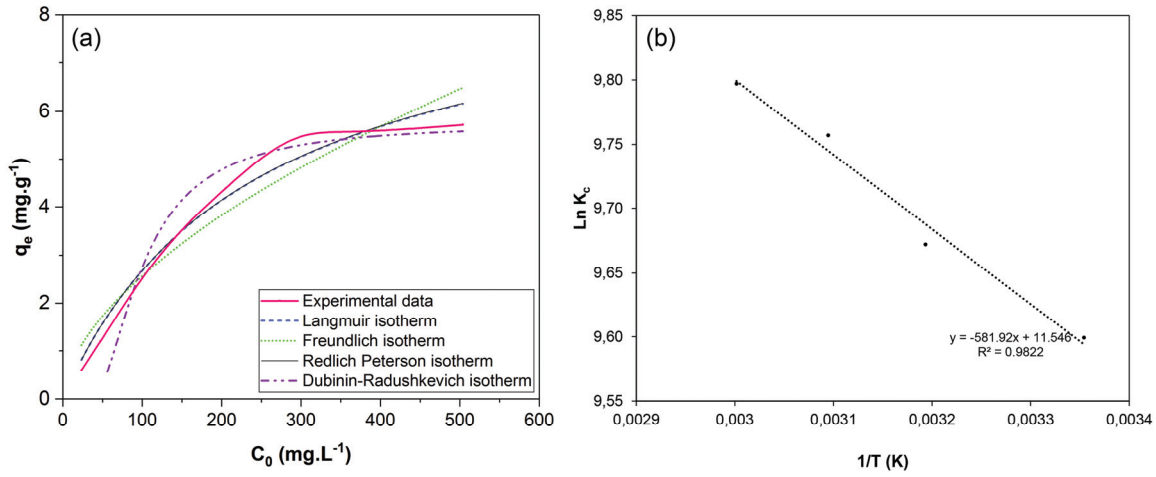

Figure 8. Cu(II) adsorption by PCP: a) isotherm fitting of Langmuir, Freundlich, Redlich-Peterson and Dubinin-Radushkevich models; b) Van 't Hoff plot for calculation of thermodynamic parameters.

Table 3. Isotherm parameters of Cu(II) adsorption by PCP deduced with nonlinear method

Model	Equation	Parameter	Value	Standard Error	Statistics	Value
Langmuir	$q_e = \frac{q_{max} K_L C_e}{1 + K_L C_e}$	q_{max} (mg g^{-1})	9.080	1.068	R_{adj}^2	0.975
		K_L (L mg^{-1})	0.004	0.001	R^2	0.979
		R_L (range) = 0.911 - 0.322				
Freundlich	$q_e = K_F C_e^{\frac{1}{n}}$	K_F (mg g^{-1})(L mg^{-1})$^{1/n}$	0.183	0.103	R_{adj}^2	0.935
		n	1.740	0.300	R^2	0.922
Redlich-Peterson	$q_e = \frac{K_{RP} C_e}{1 + a_{RP} C_e^g}$	K_{RP} (L g^{-1})	0.038	0.015	R_{adj}^2	0.969
		a_{RP} (mg L^{-1})$^{-g}$	0.004	0.013	R^2	0.979
		g	1.000	0.434		
Dubinin-Radushkevich	$q_e = q_{DR} e^{-K_{RD}\varepsilon^2}$	q_{DR} (mg g^{-1})	5.751	0.364	R_{adj}^2	0.932
		K_{DR} (mol^2 kJ^{-2})	0.0012	0.0004	R^2	0.943
		E (kJ mol^{-1})	20.315			

Table 4. Comparison of Cu(II) adsorption studies using various adsorbents

Adsorbent	Adsorption capacity (mg g^{-1})	Reference
Raw corn silk	15.35 (39.85 °C/pH 5.0)	[34]
Wheat straw	5 (pH and temperature N/S)	[58]
Apricot stones	5.90 (25 °C/pH 4.5)	[59]
Maple sawdust	9.19 (23 °C/pH 6.0)	[50]
Pine tree cones	19.27 (30 °C/pH 5.0)	[18]
Pine cone shells	6.81 (25 °C/pH 5.0)	[17]
Pine cone powder	9.08 (25 °C/pH 5.3)	This study

Thermodynamic study

The values of ΔG (KJ mol^{-1}) are directly calculated from Eq. (4), while the values of ΔH (KJ mol^{-1}) and ΔS (J.mol^{-1} K^{-1}) were evaluated from the intercept of the plot of ln K_c *versus* $1/T$ from the Van't Hoff equation (Eq. (6)) [34].

The calculated thermodynamic parameters are presented in Table 5. The negative values of ΔG indicated that adsorption is spontaneous and thermodynamically favourable. The positive value of ΔS reflects the affinity of the Cu(II) towards the PCP adsorbent. It indicates the increase of the disorder at the solid/liquid interface during the adsorption. The positive value of ΔH indicated that the adsorption of Cu(II) is endothermic. It suggests that transferring Cu(II) from the aqueous phase to the solid phase requires energy. Endothermic adsorption of Cu(II) was reported by other authors for corn silk, bentonite and sewage sludge [34,56,57].

Table 5. Thermodynamic parameters values of Cu(II) adsorption by PCP

T (K)	ΔG (kJ.mol^{-1})	ΔH (kJ mol^{-1})	ΔS (J mol^{-1} K^{-1})	Van't Hoff equation
298.15	-23.80	4.84	96.00	y = -581.92x + 11.55
313.15	-25.18			R^2 = 0.98
323.15	-26.22			
333.15	-27.14			

CONCLUSION

This research was focused on the adsorption of Cu(II) ions by PCP from aqueous solution. Characterisation confirmed the role of hydroxyl, carboxyl and phenolic groups in metal binding. The adsorption of the Cu(II) by PCP reached equilibrium in 60 min. The kinetic data showed that the pseudo-second-order kinetic model describes the adsorption of Cu(II) ions by PCP. The maximum adsorption efficiency of Cu (II) by PCP was found to be almost 91% at PCP dose of 36 g L^{-1} with a Cu(II) concentration of 100 mg L^{-1}. Particle sizes smaller than 100 μm were found to yield the highest percentage removal of Cu(II). The optimum Cu(II) removal occurred at a slightly acidic pH. Adsorption equilibrium data fitted very well the Langmuir model. The maximum Cu(II) adsorption capacity (q_{max}) obtained was 9.08 mg g^{-1}. The separation factor indicated a favourable adsorption of Cu(II) by PCP. The thermodynamic study showed that the Cu(II) adsorption was a spontaneous and endothermic process. The positive value of ΔS revealed the increase in the randomness at solid solution interface. PCP can be considered as a promising material for the removal of

Cu(II) from wastewater. It is readily available, low cost and above all, environmentally friendly.

REFERENCES

[1] M.A.A. Wijayawardena, M. Megharaj, R. Naidu, in: Adv. Agron., Elsevier Inc., 2016, pp. 175-234

[2] M. Mahurpawar, Int. J. Reseacrh-Granthaalayah 2350 (2015) 2394-3629

[3] R. Ouafi, Z. Rais, M. Taleb, M. Benabbou, M. Asri, in: O.K. Stefan E (Ed.), Sawdust Prop. Potential Uses Hazards, Nova Science Publishers, Incorporated, 2017, pp. 147-181

[4] S. Babel, T.A. Kurniawan, J. Hazard. Mater. 97 (2003) 219-243

[5] C. Palma, E. Contreras, J. Urra, M.J. Martínez, Waste Biomass Valorization 2 (2011) 77-86

[6] M.T. Islam, R. Saenz-Arana, C. Hernandez, T. Guinto, M.A. Ahsan, D.T. Bragg, H. Wang, B. Alvarado-Tenorio, J.C. Noveron, J. Environ. Chem. Eng. 6 (2018) 3070--3082

[7] M.T. Islam, C. Hernandez, M.A. Ahsan, A. Pardo, H. Wang, J.C. Noveron, J. Environ. Chem. Eng. 5 (2017) 5270-5279

[8] C.K. Jain, D.S. Malik, A.K. Yadav, Environ. Process. 3 (2016) 495-523

[9] N.S. Kumar, M. Asif, A.M. Poulose, M. Suguna, M.I. Al-Hazza, Processes 7 (2019)

[10] A.E. Ofomaja, E.B. Naidoo, S.J. Modise, Desalination 251 (2010) 112-122

[11] N.S. Kumar, M. Asif, M.I. Al-Hazzaa, Environ. Sci. Pollut. Res. 25 (2018) 21949-21960

[12] G.M.A. Bouchair Abdennour, Bouremmad Farida, Shawuti Shalima, Amayreh Mousa Y, Res. J. Chem. Environ. 23 (2019) 10-18

[13] A.I. Almendros, M.A. Martín-Lara, A. Ronda, A. Pérez, G. Blázquez, M. Calero, Bioresour. Technol. 196 (2015) 406-412

[14] H. Ucun, Y.K. Bayhan, Y. Kaya, A. Cakici, O. Faruk Algur, Bioresour. Technol. 85 (2002) 155-158

[15] D. Politi, D. Sidiras, Procedia Eng. 42 (2012) 1969-1982

[16] A.E. Ofomaja, E.B. Naidoo, S.J. Modise, J. Hazard. Mater. 168 (2009) 909-917

[17] G. Blázquez, M.A. Martín-Lara, E. Dionisio-Ruiz, G. Tenorio, M. Calero, J. Ind. Eng. Chem. 18 (2012) 1741-1750

[18] G. Değirmen, M. Kiliç, Ö. Çepelioğullar, A.E. Pütün, Water Sci. Technol. 66 (2012) 564-572

[19] R. Ouafi, Z. Rais, M. Taleb, Desalin Water Treat. 180 (2020) 185-192

[20] S.K. Lagergren, Sven. Vetenskapsakad. Handingarl. 24 (1898) 1-39

[21] G. Blanchard, M. Maunaye, G. Martin, Water Res. 18 (1984) 1501-1507

[22] W.J. Weber, J.C. Morris, J. Sanit. Eng. Div. 89 (1963) 31--60

[23] J. Zeldowitsch, Acta Physicochim. URSS 1 (1934) 364--449

[24] I. Langmuir, J. Am. Chem. Soc. 40 (1918) 1361-1403

[25] H. Freundlich, Zeitschrift Phys. Chemie 57 (1906) 386-470

[26] M.M. Dubinin, in: Dokl. Akad. Nauk SSSR, 1947, pp. 327--329

[27] O. Redlich, D.L. Peterson, J. Phys. Chem. 63 (1959) 1024-1024

[28] É.C. Lima, M.A. Adebayo, F.M. Machado, in: C.P. Bergmann, F.M. Machado (Eds.), Carbon Nanomater. as Adsorbents Environ. Biol. Appl., Springer International Publishing, Cham, 2015, pp. 33-69

[29] S.K. Bozbaş, Y. Boz, Process Saf. Environ. Prot. 103 (2016) 144-152

[30] H.N. Tran, S.J. You, H.P. Chao, J. Environ. Chem. Eng. 4 (2016) 2671-2682

[31] H.N. Tran, S.-J. You, A. Hosseini-Bandegharaei, H.-P. Chao, Water Res. 120 (2017) 88-116

[32] X. Zhou, X. Zhou, Chem. Eng. Commun. 201 (2014) 1459-1467

[33] V.S. Munagapati, V. Yarramuthi, S.K. Nadavala, S.R. Alla, K. Abburi, Chem. Eng. J. 157 (2010) 357-365

[34] M. Petrović, T. Šoštarić, M. Stojanović, J. Petrović, M. Mihajlović, A. Ćosović, S. Stanković, Ecol. Eng. 99 (2017) 83-90

[35] N. Ouazene, M.N. Sahmoune, Int. J. Chem. React. Eng. 8 (2010) 151

[36] H.L. Ornaghi Júnior, Á. de G.O. Moraes, M. Poletto, A.J. Zattera, S.C. Amico, Cellul. Chem. Technol. Cellul. Chem. Technol. 50 (2016) 15-22

[37] A.N. Kosasih, J. Febrianto, J. Sunarso, Y.H. Ju, N. Indraswati, S. Ismadji, J. Hazard. Mater. 180 (2010) 366-374

[38] Y.L. Hsieh, in: Cotton, Elsevier, 2007, pp. 3-34

[39] A.E. Ofomaja, E.B. Naidoo, Chem. Eng. J. 175 (2011) 260-270

[40] L. Segal, J.J. Creely, A.E. Martin, C.M. Conrad, Text. Res. J. 29 (1959) 786-794

[41] Y. Bulut, Z. Tez, J. Environ. Sci. 19 (2007) 160-166

[42] R.M. Ali, H.A. Hamad, M.M. Hussein, G.F. Malash, Ecol. Eng. 91 (2016) 317-332

[43] V. Fierro, V. Torné-Fernández, D. Montané, A. Celzard, Microporous Mesoporous Mater. 111 (2008) 276-284

[44] Z. Kovacova, S. Demcak, M. Balintova, Proceedings 16 (2019) 52

[45] P. SenthilKumar, S. Ramalingam, V. Sathyaselvabala, S.D. Kirupha, S. Sivanesan, Desalination 266 (2011) 63--71

[46] D. Park, Y.-S. Yun, J.M. Park, Biotechnol. Bioprocess Eng. 15 (2010) 86-102

[47] I. Morosanu, C. Teodosiu, C. Paduraru, D. Ibanescu, L. Tofan, N. Biotechnol. 39 (2017) 110-124

[48] F. Bouhamed, Z. Elouear, J. Bouzid, J. Taiwan Inst. Chem. Eng. 43 (2012) 741-749

[49] A.E. Ofomaja, E.I. Unuabonah, N.A. Oladoja, Bioresour. Technol. 101 (2010) 3844-3852

[50] M.S. Rahman, M.R. Islam, Chem. Eng. J. 149 (2009) 273-280

[51] S.A. Sadeek, N.A. Negm, H.H.H. Hefni, M.M. Abdel Wahab, Int. J. Biol. Macromol. 81 (2015) 400-409

[52] K.R. Hall, L.C. Eagleton, A. Acrivos, T. Vermeulen, Ind. Eng. Chem. Fundam. 5 (1966) 212-223

[53] A. Labidi, A.M. Salaberria, S.C.M. Fernandes, J. Labidi, M. Abderrabba, J. Taiwan Inst. Chem. Eng. 65 (2016) 140-148

[54] E. Worch, in: Adsorpt. Technol. Water Treat., DE GRUYTER, Berlin, 2012, pp. 41-76

[55] S. Yildiz, Ecol. Chem. Eng. S. 24 (2017) 87-106

[56] J. Li, J. Hu, G. Sheng, G. Zhao, Q. Huang, Colloids Surfaces A Physicochem. Eng. Asp. 349 (2009) 195-201

[57] X. Wang, X. Liang, Y. Wang, X. Wang, M. Liu, D. Yin, S. Xia, J. Zhao, Y. Zhang, Desalination 278 (2011) 231-237

[58] M. Gorgievski, D. Božić, V. Stanković, N. Štrbac, S. Šerbula, Ecol. Eng. 58 (2013) 113-122

[59] M. Petrovic, T. Sostaric, L. Pezo, S. Stankovic, C. Lacnjevac, J. Milojkovic, M. Stojanovic, Chem. Ind. Chem. Eng. Q. 21 (2015) 249-259.

REDOUANE OUAFI[1]
ANASS OMOR[1]
YOUNES GAGA[2]
MOHAMED AKHAZZANE[1]
MUSTAPHA TALEB[1]
ZAKIA RAIS[1]

[1]Engineering Laboratory of Organometallic, Molecular Materials and Environment, Faculty of Science Dhar El Mahraz, Sidi Mohamed Ben Abdellah University, Route d'immouzer, Fez, Morocco
[2]Laboratory of Biotechnology, Ecology and Preservation of Natural Resources, Faculty of Science, Dhar El Mahraz, Sidi Mohamed Ben Abdellah University, Route d'immouzer, Fez, Morocco

NAUČNI RAD

UKLANJANJE JONA BAKRA IZ VODE ADSORPCIJOM NA PRAHU BOROVIH ŠIŠARKI

U ovom radu istraživan je adsorpcioni potencijal prah borovih šišarki za uklanjanje jona bakra iz vodenih rastvora. Proces adsorpcije je bio relativno brz i završio se za 60 min. Kinetički model pseudo-drugog reda pravilno opisuje adsorpciju jona bakra pomoću praha borovih šišarki. Adsorbent je okarakterisan različitim instrumentalnim tehnikama i sprovedeni su šaržni eksperimenti da se istraži uticaj doze praha, pH rastvora, veličine čestica i početne koncentracije jona bakra na efikasnost adsorpcije. Optimalno uklanjanje jona bakra postignuto je pri blago kiselom pH, sa veličinom čestica manjim od 100 mm. Efektivna doza praha je procenjena na 36 g/l. Povećanje početne koncentracije jona bakra je praćeno smanjenjem brzine njihovog uklanjanja za skoro polovinu. Langmuirov model je bio najbolja izoterma sa maksimalnim kapacitetom adsorpcije od 9,08 mg/g. Vrednosti termodinamičkih parametara su pokazale da je adsorpcija jona bakra bio spontan i endotermni proces. Rezultati ovog istraživanja sugerišu da bi joni bakra mogli biti uklonjeni ekološki prihvatljivim procesom korišćenjem praha borovih šišarki kao jeftinog prirodnog otpada.

Ključne reči: uklanjanje jona bakra, izoterme, kinetika, prirodni otpad, prah šišarki, tretman.

CI&CEQ
Chemical Industry & Chemical Engineering Quarterly

Available on line at
Association of the Chemical Engineers of Serbia *AChE*
www.ache.org.rs/CICEQ

Chem. Ind. Chem. Eng. Q. 27 (4) 355–362 (2021) CI&CEQ

VLADIMIR PUŠKAŠ
UROŠ MILJIĆ
VESNA VUČUROVIĆ

Faculty of Technology, University of Novi Sad, Novi Sad, Serbia

SCIENTIFIC PAPER

UDC 663.2:66.067:54

THE IMPACT OF ENOLOGICAL PRODUCTS FOR TARTARIC STABILIZATION ON WINE FILTERABILITY

Article Highlights

- The impact of enological products for tartaric stabilization on wine filterability was assessed
- The experiments were carried out using Quality Filterability Test
- Used products generally did not worsen the filterability of white and rosé wine
- Products containing mannoproteins and metatartaric acid reduced red wine filterability

Abstract

The aim of this research was to evaluate the impact of the most commonly used agents for tartaric stabilization of wine, such as metatartaric acid, carboxymethyl cellulose (CMC), mannoproteins and gum arabic, on the filterability of white, rosé and red wines previously pre-filtered and prepared for the final filtration and bottling. Wine filterability after sweetening with rectified concentrated must was also assessed. The experiments were carried out using the Quality Filterability Test and the obtained results were expressed through the filterability index (FI), and maximum filterable volume (Vmax). The results confirmed that the used enological agents for the inhibition of tartaric instabilities generally did not worsen the filterability of white and rosé wines (FI<20). However, it was evident that products containing mannoproteins and metatartaric acid considerably reduced red wine filterability (FI>500). The correlation between white and rosé wine turbidity and filterability was recorded in the trials but the same trend was not registered for the red wine. The results of this study are important since membrane (final) filtration of improperly prepared wine characterized by low filterability can both increase the costs and lead to holdup on the bottling line.

Keywords: wine, filtration efficiency, tartaric stabilization, filterability index, turbidity.

Wine on the market must have an appropriate color, aroma and taste. The great majority of wines also need to be clear (without visible residues and/or turbidity). Over time, unstable wine compounds can create turbidity or crystalline sediment in bottles due to polymerization reactions. For that reason, modern wine production usually includes a clarification and stabilization phase whose goal is to remove unstable compounds and obtain a product that will be exempt of any changes in clarity during aging. The clarification and stabilization procedures need to be carried out carefully and professionally in order to minimize the consequences on the wine quality, manifested by certain removal of aromatic and phenolic substances. One of the most common wine instabilities is related to the appearance of tartaric acid salts crystals (tartrates) during aging.

Nowadays, winemaking practice involves the application of two groups of procedures to achieve wine stability on tartrate salts: the removal of tartrate crystal precursors from wine by physical methods (cold stabilization, electrodialysis or ion exchange procedures) and addition of inhibiting enological stabilizers (carboxymethyl cellulose - CMC, manno-

Correspondence: U. Miljić, Faculty of Technology, University of Novi Sad, Blvd. Cara Lazara 1, 21000 Novi Sad, Serbia.
E-mail: urosmiljic@yahoo.com
Paper received: 13 September, 2020
Paper revised: 23 November, 2020
Paper accepted: 15 January, 2021

https://doi.org/10.2298/CICEQ200913003P

proteins or metatartaric acid) that prevent the formation (nucleation and growth) of crystals and their sedimentation, or by modifying their properties thus making them soluble at lower temperatures. Any treatment of wine that causes a change in pH (blending, malolactic fermentation, acidity correction) can affect the precipitation of tartrates and therefore, it is necessary to check the tartrate stability just before bottling.

The final step in wine clarification and stabilization almost always includes filtration. The purpose of filtration is to remove all suspended particles and to achieve microbiological and physical stability of wine, while, at the same time, avoiding the changes in chemical composition and sensory characteristics of wine. Wine filtration generally implies two possibilities - depth filtration and absolute (membrane) filtration. The racking of wine after clarification and a coarse filtration (pre-filtration) usually precede the final filtration prior to bottling. A coarse filtration can be carried out by the individual or combined use of diatomaceous earth, depth filter sheets or cross flow, depending on the degree of self-clarification of wine during storage [1]. The final filtration is mostly a microfiltration.

Suspended and colloidal materials in wine are both responsible for membrane fouling. Suspended compounds include crystals, microorganisms, and large colloidal particles. Furthermore, colloids responsible for filter blockage are associative small molecules which are forming reversible aggregates through weak intermolecular bonds and macromolecules (polysaccharides, proteins and polyphenols) forming aggregates through stronger molecular bonds [2]. Smaller particles are more prone to blocking the membrane than the bigger ones which remain on the surface and usually just reduce the efficiency of filtration [3]. Some winemaking approaches such as prolonged maceration, ageing on lees etc., give wines with a higher content of macromolecules which can cause significant filter blockage [4]. Apart from these components, enological additives like arabic gum, tannins, mannoproteins and CMC can also contribute to filter blockage and a decrease in wine filterability [3]. The presence of these colloidal substances in wine and their potential negative impact on filterability cannot be evaluated only by the clarity assessment. A visual clarity of wine is assessed by determination of its turbidity (expressed in NTU units). This parameter is mostly used for assessment of a wine's suitability for bottling. A correlation between wine turbidity and its filterability does not always exist. The blocking of the filters during microfiltration can occur rapidly or slowly, regardless of the type of pre-filtration applied and the efficiency achieved. For example, a wine with a NTU reading <1.0 is considered clear enough for bottling, however, this value does not necessarily guarantee lower fouling rates of filtration media and higher filterability. On the other hand, it is also possible that wine with turbidity higher than 1.0 NTU can be easily filtered by microfilter. The differences in wine filterability can also exist among wines demonstrating similar turbidity. This is a result of differences in the origin and composition of wine colloids and particles [3].

Unlike turbidity measurements, modern filterability tests consider and include the impacts of all compounds responsible for membrane blockage in the identification of wines prone to be problematic during sterile filtration. Requirements for obtaining the objective results of filterability tests include: a) wines used for testing must be protein-stable and prepared for bottling (pre-filtered); b) use of the same filtration medium as the one going to be used for final (sterile) filtration prior to bottling process; c) membrane porosities (0.45 or 0.65 μm) need to be the same in both cases; d) tests and real filtration must be carried at similar temperatures. Filterability tests are carried out on cellulose acetate, cellulose nitrate, polyethersulfone and polyvinylidene difluoride membrane filters.

Published research literature on wine filterability is very poor. In regard to this, the impact of enological agents for tartaric stabilization on wine filterability is mostly unknown. The aim of this research was to assess the influence of most commonly used stabilizing agents such as metatartaric acid, carboxymethyl cellulose (CMC), mannoproteins and gum arabic, on the filterability and turbidity of wines previously prefiltered and prepared for final filtration and bottling. Moreover, the impact of white wine sweetening with rectified concentrated must on the same parameters was also assessed. The results of this study are important, since the exhaustion of depth medium or blocking of the membrane during final filtration can both increase the costs and lead to holdup on the bottling line.

MATERIAL AND METHODS

Wine samples

Wines used in this research were produced from grape varieties Sauvignon Blanc and Merlot grown in the Fruška Gora wine region, northern Serbia. The grape was hand-harvested at technological maturity during the 2019 harvest. White, rosé and red wines were produced in two small-scale Serbian wineries (annual production 10000-20000 L). Processing was

carried out immediately after harvest. The must was sulfited by the addition of potassium metabisulfite (0.1 g/L). Destemmed and crushed grapes were pressed in a pneumatic press for the production of white and rosé wine (3 h long maceration was applied in rosé wine production) and the must was transferred into 2000 L inox tanks for fermentation. The clarification of must was carried out by cold settling with the addition of pectolytic enzyme (Trenolin Frio, Erbslöh, Germany) in the amount of 5 mL/hL. In the case of red wine production, grape pomace was transferred into 2000 L casks after destemming and crushing. Maceration and fermentation were conducted using classical technology in open vessels with a "floating cap". The cap was punched down by hand three times daily. Alcoholic fermentation in all three wines was carried out by the use of commercial *S. cerevisiae* strain Zymaflore Delta (Laffort, France), previously rehydrated and inoculated in a 0.25 g/kg dose. The yeast nutrient Complex vit (Essedielle, Italy) was added in all three vessels in the amount of 0.25 g/L. The moment of addition was after the one-third of sugar was fermented. The fermentation temperature was maintained at 16-18 °C for white and rosé wines, and at 25 °C for the red wine. After the end of fermentation, red pomace was pressed. All wines were racked from lees 7 days after the end of fermentation, and then sulfited (0.08 g/L potassium metabisulfite). The aging of all wines lasted 6 months, during which another racking and sulfiting as needed were performed. Clarification and stabilization on proteins followed. Appropriate doses of enological agents (bentonite for white and rosé wine and gelatin and bentonite for red wine), determined by small-batch lab tests, were applied. After additional racking, wines were filtered using depth filter sheets (Seitz K series, Pall). White and rosé wines were filtered through K100 (retention rating 1-3 μm) filter sheet while red wine was filtered through K200 (retention rating 3-6 μm) filter sheet.

Filterability tests were carried out 7 days after filtration. Agents for tartaric stabilization of wine were added 48 h before the testing started. The following stabilizing agents were used: liquid gum arabic and mannoprotein (doses of 100, 200 and 300 mL/hL, commercial product Senso Ü, Erbsloh, Germany), carboxymethyl cellulose (doses 100, 150 and 200 mL/hL, commercial product EnartisStab Cellogum L, Enartis, Italy), mannoprotein (doses 50, 100 and 150 mL/hL, commercial product Claristar, Oenobrands, France) and metatartaric acid and gum arabic (doses 2, 5 and 10 g/hL, commercial product MetaGum, Erbsloh, Germany), as well as an oak tannin (doses 1, 5 and 10 g/hL, commercial product Tannivin Superb, Erbsloh, Germany) as a non-commonly used agent for tartaric stabilization. Moreover, white wine sweetening was carried out with rectified concentrated must (MCR 65° brix, Essedielle, Italy). The tests were carried out in duplicate.

Methods

Reducing sugars, ethanol content, pH, total acidity (expressed as tartaric acid), volatile acidity (expressed as acetic acid), tartaric acid content, total SO_2 content and glycerol content of wine samples were determined using a specialized and calibrated wine device working on FTIR technology called WineScan (Foss Analytics, Denmark). Wine turbidity was determined using a portable nephelometer HI83749 (Hanna Instruments, Italy).

The filterability of used white, rosé and red wines after the addition of enological agents for tartaric stabilization was evaluated using Quality Filterability Test developed by Ju.Cla.S. and Vason Group. The instrument is capable of automatically assessing and calculating three factors: the filterability index (*FI*), the modified filterability index (*MFI*) and the maximum filterable volume (*Vmax*). The filterability index of a wine is an estimation of the time needed to block a specific filter medium during filtration [3]. Around 700 mL of a wine, free of carbon dioxide, at around 20 °C is used for conducting a filterability test. The device measures the time for which 200 mL (T_{200}) and 400 mL (T_{400}) of wine pass through a membrane (cellulose nitrate, 25 mm diameter, 0.65 μm absolute porosity) under 2 bar constant pressure (Eq. (1)):

$$FI = T_{400} - 2T_{200} \tag{1}$$

Vmax (mL) represents an assessment of the maximum volume that can pass through a 0.65 μm filter before fouling. This volume was not directly measured but was calculated automatically using the following formula (Eq. (2)):

$$Vmax\,(mL) = \frac{T_{400} - T_{200}}{\frac{T_{400}}{400} - \frac{T_{200}}{200}} \tag{2}$$

The experts from scientific and industrial sectors gave different limit values which define if the wine is filterable enough. The most often used criterion under which wines could be marked as easily filterable is:

$FI < 20$

Wine stability on tartrates was assessed using the Mini Contact Test. In the first phase, the conductivity of wine samples after tempering at -4 °C for 45 min was measured. The measurement was followed

by the addition of potassium bitartrate crystals (1 g/100 ml) in all samples, which were then stored at -4 °C for 45 min for white and rosé wines, and 3 h for red wine. After the estimated time, the conductivity was measured again and the difference in conductivity (ΔS) was determined. The criterion by which wines achieved tartaric stability is ΔS<50 μS.

All measurements in the study have been done in triplicate.

Statistical analysis

Statistical analysis in the present study was performed using Statistica 12.0 (StatSoft). The statistical difference between mean values of parameters was estimated by analyses of variance (ANOVA), at the 95% confidence level. Values detected as significantly different by the use of the Duncan multiple range test were marked with different letters (a, b, c …).

RESULTS AND DISCUSSION

The filterability of wine is an important factor which has a significant effect on the costs and efficiency of the bottling stage of wine production. Many winemakers have little awareness of its importance. Moreover, available methods for determination of this factor are limited and specific equipment is required.

Prior to filterability testing, the analysis of basic chemical parameters of wine samples had been carried out (Table 1). White, rosé and red wines were characterized by usual values for alcohol content, pH, acidity etc. It should be stated that only red wine was not dry (residual sugar 5.4 g/L) and it was characterized by significantly higher values for total acidity and glycerol content. Apart from basic quality parameters, turbidity, filterability index and Vmax were also determined in control wine samples (without the addition of stabilizing agents). The values are given in Table 2 and used for comparison with the readings after the stabilizing agents' addition. According to the defined standards all wine samples could be considered clear after pre-filtration (depth filter sheets) taking into account the turbidity measurements (NTU) for white, rosé and red wines (0.5, 1.0 and 1.2, respectively). Furthermore, the results for *FI* confirm that all control wines were characterized by good filterability (*FI*<20). This study also gives the values of Vmax (expected maximal volume of wine filtered through a given filter surface area) for different wines, although there are different opinions on the accuracy and reliability of this factor. The more recent paper [5] on this subject reported that one should be very careful when making filtration decisions (questions regarding the longevity of the filter set *i.e.* the volume of filtrate obtained from one filter set etc.) based only on this factor since its calculation is based on the extrapolation and proportionality with *FI* value. *Vmax* calculation uses the data from the standard filterability test (data obtained after 400 mL of wine has been filtered) to predict a maximum filtration volume. An error in calculation comes from the fact that the cleaner the wine is, *FI* is lower and extrapolation error is higher. On the other hand, wines with aggravated filterability exhibit higher *FI*, extrapolation is smaller and the error in *Vmax* calculation tends to be smaller. Therefore, in this study we used *Vmax* value only as an indicator of approximate maximal wine volume which can be filtered. Taking in account FI and Vmax values for control wines, it is evident that rosé wine was characterized by the best filterability (*FI* = 2.4 and *Vmax* = 4185).

Table 1. Physicochemical parameters of wine samples

Parameter	White wine	Rosé wine	Red wine
Ethanol (%)	14.31	12.57	13.24
Reducing sugar (g/L)	1.8	0.6	5.4
pH	3.27	3.38	3.49
Total acidity (g/L)	5.9	5.2	8.1
Volatile acidity (g/L)	0.15	0.2	0.4
Tartaric acid (g/L)	3.4	2.1	3.6
Total SO_2 (mg/L)	115	60	40
Glycerol (g/L)	7.1	5.5	11.9

The results of this study confirmed that enological agents used nowadays for the inhibition of potassium bitartrate crystallization have significant impact on wine filterability. In general, it can be seen that the addition of different products for tartaric stabilization did not cause significant changes in white wine turbidity (exception – the addition of 200 and 300 mL/hL of liquid gum arabic and mannoprotein) and filterability index (exception - the addition of 10 g/hL of metatartaric acid and gum arabic). *Vmax* for white wines, which were characterized by good filterability (*FI* 3.4--12.8), was in the very wide range (1243-4187) which can be misleading for wine producers. Furthermore, two higher used doses of enological products were efficient in achieving tartaric stabilization of white wine, except in the case of metatartaric acid and gum arabic, where only the highest dose (10 g/hL) was recommended.

Contrary to white wine samples, the addition of stabilizing agents in rosé wine caused significant increase in the turbidity. It was evident that 48 h (the time between addition and measurement) was not long enough for stabilization of turbidity. NTU values 2.0-2.5 are a bit higher for rosé wine, however that

Table 2. The effects of enological products for tartaric stabilization application on the filterability of white, rosé and red wine samples; mark (-) means sample not stable on tartrates; mark (+) means sample stable on tartrates. Different letters in the same column for each stabilizing product (including the value for control sample) indicate significant differences between values ($p < 0.05$). n/a: determination was not possible

Product	Dosage	Wine turbidity (NTU)	Filterability index FI (s)	Vmax (mL)	Tartaric stability*
		White wine			
Control white wine sample		0.5[a]	4.3[a]	2412[b]	-
Mannoprotein	50 (mL/hL)	0.52[a]	4.5[a]	2382[b]	-
Mannoprotein	100 (mL/hL)	0.55[a]	5[a]	2135[b]	+
Mannoprotein	150 (mL/hL)	0.56[a]	6[a]	1960[a]	+
Liquid gum arabic and mannoprotein	100 (mL/hL)	0.92[a]	3.4[a]	4187[c]	-
Liquid gum arabic and mannoprotein	200 (mL/hL)	1.29[b]	4.3[ab]	2586[b]	+
Liquid gum arabic and mannoprotein	300 (mL/hL)	1.30[b]	5.4[b]	2074[a]	+
Carboxymethyl cellulose (CMC)	100 (mL/hL)	0.61[a]	5.6[a]	2000[b]	-
Carboxymethyl cellulose (CMC)	150 (mL/hL)	0.63[a]	8.7[b]	1544[a]	+
Carboxymethyl cellulose (CMC)	200 (mL/hL)	0.62[a]	8.9[b]	1483[a]	+
Metatartaric acid and gum arabic	2 (g/hL)	0.71[a]	7.4[a]	1659[c]	-
Metatartaric acid and gum arabic	5 (g/hL)	0.74[a]	12.8[b]	1243[b]	-
Metatartaric acid and gum arabic	10 (g/hL)	0.78[a]	30.5[c]	814[a]	+
		Rosé wine			
Control rosé wine sample		1.0[a]	2.4[a]	4185[a]	-
Liquid gum arabic and mannoprotein	100 (mL/hL)	2.45[b]	2.4[a]	4183[a]	-
Liquid gum arabic and mannoprotein	200 (mL/hL)	2.32[b]	2.3[a]	4295[a]	-
Liquid gum arabic and mannoprotein	300 (mL/hL)	2.10[b]	2.1[a]	4704[b]	+
Carboxymethyl cellulose (CMC)	100 (mL/hL)	2.40[b]	2.9[a]	3655[a]	-
Carboxymethyl cellulose (CMC)	150 (mL/hL)	1.70[b]	1.9[a]	4688[b]	-
Carboxymethyl cellulose (CMC)	200 (mL/hL)	2.15[b]	2.1[a]	4590[b]	+
Metatartaric acid and gum arabic	2 (g/hL)	2.14[b]	2.1[a]	4552[b]	-
Metatartaric acid and gum arabic	5 (g/hL)	2.61[b]	2.6[a]	3938[a]	-
Metatartaric acid and gum arabic	10 (g/hL)	2.34[b]	2.3[a]	4086[a]	+
		Red wine			
Control red wine sample		1.2[a]	6.5[a]	1910[b]	-
Liquid gum arabic and mannoprotein	100 (mL/hL)	1.40[a]	509	549[a]	+
Liquid gum arabic and mannoprotein	200 (mL/hL)	1.48[a]	n/a	n/a	+
Liquid gum arabic and mannoprotein	300 (mL/hL)	1.42[a]	n/a	n/a	+
Metatartaric acid and gum Arabic	2 (g/hL)	1.51[a]	830.3	438	-
Metatartaric acid and gum arabic	5 (g/hL)	1.70[b]	n/a	n/a	+
Metatartaric acid and gum arabic	10 (g/hL)	1.66[b]	n/a	n/a	+
Tannin	1 (g/hL)	1.70[a]	14[a]	1200[b]	-
Tannin	5 (g/hL)	1.92[a]	74[b]	707[a]	-
Tannin	10 (g/hL)	2.45[b]	145[c]	668[a]	-

would not represent a problem for wines scheduled for wine filtration. Just in case, the turbidity of the samples was measured again after additional 48 hours and the NTU values declined to 1.1-1.4, which is evidently more acceptable (results not shown). On the other hand, the addition of products based on mannoproteins, CMC and metatartaric acid in this study did not cause significant changes in wine filterability (*FI* was in a rather narrow range 1.9-2.9, regardless of the product used). Vmax values for rosé wine were fairly uniform (3600-4600 mL). Regarding the tartaric stability, only the highest doses of all three used products were able to stabilize rosé wine.

Unlike white and rosé, the red wine was characterized by much worse filterability after the addition of stabilizing products based on mannoproteins and metatartaric acid (CMC is not recommended for use in red wines). The determination of *FI* was possible

only in the wines where the smallest doses of these products were added, however they were far higher than acceptable (*FI*>500). The turbidity readings were below 4 which can be considered suitable for bottling according to the industry. Almost all applied doses of mannoproteins and metatartaric acid in combination with gum arabic were efficient in stabilization of the wine. Similar results and problems with fast membrane fouling during red wine filtration were also previously reported [6]. The authors reported that treated red wine (supplemented with phenolic compounds and yeast extract) showed rapid and complete blockage of the membrane (cellulose acetate, 0.2 μm, and dead-end mode under 2 bar pressure). The drop in flux was evident in the first minutes of filtration. It should be kept in mind that in practice, red wine filtration is almost never done on a membrane of such low porosity (0.2 μm). The possible solution for more efficient red wine microfiltration could be in the use of different hydrolytic enzymes (pectinase, β-glucanase). For instance, a method for determination of the (1,3)--glucanase specific activity (releasing of only glucose units) in wines was developed and through these trials the filterability of wines (taking into account the impact of β-glucans) was evaluated [7]. The authors reported the increase in the volume of wines being filtered when enzymes with glucanase activity were used (increase in *Vmax* for 37-55% after 24 h at 23 °C). Also, wine filterability did not change during 24 h in the absence of enzyme addition.

The effect of oak tannins on red wine filterability was also assessed in this study (Table 2), although these compounds are not non-commonly used agents for tartaric stabilization - they are widely used in red winemaking. Only the addition of the lowest dose of tannin was connected with the acceptable filterability (*FI* = 14), while none of the three tannin doses provided tartaric stability. The impact of tannin treatment on the wine filtration which was carried out immediately, after three days, and after eight days after the tannin addition was previously investigated [1]. The filtration was carried out through 0.45, 0.65 and 0.8 μm polyvinylidene difluoride membranes (diameter 20 mm). The addition of tannin caused an increase in the filterability index regardless of the membrane porosity used, so the wines were more difficult to filter compared to the control sample (*FI* around 15). The increase of the filterability index of a wine filtered through a 0.45 μm membrane was the most pronounced when the filtration was performed immediately and after three days (*FI* values 15 and 27, respectively). Similar results were also obtained for trials using a 0.65 μm membrane, while when a 0.8 μm membrane was used, *FI* values for control and tannin supplemented samples begin to converge. Also, it was reported that prolongation of the moment of filtration through the 0.8 μm membrane (until up to eight days from tannin addition) caused the increase in *FI* compared to the measurement immediately after the tannin addition.

As already stated, available literature on wine filterability is very poor and the impact of enological agents for tartaric stabilization on wine filterability has not been examined in detail. Previously published studies [8] stated that CMC addition can contribute to a decrease in a wine's filterability, especially if the manufacture's recommendations (addition to a wine stable on proteins at least 48 h before the final filtration) were not followed. Moreover, CMC could be partially eliminated during filtration. For instance, different doses of CMC (50, 100 and 300 mg/l) caused the increase in the filterability index (*FI* 5, 6 and 24, respectively) in comparison with a highly filterable control wine (*FI* = 0.7) [3]. This trend can be explained by the increase of colloidal compounds content coming from CMC use. At the end, the same authors [3] emphasized the importance of checking the amount of CMC remaining after microfiltration, as well as its efficiency in achieving tartaric stability. Furthermore, the effects of both wine components (yeast extract in doses up to 0.5 g/L and phenolic compounds such as anthocyanins and tannins in doses up to 1.5 g/L) and physicochemical parameters (pH 3.3 and 3.7) on the blockage of a micro-filter membrane (cellulose acetate, 0.2 μm) were investigated [6]. The filtration was carried out with both synthetic and real wine samples, in dead-end mode under 2 bar pressure. They reported that the simultaneous presence of two types of phenolic compounds (anthocyanins and tannins) had a synergistic and more pronounced contribution to membrane fouling, compared to the presence of only one compound. For instance, the presence of proteins from yeast extract (300 mg/g of proteins, free of mannoproteins) caused the increase in membrane fouling. Moreover, it was shown that a decrease in pH value of the sample facilitates the filtration. The given explanation was that with decrease of pH in wine, an increase in the representation of charged functional groups on the protein surface occurs. This is followed by the increase of repulsive forces which prevent protein aggregation and enhance flow rate of the wine during filtration. Furthermore, apart from pH, temperature also has an impact on filtration effectiveness. An increase in wine temperature causes the enhancement in its filterability as a consequence of a viscosity decrease [9].

In the case of white and rosé wine used in this study, wine turbidity was also a good indicator of wine filterability, due to good correlation between wine turbidity and *FI* measurements. On the other hand, this was not the case with the red wine used. The literature and the practice usually report cases when wines with appropriate turbidity (suitable for bottling) are not easily filterable (*FI*>20), however there are also the opposite cases where turbidity measurements are above 5 NTU while the *FI* values are acceptable (*FI*<1.5) [3].

At the end of this study, the impact of white wine sweetening with rectified concentrated must on wine turbidity and filterability was assessed 48 h after the supplementation (Table 3). Only the highest dose of rectified concentrated must cause significant increase in wine turbidity and the recorded value (1.42 NTU) is a bit out of the range recommended for bottling (<1). On the other hand, all three added doses caused a significant increase in the *FI* (30-95) which means that the obtained samples are not suitable for effective realization of final membrane filtration (required *FI*<20).

Table 3. The effects of sweetening on white wine filterability; different letters in the same column for each stabilizing product (including the value for control sample) indicate significant differences between values ($p < 0.05$)

Sample	Dosage (g/L)	Wine turbidity (NTU)	*FI* (s)	*Vmax* (mL)
Control white wine sample		0.5^{a}	4.3^{a}	2412^{c}
Rectified concentrated must doses	30	0.85^{a}	30.2^{b}	907^{b}
	90	1.06^{ab}	73.7^{c}	806^{b}
	150	1.42^{b}	94.2^{d}	665^{a}

CONCLUSION

The use of NTU values representing wine turbidity as a parameter for assessing wine filterability is not always reliable. This data by itself cannot be used for the prediction of wine interaction with filter media during microfiltration. Modern filterability tests used for obtaining of the wine filterability index have proven to be simple, rapid and reliable. The results of this study confirmed that enological agents used nowadays for the inhibition of potassium bitartrate crystallization generally do not worsen the filterability of white and rosé wines. On the other hand, the addition of products containing mannoproteins and metatartaric acid significantly declines red wine filterability. Luckily, the tartaric stabilization of red wines was generally being achieved with small doses of these products. The quantification of wine filterability is important for one making decisions in wineries since the exhaustion of depth medium or blocking of the membrane during final filtration can both increase the costs and lead to holdup on the bottling line.

Acknowledgment

Financial support from the Ministry of Education, Science and Technological Development of the Republic of Serbia (Project 451-03-68/2020-14/200134) is greatly appreciated.

REFERENCES

[1] I. Schneider, Application Report. Eaton Technologies GmbH, Langenlonsheim, 2014, p. 1

[2] P. Bowyer, G. Edwards, Aust. N.Z. Grapegrow. Winemak. 610 (2014) 82-85

[3] P. Bowyer, G. Edwards, A. Eyre, Aust. N.Z. Grapegrow. Winemak. 585 (2012) 76-80

[4] Y. El Rayess, C. Albasi, P. Bacchin, P. Taillandier, M. Mietton-Peuchot, A. Devatine, J. Membr. Sci. 385-386 (2011) 177-186

[5] P. Bowyer, Aust. N.Z. Grapegrow. Winemak. 677 (2020) 62-65

[6] Y. El Rayess, C. Albasi, P. Bacchin, P. Taillandier, J. Raynal, M. Mietton-Peuchot, A. Devatine, in Proceedings of 2nd International Congress on Green Process Engineering, 2nd European Process Intensification Conference, Venice, Italy, 2009, p. 1

[7] A. Humbert-Goffard, C. Saucier, V. Moine-Ledoux, R-M. Canal-Llaubères, D. Dubourdieu, Y. Glories, Enzyme Microb. Tech. 34 (2004) 537-543

[8] P. Bowyer, V. Moine, C. Gouty, R. Marsh, T. Battaglene, Aust. N.Z. Grapegrow. Winemak. 558 (2010) 65-68

[9] F. De La Garza, R. Boulton, Am. J. Enol. Vitic. 35 (1984) 189-195.

VLADIMIR PUŠKAŠ
UROŠ MILJIĆ
VESNA VUČUROVIĆ

Tehnološki fakultet Novi Sad, Univerzitet u Novom Sadu, Bulevar cara Lazara 1, 21000 Novi Sad, Srbija

NAUČNI RAD

UTICAJ PRIMENE ENOLOŠKIH PREPARATA ZA STABILIZACIJU NA TARTARATE NA FILTRABILNOST VINA

Cilj ovog istraživanja bio je procena uticaja najčešće korišćenih enoloških sredstava za stabilizaciju vina na tartarate, na filtrabilnost belog, roze i crvenog vina. U eksperimentima su korištena sledeća enološka sredstva: metavinske kiselina, karboksimetilceluloza (CMC), manoproteini i gumiarabika. Uzorci korištenih vina su prethodno grubo filtrirani i pripremljeni za završnu filtriraciju i flaširanje. Procenjivana je takođe i filtrabilnost vina nakon doslađivanja rektifikovanom koncentrovanom širom. Rezultati ocene filtrabilnosti tretiranih vina izraženi su preko indeksa filtrabilnosti (FI) i maksimalne zapremine koja se može filtrirati pod datim sulovima (Vmax). Rezultati su potvrdili da korišćeni enološki preparati za inhibiciju nestabilnosti vina izazvanu taloženjem tartarata, uglavnom nisu negativno uticali na filtrabilnost belog i roze vina (FI<20). Međutim, bilo je evidentno da preparati koji sadrže manoproteine i metavinsku kiselinu značajno smanjuju filtrabilnost crvenog vina (FI>500). Utvrđena je korelacija između mutnoće i filtrabilnosti belog i roze vina, a što nije bio slučaj kada je u ogledima korišteno crveno vino. Rezultati ove studije su važni jer membranska (završna) filtracija neadekvatno pripremljenog vina koje karakteriše niska filtrabilnost (visok FI), može povećati troškove proizvodnje i dovesti do zastoja na liniji za flaširanje.

Ključne reči: vino, filtracija, stabilizacija na tartarate, indeks filtrabilnosti, mutnoća.

CI&CEQ
Chemical Industry & Chemical Engineering Quarterly

Available on line at
Association of the Chemical Engineers of Serbia *AChE*
www.ache.org.rs/CICEQ

Chem. Ind. Chem. Eng. Q. 27 (4) 363–369 (2021) CI&CEQ

HOUARI AMEUR[1]
YOUCEF KAMLA[2]

[1]Department of Technology, University Centre of Naama - Ahmed Salhi, Naama, Algeria
[2]Faculty of Technology, University Hassiba Ben Bouali of Chlef, Algeria

SCIENTIFIC PAPER

UDC 66.063.8:621

NEWLY SUGGESTED SHAPES OF IMPELLERS FOR STIRRING HIGHLY VISCOUS FLUIDS IN VESSELS

Article Highlights

- The agitation of highly viscous fluids in cylindrical tanks is studied numerically
- New shapes of close clearance impellers are suggested
- The performances of the newly designed impellers are compared with those of the classical anchor

Abstract

The power consumption and flow patterns generated in a cylindrical stirred tank are determined. The anchor impeller is used to ensure the agitation of highly viscous fluids. New modifications in the impeller design are introduced to improve the stirring rates. Firstly, the lower corner of the conventional anchor is replaced by an inclined segment to obtain Case No. 1. The number of segments was then increased to reach a closed circular shape (Case No. 2). Further increase in the number of segments was introduced to reach a perfect circular blade (Case No. 3) in the vertical direction. Finally, another circular horizontal blade was added to obtain Case No. 4. From the obtained results, Case No. 4 provided a great improvement in the circulation of fluid particles inside the vessel and generated the widest well-stirred region.

Keywords: close clearance impellers, stirred tanks, highly viscous fluids, modified anchor impellers, CFD.

The stirring in cylindrical tanks is a primary operation to achieve various purposes in different industrial applications, such as the food, paint, polymer, and petroleum industries. In mixing systems, the quality of the final product is strongly related to the flow patterns generated by the stirrer [1-4]. Therefore, details on the hydrodynamics in the whole volume of the stirred tanks are highly needed to be well-known. Further difficulties are encountered during the optimization of processes when the working fluids exhibit high viscosity [5].

The stirred systems containing one or more turbines are generally used for the agitation of low viscous fluids. However, the close clearance impellers are recommended for stirring fluids with high viscosity. In this situation, the stirrer is recommended to be used at low rotational speeds, *i.e.*, under laminar flow conditions [6,7].

For instance, in polymerization processes, the efficiency of mixing should be controlled to avoid some phenomena such as dead poor mixing regions, dead areas, and hot spots [8]. If turbines are employed in the agitation of liquids with high viscosity, the rapid decay of flow velocities may be generated, which yields low blending quality [9].

Various shapes of close clearance stirrers are available in the industry, including the anchor, Maxblend, and helical ribbon. Among these impellers, the anchor has shown satisfactory results. Chhabra and Richardson [10] reported in their research study that the anchor may be utilized for the agitation of Newtonian and non-Newtonian liquids. This type of impellers generates mainly tangential flows, with secondary axial and radial flows at high rotational velocities [11]. In their study on the performance of classical anchor stirrers, Karray *et al.* [12] reported a significant deformation of the anchor arm when operating under

Correspondence: H. Ameur, Department of Technology, University Centre of Naama - Ahmed Salhi, P.O. Box 66, Naama 45000, Algeria.
E-mail: houari_ameur@yahoo.fr
Paper received: 13 October, 2020
Paper revised: 9 January, 2021
Paper accepted: 22 February, 2021

https://doi.org/10.2298/CICEQ201013005A

turbulent flow conditions. They suggested the insertion of an anchor blade to overcome this issue.

Espinosa-Solares *et al.* [13] focused on the influence of wall clearance and bottom clearance on power input. Their findings showed a decrease in power input with the augmentation of the wall and bottom clearance, which is yielded by the change in the hydrodynamics. The experiments conducted by Triveni *et al.* [14] illustrated an increase in the fraction of the well-mixed area from 0.7 to 0.95 with the rise of anchor speeds. This enhancement in the mixing quality was reached for Newtonian and non-Newtonian liquids, however the enhancement was small for highly viscous fluids. With anchor stirrers, Prajapati and Ein-Mozaffari [6] employed the CFD method to estimate the mixing details of viscoplastic fluids. Their optimization study allowed for selecting the values 0.102 and 0.079 as optimum for the stirrer width-to-vessel diameter and the stirrer clearance-to-vessel diameter ratios, respectively. In addition, the anchor with four blades performed better than that with only two blades. Ameur [15] tried to overcome the issue of the deformation of blades by inserting vertical and/or horizontal arms in the blade of the stander anchor. In another paper, Ameur and Ghenaim [16] used Scaba 6SRGT and anchor impellers in a combined configuration to improve the overall efficiency in stirring shear-thinning liquids. Recently, Kamla *et al.* [17] compared the performance of the octagonal, rectangular, and circular design of the blades. The widest well-agitated region was observed as the one with the octagonal shaped blade. However, the circular shaped blade allowed for the lowest power consumption.

In this investigation, new shapes of close clearance stirrers are suggested for the agitation of fluids with high viscosity. The performances of the newly designed impellers are compared with those of the standard anchor. The Newtonian behavior of the working liquid under the laminar flow regime is considered.

Case study

The geometrical configuration of the agitated system is highlighted in Figure 1. A cylindrical, flat-bottomed, and unbaffled vessel with a diameter D = = 300 mm and height H/D = 1 is used. The glycerol (density ρ = 1262 kg·m^{-3} and viscosity μ = 1.495 Pa·s) is used as an agitated medium. The vessel is fully filled with the liquid. All necessary details on the other geometrical parameters are given in Table 1. Four newly suggested shapes of close clearance impellers are shown in Figure 1. In Case No. 1, the lower part of the classical anchor impellers has been modified. In Case No. 2, the vertical arms of the blade have been modified to form multiples segments (five segments in each part). Further segments have been introduced in Case No. 2 to form a complete circle, which gives Case No. 3. Finally, Case No. 4 contains

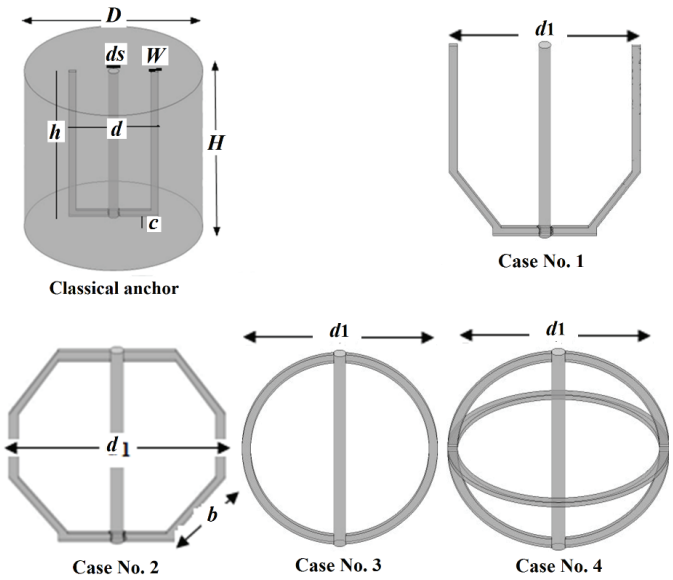

Figure 1. The different cases under study.

Table 1. Values of the geometrcial parameters of the agitation system

H/D	d/D	h/D	c/D	w/D	d_1/D	b/D	d_s/d
1	0.5	0.95	0.066	0.04	0.92	0.5	0.06

two circular shaped blades displayed in horizontal and vertical arrangements. For the classical anchor, the blade diameter is d = 150 mm. For the other cases, the blade diameter is d_1 = 276 mm.

Theoretical tools

The power number (Np) is an essential parameter to estimate the efficiency of an agitated tank. It is given as:

$$Np = \frac{P}{\rho N^3 d^5} \quad (1)$$

where P is the power consumption, and N is the impeller rotational velocity. The Reynolds number Re is the ratio between the viscous and inertia forces:

$$Re = \frac{\rho N d^2}{\mu} \quad (2)$$

The dimensionless axial and radial coordinates Z^* and R^* are defined respectively as:

$$R^* = 2R/D \quad (3)$$

$$Z^* = Z/D \quad (4)$$

The dimensionless velocity is defined as:

$$V^* = V/\pi Nd \quad (5)$$

METHOD

The study is realized via the CFD way by using the computer software (CFX). This software uses the finite volume method to solve the governing equations. The geometry and mesh of the computational domain (Figure 2) were generated with the computer tool Ansys ICEM CFD. The investigations were performed under the following considerations: steady-state, incompressible fluid, three-dimensional and laminar flow conditions. The Rotating Reference Frame (RRF) technique was employed for the modelling of rotating parts. This technique has been selected due to the absence of baffles [18-23]. To achieve the velocity-pressure coupling, a pressure-correction method of the semi-implicit method for pressure-linked equations-consistent type (SIMPLEC) was used. Due to its high precision, the second-order central scheme with the finite volume method was utilized. The grids were refined near the impeller and vessel walls to capture the flow boundary details. To determine the optimal grid size for the computational domain, the mesh density was increased by about 2. Mesh tests were carried out by checking that the additional grids did not change the velocity magnitude in regions with high gradients by more than 2.5% (Table 2). From these results, the mesh M2 with a global number of cells of about 821,584 was selected as optimal.

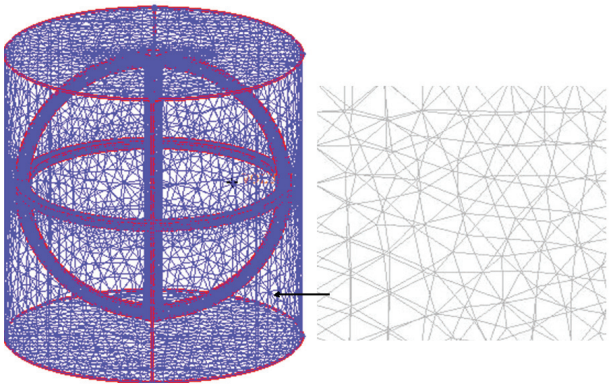

Figure 2. Meshing of the computational domain.

Table 2. Details on mesh tests for Case No. 1 at Re = 50

Parameter	M1	M2	M3
Number of cells	401,145	821,584	1,520,548
Np	1.9411	1.9622	1.9671
Time required, s	3,520	7,215	14,415

With a machine (Intel® i7 processor with 8 Gb RAM) and for a residual target 10^{-7}, the convergence was achieved after about 1700-1800 iterations, which corresponds to about 2-3 h of CPU time.

Validation

To check the good and appropriate settings of boundary conditions, as well as the selected computational grid, some computed findings were compared against the available experimental data. Figure 3a shows our results of power number that are obtained numerically and those obtained experimentally by Prajapati and Ein-Mozaffari [6]. While Figure 3b illustrates the variation of tangential velocity *vs.* vessel radius (R^*) at Re = 14. In Figure 3b, the validation is made against the experimental data of Anne-Archard *et al.* [24]. As it may be observed, the validation in both figures reveals a satisfactory agreement.

RESULTS AND DISCUSSION

Flow fields

In this section, the flow fields and velocities are highlighted at various positions in the tank and under various plots. At the mid-height of the tank (Z^* = 0.5) and for the angular position θ = 0°, the distribution of the dimensionless tangential velocity (V_θ^*) along with the tank radius (R^*) is plotted in Figure 4. The values of V_θ^* are given for the five geometrical cases under inspection. For all the computations, the line passing

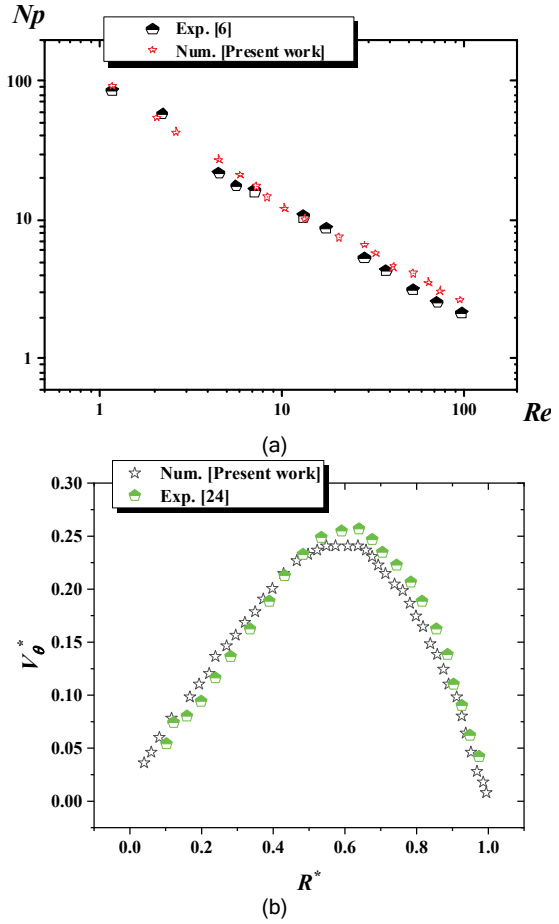

Figure 3. Validation of the computed results: a) power number (Np) vs. Reynolds number (Re); b) variation of the tangential velocity at Re = 14.

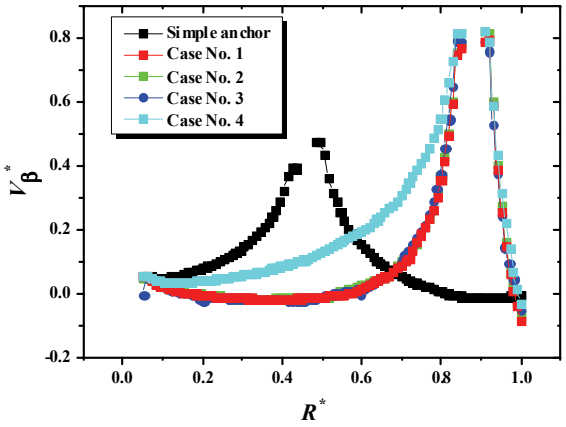

Figure 4. Tangential velocity for Re = 50, $Z^* = 0.5$, and $\theta = 0°$.

through the blade of the classical anchor impeller is taken as a reference for the angular coordinate.

As shown in this figure, V_θ^* augments gradually from the agitator shaft until reaching the highest values at the blade tip, and it decreases again until becoming negligible at the tank wall. The comparison between the different suggested shapes indicates that the maximum amount of V_θ^* is reached at the blade tip, whatever the shape of the blade. In addition, the lowest amount of the velocity is observed for the classical anchor because $d < d_1$.

The results of V_θ^* at the angular position $\theta = 90°$ are illustrated in Figure 5. At this location, the velocity changes according to parabolic profiles. From the different cases, the impeller that contains two circular blades (*i.e.*, Case No. 4) yielded the most powerful tangential flows, followed by the impeller that contains only one circular blade. A slight difference between the classical anchor, Cases No. 1-3 is observed in terms of velocity intensity. However, the difference between the mentioned cases and Case No. 4 is very large, which is due to the existence of the second circular blade.

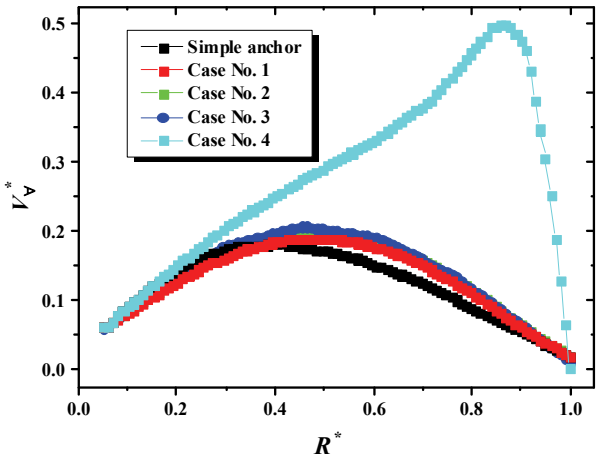

Figure 5. Tangential velocity for Re = 50, $Z^* = 0.5$, and $\theta = 90°$.

Further insight into the hydrodynamics generated by the different stirrers is provided by the results of Figures 6 and 7. The streamlines induced by the different cases are presented in Figure 6 at the mid-height of the tank for the angular position $\theta = 90°$. The classical anchor generates tangential flows in the whole vessel volume. The toroidal flow observed in this figure for the classical anchor is due to the wall effect (vessel and impeller shaft). This toroidal flow is formed in the lower part of the vessel for Cases No. 1 and 2 due to the modifications introduced in the blade. The flow is almost uniform at the lower part of the vessel for all cases, except Case No. 4, where the presence of the second horizontal blade destroyed this uniformity of the flow and generated another toroidal flow. Furthermore, the size of the toroidal structure of the flow is the highest for Case No. 4.

The results of the velocity contours at the mid-height of the tank are illustrated in Figure 7. It seems that the classical anchor has the lowest size of the

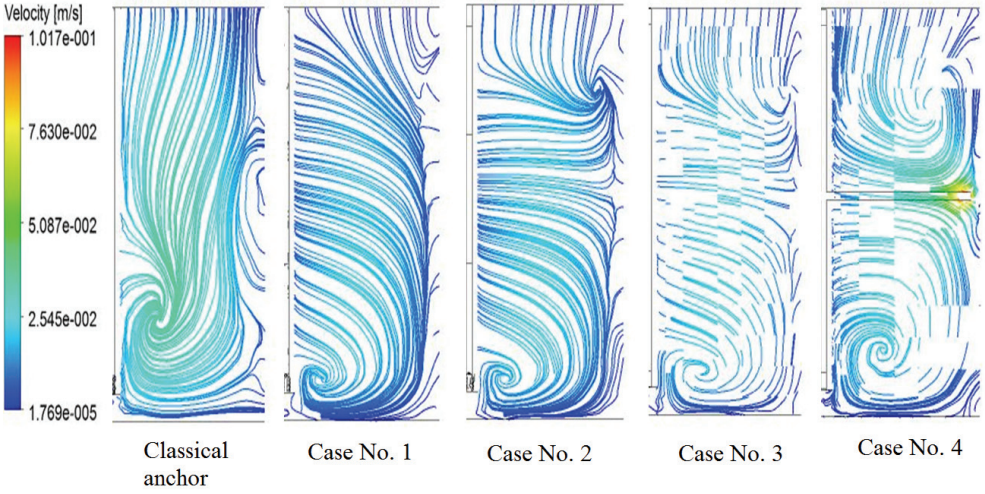

Figure 6. Streamlines for Re = 50 and θ = 90°.

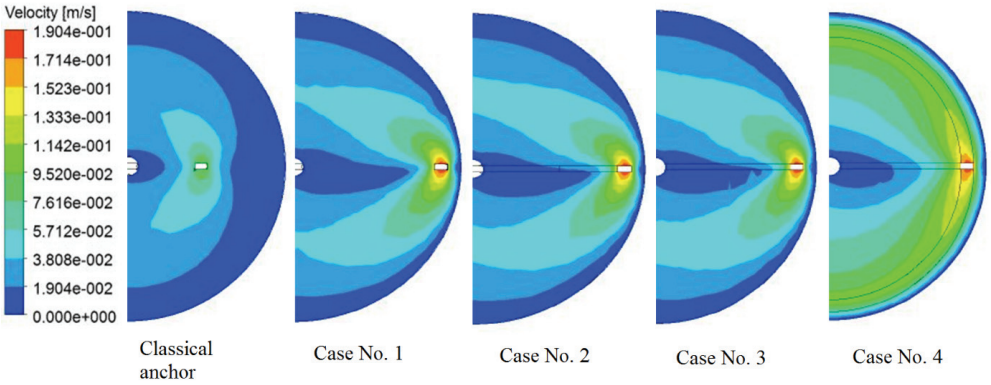

Figure 7. Well-agitated region at Re = 50, $Z^* = 0.5$.

well-stirred region. The introduction of an inclined arm at the lower part of the conventional anchor allowed a little increase in the size of the agitated area. However, a small enhancement has been obtained with Case No. 2, which remained almost the same with Case No. 3. The insertion of another horizontal circular blade (Case No. 4) has overcome the issue of the poor agitated region at some angular positions and it has given a satisfactory distribution of flow velocities. Finally, and in terms of uniformity of the flows, the studied impellers may be classified as follows: Case No. 4, 3/2, 1, and then the classical anchor.

Power consumption

The power consumption is another issue to be verified in stirred tanks. The results of the power number (*Np*) for the different geometrical configurations are given in Figure 8 for various Reynolds numbers. A continuous decrease in *Np* values is reached with the increased impeller rotational speeds (*Re*). This decrease is highly significant in the deep laminar regime.

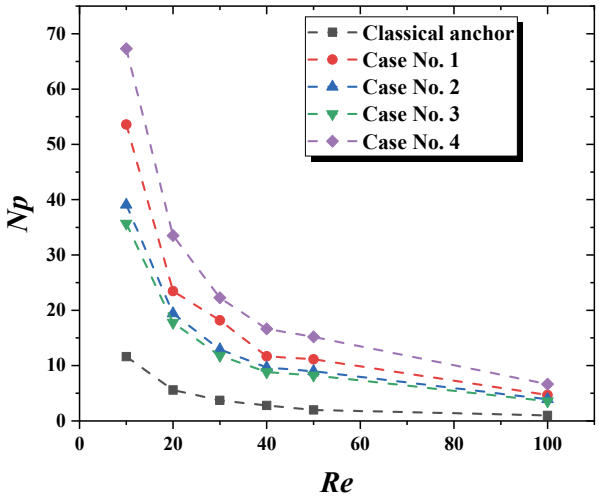

Figure 8. Power number vs. Reynolds number.

The lowest values of *Np* were reached with the classical anchor due its small blade diameter. The comparison between the classical anchor and Case No. 1 showed an increase in *Np* values by about four times due to the increased blade diameter. Moving

from Case No. 1 to Case No. 2, the power number was increased by about 20%. However, moving from Case No. 2 to Case No. 3, only a slight decrease in *Np* was observed. Adding another circular horizontal blade has yielded an increase in *Np* by about 50% in comparison between Cases No. 3 and 4. For example, at *Re* = 50, the values of the power number are 1.96, 11.13, 8.97, 8.23, and 15.19 for the classical anchor, Cases No. 1–4, respectively.

CONCLUSION

Some modifications in the classical anchor impeller have been suggested to improve the hydrodynamic characteristics in cylindrical vessels. In each part of the blade of the conventional anchor, the lower corner was replaced by an inclined segment to obtain the so referenced Case No. 1 in this study. Then, the number of these segments were increased to form a closed shape (Case No. 2). Further segments were added to obtain a perfect circular blade (Case No. 3) in a vertical position. Finally, another horizontal circular blade was added to give Case No. 4.

From the obtained results, the suggested Case No. 4 allowed a significant enhancement in the movement of the fluid particles in the entire volume of the stirred vessel. This case has given a satisfactory distribution of flow velocities and it has generated the widest well-stirred area. In terms of less power consumption, the newly suggested shapes of impeller may be classified as follows: Cases No. 3, 2, 1 and 4. For industrial applications, further studies on the newly proposed design are needed for other kinds of fluids and operating conditions to allow the good choice of the most efficient impeller.

Nomenclature

b - Length of the blade segment, m
c - Impeller off-bottomed clearance, m
D - Tank diameter, m
d, d_1 - Agitator diameter, m
d_s - Diameter shaft, m
h - Blade height, m
H - Tank height, m
N - Agitator rotational speed, s^{-1}
Np - Power number, dimensionless
P - Power, W
R - Radial coordinate, m
R^* - Dimensionless radial coordinate, $R^* = 2R/D$
Re - Reynolds number, dimensionless
V_z - Axial velocity, $m \cdot s^{-1}$
V_θ - Tangential velocity, $m \cdot s^{-1}$
W - Thickness of the blade arm, m
Z - Axial coordinate, m
Z^* - Dimensionless axial coordinate, $Z^* = Z/D$
ρ - Fluid density, $kg \cdot m^{-3}$
μ - Viscosity, Pa·s

REFERENCES

[1] S. Deshpande, K. Kar, J. Walker, J. Pressler, W. Su, Chem. Eng. Sci. 168 (2017) 495-506

[2] G. Janiga, Chem. Eng. Sci. 201 (2019) 132-144

[3] H. Ameur, Chem. Eng. Proc. Process Intensif. 154 (2020) 108009

[4] M. Foukrach, H. Ameur, Chem. Ind. Chem. Eng. Q. 26 (2020) 259-266

[5] H. Ameur, Energy 93 (2015) 1980-1988

[6] P. Prajapati, F. Ein-Mozaffari, Chem. Eng. Technol. 32 (2009) 1211-1218

[7] H. Ameur, ChemistrySelect 2 (2017) 11492-11496

[8] B. Triveni, B. Vishwanadham, T. Madhavi, S. Venkateshwar, Chem. Eng. Res. Des. 88 (2010) 809-818

[9] S. Woziwodzki, L. Broniarz-Press, M. Ochowiak, Chem. Eng. Technol. 33 (2010) 1099-1106

[10] R.P. Chhabra, J.F. Richardson, Non-Newtonian flow in the process industries: fundamentals and engineering applications, Butterworth-Heinemann, Oxford, 1999

[11] M. Ohta, M. Kuriyama, K. Arai, S. Saito, J. Chem. Eng. Japan 18 (1985) 81-84

[12] S. Karray, Z. Driss, H. Kchaou, M. Abid, Eng. Appl. Comp. Fluid Mech. 5 (2011) 315-328

[13] T. Espinosa-Solares, E.B.-D.L. Fuente, F. Thibault, P. Tanguy, Chem. Eng. Commun. 157 (1997) 65-71

[14] B. Triveni, B. Vishwanadham, S. Venkateshwar, Heat Mass Transfer 44 (2008) 1281-1288

[15] H. Ameur, J. Hydrodyn. 28 (2016) 669-675

[16] H. Ameur, A. Ghenaim, ChemistrySelect 3 (2018) 7472--7477

[17] Y. Kamla, H. Ameur, A. Karas, M.I. Arab, Chem. Pap. 74 (2020) 779-785

[18] R. Alcamo, G. Micale, F. Grisafi, A. Brucato, M. Ciofalo, Chem. Eng. Sci. 60 (2005) 2303-2316

[19] A. Khapre, B. Munshi, J. Taiwan Inst. Chem. Eng. 56 (2015) 16-27

[20] A. Hadjeb, M. Bouzit, Y. Kamla, H. Ameur, Polish J. Chem. Technol. 19 (2017) 83-91

[21] H. Ameur, Chin. J. Chem. Eng. 24 (2016) 572-580

[22] H. Ameur, Int. J. Chem. React. Eng. 14 (2016) 1025-1033

[23] H. Ameur, J. Food Eng. 233 (2018) 117-125

[24] D. Anne-Archard, H. C. Boisson, M. Marouche, in Proceedings of 18ème Congrès Français de Mécanique, Grenoble, France, 2007, pp. 27-31.

HOUARI AMEUR[1]
YOUCEF KAMLA[2]

[1]Department of Technology, University Centre of Naama - Ahmed Salhi, Naama, Algeria
[2]Faculty of Technology, University Hassiba Ben Bouali of Chlef, Algeria

NAUČNI RAD

NOVI TIPOVI MEŠALICA ZA MEŠANJE VISKOZNIH TEČNOSTI U SUDOVIMA

Određeni su snaga mešanja i obrasci strujanja u cilindričnom sudu sa mešalicom. Sidrasta mešalica je korišćena za mešanje jako viskoznih tečnosti. Uvedene su nove modifikacije u dizajnu mešalice da bi se poboljšale brzine mešanja. Prvo, donji ugao konvencionalnog sidra je zamenjen kosim segmentom (tip 1). Broj segmenata je zatim povećan da bi se postigao zatvoreni kružni oblik (tip 2). Dalje povećanje broja segmenata je uvedeno da bi se postiglo savršeno kružno sečivo (tip 3) u vertikalnom pravcu. Konačno, dodato je još jedno kružno horizontalno sečivo (tip 4). Tip 4 je značajno poboljšao cirkulaciju tečnosti unutar suda i stvorio najširu dobro izmešanu oblast.

Ključne reči: Sidraste mešalice; suds a mešanjem; jako viskozne tečnosti; modifikovane sidraste mešalice; CFD.

CI&CEQ
Chemical Industry & Chemical Engineering Quarterly

Available on line at
Association of the Chemical Engineers of Serbia *AChE*
www.ache.org.rs/CICEQ

Chem. Ind. Chem. Eng. Q. 27 (4) 371–381 (2021) CI&CEQ

DRAŽANA RADONJIĆ

Biology Department of the Faculty of Natural Sciences and Mathematics, University of Montenegro, Podgorica, Montenegro

SCIENTIFIC PAPER

UDC 504(497.16):579.26

APPLICATION OF THE MODEL OF CYLINDRICAL REACTOR FOR SELF-PURIFICATION BY INDIGENOUS MICROORGANISMS

Article Highlights

- Kinetic model of the autotrophic biofilm reactor is researched through its efficiency in the water
- The level of auto-purification is proven higher with the help of the kinetic model
- Decrease in NSAID concentrations is proven, which poses a significant ecological restoration aspect
- Study presents an excellent theory to better regional development and ecological sustainability

Abstract

Pharmaceutically active compounds (PhACs), in particular, nonsteroidal anti-inflammatory drugs (NSAIDs) are in increasingly wider usage, and as such are more and more frequently part of the organic matter of recipient rivers, especially in their lower courses. To indicate their significance as pollutants, as well as the significant role that the presence of autochthonous microflora plays in solving this issue, we undertook to perform this experiment. The experiment, titled "Application of the model of cylindrical reactor in self-purification by indigenous microorganisms", was conducted during a one-year period at the location of Vukovci, in the lower course of the Morača river. Assuming that the concentration of NSAIDs and PhACs in water can be reduced through self-purification, it has been proven that such processes result in a modification of phenotype in the indigenous microbiological population. Having the above-mentioned premise in mind, we constructed the experiment model, which entails kineticism of water, whereas the defined volume flow rate per unit time was 0.005 m/s, through the known distance of 432 m. Over one year of application of the model of the cylindrical reactor for enhancing self-purification capacity by indigenous microorganisms, auto-purification increased by 28.05%, the phenotype of the indigenous microorganisms changed by 24.62%, whereas the total concentration of particular PhACs, micropollutants, and NSAIDs decreased by 4.19%.

Keywords: pharmaceutically active compounds (PhACs), nonsteroidal anti-inflammatory drugs (NSAIDs); self-purification, water kineticism, indigenous microorganism phenotype.

Within natural aquatic environments, various physical, chemical, and biological processes occur which affect the content, transformation and fluctuation of the water constituents [1]. In most cases, river and lake waters are contaminated by waste, sewage, and pharmaceuticals, including nonsteroidal anti-inflammatory drugs (NSAIDs) and their degradation products [2-5]. Montenegro as a country, especially its central region, along with the mountain range surrounding it, is considered a hydrologically dense and rich area. An estimated average amount of 614 m³/s flows through its surface, which amounts to 19.3

Correspondence: Biology Department of the Faculty of Natural Sciences and Mathematics, University of Montenegro, 81000 Podgorica, Montenegro.
E-mail: drazana.radonjic@biaseparationscro.com
Paper received: 26 November, 2020
Paper revised: 22 February, 2021
Paper accepted: 1 March, 2020

https://doi.org/10.2298/CICEQ201126006R

km³ per year, with an average module of 44.4 l/s/km³. Waterflows of equal or greater capacity than this appear on less than 3% of the Earth's surface. The longest and largest river in Montenegro is Morača, with a flow length of 110 km [6].

The Morača river, with an annual intake of 4,898,300 m^3 of treated water is mostly polluted due to the continuous human impact caused by large-scale urban, industrial, and agricultural activities, which affect this water source and the ecosystem it sustains [7]. Compounds that are frequently studied in the aquatic environment are analgesics and anti-inflammatories (such as diclofenac, ibuprofen, naproxen, acetylsalicylic acid, and paracetamol) [8].

However, out of the existing and theoretically feasible surface water purification methods, there are none currently implemented in Montenegro. At present, river water purification technologies can be categorized into physical, chemical, biological, and ecological methods. Physical methods include aeration and sediment dredging [9]. Chemical methods include chemical precipitation [9] and the application of chemical algaecide [10]. Biological methods include bioremediation [11], biofilms [12], contact oxidation [13], and membrane bioreactor technology [14]. Ecological methods include ecological ponds [15], plant purification treatment [16], ecological floating beds [17], and constructed wetlands [18]. They also offer ecological benefits: they have been demonstrated to be an economical and efficient sewage treatment and management method [19], and they have become a preferred ecological method to improve the water quality of rivers in cities around the world.

As a result of the above-stated information, developing an appropriate water purification method that uses the known property of microorganisms to use pollutants in their nutrition as the basic source of carbon, whereby the properties of the microorganisms are altered, was our primary objective. These microorganisms are categorized as natural purificators – self-purificators. Self-purification, in the ecological sense, represents the process of the ecosystem itself adapting and learning to face all changes and occurrences accordingly. It can also be seen as the basis for self-support that the system provides in case its growth and development are disturbed.

Auto-purification or self-purification is a process by which the system adequately faces all the changes and occurrences almost independently. The relationship between facultative oligotrophic and heterotrophic (index FO/H) represents one of the most significant microorganism parameters used to estimate water properties from an ecological aspect [20,21] and is a very good indicator of water self-purification capacity [22]. An idea for categorization of water self-purification capacity based on the relationship between FO/H [23], describes self-purification capacity of water as low (<1), sufficient (>1), and if >10 as good capacity of self-purification.

Therefore, we ran a pilot project in which we tested the applicability of the developed cylindrical reactor mathematical model.

By definition, a cylindrical reactor is a chemical reactor and an open system. However, the principles developed for chemical reactors can be applied to most, if not all, chemically reacting systems (*e.g.*, atmospheric chemistry, metabolic processes in living organisms, etc.) [24]. It is important to highlight the significance of its approximate ideal drift, which means there is no fusion inside the moving reactionary compound in the course of the flow (axial direction). The reactor resembles a line of elementary volumes of the reactionary compound (reaction compound inside the differential volume of that sort is homogenous), and the volumes passing through the reactor do not mix with the reactionary mass (Figure 1a).

On its way from the entrance to the exit, a hypothetical elementary (differential) volume spends a certain amount of time in the reactor, during which the composition of the reactionary mass changes [25]. According to that, the values of the dependent variables are the position functions on the z-axis.

Because of its simple cylindrical design (Figure 1b), free of any additional mixing devices, it is often used. Setting the component A balance (indigenous microorganisms) as the differential volume of the reactor, results in the basic equation of multiplication of component A (indigenous microorganisms):

$$FA - (FA + d\,FA) - r\,A\,d\,V = 0$$
$$-d\,FA - r\,A\,d\,V = 0$$

FA - molar flow rate for indigenous microorganisms in the cylinder; *dFA* - molar velocity differential element for indigenous microorganisms; *dV* - differential volume element; *rA* - the numerical value of indigenous microorganisms.

Therefore, the development of optimization functions of the model means that the number of replicas of indigenous microorganisms that would be self-supporting to the whole system should be met, which was our goal at the beginning.

However, the system also has its flaws. The main shortcoming is the size of the system itself, as it needs a large surface, and must be kept in the state of kinetic energy at all times. Also, an adequate flow

rate through the cylindric pipe must be determined, lasting no longer than 24h, to lower the temperature inside the reactor and at the same time keep the active oxygen that creates aerobic conditions. This paper describes a trial construction system of the cylindrical reactor for the self-purification of indigenous microorganisms. These results serve as support for the promotion and application of this technology.

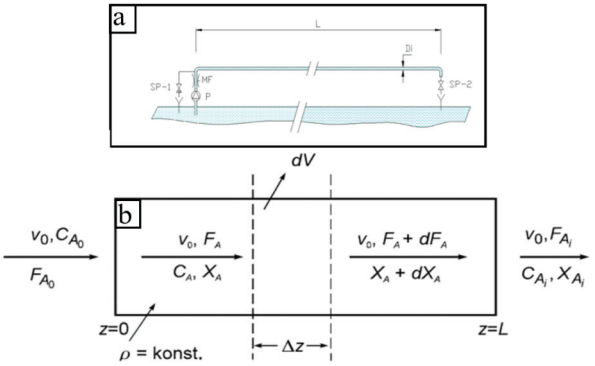

Figure 1. a) An example of the "cylindrical reactor for the purpose of self-purification by indigenous microorganisms" SP-1 water sampling site before entering the reactor; MF flow meter; P-pump; L-length of hose-cylindrical reactor; Di-section / diameter of the reactor hose; SP-2 designation for the point at the outlet of the hose / reactor where a water sample is taken; b) cylindrical reactor for enhancing self-purification capacity by indigenous microorganisms: v_0-volume flow (flow rate at the beginning), C_{A0}-concentration of reactant (in our case the number of indigenous microorganisms at the beginning); F_{A0}-molar flow rate of indigenous microorganisms at the beginning; FA-molar flow rate for indigenous microorganisms in the cylinder; CA-concentration of reactant (in our case indigenous microorganisms in the cylinder); XA-conversion of reactant reaction in our case of indigenous microorganisms; dV-differential volume element; z-axial direction; ρ-density; dFA-differential element of molar velocity for indigenous microorganisms; dX_A-differential element of conversion of the reactant reaction, in our case of indigenous microorganisms; L-length of reactor; F_{Ai}-molar flow of indigenous microorganisms at the outlet; C_{Ai}-concentration of indigenous microorganisms at the outlet; X_{Ai}-conversion of reactant reactions at the outlet (in our case of indigenous microorganisms).

EXPERIMENTAL

Model design

The model design of the cylindrical reactor for the self-purification of indigenous microorganisms is shown in Figure 1b. It consists of a built-in pump (P), flow meter (MF), rotameter, specifically with the ability to regulate the rate of the flow, and a long pipe (L) that represents a cylindrical reactor. Hypothetically, we have different flow rates in the pipe. The highest velocity, both theoretically and practically, is during laminar flow in the middle of the pipe's (*Di*) axis, which is parabolically arranged so that its outermost radius amounts to zero.

Average velocity is calculated by a continuity equation, flow Q = const, the maximum velocity of 0.005 m/s is adopted (*Di*), considering that in the worst case, the pipe can reach laminar flow that, compared to the turbulent velocity, has a higher velocity in the axis. Based on that, we can calculate the length of the cylindrical reactor:

$$L = Vmax \times 3600\text{s} \times 24\text{h} = 0.005\ E \times 3600\text{s} \times 24 = \\ = 432\text{m}$$

Samples were taken from localities SP1 and SP2. The water sample taken from locality SP1 was taken before the water entered the cylindrical reactor, and it is a so-called "native sample". The sample from locality SP2 was taken from the cylindrical reactor's faucet (water sample is taken from the kinetic reactor of indigenous microorganisms after a reaction lasting 24 h). The objective of the experiment has been to prove that under these conditions, facultative oligotrophs can increase their number and can affect modifications in the concentration of certain pharmaceuticals in water; accordingly, it would provide the grounds for the assumption that the same applies to other microorganisms.

Study area

The river Morača has its source at the topographic point of 975 m above the springs which flow down the Javorje and Zebalci slopes, with the largest of them being Javor and Rzav creeks. Morača is 113 km long, which makes it the longest river in Montenegro. We tested the locality Vukovci, situated at an altitude of 49 m.

The coordinates of the research location are 42°20′02″ N, 19°11′60″ E. The average yearly temperature at the locality Vukovci is 23.25 °C, and the average annual precipitation is 116.92 mm. The highest temperature recorded during the summer was 42.0 °C, and the lowest temperature recorded during the winter was -2.1 °C.

Additionally, this is the most densely populated area in Montenegro and is part of the central region. In 1948, the population of this region reached 128,872 which was equal to 34.2% of the total population, while in 2011, the central region accounted for 47.3% of the total population.

The river flows into the Skadar lake, the largest still body of freshwater in Montenegro. The main hydrological parameters of the river Morača are Q abs-

olute minimum: 5.5 m^3/s; *Q* average: 140 m^3/s; *Q* absolute maximum: 900 m^3/s. The annual average flow of the river Morača on locality Vukovci is 104,125 m^3/s.

Data collection and analysis

The quality of the water samples was monitored over a one-year period from September 2017, to December 2018. Samples were taken monthly, on the 5th day of each month, in the morning.

Samples taken for chemical analysis were collected using glass bottles with a capacity of 1 liter. To determine the concentrations of dissolved oxygen in water, Winkler's bottles with coded stoppers were used, with oxygen being immediately fixed by adding 1 ml KI and 1 mL $MgCl_2$ [26].

Sampling for microbiological analysis was performed in pre-sterilized glass bottles. Sampling bottles were washed and dried, then sterilized for one hour at 190 °C in a dry sterilizer. The sampling included the following procedures: the sampling for microbiological analysis was done by quickly submerging prepared bottles, to avoid contamination of the bottle. Samples were transported to the laboratory in a portable fridge. Microbiological analysis of the samples was performed at the Hydrobiological Institute of Montenegro, Department of Biology [27].

Samples intended for saprobiological analysis were taken using a 25 μm mesh plankton net, and they were analyzed without being fixated, or fixated using 96% alcohol.

Community-level physiological profiling of the microbial community (CLPP) is based on the BIOLOG microbial identification system in the Microbiological lab at Hemomont d.o.o, Podgorica, Montenegro. The BIOLOG system functions by identifying microorganisms on the phenotype level. It is especially important because every living community can react with 95 different sources of carbon on a microtiter plate. Prokaryote communities represent functional units that have the metabolic characteristics of bacteria, hence CLPP is used as a sensitive and fast method to identify the potential diversity of microbial communities. By degrading the sources of carbon, we reduce one out of 95 microbial mediums found in cupolas (not the one in the position (1,1) as it represents negative control), and we notice changes in the shades of orange. Those color changes manifest through the optical distance measurements (OD), and the change of the shade itself can identify the microbial community through the average metabolic response (AMR).

Average metabolic response (*AMR*) is by definition the average respiration of carbon sources used by microbial communities, and is predictable, measurable, and can be compared between communities

$$AMR = \Sigma\left(O.D.well - O.D.neg\right) / 95$$

where (*O.D.well*-*O.D.neg*) is the relation between measured values of optical density and negative control [28].

Analysis of PhACs (NSAID) in water samples

River water (100 mL) was collected to determine the presence of PhACs (NSAIDs) in the aqueous phase. River samples were filtered through 1 μm glass fiber filters followed by 0.45 μm nylon membrane filters and kept at -20 °C until analysis. Water samples were analyzed for PhACs according to [29]. Ultrapure water (100 mL) was spiked with a mixture of the target analytes and subsequently subjected to the extraction method. Briefly, 3mL of EDTA 1M (4 vol.%) was added to the water samples. A Baker vacuum system (J. T. Baker, The Netherlands) was used to pre-concentrate the samples in Oasis HLB cartridges (60 mg, 3 mL). They were loaded with 100 mL of water samples and eluted with 6 mL of methanol. The extracts were evaporated under a gentle nitrogen stream and reconstituted with 1 mL of the methanol-water mixture (volume ratio for PhACs), and 10 mL of IS mixture (1 mg/L) was added to the final extract. Method detection limits (*MDL*) and method quantification limits (*MQL*) were set as the minimum detectable amount of analyte with a signal-to-noise of 3 and 10, respectively. *MDL* and *MQL*s have been calculated as the average of those estimated in real samples and in the spiked samples. Chromatographic separations were carried out with a Waters Acquity Ultra-Performance™ liquid chromatography system, equipped with two binary pumps systems (Milford, MA, USA) using an Acquity HSS T_3 column (50 mm×2.1 mm i.d., 1.8 μm particle size) for the compounds analyzed under positive electrospray ionization (PI) and an Acquity BEH C18 column (50 mm×2.1 mm i.d., 1.7 μm particle size) for the ones analyzed under negative electrospray ionization (NI), both purchased from Waters Corporation. For the analysis in PI mode, the optimized separation conditions were as follows: solvent (A) methanol, solvent (B) 10 mM formic acid/ammonium formate (pH 3.2) at a flow rate of 0.5 mL/min. The gradient elution was: initial conditions 5% A; 0-4.5 min, 5-95% A; 4.5-4.6 min, 100% A; 4.6-6.0 min, 100% A; from 6.0 to 6.1 return to initial conditions; 6.1-6.7, equilibration of the

column. The analysis in NI mode was performed by using acetonitrile (A) and 5 mM ammonium acetate/ammonia (pH=8) (B) at a flow rate of 0.6 mL/min. The gradient elution was: 0-1.5 min, 0-60% A; 1.5-2.0 min, 100% A; 2.0-3.0 min, 100% A; 3.20 min return to initial conditions; 3.20-3.70 min, equilibration of the column. The sample volume injected was 5 µL, and sample analysis was repeated three times. UPLC instrument was coupled to a 5500 QTRAP hybrid triple quadrupole-linear ion trap mass spectrometer (Applied Biosystems, Foster City, CA, USA) with a turbo ion spray source. Compound-dependent MS parameters (declustering potential (DP), collision energy (CE) and collision cell exit potential (CXP)) were optimized by direct infusion of individual standard solutions of each compound at 20 µg/L.

All data were obtained and processed using Analyst 1.5.1 software, and the end value was obtained by adding the repeated values and dividing them by three.

Saprobity Index (*SI*)

Samples intended for saprobiological analysis were taken by using a 25 µm mesh plankton net, and they were immediately analyzed without being fixated, or fixated using 96% alcohol.

The saprobity index was calculated according to Pantle-Buck method. This system involves the application of the standard sampling techniques (Grginčević and Pujin, 1986).

Phytoplankton analysis with the application of the saprobity system, as noted in [30], determination of phytoplankton in the tested water sample, along with specifying the relative frequency (u) of each type, by using the numbers 1,3,5, whereas in this study, in addition to listed numbers 1, 3 and 5, the abundance was also reported by numbers 2, 4 and 10, depending on the frequency of microalgae, which is rather common in research of this kind.

Saprobity index (*SI*) is determined by using a method explained in [30] by applying a species value index as described in [31].

Preparation for SEM:

- Freshly collected diatom material can simply be air dried onto a small coverslip (Ø 12 mm) or filtered through a 2.5 µm Millipore® filter.
- Cleaned material can be prepared in a similar manner.
- After air drying, the sample should be placed in a desiccator containing silica gel for 24 h to make sure that it is completely dehydrated before continuing with further preparation.
- When dry, the coverslip or filter should be mounted on an aluminum microscope stub with carbon tape and sputter-coated with gold-palladium.
- The samples are now ready for examination.
- 10-15 kV is usually an adequate voltage for examining diatoms.
- Image analysis is the most advanced technology for a broad range of functions such as digital image acquisition, image processing, sample analysis, database archiving, and results/report documentation [32]. A recommended software package is “analySIS” which has several expansion versions and configurations. Version 3.1 provides live overlay, 3-D surfaces, automatic scale bar, and many other functions. It is relatively user-friendly, however, expert advice is required for the most benefit.

RESULTS AND DISCUSSION

The system of the kinetic model of the reactor was operating from 05/09/2017 to 05/09/2018. Over this time, the system proved sustainable, micropollutant (NSAIDs) removal efficiency slowly stabilized, and the indicators, *i.e.*, saprobity index, auto-purification level, and the concentration of dissolved oxygen in water (DO) showed that water quality was improving. Oligotrophic microorganism phenotype monitoring showed that native samples differ from those taken 24 h after the samples passed through the kinetic reactor.

Following an empirically determined incubation period, color patterns in the 96-well matrix and intensity (O.D.) of color formation can be used to determine AMR to describe the microbial community. According to that, native sample AMR (Figure 2) ranged from 0.8 to 1.94. Initially, the values of the native sample AMR, *i.e.*, of the sample before entering into the cylinder collector, were almost identical, except for the 0.8 minimum in September 2018. In December 2018, the native sample AMR value was 1.71. The AMR values of the kinetic cylindrical reactor sample were higher and ranged from 1.3 to 2.17.

The average mean result AMR for the sample before entering into the cylinder amounted to 1.42, while the average mean result AMR after the samples passed through the kinetic reactor amounted to 1.96 (Figure 2). Standard deviation is a significant statistical element that shows us how close the values in a data set are to the mean. For the native sample AMR, the standard deviation was 0.38, and for the kinetic cylindrical reactor sample, the standard deviation was higher by 0.05. The standard deviation value being

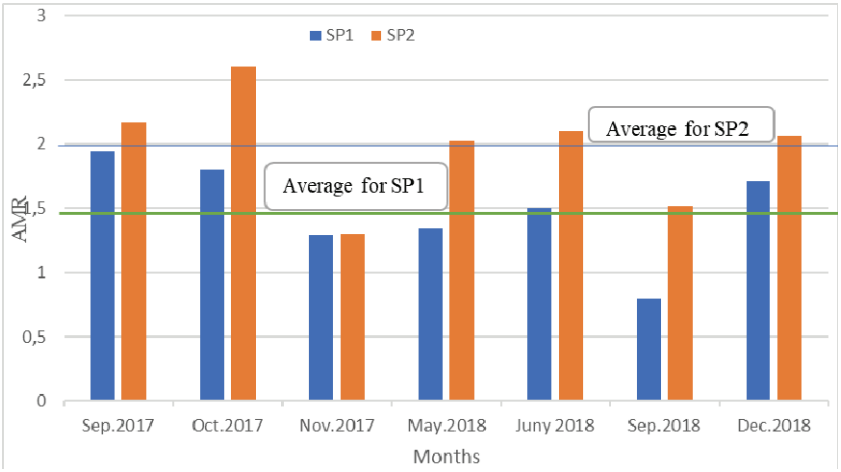

Figure 2. AMR average for research locations SP1 and SP2 for oligotrophic microorganisms.

this low only leads us to conclude that the results are mostly the closest to the average mean result.

The water contains 8.3 mg/L of dissolved oxygen at the temperature of 25 °C and it is of huge importance for many microorganisms in the water. During the operation of the model of the kinetic reactor, we established that the *DO* values in the analyzed samples were significantly higher and ranged from 9.5 to 16.9 mg/L. The average *SP*1 value was 12.64 mg/L, while the average *SP*2 value was 12.52 mg/L (Figure 3).

The average native sample value mg/L of dissolved O_2 is negligibly higher (0.12) compared to the value of dissolved O_2 in the water samples for the indigenous microorganisms of the kinetic cylindrical reactor sample. We assume that the sustainability of the system is based on the presence of the microorganisms that are capable of auto-purification, hence breaking down the micropollutants.

Based on the water self-purification categories, depending on the FO/H index, during the operating of the model (Figure 4), both *SP*1 and *SP*2 show good self-purification ability. The average FO/H mean index for *SP*1 amounted to 1.88, while the average FO/H mean index for *SP*2 amounted to 2.62 (Figure 4). FO/H range value for *SP*1 was 1.17, while the same *SP*2 value amounted to 1.98. The FO/H index values for *SP*2 were 28.05% higher compared to *SP*1 samples. Such auto-purification values are followed by the values of the NSAIDs in water samples *SP*1 and *SP*2 at the Vukovci location. During the study, we examined acetaminophen (paracetamol) which is used for reducing fever and treating pain in people of all ages [33], salicylic acid, as one of the most important components in the pharmaceutical industry [34], carbamazepine, which is used to prevent and control seizures, known as an anticonvulsant or antiepileptic drug [35], and ketoprofen class of nonsteroidal anti-inflammatory drugs (NSAID) with analgesic and antipyretic effects [36] in micropollutant concentrations at the research sites (Figure 5). With the model of the cylindric reactor for self-purification by

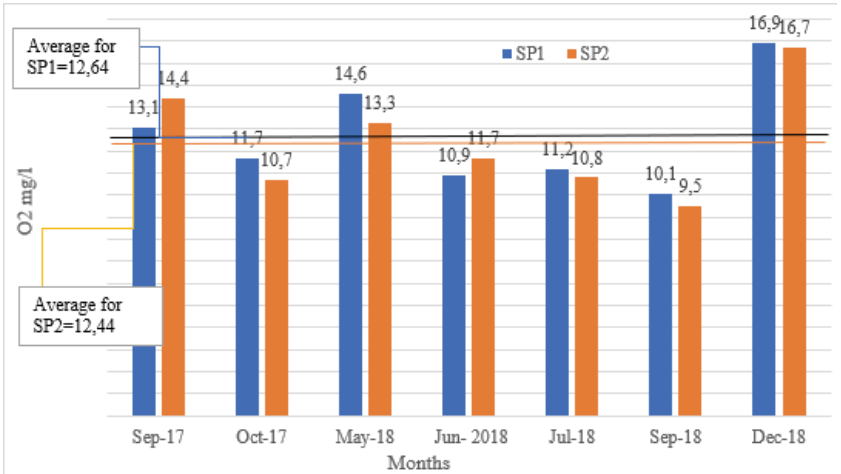

Figure 3. Dissolved oxygen concentration in the water (DO) values for locations SP1 and SP2, Vukovci locality.

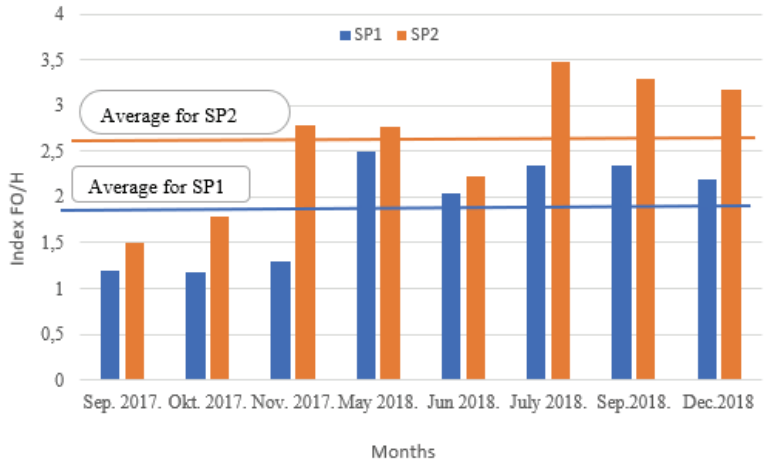

Figure 4. Index FO/H at the Vukovci locality for locations SP1 and SP2.

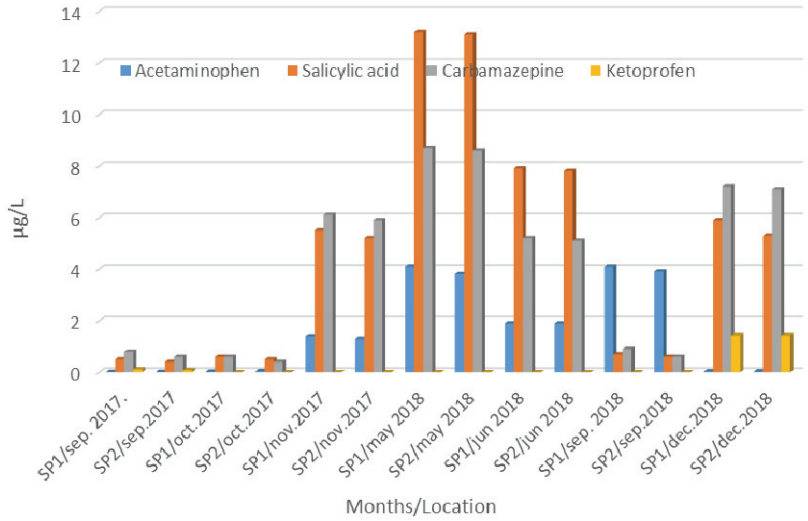

Figure 5. NSAID presence on Vukovci locality for locations SP1 and SP2.

indigenous microorganisms, we proved a 4.19% decrease in micropollutant (NSAIDs) in *SP*2 samples. When observing the pharmaceuticals individually, we noticed that the average value for the acetaminophen *SP*1 was 1.65, and 1.56 for *SP*2, with the standard deviation difference of 0.12 in favor of the *SP*1 (1.83). SP1 range value was 4.09, while that value amounted to 3.89 for *SP*2. Statistical values of the salicylic acid showed that the results for *SP*1 and *SP*2 do not differ significantly, with the averages for *SP*1 and *SP*2 being 4.9 and 4.7, respectively. Standard deviation was even for both samples, 4.73 for *SP*1, and 4.72 for *SP*2. The average mean for carbamazepine *SP*1 value was 4.21, and the average mean for *SP*2 was 4.04. The standard deviation for *SP*1 was 3.39, and 4.04 for *SP*2. *SP*1 ketoprofen range value was 1.32, and 1.35 for *SP*2, with the maximal value for *SP*1 and *SP*2 being 1.43. Minimal *SP*1 and *SP*2 values were 0.11 and 0.08, respectively. During researching, ketoprofen values for October and November of 2017, as well as May, June, and September of 2018, were under the method detection limits (*MDL*).

During the experiment, it was especially important to prove that the system does not significantly affect the composition of the microalgae/saprobity index (*SI*).

SI value for the Vukovci locality, as well as locations *SP*1 and *SP*2 (Figure 6), was increasing in *SP*1 up until May 2018. By monitoring the system operation in May 2018, we noted that the value of *SP*2 saprobity index was higher than the value in *SP*1. Then, the *SP*1 saprobity index went up during June and July 2018, until September and December of 2018, when the *SP*1 saprobity index significantly surpassed the *SP*2 value. The average saprobity index value for *SP*1 was higher than the average *SP*2 value by 0.38 (Figure 6). Standard deviation of the "sum sample" amounted to 0.39 which clearly indi-

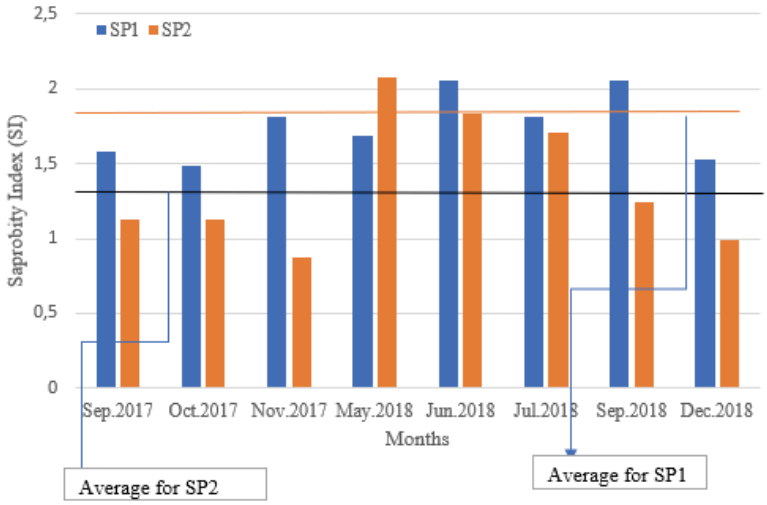

Figure 6. Saprobity index for Vukovci locality at locations SP1 and SP2.

cates that the results are grouped mostly around the average mean value, as well as low dispersion compared to the overall sample. The most prevalent division was *Bacillariophyta*, while the most prevalent species were *Cymbella lanceolata*, *Fragilaria crotonensis* and *Cymbella ehrenbergii*, captured using SEM microscope.

During the summer months, the water level at Vukovci site fell below the zero point. During that period (August-October), operating the kinetic cylindrical reactor was very difficult and saprobity index values (Figure 6) were at their highest. When the system normalized, heavy rainfall was recorded from November to June, which played a key role in the improvement of the system results.

As Figures 4 and 5 show, there is a significant connection between FO/H index, self-purification, and NSAID concentration in water samples at the Vukovci locality. By correlating these two variables using the Pearson correlation coefficient, we are able to support our results mathematically. The calculated *r*-value is 0.484, which allows us to establish a moderately positive ratio between those two variables [37]. The coefficient of determination amounts to 23%, therefore we can claim that 23% of one variable in water (FO/H index) was caused by the concentration value of the second variable in the water (NSAID concentration). Integrated effect: self-purification index, dissolved oxygen in water, removal of NSAIDs from water samples, saprobity index, complied with the

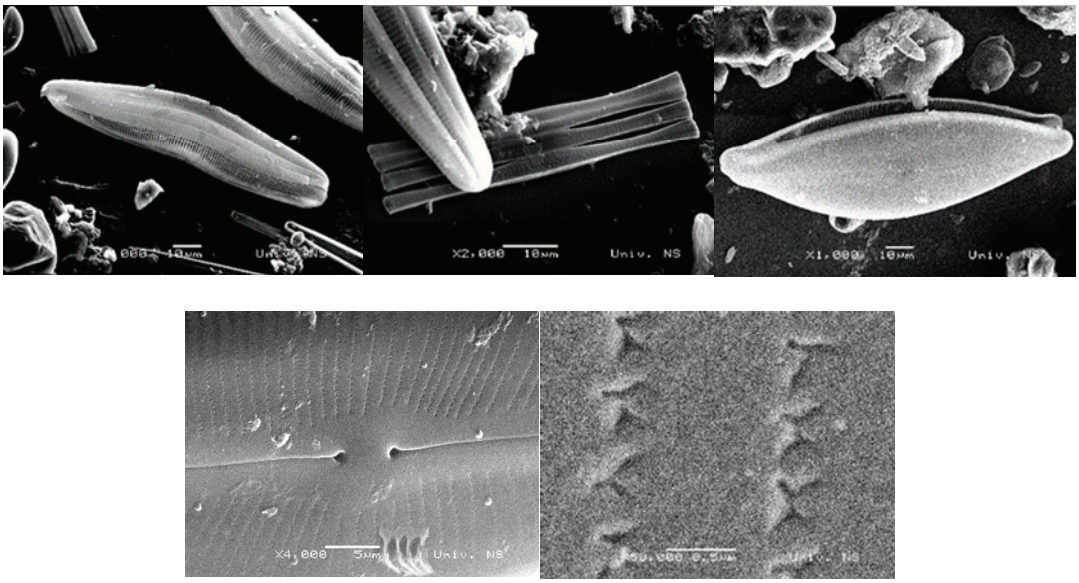

Figure 7. SEM micrographs of diatoms collected from Morača river; from left to right, first row: Cymbella lanceolata, Fragilaria crotonensis, Cymbella ehrenbergii; second row: Cymbella ehrenbergii, both.

development and change in the phenotype of the indigenous facultative oligotrophic microorganisms in the water.

During September 2017, optimal conditions regarding air and water temperature enabled our system to function optimally, and therefore the difference in the adaptation of the phenotype of indigenous oligotrophic microorganisms shown as the *AMR* value was higher by 10.6% at the *SP*2 location compared to the *SP*1, and also the value of the auto-purification index in *SP*2 was higher by 20% than the value in *SP*1.

Regarding the saprobity index, the value in location *SP*1 was 28.5% higher than the value in *SP*2. The *SP*2 values were noticeably higher until November 2017, when the difference in the phenotype of indigenous facultative oligotrophic microorganisms amounted to only 0.08%.

The CLPP approach has sufficient sensitivity to detect acute contaminant impact on the physiological processes of the indigenous microbial community while providing data for the evaluation of chronic stress-induced adaptations in microbial community structure. By examining the AMR relation for *SP*2 and *SP*1, the most significant difference in their results was noted during October 2017, when the difference amounted to 0.8, and then during the September sampling, when it amounted to 0.68. Of course, microbial communities have great potential for temporal or spatial change, and thus represent a powerful tool for understanding community dynamics in both, basic and applied ecological contexts [5]. This proves that the system has satisfactory self-purification ability. Water quality is directly correlated to its chemistry at numerous locations along the course of rivers, but also is the result of geomorphological conditions, as well as anthropological influence.

The dissolved oxygen content of water ranged from 9.5 to 16.9 mg/L during the operating of the system; therefore, the system was supersaturated with oxygen. The saprobity index was highly oligotrophic [38] during 57.15% of our analysis for *SP*1, and 85.22% of our analysis for *SP*2; for the rest of the analysis it was β-mesosaprobic. This proves that our system is sustainable.

CONCLUSION

One-year observation of the system of “cylindrical reactor for self-purification by indigenous microorganisms” showed that the system has sufficient auto-purification capacity and therefore actively improves the water quality. It was mature and stable throughout the entire year. The FO/H index values were 28.05% higher in the *SP*2 samples than the values in *SP*1. This model showed a total decrease of 4.19% of the selected pharmaceuticals and micropollutants in samples taken at location *SP*2, *i.e.*, post-reactor samples, compared to the same NSAID concentration in the *SP*1 or native sample. Indigenous microorganisms actively affected NSAID degradation.

The *AMR* for *SP*2 was 24.62% higher than for *SP*1, which proves the phenotypic adaptivity of facultative oligotrophic microorganisms. Saprobity level was highly oligotrophic for over 50% of the samples, the highest being *Bacillariophyta.*

The system integrates water purification and ecological restoration. Based on the “close to nature, multi-functional and sustainable” concept of ecological restoration, the study provides an excellent theory and practice to promote a healthy river environment and the sustainable ecological, economic, and social development of the region.

REFERENCES

[1] D. Radonjić, M.Sc. Thesis, University of Montenegro, 2007, p. 85. (in Serbian)

[2] K.D. Balke, U. Beims, F.W. Heers, B. Hoelting, R. Homrighausen, G. Matthess, Groundwater Exploitation. Hydrogeological Textbook Vol. 4, Berlin-Stuttgart, 2003, p. 1-740

[3] K.D. Balke, in Surplus or Absence of Chemical Components in Water and Its Consequences for Public Health, K.D. Balke, Y. Zhu, Eds., Water and Development, Geology Press, Beijing, 2003, pp. 36-42

[4] K.D. Balke, C. Griebler, Groundwater Use and Groundwater Protection, Groundwater Ecology Wien, Facultas UTB, 2003, pp. 1-495

[5] F. Remmler, U. Schulte-Ebbert, Vom Wass. 101 (2003) 77-90

[6] D. Mrdak, Evaluation of environmental impact of the Morača dam on fish Fauna of the Morača River and the Skadar Lake, https://ozonniksic.files.wordpress.com/ /2011/05/riblja-fauna_moraca-i-skadarsko-jezero.pdf, accessed 7 July 2020 (in Montenegrin)

[7] Ministry of Sustainable Development and Tourism of Montenegro, Annual Report on the Situation in the Field of Water Supply, Waste and Wastewater Management, Implementation of Priority Activities in Public Utilities in 2014, with Proposal of Priority Projects for Municipal Infrastructure Construction in 2016 and Proposed Measures, https://www.google.com/search?q=12_140_17_12_2015.pdf&rlz=1C1GCEU_enSI891SI891&oq=12_140_17_12_2015.pdf&aqs=chrome, accessed 7 January 2021 ((in Montenegrin)

[8] M. Gros, M. Petrović, A, Ginebreda, D. Barceló, Environ. Int. 36 (2010) 15-26

[9] H. Fathollahzadeh, F. Kaczala, A. Bhatnagar, W. Hogland, Chemosph. 119 (2015) 445-451

[10] P. Kasprzak, T.Gonsiorczyk, H.P. Grossart, M. Hupfer, R. Koschel, T. Petzoldt, G. Limnolo. 70 (2018) 33-48

[11] X. Jin, L. Bi, T. Lyu, J. Chen, H. Zhang, G. Pan, Water Res. 165 (2019) 1150

[12] L. Vezzulli, C. Pruzzo, M. Fabiano, Mar. Pollut. Bull. 49 (2004) 740-751

[13] X. Cai, L.Yao, Q. Sheng, L. Jiang, T. Wang, R.A. Dahlgren, H. Deng, Environ. Technol. 1 (2019) 1-34

[14] J. Xu, S.L. Lo, Desalin. Water Treat. 156 (2019) 32-37

[15] B.T. Rushton, B.M. Bahk, Water Sci. Technol. 44 (2001) 531-538

[16] T. Jurczak, A. Wojtal-Frankiewicz, Z. Kaczkowski, Z. Oleksinska, A. Bednarek M. Zalewski, J. Environ. Manag. 217 (2018) 919-928

[17] L. Yu, Y. Zhang, C. Liu, Y. Xue, H. Shimizu, C.Wang, C. Zou, Ecol. Eng. 136 (2019) 134-140

[18] G. Liu, T. He, Y. Liu, Z. Chen, L. Li, Q. Huang, Z. Xie, Y. Xie, L.Wu, J. Liu, Environ. Sci. Pollut. Res. 26 (2019) 12867-12880

[19] D. Konnerup, T. Koottatep, H. Brix, Ecol. Eng. 35 (2009) 248-257

[20] N. Đukić, Water Technology, Faculty of Technology and Metallurgy, Belgrade, 2000, p.200 (In Serbian)

[21] D. Radonjić, Spec. paper, University of Belgrade, Belgrade, 2003 (In Serbian)

[22] A. Vasileska, L. Lokoska. Acta Zool. Bulg.13 (2019) 33-37

[23] W. Kohl, Arch. Hydrobiol. 44 (1975) 392-461

[24] M. Davis, R. Davis, Fundamentals of Chemical Reaction Engineering, https://authors.library.caltech.edu/25070/1/ /FundChemReaxEng.pdf (accessed14.01.2021)

[25] V. Kosar, Reactors and Bioreactors, University of Zagreb, Zagreb, 2017, p. 26 (in Croatian)

[26] K.H. Mancy, T. Jaffe, Analysis of Dissolved Oxygen in Natural and Waste Waters.Publ. No. 99-WP-37, U.S. Public Health Serv., Washington, DC, 1966, p. 94

[27] ISO6222, 1999 Water Quality -Enumeration of Culturable Microorganisms-Colony Count by Inoculation in a Nutrient Agar Culture Medium. International Organization for Standardization (ISO), https://www.iso.org/obp/ui/ /#iso:std:iso:6222:ed-2:v1:en (accessed 10 July 2020)

[28] J.L. Garland, Microbiol. Ecol. 24 (1997) 89-300

[29] M. Gros, S. Rodríguez-Mozaz, D. Barceló, J. Chromatogr., A 1248 (2012) 104-121

[30] R. Pantle, H. Buck, Wasserfach 96 (1955) 604-660

[31] P. Gulyas, List of saprobiological indicator species, Környezetgazdálkodási Intézet, Debrecen, 1998, p.128 (in Hungarian)

[32] J.C. Taylor, W.R. Harding,C.G.M. Archibald, A Methods Manual for the Collection, Preparation and Analysis of Diatom, https://docs.niwa.co.nz/library/public/ /1770054839.pdf (accessed 19.09.2019)

[33] Paracetamol-Wikipedia, https://en.wikipedia.org/wiki/ /Paracetamol (accessed14.01.2021)

[34] Medical Definition of Salicylic acid, https://www.medicine-net.com/salicylic_acid/definition.htm (accessed14.01.2021)

[35] Carbamazepine, https://www.webmd.com/drugs/2/drug-1493-5/carbamazepine-oral/carbamazepine-oral/details (accessed14.01.2021)

[36] Ketoprofen, https://sl.wikipedia.org/wiki/Ketoprofen (accessed14.01.2021)

[37] J. Cohen, Statistical Power Analysis for the Behavioral Sciences, http://www.utstat.toronto.edu/~brunner/old-class/378f16/readings/CohenPower.pdf (accessed 19.08.2019)

[38] MZS 12749, 1993-Hungarian water quality standards, https//www.mszt.hu (accessed 15.08.2019).

DRAŽANA RADONJIĆ

Odsjek za biologiju,Prirodno-matematički Fakultet (PMF) u Podgorici, 81000 Podgorica, Crna Gora

NAUČNI RAD

PRIMJENA MODELA CILINDRIČNOG REAKTORA U CILJU SAMOPREČIŠĆAVANJU KORIŠTENJEM AUTOHTONIH MIKROORGANIZAMA

Farmaceutski aktivne komponente (PhACs), a posebno nesteroidni antiinflamatorni lekovi (NSAID) su u sve široj upotrebi i kao takvi su sve češće deo organske materije recipijentnih reka, posebno u njihovom donjem toku. Da bismo ukazali na njihov značaj kao zagađivača, kao i na značajnu ulogu koju prisustvo, autohtone mikroflore igra u rešavanju ovog pitanja, preduzeli smo da izvedemo ovaj eksperiment. Eksperiment pod nazivom „Primjena modela cilindričnog reaktora u cilju samoprečišćavanju korištenjem autohtonih mikroorganizama" sproveden je u periodu od godinu dana na lokalitetu Vukovci, u donjem toku rijeke Morače. Pod pretpostavkom da se koncentracija NSAID i PhACs u vodi može smanjiti samoprečišćavanjem, dokazano je da takvi procesi rezultiraju modifikacijom fenotipa u autohtonoj mikrobiološkoj populaciji. Imajući u vidu navedenu predpostavku, konstruisan je eksperimentalni model, koji podrazumeva da se voda kreće. Pri tome je definisana zapreminska brzina protoka po jedinici vremena i ona je iznosila 0,005 m/s; dužina cilindričnog reakora je iznosila 432 m. Za godinu dana primene modela cilindričnog reaktora za povećanje kapaciteta samoprečišćavanja od strane autohtonih mikroorganizama, autoprečišćavanje je povećano za 28,05%, fenotip autohtonih mikroorganizama se promenio za 24,62%, dok je ukupna koncentracija pojedinih PhACs, mikrozagađivača i NSAID smanjena za 4,19.

Ključne reči: farmaceutski aktivne komponente (PhACs), nesteroidni antiinflamatorni lekovi (NSAID), samoprečišćavanje, kretanje vode, fenotip autohtonih mikroorganizama.

CI&CEQ
Chemical Industry & Chemical Engineering Quarterly

Available on line at
Association of the Chemical Engineers of Serbia *AChE*
www.ache.org.rs/CICEQ

Chem. Ind. Chem. Eng. Q. 27 (4) 383–394 (2021) CI&CEQ

SENKA GUDIĆ[1]
LADISLAV VRSALOVIĆ[1]
ANA RADELJIĆ[1]
EMEKA EMANUEL OGUZIE[2]
IVANA IVANIĆ[3]
STJEPAN KOŽUH[3]
MIRKO GOJIĆ[3]

[1]University of Split, Faculty of Chemistry and Technology, Department of Electrochemistry and Materials Protection, Split, Croatia
[2]Federal University of Technology Owerri, Africa Centre of Excellence in Future Energies and Electrochemical Systems (ACE-FUELS), Owerri, Nigeria
[3]University of Zagreb, Faculty of Metallurgy, Sisak, Croatia

SCIENTIFIC PAPER

UDC 669.35:620.193:66.09

COMPARISON OF CORROSION BEHAVIOR OF COPPER AND COPPER ALLOYS IN AQUEOUS CHLORIDE SOLUTION

Article Highlights

- A detailed comparison of the corrosion behavior of Cu and 4 Cu alloys in NaCl solution was given
- EIS results indicate that sample resistance is the consequence of the formation of a barrier layer
- Alloying elements have a positive effect on copper passivation and surface film properties
- SEM/EDS analyses have shown that Cu alloys all had thicker and more protective barrier layers

Abstract

A comparative corrosion study of Cu and Cu-Al, Cu-Al-Ni, Cu-Al-Mn and Cu-Al-Mn-Ni in 0.5 mol dm^{-3} NaCl solution was performed using an open circuit potential, potentiodynamic polarization and electrochemical impedance spectroscopy measurements (EIS). Scanning electron microscopy/energy-dispersive X-ray spectroscopy (SEM/EDS) analysis was used to evaluate corrosive damage on the sample surface after polarization measurements. The reported results suggest that the alloying elements have reduced cathodic and anodic current densities in the Tafel region, increased anodic currents at higher anodic potentials, and slightly displaced corrosion potential towards more positive values. Overall, impedance increased in the following order: Cu < Cu-Al < Cu-Al-Ni < Cu-Al-Mn < Cu-Al-Mn-Ni. This indicates that Cu alloys possess better corrosion resistance. SEM and EDS analysis after polarization measurements showed uniform dissolution of pure Cu, as well as the presence of a surface oxide layer, consisting of a mixture of the corresponding alloying elements, on all investigated alloys. Aggressive anodic polarization severely damaged the barrier layers on the Cu alloy specimens.

Keywords: copper alloys, corrosion, electrochemical methods, polarization, shape memory alloys, SEM/EDS.

Copper and its alloys have significant practical applications due to their high electrical and thermal conductivity, workability, and good corrosion resistance in a variety of environments. These materials have been used in the production of condenser tubes for ships, heat exchanger tubing materials in power plants, and other industries, such as pipeline networks, valves, pumps, fittings, etc. [1-5]. Cu-Al alloys, also known as aluminium bronzes, with aluminium contents up to 14 wt.%, exhibit an excellent combination of strength and corrosion resistance, making them one of today's most important engineering materials for highly stressed components in corrosive environments. Stress-corrosion fatigue resistance of Cu-Al alloys exceeds that of austenitic stainless steels. Additionally, they can be machined or ground and are readily weldable [4,6,7]. Upon addition of Ni or/and Mn to Cu-Al alloys, new alloys can be produced that exhibit specific properties, including Cu shape memory alloys (SMAs). An SMA remembers its original shape, returning to its pre-deformed shape upon heating [8]. At high temperatures, SMAs exist in

Correspondence: L. Vrsalović, University of Split, Faculty of Chemistry and Technology, Ruđera Boškovića 35, 21000 Split, Croatia.
E-mail: ladislav@ktf-split.hr
Paper received: 1 July, 2020
Paper revised: 3 December, 2020
Paper accepted: 1 March, 2021

https://doi.org/10.2298/CICEQ200701007G

an austenite phase, and upon cooling below the transformation temperature, the austenite transforms to a thermoelastic martensite. Cu-Al-Ni and Cu-Al-Mn SMAs have been extensively investigated and have found practical usage in actuator and sensor manufacturing, electronics, computers parts, automotive and aircraft industries, robotics, and civil engineering industry, etc. [9-13].

Due to the wide application of Cu and Cu alloys, these materials come into contact with various aggressive media that can significantly affect their durability and change their properties, so understanding the mechanisms of corrosion in Cu alloys is important for many contemporary applications, including microelectronics, robotics, aerospace industry, or as canister materials for nuclear waste storage. In these cases, even extremely small corrosion rates may be detrimental, due either to the small amount of material present or the long lifetimes required.

The corrosion behaviour of copper and its alloys strongly depends on the electrolyte composition in contact with the metal surface, as well as elements present in the alloys. Most published results have been obtained in chloride-containing media, as chlorides are one of the most common corrosive agents in nature and copper alloys are considered promising materials for marine applications [14-18].

Investigations of anodic Cu dissolution have shown that in the absence of complexing substances in the electrolyte (*i.e.*, Cl^-, NH_3, etc.), dissolution takes place in two stages [14]:

$$Cu \leftrightarrow Cu^+ + e^- \quad \text{(fast reaction)} \tag{1}$$

$$Cu^+ \leftrightarrow Cu^{2+} + e^- \quad \text{(slow reaction)} \tag{2}$$

In the presence of complexing Cl^-, consideration should be given to the possibility of $CuCl_2^-$ complex formation. In the region near the corrosion potential and at Cl^- concentrations less than 1 mol dm^{-3}, the Cu dissolution mechanism takes place in two stages. The first stage is CuCl formation, which is adsorbed on the surface of the electrode, according to reaction (3) [15,19,20]:

$$Cu + Cl^- \leftrightarrow CuCl_{ads} + e^- \tag{3}$$

Upon reaction with another Cl^-, the adsorbed compound on the electrode surface is dissolved, forming a soluble $CuCl_2^-$ complex (reaction (4)). Further, the $CuCl_2^-$ complex on the electrode surface is subject to a hydrolysis reaction, which leads to the formation of Cu_2O (reaction (5)) [15,19,20]:

$$CuCl + Cl^- \leftrightarrow CuCl_2^- \tag{4}$$

$$2CuCl_2^- + H_2O \rightarrow Cu_2O + 4Cl^- + 2H^+ \tag{5}$$

$CuCl_2^-$ diffuses from the surface to the mass of the solution, a slow process in the Cu dissolution reaction. As a result of these reactions, layers of corrosion products are formed on the surface (mostly as oxide, hydroxide or chloride), which can slow the rate of anodic dissolution, as well as the cathodic reaction. This can be represented by equation (6) in neutral aerated solution [15,16,20]:

$$O_2 + 2H_2O + 4e^- \rightarrow 4OH^- \tag{6}$$

Aluminium is one attractive alloying element used to enhance the corrosion resistance of copper-based alloys. Addition of aluminium to a Cu-based alloy increases its corrosion resistance due to the formation of a protective alumina (Al_2O_3) layer, along with Cu_2O, which builds up quickly on the surface exposed to the corrosive environment. The formation of these stable passive layers on Cu-Al alloys is mainly due to the higher affinity of aluminium towards oxygen than copper in salt solution and considerable stability of Al_2O_3 over Cu_2O [7,21,22].

Cu-Ni alloys have been widely studied in NaCl solutions, but published results regarding the dissolution process are contradictory. Some authors pointed out that selective removal of nickel is predominant [23,24], while others have suggested that the main process is the de-alloying of copper [25]. Investigations on corrosion resistance of Cu-Ni alloys in chloride solution, performed by Milošev and Metikoš-Huković [26,27], have indicated a passive layer on Cu-$_x$Ni alloys (x in range 10-40 wt.%), consisting of an outer $CuO/Cu(OH)_2$ layer overlaying a Cu_2O barrier layer with incorporated nickel cations. This incurporation takes place because of the defective inner Cu_2O layer structure, which can accept large amounts of foreign ions, such as nickel or iron. Recent studies have confirmed that the presence of nickel is important in the passivation of Cu-Ni alloys because of its incorporation into the oxide layer, reducing the number of cation vacancies in Cu(I) oxide formed on the corroded alloy surface [22,28-30]. Incorporation of nickel and iron (in Cu-Ni-Fe alloys) leads to a decrease in both ionic and electronic conductivities of the oxide film [26,31].

Nady *et al.* have shown that an increase in nickel content decreases the corrosion rate of Cu-Al-Ni ternary alloys in chloride solutions [30]. However, Badawy *et al.* have reported that the corrosion rate of Cu-Al-Ni SMAs increased with increasing Ni content. They explained this behaviour by the fact that, according to the Pourbaix diagrams, Cu and Al form

the most stable species, but Ni is active in the same conditions. Thus, the increase in i_{corr} for alloys with higher Ni content was interpreted by the dissolution of Ni with the formation of Ni^{2+} [31].

The addition of Mn in small amounts to the Cu-Al alloys influences alloy microstructure, *i.e.* reduces the crystal grain size. Specifically, Mn diffuses easily and rapidly disperses through the alloy mass, accumulating on the grain boundaries, thus preventing further grain growth [21,32]. Studies have shown that such microstructure refining, with the improvement of mechanical properties also increases alloy corrosion resistance as this fine microstructure positively affects the compactness and stability of the passive oxide film [21].

Also, the addition of some other alloying elements, like beryllium in Cu-Al alloys, leads to increased resistivity towards intergranular corrosion due to the diffusion of beryllium atoms into grain boundaries, which, in turn, deactivates the grain boundaries [33]. Beneficial influence on corrosion resistance has been achieved by alloying Cu-Al-Ni alloys with Ti and Ag nanoparticles [21,34]. Decreasing grain size as a result of Ti addition (similar to Mn addition) leads to the formation of a passivation film, resulting in an increase of its resistance to pit nucleation. Moreover, the presence of Ti and Mn in the passivation film (in a form of Al_2TiO_5, TiO_2, $TiCl_2$, $CuMnO_2$ and Mn_2O_3) protects the SMAs from the aggressive action of Cl^- better than corrosion layers in the base alloy, while the presence of Ag nanoparticles leads to formation of the corrosion products silver chloride, cuprous oxide, aluminium oxide/hydroxide, and silver oxide, which act as protective layers and improve the corrosion resistance of Cu-Al-Ni-Ag SMA. In this paper, results of a comparative electrochemical behaviour study of pure copper and Cu-Al, Cu-Al-Ni, Cu-Al-Mn, and Cu-Al-Mn-Ni alloys in 0.5 mol dm^{-3} NaCl solution are presented.

EXPERIMENTAL

Chemical compositions of materials used in this investigation are given in Table 1.

The working electrodes were prepared by cutting appropriate metal rods to small cylindrical specimens, which were then soldered to isolated Cu wires for good electrical contact. Electrodes were isolated with Polirepar S protective mass so that only a circular cross-section (0.5 cm^2) was exposed to the electrolyte. Prior to every experiment, the electrode was ground and polished with successive wet SiC emery papers (from 400 to 1500) using a Metkon Forcipol 1V grinder and polisher. Samples were polished with Al_2O_3 polishing paste (particle size 0.05 μm), ultrasonically degreased in ethanol, rinsed with deionized water, and immersed in electrolyte solution. Measurements were carried out in a water-jacketed glass electrochemical cell equipped with platinum foil as a counter electrode and a saturated calomel electrode (SCE) as the reference electrode. The SCE was connected to the cell via a Luggin capillary, and the electrochemical cell was connected to a Huber Kiss heating and cooling circulator at 20 °C. Measurements were performed in 0.5 mol dm^{-3} NaCl solution, prepared by dissolution of pure NaCl salt, obtained by Kemika Zagreb, in a measuring flask with deionized water.

A potentiostat/galvanostat (Princeton Applied Research; PAR; M273A) connected with a PAR M5210 lock-in amplifier was employed for electrochemical measurements. Open circuit potential measurements (E_{OC}) were carried out in 60-min time periods, and potentiodynamic polarization tests were conducted in the potential region from −0.250 V *vs.* E_{OC} to 1.1 V with a scanning rate of 0.5 mV s^{-1}. Impedance spectra were recorded at E_{OC} in the frequency range of 50 kHz to 30 mHz with five points per decade and an AC voltage amplitude of ±10 mV. The experimental impedance spectra were analysed and interpreted on the basics of the equivalent circuit program of Boukamp [35].

For every investigated sample, the same experimental procedures were applied for comparison of obtained results. The prepared electrode was immersed in electrolyte, and immediately thereafter E_{OC} measurements were performed. Afterwards, EIS measurements were conducted with the same electrode at E_{OC}, and at the end, potentiodynamic polarization

Table 1. Chemical compositions of investigated samples

Material	Composition, wt.%
Cu	99.90
Cu-Al	90.90 Cu, 9.10 Al
Cu-Al-Ni	84.67 Cu, 11.29 Al, 4.05 Ni
Cu-Al-Mn	82.30 Cu, 8.30 Al, 9.40 Mn
Cu-Al-Mn-Ni	82.00 Cu, 13.00 Al, 2.50 Mn, 2.50 Ni

was applied as the last destructive electrochemical method.

After potentiodynamic experiments, electrode surfaces were ultrasonically cleaned in deionised water to remove loose corrosion products, dried in a desiccator, and, then, analyzed by a scanning electron microscope (SEM; Tescan Vega TS5136LS). Quantitative analysis of elements on the electrode surface was determined by energy dispersive spectroscopy (EDS).

RESULTS AND DISCUSSION

Open circuit potential measurements

Figure 1 illustrates the E_{OC} decay for all studied electrodes in 0.5 mol dm^{-3} NaCl solution. The change of E_{OC} is the consequence of changes that occur due to non-equilibrium electrochemical processes at the electrode/solution interface. Specifically, the established E_{OC} value depends on the conditions of the measurement being performed, the composition and state of the surface of the examined metal sample, the characteristics of the electrolyte solution, and the exposure time of the metal sample to electrolyte. After some time, the value of the E_{OC} will be set around a certain equilibrium value.

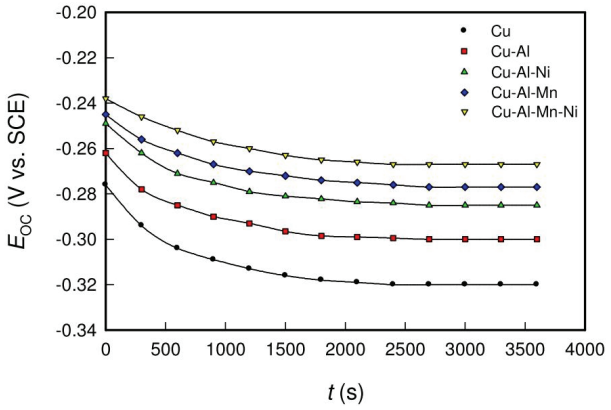

Figure 1. Open circuit potential vs. time curves for investigated samples in 0.5 mol dm^{-3} NaCl solution.

From Figure 1, all tested samples show similar trends in potential changes over time; a steady negative shift of E_{OC} is observed, after which stable values are established. The same trend was observed for all investigated samples: E_{OC} values shift towards more negative values over time. Similar behavior was observed for Cu and Cu alloys in NaCl solutions in the literature [5,7,16,18,31,36]. Alfantasi *et al.* [18] attributed this behaviour to breakdown of the oxide film, exposing underlying Cu alloy surfaces to the electrolyte and can lead to the dealloying and simultaneous dissolution of Cu and Al or Zn in Cu-Al and Cu-Zn alloys. In the case of Cu-Ni alloys, dealloying is more difficult due to the small differences between the Cu and Ni standard reversible potentials.

Figure 1 shows that the steady state potential was achieved within 40 min of electrode immersion in the solution. Values of E_{OC} for all the Cu alloys were more positive than Cu, as follows: Cu < Cu-Al < Cu-Al-Ni < Cu-Al-Mn < Cu-Al-Mn-Ni. This suggests that Cu presents a more active surface than all Cu alloys.

Potentiodynamic polarization measurements

Polarization experiments enabled the effects of alloying elements on the anodic and cathodic partial reactions of Cu to be assessed over a wide range of potentials in the NaCl environment. The anodic dissolution of Cu and Cu alloys in chloride-containing solutions has been extensively reported in the literature [15-27,31,36-41], revealing that the mechanism of anodic polarization is mostly controlled by mass-transport of chlorides. Generally, Cu is considered to be uniformly dissolved throughout the surface, creating a layer of corrosion products composed mainly of CuCl (which easily converts into soluble $CuCl_2^-$ complexes) and Cu_2O. Figure 2 shows the potentiodynamic polarization curve for the Cu electrode in 0.5 mol dm^{-3} NaCl solution. Consistent with previous reports for Cu in chloride media [15,34,38], the anodic polarization curve consists of three regions with distinctive features: a Tafel region, a region where the current peaks and then drops to a minimum, and a region of high anodic potentials, with an increase in anodic current density due to the corrosion product film breakdown and continuation of Cu dissolution with formation of Cu(II) species.

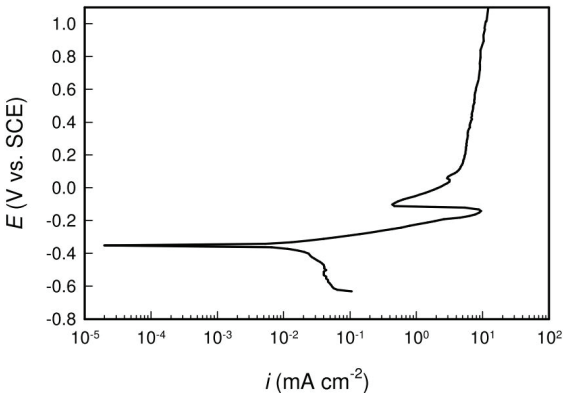

Figure 2. Potentiodynamic polarization curves for Cu in 0.5 mol dm^{-3} NaCl solution.

The potentiodynamic polarization curves of the Cu and Cu-alloy specimens in 0.5 mol dm^{-3} NaCl

solution are shown in Figure 3. The plots show clearly that all Cu alloys display similar polarization features to pure Cu, with distinct active-pseudo passive transitions in the studied potential range. The five anodic curves exhibited typical Tafel-type active regions, where the logarithm of corrosion current density (log *i*) was proportional to the potential (*E*) with similar anodic slopes. Determined values of anodic Tafel slopes were close to the 60 mV/dec for Cu and Cu alloys. This implies that anodic behavior of these Cu alloys in chloride solutions is dominated by the diffusion rate of soluble cuprous chloride ion complexes ($CuCl_2^-$), formed during the dissolution of copper and its alloys and confirmed in the literature [18,37,42]. When Al is present on the electrode surface, one corrosion product will be aluminium chloride salt, which can be dissolved as aluminium chloride ions, in addition to the dissolution of copper as a copper chloride complex ion [43]. In spite of Al dissolution, the apparent Tafel slopes of Cu-Al and other investigated alloys have similar values to pure copper, suggesting that the same rate-determining step is operating for both pure copper and copper-based alloys [37,42].

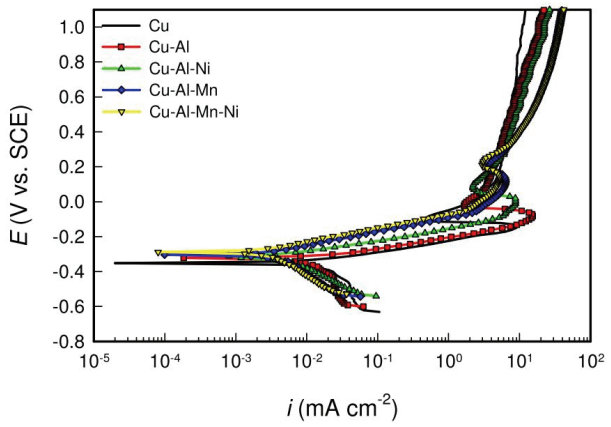

Figure 3. Potentiodynamic polarization curves of investigated samples in 0.5 mol dm^{-3} NaCl solution.

This means that the alloying elements did not notably modify the copper dissolution mechanism in the anodic Tafel region. However, the presence of alloying elements caused some changes in the polarization behavior of the Cu electrode, which reduces the cathodic and anodic current densities within the Tafel region, increasing the anodic currents at higher potentials and slightly displacing the corrosion potential towards more positive (noble) values. At higher anodic potentials outside the Tafel region, all anodic curves reached maximum values at different anodic potentials. Afterwards, the anodic current densities dropped due to slower anodic dissolution through the formed surface film of corrosion products. The film's coverage on the electrode surface temporarily delays the current density increase and then continues further as the electrode potential becomes more positive. Breakdown of surface films at higher anodic potentials lead to intensive dissolution, and anodic current density increases.

Corrosion parameters, such as corrosion potential (E_{corr}), values of anodic and cathodic Tafel slopes (b_a and b_c), and corrosion current density (i_{corr}), are determined by polarization curve analysis, and the obtained values for each sample are shown in Table 2. Polarization resistance (R_p) values were calculated using the Stern-Geary equation [44] and are also shown in Table 2.

Interestingly, the observed variations in the Cu alloys' behaviour are concomitant with the increase in amounts of alloying elements and decrease in Cu content, as reflected in Table 1. Table 2 shows E_{corr} values of the Cu alloys to be nobler than pure Cu, and the trend coincides exactly with the trend of E_{OC} values in Figure 1. The anodic current densities in the Tafel region (as well as i_{corr} values from Table 2) are lower in Cu alloys compared to pure Cu, as follows: Cu > Cu-Al > Cu-Al-Ni > Cu-Al-Mn > Cu-Al-Mn-Ni. The transition from peak to minimum current occurred at increasingly higher potentials for the different Cu alloy specimens, in concise agreement with the trend of E_{corr}. However, at the high potential region, the trend of current density reverses and the anodic current densities of the Cu alloys surpass pure Cu as follows: Cu < Cu-Al < Cu-Al-Ni < Cu-Al-Mn < Cu-Al-Mn-Ni. Similar behaviour was reported by Sun [39] for Cu-based metal matrix composites, attributed to an increase in the galvanic current contribution for the alloy specimens at high potentials. Moreover, the reduced Cu content in the alloys means that contribut-

Table 2. Corrosion parameters for investigated samples obtained from polarization measurements

Sample	E_{corr} (mV)	b_a (mV dec^{-1})	b_c (mV dec^{-1})	i_{corr} (μA cm^{-2})	R_p (kΩ cm^2)
Cu	-351.01	65.77	242.31	13.95	1.61
Cu-Al	-324.44	65.63	220.50	6.56	3.89
Cu-Al-Ni	-316.42	69.01	211.12	5.17	4.37
Cu-Al-Mn	-300.59	83.34	241.43	3.48	7.74
Cu-Al-Ni-Mn	-290.40	81.27	250.68	2.83	9.43

ions from the expected polarization behavior of Cu would be reduced.

Impedance measurements

Impedance measurements on Cu and Cu alloys were performed at the E_{OC} after 60 min of electrode stabilization in NaCl solution. The obtained results are presented in Nyquist and Bode complex planes (Figure 4).

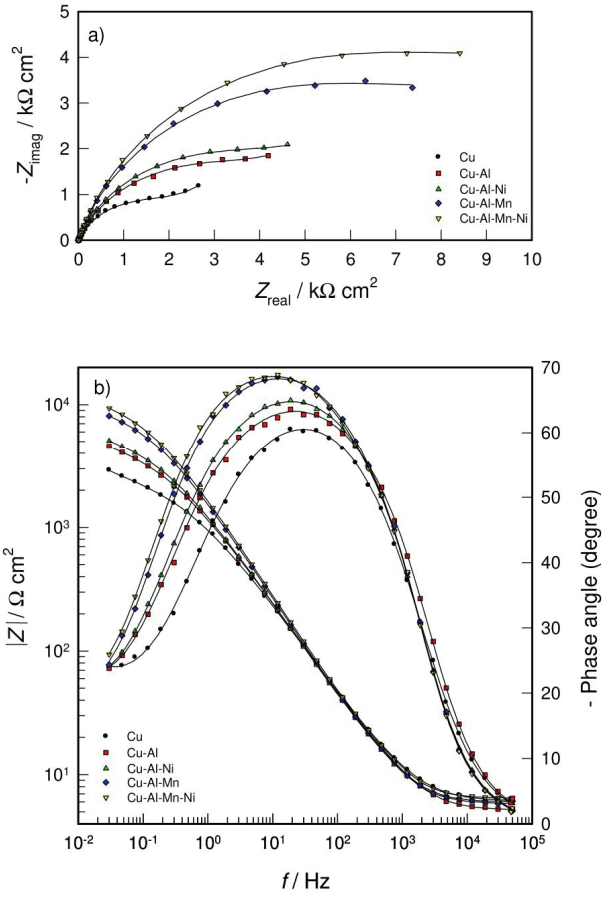

Figure 4. Nyquist (a) and Bode (b) plots of investigated samples in 0.5 mol dm^{-3} NaCl solution.

The Nyquist plots for all examined samples show evidence of two time constants that partially overlap. The Bode plots at medium frequencies with negative slopes and phase angles, approaching -70°, confirm the capacitive behavior of the examined systems, suggesting that a corrosion product surface film is formed on all tested materials. Similar observations have been reported in the literature [28,45-50]. All the tested samples show similar responses in Nyquist and Bode plots at E_{OC}, implying that the processes at the metal/solution interface for each system are similar. However, the overall impedance increased as follows, Cu < Cu-Al < Cu-Al-Ni < Cu-Al-Mn < Cu-Al-Mn-Ni, indicating that the Cu alloys possess better corrosion resistance.

In mathematical analysis of impedance diagrams, a constant phase element, CPE, is often used instead of an "ideal" capacitor to compensate for the depressed nature of the capacitive loops. The impedance, Z_{CPE}, of CPE is described by Eq. (7) [50]:

$$Z_{KFE} = \left[Q(jw)^n \right]^{-1} \tag{7}$$

with $-1 \leq n \leq 1$ and $j = \sqrt{-1}$, while Q is a frequency independent constant, defined as pure capacitance for $n = 1$, resistance for $n = 0$, and inductance for $n = -1$. Diffusion processes are characterised by the value of $n = 0.5$.

The equivalent circuit proposed to fit the experimental data is shown in Figure 5.

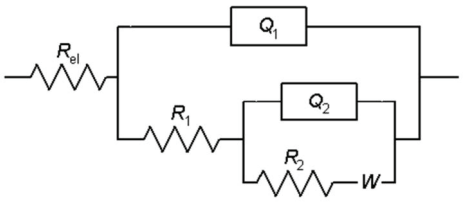

Figure 5. Proposed equivalent circuit for modelling the impedance data.

The CPEs, Q_1 and Q_2, represent the capacitances C_1 and C_2. The first time constant, Q_1R_1, observed in the high frequency region results from the fast charge transfer process in the metal dissolution reaction. In this case, R_1 represents the charge transfer resistance, and Q_1 replaces the capacitance of the electrical double layer. To account for the surface corrosion product layer and diffusion process in the low frequency region, additional equivalent circuit parameters were introduced, such as R_2 for the surface layer resistance, Q_2 for the CPE element of the surface layer (Q_2 replaces the capacitance of surface layer), and Warburg impedance, W, for the diffusion process. The calculated equivalent circuit parameters for all tested alloys are presented in Table 3.

The double layer capacitance (Q_1), surface layer capacitance (Q_2), and diffusion coefficient (W) decrease, while the charge transfer resistance (R_1) and surface layer resistance (R_2) increase in the following order: Cu < Cu-Al < Cu-Al-Ni < Cu-Al-Mn < Cu-Al-Mn-Ni.

Indeed, the impedance response of the Cu alloy specimens should be controlled largely by Cu dissolution, since Cu is the main constituent of these alloys and is also highly active in chloride-containing solutions. Furthermore, according to the plate capacitor

Table 3. Equivalent circuit parameters for investigated samples

Sample	$Q_1 \times 10^6$ (Ω^{-1} s^n cm^{-2})	n_1	R_1 (Ω cm^2)	$Q_2 \times 10^6$ (Ω^{-1} s^n cm^{-2})	n_2	R_2 (kΩ cm^2)	$W \times 10^3$ (Ω^{-1} s^n cm^{-2})
Cu	55.78	0.86	19.92	177.14	0.63	2.38	1.76
Cu-Al	49.01	0.88	23.17	160.36	0.65	4.56	1.51
Cu-Al-Ni	49.89	0.90	25.68	150.92	0.66	5.19	1.43
Cu-Al-Mn	42.22	0.91	29.15	106.72	0.71	8.65	1.12
Cu-Al-Ni-Mn	40.15	0.91	33.26	98.49	0.72	10.17	0.97

model, the surface film capacitance is inversely proportional to thickness, d (according to $C = \varepsilon_o \varepsilon / d$, ε_o is the permittivity of vacuum and ε the relative permittivity of the film). Therefore, the reduction of the surface layer capacitance element, *i.e.*, parameter Q_2 (from 177.14 for Cu to 98.49 Ω^{-1} s^n cm^{-2} for the Cu-Al-Mn-Ni alloy), corresponds to an increase in the thickness of the surface layer in the same order. This direction of changes points to the fact that Al, Ni, and Mn reinforce the corrosion product layer at E_{corr} and effectively prevent alloy corrosion.

SEM/EDS analysis

The observed similarities in the electrochemical corrosion behavior of the studied Cu and Cu alloys means that the alloying elements did not modify the dissolution mechanism of Cu. Indeed, the impedance data show that the main effect of the alloying elements was to reinforce and thicken the corrosion product (barrier) layer and make it more protective; hence, the corrosion resistance of the tested samples increased in the following order: Cu < Cu-Al < Cu-Al-Ni < Cu-Al-Mn < Cu-Al-Mn-Ni. Polarization experiments, however, revealed that the protective effect of the corrosion product layers on the Cu alloy surfaces failed at high anodic potentials. Such failure implies that the protective barrier layer might have been compromised at high anodic potentials. To further probe these observations, SEM and EDS surface investigations were undertaken. Ultrasonic cleaning of the Cu surface in deionized water after potentiodynamic polarization measurements removed loose and porous corrosion products, enabling clear SEM visualization of the post-polarization corrosion morphology of Cu and Cu alloys.

The SEM/EDS image of the corroded Cu and SEM images of corroded Cu alloy specimens after potentiodynamic polarization are presented in Figures 6 and 7, respectively.

Two distinct features are observed from the SEM images in Figures 6 and 7. Firstly, the Cu alloy specimens all have thicker and more protective barrier layers than pure Cu, in agreement with the impedance data. Secondly, the aggressive anodic polarization at high potentials caused a breakdown of the corrosion product barrier layers on the alloy surfaces, consistent with polarization data. Indeed, EDS analysis of the corroded Cu surface (Figure 6) showed a high surface concentration of Cu, almost completely free of corrosion products (with only a minimal presence chlorine and oxygen). Cu is generally thought to dissolve in chloride solution according to reactions 1-5 (shown in the introduction), creating a layer of corrosive products composed mainly of CuCl, which easily passes into the soluble $CuCl_2^-$ complex, and Cu_2O. The corrosion product layer has poor protective

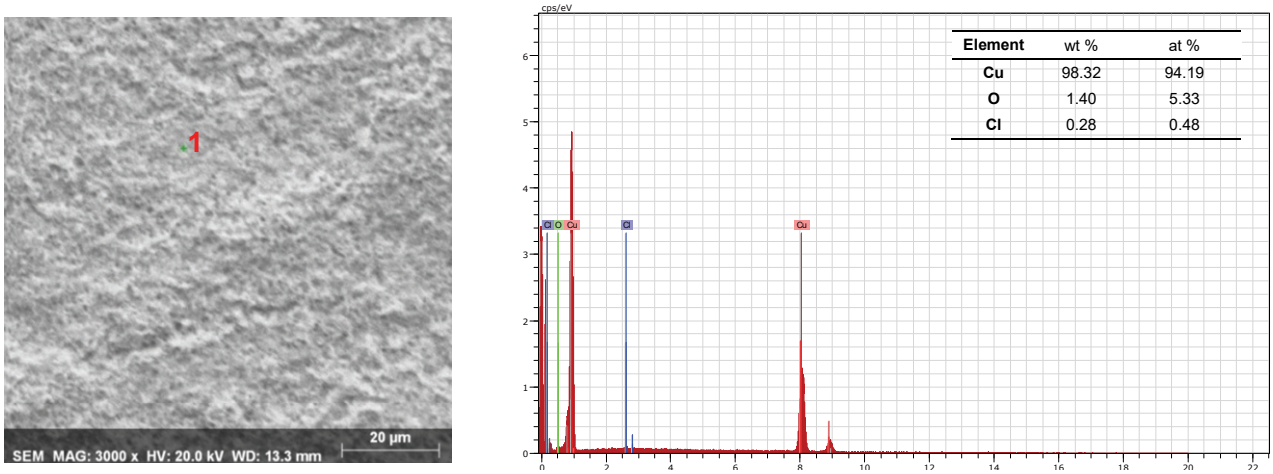

Figure 6. SEM/EDS analysis of the corroded Cu electrode surface (magnification 3000X).

properties; it is porous and does not prevent further diffusion of $CuCl_2^-$ from the electrode surface to the electrolyte solution. Ultrasonic cleaning of the Cu surface in deionized water after the polarization measurements completely removed the porous layer of corrosion products. This was confirmed by SEM/EDS surface investigations, showing rough irregular surfaces caused by corrosion dissolution and a high surface concentration of Cu, almost completely free of corrosion products, *i.e.*, the presence of chlorine and oxygen was confirmed in very small percentages (Figure 6).

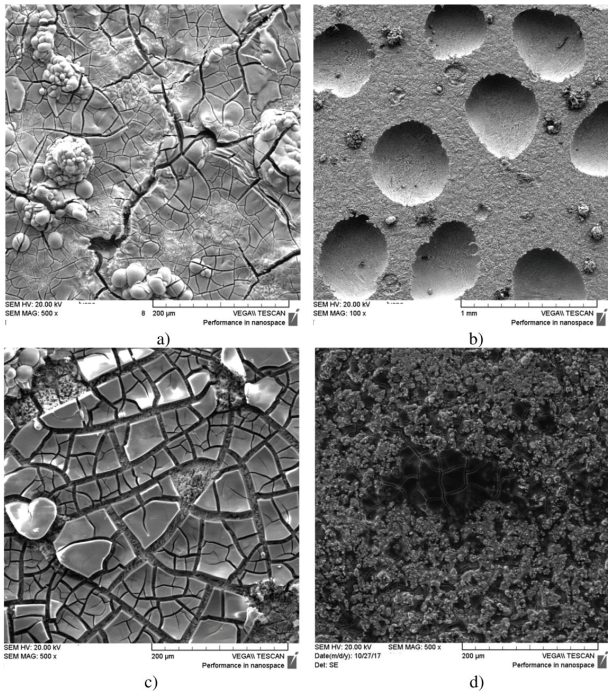

Figure 7. SEM images of corroded electrode surfaces: a) Cu-Al (magnification 500X), b) Cu-Al-Ni (magnification 100X), c) Cu-Al-Mn (magnification 500X), and d) Cu-Al-Mn-Ni (magnification 500X).

For more efficient characterization of the chemical composition of corroded alloy surfaces, EDS analyses were carried out at different locations - the intact remnant of the barrier layer and the bare metal surface beneath the cracked portions of the corrosion product (as shown in Figure 8 and presented in Table 4 for all investigated alloys).

The corrosion surface of Cu-Al alloys may be composed of different products (Cu_2O, $CuCl_2$, Al_2O_3, $AlCl_4$, etc.) [7]. Al reacts with Cl^- and forms $AlCl_4^-$, according to reaction (8). Since the chlorides are thermodynamically unstable in the presence of oxygen, chlorides react with water and form an Al_2O_3 oxide layer (reaction (9)). The formation of Al_2O_3, as an additional passivation process, protects the sample surface [7]:

$$Al + 4Cl^- \rightarrow AlCl_4^- + 3e^- \quad (8)$$

$$2AlCl_4^- + 3H_2O \rightarrow Al_2O_3 + 8Cl^- + 6H^+ \quad (9)$$

The high corrosion resistance of Cu-Al and other multicomponent alloys containing Al is primarily due to the presence of a bi-layered, structured corrosion product, with a protective inner thin compact layer, comprising mainly Cu_2O and Al_2O_3, and an outer porous layer enriched with copper, mainly in the form of Cu_2O [30,31,51,52].

SEM/EDS surface analysis was conducted after potentiodynamic polarization of the sample (Figures 6b and 8a). SEM images show the Al_2O_3 layer, which cracked because of the aggressive anodic polarization, along with aggregates of the porous layer that are held tighter on the surface and are not removed by ultrasonic cleaning (Al_2O_3 porous layer containing Cu_2O and CuCl). EDS analysis (Figure 8b and Table 4) indicated a high surface concentration of Al and O (position 1) and porous layer aggregates (position 2) with O and Al, as well as minor percentages of Cu and Cl. Furthermore, under the oxide layer, *i.e.*, in its cracks, a high concentration of Cu was confirmed, while Cl was practically absent (position 3).

SEM images of the Cu-Al-Ni alloy shows a rather thick and loose corrosion product layer, with pit-like cavities spread around, similar to previous investigations [53]. The EDS analysis at positions outside and inside the cavities indicates high percentages of Al, O and Ni, in addition to Cu. The higher corrosion resistance of Cu-Al-Ni alloys compared to Cu-Al, according to literature, is attributed to the incorporation of Ni^{2+} into a Cu_2O film, which consumes cation vacancies [54,55]. According to the "point defect" model [54,55] of movable cationic vacancies (V_{Cu}-(ox)), vacant cationic sites are formed by dissolving the Cu_2O surface layer:

$$Cu_{Cu}(ox) \rightarrow Cu^+(aq) + V_{Cu}\text{-}(ox) \quad (11)$$

A neutral complex forms by "jumping" Ni in the vacant cationic site on the surface of the alloy, according to reaction (12):

$$Ni_{Ni}(m) + 2V_{Cu}\text{-}(ox) \rightarrow \left[Ni_{Cu}(V_{Cu})_2\right] + 2e^- \quad (12)$$

The formation of this complex affects the reduction of ionic conductivity of the barrier oxide layer, which ultimately increases corrosion resistance of the alloy.

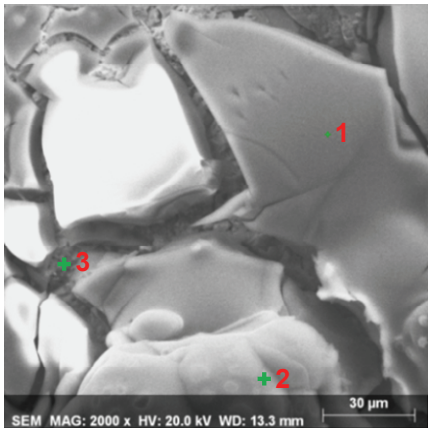

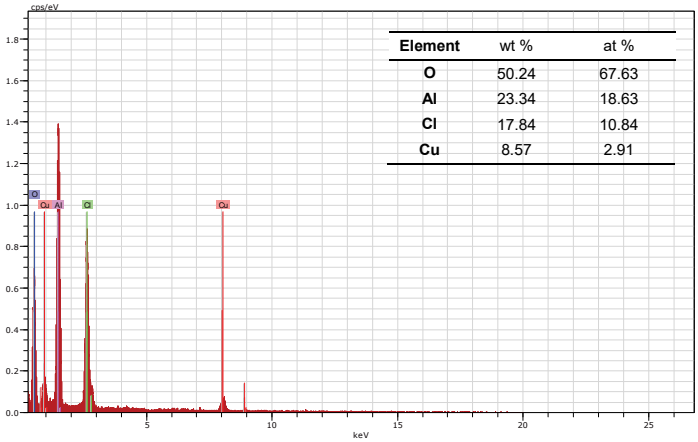

Element	wt %	at %
O	50.24	67.63
Al	23.34	18.63
Cl	17.84	10.84
Cu	8.57	2.91

a)

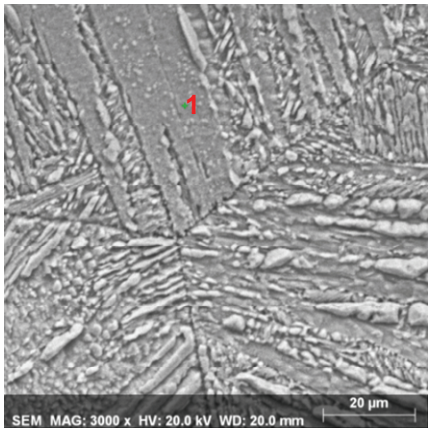

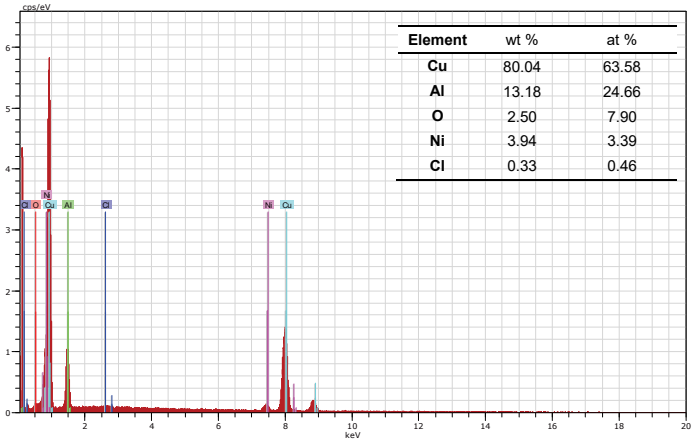

Element	wt %	at %
Cu	80.04	63.58
Al	13.18	24.66
O	2.50	7.90
Ni	3.94	3.39
Cl	0.33	0.46

b)

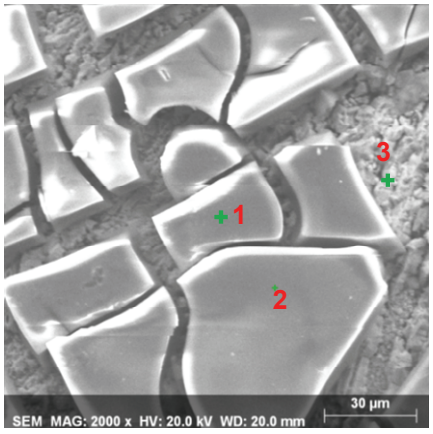

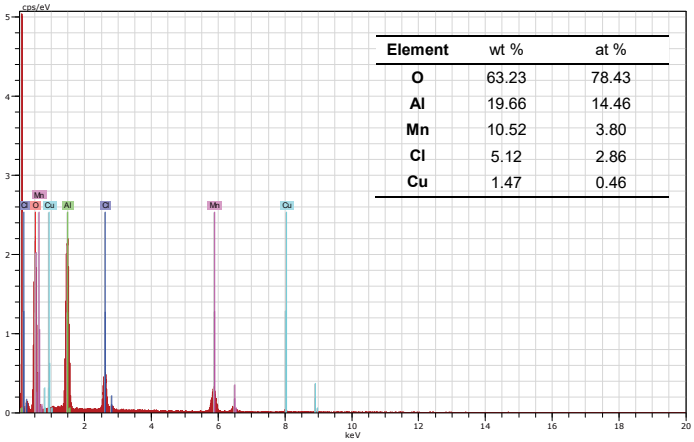

Element	wt %	at %
O	63.23	78.43
Al	19.66	14.46
Mn	10.52	3.80
Cl	5.12	2.86
Cu	1.47	0.46

c)

Figure 8. SEM images and EDS analyses after polarization measurements for: a) Cu-Al (position 1), b) the Cu-Al-Ni alloy surface (inside pit) in NaCl solution (position 1), c) the Cu-Al-Mn alloy surface (position 1) in NaCl solution, and d) the Cu-Al-Mn-Ni alloy surface (position 1) in NaCl solution.

Table 4. EDS chemical composition results for corrosion surface layers on copper alloys

Element	Position 2, corrosion product		Position 3, bare metal surface	
	Cu-Al			
	wt.%	at.%	wt.%	at.%
O	48.19	65.01	0.08	0.33
Al	25.62	20.50	0.74	1.72
Cl	20.79	12.66	0.16	0.28
Cu	5.40	1.84	99.02	97.67
	Cu-Al-Ni			
	Position 1		Position 2	
O	2.5	7.9	3.34	10.40
Al	13.18	24.66	12.51	23.10
Cl	0.33	0.46	0.37	0.52
Ni	3.94	3.39	4.11	3.49
Cu	80.04	63.58	79.67	62.49
	Cu-Al-Mn			
	Position 2		Position 3	
O	54.60	72.40	0.28	1.09
Al	19.71	15.50	0.50	1.15
Mn	11.81	4.56	4.07	4.60
Cl	10.98	6.57	0.15	0.26
Cu	2.91	0.97	95.00	92.89
	Cu-Al-Mn-Ni			
	Position 2		Position 3	
O	38.10	57.78	-	-
Al	31.52	21.57	2.10	4.80
Cl	16.76	15.07	-	-
Ni	5.58	2.31	0.98	1.03
Cu	4.51	1.72	96.23	93.39
Mn	3.52	1.55	0.69	0.78

Recent investigations of Nady *et al.* [56] have shown the possibility of forming passive $Ni(OH)_2$ and NiO surface layers in the ternary Cu-Al-Ni alloys in neutral and moderately alkaline solutions, which can further increase resistance of the protective surface layer. EDS analysis showed the presence of Ni on the surface in substantial percentages in all investigated positions.

The SEM image of the Cu-Al-Mn alloy surface shows a more extensively cracked structure of the barrier layer due to polarization treatment. Studies have shown that Mn rapidly diffuses through the alloy, accumulating on grain boundaries and refining the microstructures, leading to improved corrosion resistance, as observed [21,52,56]. The fine microstructure positively affects the compactness and stability of the barrier layer formed on the alloy. Because of the high affinity of Mn towards oxygen, the surface layer on the Cu-Al-Mn alloy contains Mn oxide, as proven by EDS surface analysis. According to the EDS analysis (Figure 8c and Table 4), the top layer (positions 1 and 2) contains high concentrations of O, Al, and Mn (*i.e.* the mixture of Al and Mn oxides) and a smaller amount of Cl and Cu. Further, under the oxide layer, *i.e.* in its cracks (position 3), a large percentage of Cu and lower percentages of Mn, Al, and O are confirmed, while Cl is practically absent. This indicates the naked site of the alloy is covered with a thin oxide layer. Interestingly, the severity and regularity of the cracks on the Cu-Al-Mn alloy surface could be linked to Mn-induced microstructure refinement. Saud and associates reported that Mn addition to Cu-Al-Ni alloy could lead to an 80% reduction in grain sizes, thereby improving the alloys' barrier layer formation and corrosion resistance [21].

According to the literature, the addition of the fourth alloy element in small quantities can improve the mechanical and anti-corrosive properties of alloys

[21,57,58]. For this reason, four-component Cu-Al--Mn-Ni alloys were studied in this paper, as well. The SEM images of the anodically polarized Cu-Al-Mn-Ni alloy (Figures 7 and 8d) show a thick and loose corrosion product layer (as observed for Cu-Al-Ni) that is severely and uniformly damaged (as seen for Cu-Al--Mn). According to EDS analysis, the top layer contains a mixture of Al and Mn oxides, as well as Ni and Cu, while the bare surface below was free of O and Cl, with lower percentages of Al, Ni, and Mn. These results are in complete agreement with results of the corrosion study with Cu-Al-Ni-Mn alloy in 3.5% NaCl solution, performed by Saud *et al.*, confirming that the corrosion products around the damaged areas are rich in Al/Mn oxides and depleted in Cu, while they were dominant on bare metal alloy surfaces with the highest percentage [21].

CONCLUSIONS

- The addition of Al, Ni, and Mn moves the E_{OC} to more positive values.
- Polarization measurements have shown that the alloying element has no significant influence on the copper dissolution mechanism in the Tafel region, where anodic reaction of Cu dissolution was controlled by diffusion of soluble $CuCl_2^-$ in the mass of the solution, (Tafel slope around 60 mV dec^{-1}). The corrosion resistance increases in order: Cu < Cu-Al < Cu--Al-Ni < Cu-Al-Mn < Cu-Al-Mn-Ni. This order was reversed at high anodic potentials, with the Cu alloys displaying higher anodic currents than Cu.
- EIS results indicate that the corrosion resistance of the samples is a consequence of the formation of a barrier layer, whose properties depend on the chemical composition of the alloy, *i.e.*, the type and content of the particular alloying elements. Al, Ni, and Mn have positive effects on barrier layer formation, and the surface film properties become better (higher resistance and thickness, more compact structure).
- SEM/EDS analyses showed that Cu alloys all had thicker and more protective barrier layers, which were severely damaged by extensive anodic polarization. The presence of an oxide layer, consisting of a mixture of dispersing alloying elements, was found on the alloy surfaces.

Acknowledgements

This work was fully supported by the Croatian Science Foundation under project IP-2014-09-3405.

REFERENCES

[1] R. Grecu, A. Samide, G. Eugenia Iacobescu, N. Cioatera, A. Popescu, Chem. Ind. Chem. Eng. Q. 25 (2019) 267--275

[2] V. Grudić, I. Bošković, A. Gezović, Chem. Biochem. Eng. Q. 32 (2018) 299-305

[3] N.D. Nikolić, P.M. Živković, M.G. Pavlović, Z. Baščarević, J. Serb. Chem. Soc. 84 (2019) 1209-1220

[4] J.R. Davis in: Alloying understanding the basics, ASM International, Materials Park, OH, 2004

[5] L. Vrsalović, E. Oguzie, M. Kliškić, S. Gudić, Chem. Eng. Comm. 198 (2011) 1380-1393

[6] R.C.N. Liberto, R. Magnabosco, N. Alonso-Falleiros, Corrosion 63 (2007) 211-219

[7] M.A. Shaik, K.H. Syed, B.R. Golla, Corros. Sci. 153 (2019) 249-257

[8] S. Sathish, U.S. Mallik, T.N. Raju, J. Miner. Mater. Char. Eng. 2 (2014) 71-77

[9] M. Sreekumar, T. Nagarajan Singaperumal, Ind. Robot 34 (2007) 285-294

[10] R. Dasgupta, J. Mater. Res. 29 (2014) 1681-1698

[11] L. Mikova, S. Medvecka-Benova, M. Kelemen, F. Trebuna, I. Virgala, Metalurgija 54 (2015) 169-172

[12] L. Vrsalović, I. Ivanić, S. Kožuh, B. Kosec, M. Bizjak, J. Kovač, U. Gabor and M. Gojić, Corros. Rev. 37 (2019) 579-589

[13] S.N.S. Al-Humairi, Cu-Based shape memory alloys: modified structures and their related properties, Intech open books, 2019, DOI: 10.5772/intechopen.86193

[14] C. Deslouis, B. Tribollet, G. Mengoli, M.M. Musiani, J. Appl. Electrochem. 18 (1988) 374-383

[15] G. Kear, B.D. Barker, F.F. Walsh, Corros. Sci. 46 (2004) 109-135

[16] Y. Van Ingelgem, A. Hubin, J. Vereecken, Electrochim. Acta 52 (2007) 7642-7650

[17] M.M. Antonijević, S.M. Milić, M. B. Petrović, Corros. Sci. 51 (2009) 1228-1237

[18] A.M. Alfantazi, T.M. Ahmed, D. Tromans, Mater. Des. 30 (2009) 2425-2430

[19] H.P. Lee, K. Nobe, J. Electrochem. Soc. 133 (1986) 2035-2043

[20] K.F. Khaled, Mat. Chem. Phys. 125 (2011) 427-433

[21] S.N. Saud, E. Hamzah, T. Abubakar, H. R. Bakhsheshi--Rad, Trans. Nonferrous Met. Soc. China 25 (2015) 1158--1170

[22] M. Gojić, L. Vrsalović, S. Kožuh, A. Kneissl, I. Anžel, S. Gudić, B. Kosec, M. Kliškić, J. Alloys Compd. 509 (2011) 9782-9790

[23] R.G. Blundy, M.J. Pryor, Corros. Sci. 12 (1972) 65-75

[24] H. Shih, H. W. Pickering, J. Electrochem. Soc. 134 (1987) 1949-1957

[25] S. Petetin, J. Crousier, J.P. Crousier, Mater. Chem. Phys. 10 (1984) 317-329

[26] I. Milošev, M. Metikoš Huković, Electrochim. Acta 42 (1997) 1537-1548

[27] I. Milošev, M. Metikoš-Huković, J. Appl. Electrochem. 29 (1999) 393-402

[28] A. Schussler, H.E. Exner, Corros. Sci. 34 (1993) 1803--1811

[29] W.A. Badawy, R.M. El-Sherif, H. Shehata, Electrochim. Acta 54 (2009) 4501-4505

[30] H. Nady, N.H Helal, M.M. Rabiee, WA. Badawy, Mater. Chem. Phys. 134 (2012) 945-950

[31] W. Badawy, M. El-Rabiee, N. Helal, H. Nady, Electrochim. Acta 56 (2010) 913-918

[32] A.O. Moghaddam, M. Ketabchi, R. Bahrami, Trans. Nonferrous Met. Soc. China 23 (2013) 2896−2904

[33] H.H. Kuo, W.H. Wang, Y.F. Hsu, C.A. Huang, Corros. Sci. 48 (2006) 4352-4364

[34] G. Kear, F.C. Walsh, D.B. Barker, K.S. Stokes, EuroCorr 2000, Institute of Corrosion, Leighton Buzzard, 2000

[35] B.A. Boukamp Equivalent Circuit, University of Twente, Twente, 1989

[36] L. Vrsalović, S Gudić, D. Gracić, I. Smoljko, I. Ivanić, M. Kliškić, E. E. Oguzie, Int. J. Electrochem. Sci. 13 (2018) 2102 – 2117

[37] S.N. Saud, E. Hamzah, T. Abubakar, H.R. Bakhsheshi--Rad, Mater. Corr. 66 (2015) 527-534

[38] A.V. Benedetti, P.T.A. Sumodjo, K. Nobe, P.L. Cabot, W. Proud, Electrochim. Acta 40 (1995) 2657-2668

[39] H. Sun, J.E. Orth, H.G. Wheat, JOM 45 (1993) 36-41

[40] M.M. Antonijević, S.C. Alagić, M.B. Petrović, M.B. Radovanović, A.T. Stamenković, Int. J. Electrochem. Sci. 4 (2009) 516-524

[41] A. El Warraky, H.A. El Shayeb, E.M. Sherif, Anti-Corros. Methods 435 Mater. 51 (2004) 52-61

[42] G.C. Serra, A.V. Benedetti, R.D. Noce, J. Braz. Chem. Soc. 8 (2010) 1530-1536

[43] Y.G. Chun, S.I. Pyun, H.C. Kim, Mat. Lett. 20 (1994) 265--270

[44] M. Stern, A.L. Geary. J. Electrochem. Soc. 104 (1957) 56-63

[45] G. Cicileo, B. Rosales, F. Varela, J. Vilche, Corros. Sci. 41 (1999) 1359-1375

[46] D. Zhang, L. Gao, G. Zhou, Appl. Surf. Sci. 225 (2004) 287-293

[47] A. Srivastava, R. Balasubramaniam, Mater. Corros. 56 (2005) 611-618

[48] W.A. Badawy, K.M. Ismail, A.M. Fathi, Electrochim. Acta 50 (2005) 3603-3608

[49] E. Sherif, S.M. Park, Electrochim. Acta 51 (2006) 4665--4673

[50] I.D. Raistrick, J.R. Macdonald, D.R. Franceschetti. in Impedance Spectroscopy, J.R. Macdonald (Ed.), J. Wiley & Sons, New York, 1987

[51] W.A. Badawy, F.M. Al-Kharafi, A.S. El-Azab, Corros. Sci. 41 (1999) 709-727

[52] J.A. Wharton, R.C. Barik, G. Kear, R.J.K. Wood, K.R. Stokes, F.C. Walsh, Corros. Sci. 47 (2005) 3336-3367.

[53] [53] L. Vrsalović, I. Ivanić, S. Kožuh, S. Gudić, B. Kosec, M. Gojić, Trans Nonferrous Met. Soc. China 28 (2018) 1149-1156

[54] D.D. Macdonald, M. Urquidi, J. Electrochem. Soc. 132 (1985) 555-558

[55] D.D. Macdonald, J. Electrochem. Soc. 139 (1992) 3434--3449

[56] H. Nady, M.M. El-Rabiei, M. Samy, W.A. Badawy, J. Bio-Tribo-Corros. 6 (2020) 22

[57] G.N. Sure, L.C. Brown, Metall. Mater. Trans., A 15 (1984) 1613-1621

[58] V. Sampath, Smart Mater. Struct. 14 (2005) S253-S261.

SENKA GUDIĆ[1]
LADISLAV VRSALOVIĆ[1]
ANA RADELJIĆ[1]
EMEKA EMANUEL OGUZIE[2]
IVANA IVANIĆ[3]
STJEPAN KOŽUH[3]
MIRKO GOJIĆ[3]

[1]University of Split, Faculty of Chemistry and Technology, Department of Electrochemistry and Materials Protection, Split, Croatia
[2]Federal University of Technology Owerri, Africa Centre of Excellence in Future Energies and Electrochemical Systems (ACE-FUELS), Owerri, Nigeria
[3]University of Zagreb, Faculty of Metallurgy, Sisak, Croatia

NAUČNI RAD

POREĐENJE KOROZIONOG PONAŠANJA BAKRA I LEGURA BAKRA U HLORIDNOM RASTVORU

Studija poređenja korozionog ponašanja Cu i Cu-Al, Cu-Al-Ni, Cu-Al-Mn i Cu-Al-Mn-Ni u 0,5 mol dm^{-3} NaCl rastvoru sprovedena je merenjem potencijala otvorenog kola, potenciodinamičkom polarizacijom, i merenjem metodom elektrohemijske impedansne spektroskopije (EIS). Skenirajuća elektronska mikroskopija/energetska disperzivna rendgenska spektroskopija (SEM/EDS) korišćena je za procenu korozijonog oštećenja na površini uzoraka nakon polarizacionih merenja. Dobijeni rezultati ukazuju da legirani elementi dovode do smanjenja gustine katodne i anodne struje u Tafelovom području, povećanja anodne struje pri višim anodnim potencijalima i blagog pozitiviranja korozionog potencijala. Sveukupno, impedancija raste sledećim redosledom: Cu < Cu-Al < Cu-Al--Ni < Cu-Al-Mn < Cu-Al-Mn-Ni. Ovo ukazuje na to da Cu legure imaju bolju otpornost na koroziju. SEM snimci površine uzoraka i EDS analiza nakon polarizacionih merenja pokazuju jednolično rastvaranje čistog Cu, kao i prisutnost površinskog oksidnog sloja, sastavljenog od oksida odgovarajućih legirajućih elemenata, na površini ispitivanih legura. Destruktivna anodna polarizacija dovodi do značajnih oštećenja barijernih slojeva na uzorcima legura.

Ključne reči: legure bakra, korozija, elektrohemijske metode, polarizacija, legure sa memorijom oblika, SEM/EDS.

CI&CEQ
Chemical Industry & Chemical Engineering Quarterly

Available on line at
Association of the Chemical Engineers of Serbia AChE
www.ache.org.rs/CICEQ

Chem. Ind. Chem. Eng. Q. 27 (4) 395–402 (2021) CI&CEQ

ASHRAF M. ASHMAWY[1]
EL-SAYED M. ELNAGGAR[1]
MANAL G. MOHAMED[2]
MOHAMED F. HAMAM[3]

[1]Chemistry Department, Faculty of Science (boys), Al-Azhar University, Egypt
[2]Petrochemical Department, Egyptian Petroleum Research Institute, Egypt
[3]Chemical Lab Sector, Qarun Petroleum company, Egypt

SCIENTIFIC PAPER

UDC 678:665.61

NOVEL ALLYL-ESTER-BASED POLYMERS AS FLOW IMPROVERS FOR WAXY CRUDE OIL

Article Highlights

- Preparation and polymerization of para-decyloxy allyl benzoate (I10)
- The homo- (HI10) and copolymer (MHI10) were evaluated as effective pour point depressants
- MHI10 exerted the highest effect on the pour point depression and rheological parameters
- The efficiency of the additives increased by increasing their concentrations from 1000 to 5000 ppm

Abstract

The deposition of paraffin wax from crude oil at low temperatures due to wax deposition, high pour point, high viscosity, and weak flow capability is among the critical and persisting challenges faced by the petroleum industry. In this study, a new para-decyloxy allyl benzoate (I10) was prepared, polymerized into HI10, and copolymerized with dioctadecyl maleate into MHI10 via the free-radical polymerization method employing azobisisobutyronitrile and toluene as the initiator and solvent, respectively. The prepared monomer was characterized by spectroscopic analyses (Fourier-transform infrared (FT-IR)) and proton nuclear magnetic resonance. Further, the polymers were characterized by FT-IR, and their average molecular weights were determined by gel permeation chromatography. The prepared compounds were taken in different concentrations and then tested as flow improvers of Qarun waxy crude oil using pour point depression and rheological parameters. The results of this test indicated that MHI10 exerted the highest effect on pour point reduction and the rheological parameters (yield value and apparent viscosity). Moreover, an increase in the efficiency of the additives was observed after increasing their concentration from 1000 to 5000 ppm.

Keywords: flow improver, pour point depressant, allyl benzoate, waxy crude oil.

As temperature decreases in the winter season, paraffin crystals begin to grow and create a crystalline net that traps the molecules of liquid hydrocarbon; this process continues until the crude oil cannot flow [1-3]. The precipitation of paraffin is one of the main challenges in the production and transport of crude oil via pipelines. The wax crystals of paraffins are generally irregularly shaped (platelet- or needle-like) and can form a continuous three-dimensional (3D) network at relatively low concentrations (~1 wt.%) [4,5].

Paraffin deposition significantly affects the production process as it entails removing the formed deposits, maintenance, increased costs of production and transport, well shutdown, and the failure of equipment [6]. Among the different available techniques and methods for eliminating or alleviating problems associated with waxy crude oil transportation and/or production, using flow improvers as additives is the most used method to change the rheological behaviors of petroleum. There are several types of improvers for improving crude oil flow. Among them, there are improvers based on surface active agents [7,8]. These improvers employ the adsorption mech-

Correspondence: A.M. Ashmawy, Chemistry Department, Faculty of Science (boys), Al-Azhar University, 11884, Egypt.
E-mail: ashraf_ashmawy2002@azhar.edu.eg; ashaf_ashmawy2002@yahoo.com
Paper received: 11 October, 2020
Paper revised: 21 December, 2020
Paper accepted: 15 March, 2021

https://doi.org/10.2298/CICEQ201011008A

anism of wax crystal surfaces such as petroleum sulfonate, polyoxyethylene, and alkylamine. Polymer-type-based additives such as alkyl acrylate copolymer and vinyl acetate copolymer and their derivatives [9,10] are the main additives used for improving the flowability of high-wax-content crude oils at low temperatures. Notably, various crude oils are not affected in a similar fashion by polymer additives, and not all polymers are necessarily effective on all crudes [11]. It is presumed that effective additives have a good match between the polymer and crude for parameters such as composition, structure, and content. The inhibition of wax crystallization occurs by cocrystallization or adsorption and nucleation in the presence of a polymer [9]. Many copolymers are utilized as inhibitors of wax precipitation [7,12,13]. Further, poly(ethylene-co-vinyl acetate) (EVA), poly(ethylene-co-butene) [14,15], poly(α-olefins), poly(alkyl acrylates) [16], poly(alkyl methacrylates) [17,18] and maleic anhydride copolymers containing vinylic esters are some of the most efficient commercially available pour point depressants (PPDs). Allyl compounds comprise a large group of ethylenic compounds exhibiting unique reactivities. Allyl methacrylate (AMA) is an ester of methacrylic acid; it is used as a flow improver in oil additives. In this work, we aim to synthesize a para-decyloxy allyl benzoate ester homopolymer (HI10) and a copolymer (MHI10) with dioctadecyl maleate (DM). The synthesized compounds were evaluated as flow improvers for Egyptian waxy crude oil. Through rheological improvement and pour point depression, the yield point and plastic viscosity values were correlated to the pour point results.

EXPERIMENTAL

Materials

Stearyl alcohol (99%), dicyclohexylcarbodiimide (DCC), 4-(dimethylamino)pyridine (DMAP) and 4-hydroxybenzoic acid were obtained from Sigma Aldrich; maleic anhydride (99%) was obtained from Acros; toluene and ethyl alcohol were obtained from Morgan; 2,2′-azobisisobutyronitrile (AIBN, 98%) was obtained from Merck Chemicals; and 1-bromodecane (97%) was obtained from Alfa Aesar. Crude oil was obtained from the western desert of Egypt (QN field - Qarun Company).

Preparations

Preparation of para-decyloxy benzoic acid

First, 1-bromodecane (0.033 mol) was added drop-wise to a solution of ethyl-4-hydroxy benzoate (0.033 mol) with stirring in 50 mL of ethanolic potassium hydroxide (0.04 mol). The stirring proceeded for 2 h at 60 °C and then overnight at room temperature. The resulting ester was directly hydrolyzed by adding potassium hydroxide (0.33 mol) and heating under reflux for 2 h. Then, the cold solution was added to cold dilute hydrochloric acid under stirring. The resulting acids, after being crystallized twice from glacial acetic acid, were confirmed to be pure by thin-layer chromatography and exhibited phase-transition temperatures that agreed with the temperatures reported in literature [19].

Preparation of para-decyloxy allyl benzoate (I10)

Molar-equivalent quantities of both allyl alcohol and para-decyloxy benzoic acid were dissolved in methylene dichloride. To the resulting solution, DMAP was added as a catalyst and then DCC was added, and the solution was left to stand overnight at room temperature with stirring. Thereafter, the solution was filtered, the solute was distilled, and the residue was recrystallized by acetic acid [19].

Syntheses

Synthesis of (DM)

The dioctadecyl maleate (DM) was prepared using molar equivalent quantities of maleic anhydride and stearyl alcohol in the presence of toluene, which was the solvent, and *p*-toluene sulfonic, which was the catalyst. The reaction was performed for 3.5 h at 95 °C [20].

Synthesis of para-decyloxy allyl benzoate polymer (HI10)

The homopolymer was synthesized *via* free-radical polymerization in a nitrogen atmosphere with constant stirring. The polymerization was conducted in a toluene solution for 13 h at 120 °C utilizing AIBN (0.1 wt.%) as the initiator. The solid polymer was separated and purified, and the synthesis process used for the polymer is shown in Scheme 1.

Synthesis of para-decyloxy allyl benzoate-DM copolymer (MHI10)

The copolymer was synthesized via free-radical polymerization in a nitrogen atmosphere with constant stirring. A mixture containing an equal amount of the monomer ((I10) and DM in 30 mL toluene was prepared, and then, the initiator (AIBN, 0.1 wt.%) was added. The reaction proceeded with continuous stirring for 8 h at 120 °C. The solid polymer was separated and purified, and the synthesis process is shown in Scheme 1.

Characterizations of the prepared compounds

The prepared polymers (HI10, MHI10) were characterized using Fourier-transform infrared (FT-IR)

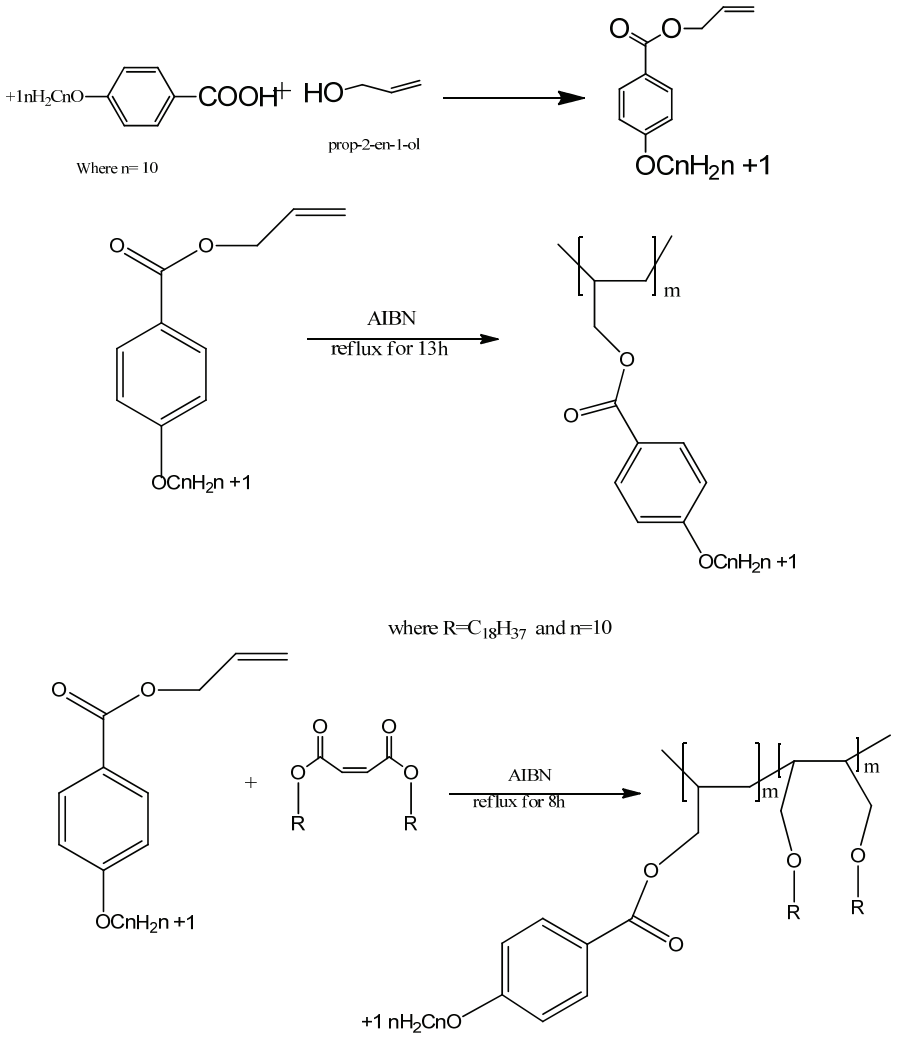

Scheme 1. Syntheses of HI10 and MHI10.

spectroscopy. The spectra were recorded on a PerkinElmer Spectrum 100 FT-IR spectrometer utilizing a KBr cell; four scans were taken, and the wavenumber range was 450-4000 cm^{-1}. The proton nuclear magnetic resonance (^{1}H-NMR) spectra were recorded on a Varian 300 (Cairo University) spectrometer utilizing tetramethylsilane (TMS) as the internal stander.

Evaluation tests

The effects of the prepared polymers as flow improvers (QN field) on the Egyptian waxy crude oil were evaluated through the rheological parameters and pour point depression. The pour point was measured according to the American Society for Testing and Materials Standard Test Procedure for Pour Point of Crude Oils (ASTM D97), employing the Koehler cloud and pour point refrigerator at different concentrations (1000-5000 ppm) of the prepared additives in the crude oil. The rheological measurements were conducted with a Brookfield DV-III Ultra Rheometer that was equipped with a thermostat cooling system and temperature control. The Brookfield rheometer was employed to measure the dynamic viscosity of virgin and additive-treated crude oils, which was prepared using optimum doses of additive, at different temperatures below and above the pour point (20, 24 and 32 °C), and the yield stress and dynamic viscosity values were determined. The microscopic structures of the crude oils untreated/treated with the prepared additives were observed using polarized-light microscopy; an Olympus BX41-P polarizing microscope was used to observe the wax crystal morphologies.

RESULTS AND DISCUSSION

Characterizations of the crude oil

Table 1 shows the physicochemical properties of the studied crude oil.

Table 1. Physicochemical properties of the crude oil - analysis of the QN field oil

Test	Method	Result
Specific gravity @ 60/60 °F	ASTM D1298	0.8217
API gravity @ 60 °F	ASTM D1298	40.7
BS & W, vol.%	ASTM D4007	0.1
Water content, vol.%	IP 74/70	0.1
Pour point, °C	ASTM D97	24
Viscosity kinematics @ 40 °C cSt.	ASTM D445	5.72
Wax content, wt.%	UOP 46/64	10.08
Conradson carbon residue, wt.%	IP 13/94	1.1
Ash content, wt.%	IP 4/94	0.005
Sediment by extraction, wt.%	IP 24/55	0.001
Sulfur content, wt.%	ASTM D4294	0.38
Average carbon number (*n*)	IP372/85 (GLC)	18.16
Resin content, wt.%	ASTM 5062-09	3.56
Asphaltene content, wt.%	IP 143/57	0.74

Confirmation of the structures for the prepared compounds

IR spectroscopy

In Figure 1a, the C-H stretching vibrations of the CH_3 and CH_2 groups were observed as strong absorption bands at 2918 and 2850 cm^{-1}. The carbonyl ester stretching bands appeared at 1718 cm^{-1} [21] because of the π-bond characteristic of the carbonyl group, the C-O stretching vibration was observed at 1253 cm^{-1}, and the ν(C=C) aliphatic band appeared at 1643 cm^{-1}. Regarding DM, ν(C=C) appeared at 1641 cm^{-1} and the carbonyl ester stretching bands appeared at 1729 cm^{-1}.

Figures 1b and c show that the C=C aliphatic band disappeared in the homopolymer and copolymer. This indicated the conversion of the monomer into a homopolymer. The carbonyl ester stretching bands of DM and I10 coappeared as a broad band at 1719 cm^{-1}.

^{1}H-NMR spectroscopy

Figure 2 shows the peaks, which are assigned as follows: δ at 0.8 ppm for the CH_3 protons; δ at 1.25 ppm for the $(CH_2)n$, (k) (l); and δ at 7.7 and 6.8 ppm for the benzene ring.

Molecular weight measurements

Molecular weights and polydispersities of the prepared homopolymer and copolymer were measured, and the results are presented in Table 2.

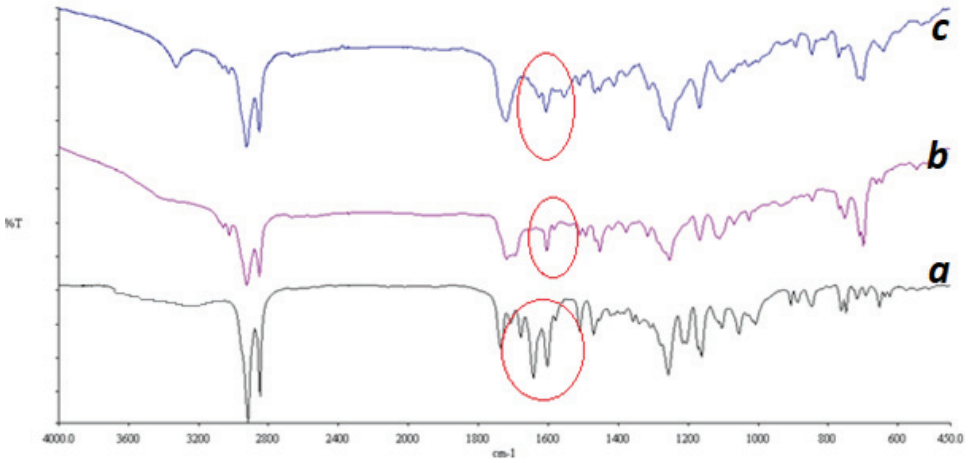

Figure 1. IR spectra of: (a) I10, (b) HI10, and (c) the copolymer (I10, HI10, and MHI10).

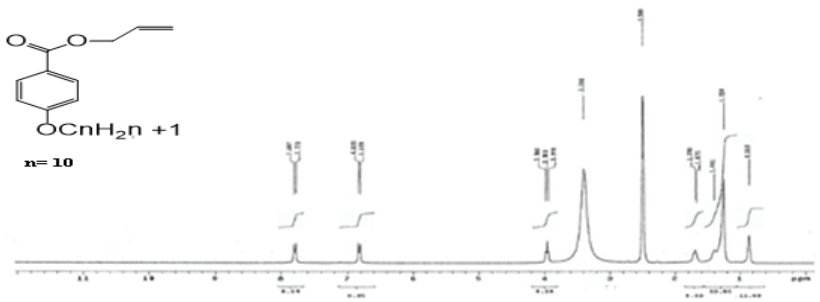

Figure 2. ^{1}H-NMR of I10.

Table 2. Molecular weights and polydispersities of the polymer and copolymer

Additive	M_n	M_{Z+1}	Mw (g/mol)	Polydispersity
HI10	6100	6920	6684	1.096
MHI10	9080	15750	10415	1.147

Evaluations of the prepared compounds as flow improvers

Pour point

The pour point is the lowest temperature at which crude oils can be stored or handled without congealing. The pour point is generally 10-20 °C lower than the cloud point (the temperature at which wax appears).

The data in Table 3 shows that all the prepared additives were effective in reducing the pour point of Qarun crude oil. The pour point depression was directly proportional to the concentrations of the prepared additives in all the additives. Additive concentrations increased from 1000 to 5000 ppm as the pour point temperature decreased. The maximum pour point depression was attained at a concentration of 5000 ppm. The pour point further decreased as the concentrations of the additives were further increased, implying that the additives could crystallize with the paraffin wax and modify their crystal structures within this concentration range. The prepared additives reduced the pour point temperatures from 24 to 9 °C (ΔP = +15 °C). The copolymer was more efficient because it contained a long aliphatic DM side chain that increased the cocrystallization with the wax molecules during the formation of the wax crystals, thereby directly affecting the efficiency of the polymer additive. Further, increasing the polar part (the two ester groups) inhibited the further agglomeration of wax, thus reducing or (in the best cases) preventing the wax crystal formation process.

Table 3. Effects of the structures and concentrations of the prepared compounds on the pour points of the crude oil

Polymer	Dose (ppm)				
	0	1000	2000	3000	5000
HI10	-	21	18	18	15
MHI10		18	15	15	9

The highest reduction in the pour point, *i.e.* a pour point depression from 24 to 9 °C (ΔP = +15 °C), was achieved with MHI10, where the interaction of the long alkyl groups (C18) with the paraffin fraction of the oil occurred through an adequate matching between them as the average number of carbons in the paraffin wax of Qarun crude oil is 18 (Table 1) [22]. The pour point depression efficiency was enhanced by the presence of a benzene ring in all the additive structures. The benzene ring matches well with the aromatic resins and asphaltene, thus increasing the solubility of the additive and interaction between the crude oil paraffin and additive [23].

Viscosity measurements

The chemical treatment of crude oils with PPDs is a general practice in the oil industry to maintain an acceptable state of fluidity in the crude oil even at low temperatures. The prepared additives interacted with the crude oil; consequently, they modified the morphology and crystal structure of the wax, and the formed crystal aggregates were easily destroyed when the oil was subjected to shear test and produced particles with shapes and sizes that were different and conducive to a different rheological behavior [24,25].

The performances of the additives as flow improvers in the tested crude were evaluated through rheological measurements at optimum concentrations (5000 ppm). The tests were performed for treated and untreated crude oils at temperatures below and above their pour points: 20, 24 and 32 °C. The shear revealed the effects of the additives on the viscosities and rheological behaviors of the waxy oils [26,27]: an increase in the shear rate reduced the apparent viscosity of the waxy oils [28]. Generally, lowering the temperature of crude oils increases their pour points, yield stress, viscosity, and progressive wax deposition [29]. The yield stress measurements were determined from the relationship between the shear rate and shear stress values, which were measured using the Brookfield viscometer. The yield value is an essential viscosity parameter, which offers beneficial information about the flow of crude oils below their pour point.

The shear stress-shear rate and viscosity-shear rate data of the untreated and additives-treated crude oils are plotted in Figures 3-5, which illustrate the fitted experimental rates, and an interception with the *Y*-axis represents the yield value. For the untreated crude oil yield stress and plastic viscosity and the values of the treated crude oil, it was observed that the shear stress sharply increased at all the tested temperatures by increasing the shear rate so that the cold flow pattern follows non-Newtonian pseudoplastic rheological behavior.

Increasing the shear stress sharply by increasing the shear rates of the treated and untreated crude oils caused a partial breakdown of the gel wax structure in the crude oil matrix, which caused a steep increase in the shear stress. The additives reduced the dynamic viscosity, and the decrease was more

significant at lower shear rates than at higher ones. The apparent viscosity was constantly obtained at high shear rates, where the equilibrium steady-state was also obtained. When the optimum concentrations of the selected additives were applied, they precipitated with the wax crystals and modified their morphologies, thereby inhibiting their aggregation and depressing the pour point of the crude oil. This behavior is reflected by the significant drop in the yield values. Figures 3-5 indicate that all the cold-flow properties were improved by increasing the concentration of the additive in the sample. Further, an increase in the chain length [30] also corresponded to improved efficiency. The decrease in the viscosity depended on the temperature and additive concentration.

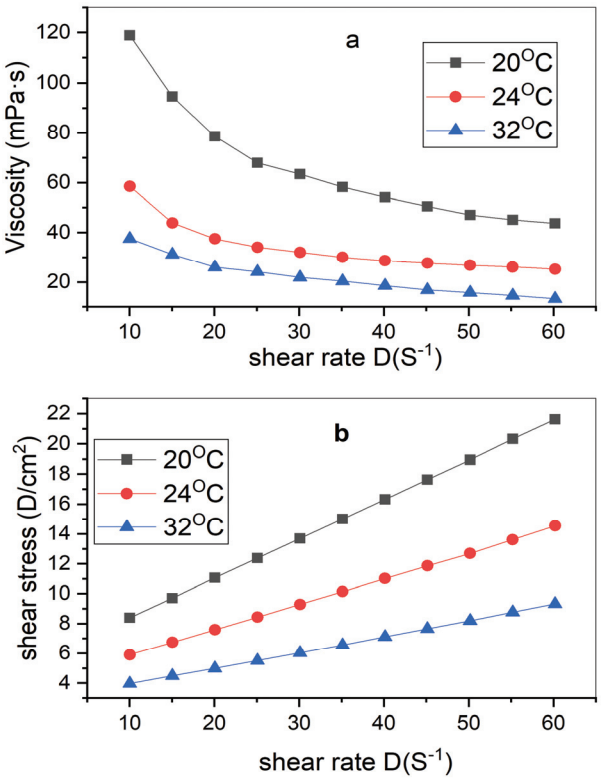

Figure 3. a) Relation between the shear rate and viscosity of the untreated crude oil; b) relation between the shear rate and shear stress of the untreated crude oil.

The depression in the yield stress was reflected by the apparent viscosity values, which were notably depressed compared to those of the untreated crude oil (Table 4). The obtained results of the viscosity and pour point correlated well. This can be explained in terms of the ability of the additives to establish a strong interaction with the wax crystals to modify their structure and form small crystals. Furthermore, the additives inhibited the formation of the agglomeration of wax crystals, thereby depressing the pour point.

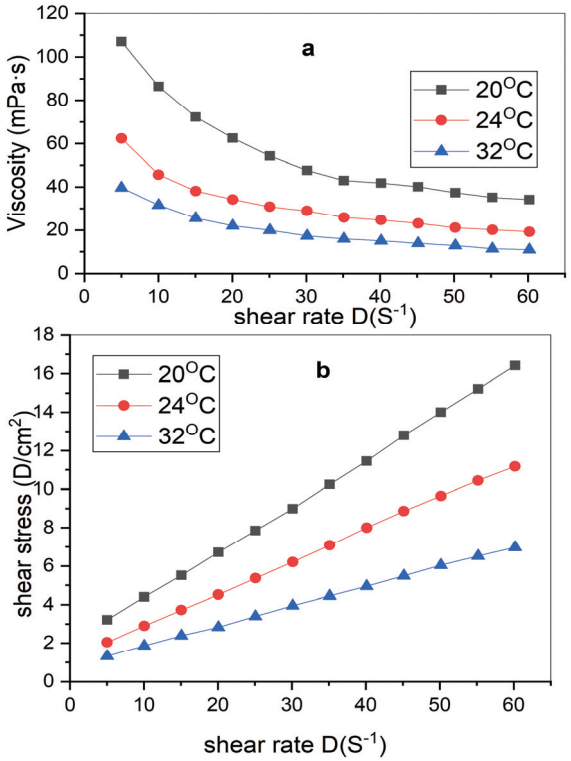

Figure 4. a) Relation between the shear rate and viscosity of HI10; b) relation between the shear rate and shear stress of HI10.

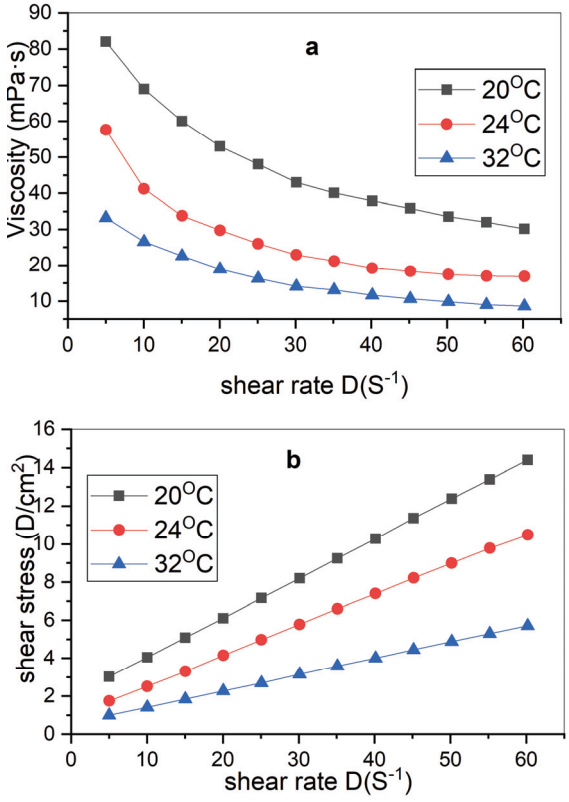

Figure 5. a) Relation between the shear rate and viscosity of MHI10; b) relation between the shear rate and shear stress of MHI10.

From the previously discussed results, MHI10 achieved better rheological enhancement than HI10. This can be explained as follows: the increase in the high polarity of oxygen in the ester groups of DM along the polymer chain might have prevented the agglomeration of the wax crystals in the crude oil. Additionally, the interaction of the long alkyl groups (C18) with the paraffin fraction of the oil occurred through an adequate matching between them, because the average number of carbons in the paraffin wax of QN crude oil is 18 (Table 1) [22]. Therefore, the flow improvers (additives) reduced the pour point, viscosity, and yield stress by cocrystallizing with normal paraffin molecules to inhibit the growth of wax crystals, implying a balance between the rates of crystal growth and cocrystallization [31].

Optical microscopy analysis

Photomicrography is a fast and simple evaluation tool that can reveal the modification that was induced by the wax dispersants and flow improver according to the type of waxy crude oil. When the waxy crude oil was cooled below its cloud point, its wax constituent tended to separate from the liquid phase and crystallize.

Photomicrography analysis is also applied to understand the flow characteristics in terms of the modification of the morphology of the wax crystal through additional laboratory tests. The decrease in the size and morphology of the wax crystals is due to the action of the PPD molecules that acted as nucleation centers in a manner that could induce the formation of many small crystals (Figure 6).

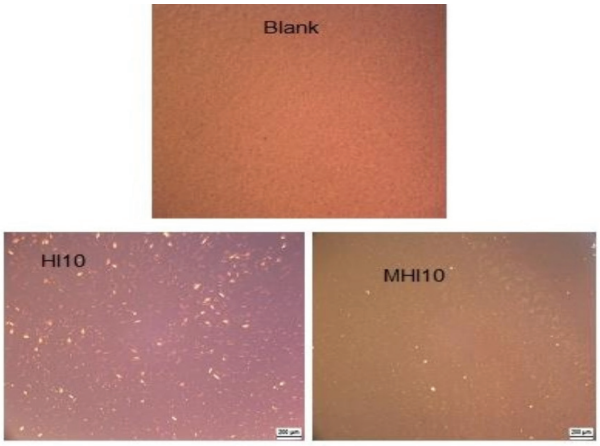

Figure 6. Photomicrographs of the untreated crude oil and the crude oil that was treated with 5000 ppm of the prepared polymers.

This might be because the additive cocrystallizes with the wax crystals and thus prevents the growth of the wax crystals, thereby keeping crystals small and apart. Thus, the waxy modifier correlated well with the improved flow parameters and pour point.

CONCLUSIONS

From the results obtained in this work, the following conclusions can be derived:

- The prepared materials could function as flow enhancers of petroleum crude.
- The higher the concentration of the additive, the lower the pour point and viscosity of the crude oil.
- Co-polymerization with DM resulted in a very effective polymer that was more effective than the homopolymer and ester.
- The result indicated that the most effective additive quantity for all prepared polymers is 5000 ppm.

Photomicrography, as a simple and rapid analytical tool, was employed to elucidate the changes in the wax structure that were induced by the PPD additives. It confirmed that the wax crystals were generally dispersed according to the concentration of the additive.

REFERENCES

[1] H.P. Soni, D.P. Bharambe, (2006)
[2] M.d.C. Garcia, L. Carbognani, A. Urbina, M. Orea, Pet. Sci. Technol. 16 (1998) 1001-1021
[3] L.V. Castro, E.A. Flores, F. Vazquez, Energy Fuels 25 (2011) 539-544
[4] R. Hoffmann, L. Amundsen, J. Pet. Sci. Eng. 107 (2013) 12-17
[5] F. Yang, B. Yao, C. Li, G. Sun, X. Ma, Fuel 199 (2017) 4--13
[6] M. Sanjay, B. Simanta, S. Kulwant, SPE Prod. Facil. 10 (1995) 50-54
[7] F. Yang, Y. Zhao, J. Sjöblom, C. Li, K.G. Paso, J. Dispers. Sci. Technol. 36 (2015) 213-225
[8] S.M. Ahmed, T.T. Khidr, D.A. Ismail, J. Dispers. Sci. Technol. 39 (2018) 1160-1164
[9] J. Qian, G. Qi, X. Ding, S. Yang, Fuel 75 (1996) 307-312
[10] E.F. Jordan Jr, S. Smith Jr, R.D. Zabarsky, A. Wrigley, J.Appl. Polym. Sci. 22 (1978) 1547-1567
[11] I. Ei-Gamal, I. Ei-Mansey, in, Petrochem, 1993.
[12] A. Al-Sabagh, S. El-Hamouly, T. Khidr, R. El-Ghazawy, S.A. Higazy, J. Dispers. Sci. Technol. 34 (2013) 1585--1596
[13] J.B. Taraneh, G. Rahmatollah, A. Hassan, D. Alireza, Fuel Process. Technol. 89 (2008) 973-977
[14] A. Radulescu, D. Schwahn, J. Stellbrink, E. Kentzinger, M. Heiderich, D. Richter, L.J. Fetters, Macromolecules 39 (2006) 6142-6151

[15] X. Guo, B.A. Pethica, J.S. Huang, R.K. Prud'homme, D.H. Adamson, L.J. Fetters, Energy Fuels 18 (2004) 930--937

[16] A. Al-Sabagh, T. Khidr, H. Moustafa, M. Mishrif, M. Al--Damasy, J. Dispers. Sci. Technol. 38 (2017) 1055-1062

[17] Y. Song, S. Han, T. Ren, Pet. Sci. Technol. 28 (2010) 860-867

[18] F. Chen, J. Liu, T. Yang, S. Yin, B. Su, M. Xie, B. Dai, S. Han, Y. Xue, Fuel 268 (2020) 117392

[19] A.M. Ashmawy, S.K. Attia, M.I. Nessim, E.S.M. Elnaggar, A.A. El-Bassoussi, Mol. Cryst. Liq. Cryst. 668 (2018) 78-90

[20] R.G. Kadesch, J. Am. Oil Chem. Soc. 31 (1954) 568-573

[21] Y. Yulizar, T. Utari, D.P. Ananda, Int. J.Technol. 7 (2016) 158-167

[22] C.C. Patton, B.M. Casad, Soc. Pet. Eng. J. 10 (1970) 17--24

[23] E. Joonaki, A. Hassanpouryouzband, R. Burgass, A. Hase, B. Tohidi, ACS Omega 5 (2020) 7124-7134

[24] A.L. Machado, E.F. Lucas, G. González, J. Pet. Sci. Eng. 32 (2001) 159-165

[25] A.L. Machado, E.F. Lucas, Pet. Sci. Technol. 19 (2001) 197-204

[26] H. Li, J. Zhang, Fuel 82 (2003) 1387-1397

[27] S. Battarjee, A. El-Azim, Egypt. J. Petrol. 6 39-52

[28] T.J. Behbahani, Pet. Sci. 13 (2016) 155-166

[29] L.M.S.L. Oliveira, R.C.P. Nunes, Y.L.L. Ribeiro, D.M. Coutinho, D.A. Azevedo, J.C.M. Dias, E.F. Lucas, J. Braz. Chem. Soc. 29 (2018) 2158-2168

[30] A. Al-Sabagh, M. Betiha, D. Osman, T. Mahmoud, J. Appl. Polym. Sci. 136 (2019) 47333

[31] J. Xu, S. Xing, H. Qian, S. Chen, X. Wei, R. Zhang, L. Li, X. Guo, Fuel 103 (2013) 600-605.

ASHRAF M. ASHMAWY[1]
EL-SAYED M. ELNAGGAR[1]
MANAL G. MOHAMED[2]
MOHAMED F. HAMAM[3]

[1]Chemistry Department, Faculty of Science (boys), Al-Azhar University, Egypt
[2]Petrochemical Department, Egyptian Petroleum Research Institute, Egypt
[3]Chemical Lab Sector, Qarun Petroleum company, Egypt

NAUČNI RAD

NOVI POLIMERI NA BAZI ALIL-ESTRA KAO POBOLJŠIVAČI PROTOKA ZA VOSKASTU SIROVU NAFTU

Taloženje parafinskog voska iz sirove nafte na niskim temperaturama, zbog visoke tačke stinjavanja, visokog viskozitet i slabe sposobnosti tečenja je među kritičnim i stalnim izazovima sa kojima se suočava naftna industrija. U ovom radu, pripremljen je novi para-deciloksi alil benzoat (I10), polimerizovan u HI10 i kopolimerizovan sa dioktadecil maleatom u MHI10 metodom polimerizacije slobodnih radikala koristeći azobizizobutironitril i toluen kao inicijator i rastvarač, redom. Pripremljeni monomer je okarakterisan spektroskopskim analizama (FT-IR) i protonskom nuklearnom magnetnom rezonancom. Dalje, polimeri su okarakterisani FT-IR, a njihove prosečne molekulske mase su određene gel permeacionom hromatografijom. Pripremljena jedinjenja su uzeta u različitim koncentracijama i zatim testirana kao poboljšači tečenja Karunove voskaste sirove nafte korišćenjem smanjenja tačke tečenja i reoloških parametara. Rezultati ovog testa su pokazali da je MHI10 imao najveći efekat na smanjenje tačke tečenja i reološke parametre (granično smičuće naprezanje i prividni viskozitet). Štaviše, povećanje efikasnosti aditiva je primećeno nakon povećanja njihove koncentracije sa 1000 na 5000 ppm.

Ključne reči: poboljšivač tečenja, depresor tačke tečenja, alil benzoat, voskasta sirova nafta.

CI&CEQ
Chemical Industry & Chemical Engineering Quarterly

Available on line at
Association of the Chemical Engineers of Serbia *AChE*
www.ache.org.rs/CICEQ

Chem. Ind. Chem. Eng. Q. 27 (4) 403–415 (2021) CI&CEQ

TIANA MILOVIĆ[1]
OGNJEN RUDIĆ[2]
SAEEDA OMRAN FURGAN[1]
MIROSLAVA RADEKA[1]
MIRJANA MALEŠEV[1]
VLASTIMIR RADONJANIN[1]
SEBASTIAN BALOŠ[1]
MIRJANA LABAN[1]

[1]Faculty of Technical Sciences, University of Novi Sad, Novi Sad, Serbia
[2]Institute of Technology and Testing of Building Materials (IMBT-TVFA), Graz University of Technology, Graz, Austria

SCIENTIFIC PAPER

UDC 691.3:666.942

EFFECTS OF SOFT WATER ATTACK ON PORTLAND AND NATURAL ZEOLITE BLENDED CEMENTS

Article Highlights

- Ordinary Portland cement was partially substituted in pastes with natural zeolite from Serbia
- Paste specimens were exposed to simulated soft water attack via leaching in deionised water
- Hydration products in blended cement pastes remained stable during leaching in deionised water
- Specimens with 10% of natural zeolite had the highest compressive strength values after 90 days

Abstract

The durability of concrete infrastructure is related to the properties of the applied concrete and the effects of the aggressive external environment on it. When concrete is directly exposed to soft water, the leaching of calcium ions from hardened cement or cement-based pastes occurs, causing reduction in strength and further deterioration of the concrete structure. This paper presents the experimental results of soft water attack effects on phase composition and compressive strength of blended cement pastes, when cement is replaced with 0, 10, 20 and 30% of natural zeolite. In order to simulate soft water attack in laboratory conditions, paste specimens were exposed to leaching in deionised water up to 180 days. The evaluation of the changes in phase composition (ettringite, portlandite, calcium silicate hydrate gel) due to calcium ion leaching was made based on X-ray diffraction analysis, Fourier-transform infrared spectroscopy and paste compressive strength tests. The presence of portlandite and ettringite after 180 days of exposure to deionised water indicates that leaching did not influence the stability of the hydration products in blended cement pastes. Moreover, blended cement paste with 10% of natural zeolite had a higher compressive strength than the reference one.

Keywords: Ca-clinoptilolite, compressive strength, deionised water, FTIR spectroscopy, leaching, XRD analysis.

The environmental concerns related to the decrease of global warming and maintaining natural resources have renewed the interest for the replacement of Portland cement (PC) by supplementary cementitious materials (SCMs) with pozzolanic properties and low embodied CO_2 footprint [1]. Pozzolana additives have little or no cementing properties but will as powders react with calcium hydroxide when water is present. The availability of many industrial by-products (fly ashes from coal-fired electricity production, blast furnace slag, etc.), commonly used as SCMs, in large and consistent quantities, and their full exploitation in certain countries, has heightened the need for the use of local natural pozzolanic materials as zeolitised tuffs, vitreous pumices and ashes, diatomaceous earth, etc. [2]. Zeolitised tuffs are widely abundant in the world and present in almost every country. They contain fine microcrystalline zeolite that binds nonzeolitic minerals like clay minerals, feldspars and glasses [3]. Some of these phases have pozzolanic

Correspondence: M. Radeka, Faculty of Technical Sciences, University of Novi Sad, Trg Dositeja Obradovića 6, 21000 Novi Sad, Serbia.
E-mail: mirka@uns.ac.rs
Paper received: 20 November, 2020
Paper revised: 17 February, 2021
Paper accepted: 20 March, 2020

https://doi.org/10.2298/CICEQ201120009M

properties (zeolite, clay minerals, glasses), while the others (quartz, feldspars) are inert. Natural zeolites (NZs) with Ca-clinoptilolite and Ca-heulandite as main mineral phases [4] dominate in Serbia. The use of NZs as SCMs is of importance because of their accessibility [3,5] proper pozzolanic activity [1,5], sulphate resistance [6], the ability to prevent the expansion due to alkali-aggregate reaction [5] and enhanced durability in terms of electrical resistivity, chloride diffusion, oxygen permeability and water absorption [5]. On the other hand, NZ blended cement requires more water [7] and the strength develops gradually over long time [5]. Most of these properties derive from NZs being pozzolanic materials which inherently change the microstructure of hydrated products. However, the reactivity of NZs in pozzolanic reactions as well as some specific durability properties depends primarily on zeolite-specific structure along with nonzeolitic mineral structure, among other parameters. One of the durability properties which has not been extensively researched is the leaching of concretes based on zeolite binder caused by the attack of soft water. A number of studies have been published on leaching of cement-zeolite composites; they are aimed at valorising the stabilisation of harmful wastes (*e.g.*, zinc-saturated zeolite [8]), immobilisation of heavy metals [9,10], solidification the intermediate-level radioactive waste [11], etc. Leaching caused by soft water appears when concrete structures are exposed to soft water attack, such as rainwater and other low ion content waters (found in lowland streams and rivers, as well as in mountainous areas in springs 12]). Leaching is present in concrete infrastructures such as hydro structures (dams, water tanks, and other allied structures [13]), tunnels [12,14], tanks, retaining walls, etc.

At the core of the leaching process under the aforementioned conditions is the diffusion of ionic species from the pore solution (mainly Ca^{2+} and OH^-) to the surrounding soft water, caused by the concentration gradient [15]. Although leaching is a slow process under normal conditions [16], chemical processes considered during degradation also affect continuous, long-lasting zeolite blended cement hydration process.

The zeolite structure is a microcrystalline one, formed of Si^{4+} and Al^{3+} tetrahedrally coordinated by oxygen atoms and thus interconnected to form rings and channels of various sizes. These complex structures create different types of zeolite frameworks with an open network [3]. The substitution of Si^{4+} by Al^{3+} results in a negative excess charge of the framework balanced by exchangeable alkali (Na, K) and/or alkaline earth (Ca, Mg, Ba) ions [17] located in the channels together with variable amounts of water. The ions and the water are loosely bound to the framework. Therefore, the cations placed in the channels are exchangeable, while water is subject to reversible hydration. Therefore, the zeolite structure could be characterised as the one with: great surface area, varying Si/Al ratio, different types and amounts of exchangeable cations and water. Ca^{2+} as an exchangeable cation dominates in Serbian NZs.

The influence of exchangeable cations, specifically Ca^{2+}, on hydration is the most prominent through the impact on the chemical reactions leading to the formation of hydrated products [18,19]. Zeolite pozzolanic reaction goes through the following steps: *i*) cation exchange, *ii*) dissolution, *iii*) breakdown and/or conversion of the zeolite into amorphous material, followed by *iv*) the precipitation of hydrated products [20]. The release of exchangeable cations from the zeolite framework has a crucial role on the reaction rate and hydration product assemblages [21]. Snellings *et al.* [21] have shown that Na^+ ion is more readily exchanged from Na^+-containing zeolite in comparison to K^+ and Ca^{2+}-containing zeolites. Alkali ions are more efficient in raising pore solution pH value than earth-alkali ions. The pH value of the pore solution determines the dissolution rate and formed hydrated assemblages. Several publications related to the dissolution where the reactant is the glassy phase documented that released Ca^{2+} control the dissolution and precipitation of silica [19,22]. As reported by Newlands and Macphee [22] and Skibsted and Snellings [19], for the pore solution pH values greater than 11 (cement-relevant values) there is a tendency of aluminosilicate phases being formed as hydrated products (calcium silicate hydrate (C-S-H) or calcium (aluminate) silicate hydrate (C-(A)-S-H) gel with low calcium/silicon (Ca/Si) ratio) [23]. The formation of these products is highly productive concerning the physico-mechanical properties of concrete. Luke [24] showed that similar results were obtained for zeolite pozzolanic reaction. Namely, alkali contribution to the pore solution increased with the rise of zeolite content. The prevailing creation of C-S-H and C-A-S-H gels after the destruction of the aluminosilicate framework was also confirmed when the pore solution was alkaline.

When pH is close to a neutral value, the glass network is disrupted by Ca^{2+} and aluminium leaching thus forming Si-O-Al species. In addition, in these conditions the dissolution process is slow so the modification of the glass surface and the formation of these species do not beneficially impact final material

properties. Similar results were reported by Ragnarsdóttir [25], obtained by the analyses of dissolution kinetics of heulandite.

The progress in leaching depends on the stability of PC hydrated products (portlandite, aluminates, C-S-H gel) when Ca^{2+} leach out due to the differences in concentrations between the pore solution and soft water. The most valuable hydrated product is C-S-H gel due to its large amount (50-70% by volume) and good mechanical properties [26,27]. At the start of the process, Ca^{2+} originates from calcium hydroxide (portlandite) which is the most soluble hydration compound. As long as it is present in a crystalline form as portlandite it controls the solubility of C-S-H gel. The buffering effect of calcium hydroxide will keep C-S-H gel stable [28].

Besides the solid phase containing hydrated products, hydrated cement paste contains pores of different sizes. These pores comprise soluble ions making a highly basic pore solution (pH>12.7). The dissolution of portlandite occurs when Ca^{2+} concentration in pores is lower than 22 mmol/l (pH<12.5) [29]. It presents a degradation mechanism (decalcification, calcium leaching) characterised by primarily dissolute portlandite followed by dissolution of cement hydrates (ettringite and C-S-H gel). C-S-H gel decalcifies in the range 8.8<pH<10.5 depending on the Ca/Si mole ratio [29]. Actually, the Ca/Si ratio depends on Ca^{2+} concentration in pore solution. A higher Ca/Si ratio corresponds to a higher pH value of pore solution. When C-S-H gel decalcifies, Ca/Si ratio decreases [26]. Leaching is divided into two phases: dissolution and diffusion [29]. The outward diffusion of Ca^{2+} from the pore solution to the bulk is controlled by concentration gradient as well as by porosity and pore size distribution of concrete.

The addition of a SCM (natural pozzolans, by-product materials like ashes, glass, slags, silica fume) to PC plays an important role in the improvement of the resistance to decalcification. They form a denser structure (low porosity) [30], decrease portlandite content and form a more stable C-S-H structure (lower Ca/Si ratio) [2,18]. It was reported that the stopping of leaching could be efficiently achieved when the most effective pozzolan, silica fume, is used as a SCM [26]. However, the research presented in this paper focuses on the estimation whether Ca-clinoptilolite, as the main mineral phase in the utilized NZ, could affect leaching. It can be assumed to be the additional source of Ca^{2+} and in this respect could have the buffering capacity. On the other hand, as a material with pozzolanic properties, it reduces porosity and refines the pore structure of binder, further mitigating the leaching process.

All these observations are significant in terms of knowledge that in this investigation NZ having prolonged hydration [19] will be exposed to concurrent processes: leaching and hydration.

The properties of hardened NZ blended cements also depend on the properties of other tuff constituents, such as clay. If clay particles are present, many properties of concretes are compromised primarily due to their size (~5 μm) and, consequently, high surface area, thus influencing hydration characteristics and the ability to strongly modify the flow behaviour of liquids [31].

This paper presents laboratory evaluation of NZ from a Serbian deposit [4] as a SCM in blended cement pastes regarding: *i*) characterisation of physical, chemical and mineralogical properties of NZ, *ii*) establishing whether the release of Ca^{2+} during pozzolanic reaction will enable high pore solution pH value while the cement based pastes with NZ as a SCM are exposed to soft water and, consequently, C-S-H formation and stability and *iii*) determination of the compressive strength of reference and Ca^{2+}-containing NZ (NZ-Ca) blended cement paste after 28, 60, 90 and 180 days of exposure to soft water.

MATERIALS AND METHODS

Materials

Physical and chemical properties of component materials and mixture compositions

For the experimental investigation of the influence of NZ-Ca as an SCM in blended cement pastes on their properties, the following component materials were used:

- PC (CEM I 42.5R, Lafarge-BFC, Serbia), standard EN 197-1:2011 [32];
- NZ-Ca from a quarry in Igroš (Brus, Serbia) with particle size less than 125 μm;
- Deionised water.

The physical and chemical properties of PC and NZ-Ca were determined according to the methods prescribed in specified standards and presented in Tables 1 and 2, respectively.

The results provided in Table 1 indicate that the physical properties of PC are in accordance with the requirements given in EN 197-1:2011 [32]. The obtained physical properties of NZ-Ca were compared with the requirements for fly ash given in EN 450-1:2012 [37]. NZ-Ca fulfilled the criteria for the initial setting time, soundness, as well as the criteria for the fineness characteristic of category N. NZ-Ca

Table 1. Physical properties and test methods for PC and NZ-Ca

Physical property	Test method	PC	NZ-Ca
Density (g/cm^3)	EN 1097-7:2008 [33]	3.13	2312.0
Blaine specific surface (cm^2/g)	EN 196-6:2010 [34]	4190	5390
BET specific surface (m^2/g)	-	1.55	78.2
Fineness - (wt. %) + 45 μm	EN 196-6:2010 [34]	4.89[a]	32.78[b]
	EN 451-2:1995 [35]		
Standard consistency (%)	EN 196-3:2005 [36]	30.0	40.6
Initial setting time (min)	EN 196-3:2005 [36]	200	185
Finish setting time (min)	EN 196-3:2005 [36]	310	302
Soundness - Le Shatelier (mm)	EN 196-3:2005 [36]	0.5	0.5
Activity index, at age of 28 days (% of control)	EN 450-1:2012 [37]	-	85.60
Activity index, at age of 90 days (% of control)	EN 450-1:2013 [37]	-	90.00

[a]Fineness of PC was determined in accordance with EN 196-6:2010 [34]; [b]fineness of NZ-Ca was determined in accordance with EN 451-2:1995 [35]

also satisfied the criteria for activity index and was classified as a pozzolanic material or type II addition. The density of PC was higher than the one for NZ-Ca, Table 1, suggesting that NZ-Ca blending would lower the overall specific gravity of the blended pastes unlike that of the reference specimen. Additionally, higher values of Blaine finesse and BET surface area of NZ-Ca in comparison to PC indicated a prominent porous structure [38].

Table 2. Chemical composition of PC and NZ-Ca; L.O.I. - loss of ignition

Chemical composition, (wt.%)	PC	NZ-Ca
SiO_2	20.98	62.78
Al_2O_3	5.51	12.20
Fe_2O_3	2.58	2.37
CaO	61.96	5.09
MgO	2.50	2.65
Na_2O	0.22	0.42
K_2O	0.74	0.74
P_2O_5	-	0.05
SO_3	3.60	0.01
Cl	-	0.05
L.O.I.	1.35	12.36

The chemical composition of NZ-Ca was determined by energy-dispersive X-ray fluorescence, ED--XRF (Spectro XEPOS C, Germany), while the one of PC was assessed by wet chemical analysis according to EN 196-2:2013 [39].

As shown in Table 2 the sum of SiO_2, Al_2O_3 and Fe_2O_3, which is relevant for pozzolanic reaction, is greater than 70% allowing the classification of NZ-Ca into silicate mineral additions conforming to EN 450--1:2012 [37]. Moreover, Si/Al ratio amounting to 4.9 indicates that NZ-Ca is rich in Si and, therefore, exhibits a high long-term pozzolanic activity. The alkali content does not exceed 5%. According to the loss of ignition results, NZ-Ca could not be classified into any category proposed by the standard EN 450-1:2012 [37].

The cation-exchange capacity (*CEC*) analysis results for NZ from Igroš, obtained by Kasic *et al.* [4], demonstrate the highest exchange capacity of calcium of all other cations (K, Na and Mg).

Mixture compositions

Table 3 summarises mixture proportions of the reference and three blended cement pastes, containing 10, 20 and 30% of NZ-Ca as an SCM per cement mass.

Table 3. Mixture proportions for reference and blended cement pastes

Mixture	PC (g)	NZ-Ca (g)	Deionised water (ml)
C	450	-	225
CZ 10	405	45	225
CZ 20	360	90	225
CZ 30	315	135	225

Experimental program

The following tests were conducted on hardened pastes:

- Mineralogical characterisation (XRD and FTIR), at the age of 28, 60 and 180 days, after the exposure to deionised water.
- Compressive strength, at the age of 28, 60, 90 and 180 days after the exposure to deionised water.

Methods

The method for determining calcium leaching used in this study (leaching in deionised water) is less efficient than the one involving the exposure to 6 M

NH_4NO_3, which is a common practice method. The use of the method of leaching by water was selected to observe the impact of NZ-Ca in the conditions when pozzolanic reaction and leaching are concurrent processes. In this case, the "excess" of Ca^{2+} could take part in the leaching process. In that way, the calcium leaching of both C-S-H gel and other products of hydration would be retarded.

Preparation of paste specimens

The prism specimens with the dimensions of 10 mm×10 mm×60 mm were prepared to follow the influence of binder composition on mechanical and structural changes caused by the exposure to deionised water. These paste specimens were kept in moulds for 1 day and then submerged in deionised water for testing leaching up to the age of 28, 60, 90 and 180 days. Leaching was tested using polyethylene containers. Reference and each type of blended cement pastes were immersed in separate sealed containers filled with deionised water. The ratio of the volume of deionised water to the mass of pastes (L/S ratio) was 50. The leaching water was not renewed. The leaching water volume was maintained constant.

The leaching water pH values (Wissenschaftlich-Technische Werkstatten GMBH, Multi 3320) were determined after 28, 60 and 180 days of exposure to deionised water. The changes in pH value as a function of paste type and time are given in Table 4. The initial pH value of deionised water was 6.6 and was not de-aired.

Table 4. Change of leaching water pH value with time

Paste type	14 days	28 days	60 days	180 days
C	11.97	11.55	8.80	8.70
CZ 10	11.94	12.18	12.02	11.90
CZ 20	12.05	12.20	11.80	11.60
CZ 30	9.98	9.26	8.60	8.40

The pH value showed the tendency to converge to constant values implying that solid and liquid phases are in equilibrium.

Compressive strength test was performed on paste specimens 10 mm×10 mm×60 mm, while the surface of ten degraded paste specimens (0.5 mm) was taken for mineralogical and structural analyses after the exposure to deionised water.

The degraded depth was determined by BSE-EDS analysis. For these analyses, the specimens (paste cross sections - 10 mm×10 mm) were prepared according to the following procedure: *i*) immersion into isopropyl alcohol for 7 days, *ii*) drying in a vacuum chamber for 8 hours, *iii*) impregnation with low viscosity epoxy resin, *iv*) polishing and *vi*) coating in gold. BSE-EDS analyses were performed by SEM-EDS device (JEOL, Tokyo). The EDS analyses were conducted at magnification of 1000, an acceleration voltage of 10 keV (software INCA 4.04, Oxford Instruments) and at specific depths (up to 0.6 mm from the surface of the specimens). Not less than 20 measurements were carried out in this region up to 0.6 mm. The collection time of each spectrum was 60 seconds. The results of EDS analyses were converted to oxide percentages and normalised to 100%.

Based on the results of EDS analyses, a profile of calcium oxide content was formed in the region up to 0.6 mm in depth from the surface of the specimen, Figure 1. The distances at which the content of calcium oxide converges to constant percentage values were regarded as the criteria for the transition from an altered zone to the sound one. The Figure 1 shows that this transition occurs at a distance of about 0.5 mm for all specimens. It can also be observed that the precipitation of $Ca(OH)_2$ appears (abrupt increase of CaO concentration) in the specimens with CZ 10, CZ 20 and CZ 30 on the outer surface that was exposed to leaching.

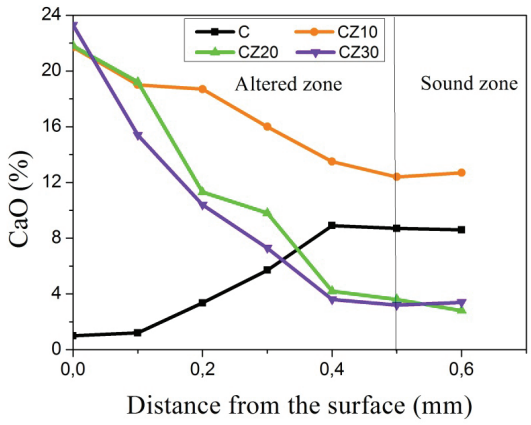

Figure 1. Profiles of calcium oxide content determined by BSE-EDS analyses according to the distance to the paste's surfaces.

The specimens from each mixture were denoted in the way specified in Table 3.

Methods for characterisation of NZ-Ca, PC and pastes

XRD analysis was used for NZ-Ca and pastes characterisation, FTIR for NZ-Ca, PC and pastes, while compressive strength analysis was performed on paste specimens after the exposure to deionised water.

Mineralogical and structural analysis was performed by XRD analysis (Philips PW1710 device)

under the following experimental conditions: monochromatic CuKα radiation with 1.5418 Å wavelength in the 10-60° of 2θ range, scan rate 0.02° and 0.5 s per step. These investigations were complemented with FTIR (Thermo-Nicolet Nexus 670 FTIR spectrometer, spectral resolution of 4 cm^{-1}, range of 400–4000 cm^{-1}, 32-averaged scans per one measurement, KBr pellet technique) method, primarily in order to obtain an integral view of the structural changes of NZ-Ca blended cements.

After the exposure to deionized water during 28, 60, 90 and 180 days, 10 prism specimens per mixture were broken in flexure, and each half was tested for strength in compression by a hydraulic compression testing machine with a range of 50 kN. The characteristic compressive strength for every type of paste was determined as the average value of 20 test results.

RESULTS AND DISCUSSION

Characterisation of XRD diffractogram of NZ-Ca sample and FTIR spectra of PC and NZ-Ca samples

XRD diffractogram of NZ-Ca sample

The mineralogical composition of NZ-Ca is complex, Figure 2. According to XRD analysis, the used NZ-Ca consists mainly of clinoptilolite $(Na,K,Ca)_5Al_6Si_{30}O_{72}18H_2O$) (JCPDS: 025-1349) and smectite $(Na,Ca)_{0.33}(Al,Mg)_2(Si_4O_{10})(OH)_2{\cdot}nH_2O$ (JCPDS: 29-1497), Figure 2. It is difficult to determine the influence of smectite on the characteristics of fresh and hardened pastes based solely on chemical composition. In general, smectite has several unique physicochemical properties important for the performances of fresh and hardened concretes based on NZ blended cements. The most significant ones are: *i*) large cation exchange capacity, *ii*) surface area that is chemically active and *iii*) cation hydration between smectite units. The most common smectite exchangeable ions are Ca, Mg, Na and H. The role of exchangeable cations is of importance for hydration characteristics [40]. The hydration capability of natural smectite clays influences swelling. The range from strongly swelling to non-swelling depends on the smectite clay species and on the ratio of Na and exchangeable Ca plus Mg ions. When smectite clays have Ca and Mg as predominant exchangeable cations, they are essentially non-swelling, while Na is susceptible to swelling by water adsorption. The highest adsorption sometimes occurs when approximately one quarter to one fifth exchangeable ions are Ca and Mg.

The influence of the properties of smectite as a secondary mineral phase in NZ-Ca on the pozzolanic reaction of clinoptilolite in NZ-Ca and leaching arises from the dependence of the decalcified cement pastes' properties on calcium concentration. Namely, it has been suggested [40] that smectite could also have an impact on certain properties related to pozzolanic activity (high cation exchange capacity, great specific surface area) and consequently on leaching. Calcium concentration could be disrupted locally on the spots in NZ-Ca where smectite is present due to: *i*) its own large cation exchange capacity and *ii*) the fact that Na^+ in the pore solution reduces the dissolution of Ca^{2+} because of a common ion effect. These two effects could locally change pore solution pH values and calcium concentration.

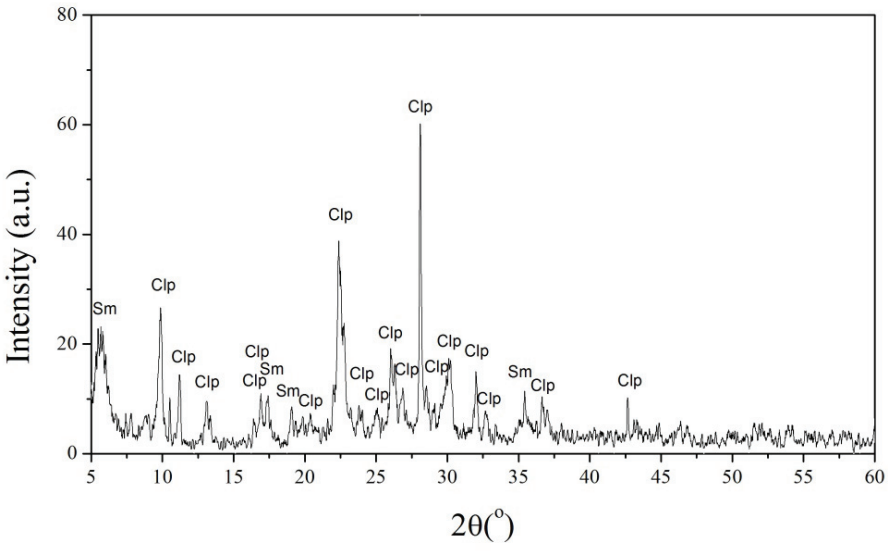

Figure 2. XRD diffractogram of NZ-Ca (Clp - clinoptilolite; Sm - smectite).

In addition, the presence of Na^+ can increase swelling which could influence the mechanical properties, specifically a decrease in the strength of CZ pastes.

FTIR spectra of PC and NZ-Ca samples

FTIR analysis of PC, Figure 3, revealed the absorption peaks at 460 and 520 cm^{-1} related to the presence of Al-O bonds with Si-O. The peak at 993 cm^{-1} is assigned to Si-O asymmetric vibrations characterising mainly C_2S or C_3S phases [41]. The absorption peak at 1110 cm^{-1} (attributed to S-O bonds) was also registered, showing the presence of gypsum in cement. The absorption peaks observed at 874, 1422 cm^{-1} as well as the group of peaks at 2850-3000 cm^{-1} indicated the presence of C-O molecular group vibration, while the absorption peaks at 1643 and 3455 cm^{-1} are characteristic of OH^- and water molecules in the structure. The data obtained by the FTIR analysis of NZ-Ca, Figure 3, pointed to the presence of the Si-O stretching band at 1044 cm^{-1}. Its position is dependent on Si/Al ratio [42] since the peak position moves towards lower wavelengths with the reduction in the value of this ratio. The given peak is assigned to the asymmetric Si-O and Al-O stretching vibrations. Shoulders at 3623 and 1208 cm^{-1} indicated the presence of the Si-OH stretching and Si-O-Si asymmetric stretching vibrations in the internal tetrahedra of NZ-Ca, respectively. The intensities of absorption peaks at 1422 and 720 cm^{-1}, characteristic of C-O molecular vibrations, can be ascribed to the carbonation of specimens during manipulation.

Al-O bonds and Si-O bonds generate vibration peaks at 460 and 520 cm^{-1}. Since the bands in the 500-800 cm^{-1} interval of the FTIR spectra of NZ-Ca could be related to pseudo-lattice vibrations, the registered clinoptilolite absorption peaks at 600 cm^{-1} implied the presence of a silica-rich structure. Three absorption bands at 3623, 3437 and 1637 cm^{-1} are characteristic of isolated OH^- stretching vibration, hydrogen-bonded OH^- to oxygen ions and the usual bending vibration of zeolite water, respectively.

Characterisation and time evolution of specimens exposed to leaching by XRD diffractograms, and FTIR spectra for reference and NZ-Ca blended cement pastes

XRD diffractograms

The assessment of the reaction products, performed by XRD analysis, contributed to the understanding of structural changes during hydration reactions, Figure 4. A noteworthy decrease in the intensity of portlandite (JCPDS: 073-5492), especially in the case of the pastes with the highest replacement ratio of NZ-Ca, (CZ 30), indicates a noticeable progression of the pozzolanic reaction. Nevertheless, portlandite was still present at the age of 180 days, in the case of all blended cement pastes. The noticed decline of clinoptilolite peaks with hydration time was associated with the decomposition of the zeolite phase. Small but notable peaks related to the clinoptilolite mineral phase could be distinguished, indicating the ongoing pozzolanic reaction continued up to 180 days especially in the case of the specimens with a higher content of NZ-Ca.

C-S-H (JCPDS: 03-0606) formation was detected, regardless of the age and exposure to deionised water, and was identified due to the existence of diffraction peaks at approximately 29.30 and 31.81° within the registered hump in the range of 2θ 25-35°, Figure 4. Namely, the low intensity diffraction peak at 2θ value 29.30° indicates the existence of a low crystallinity C-S-H mineral phase.

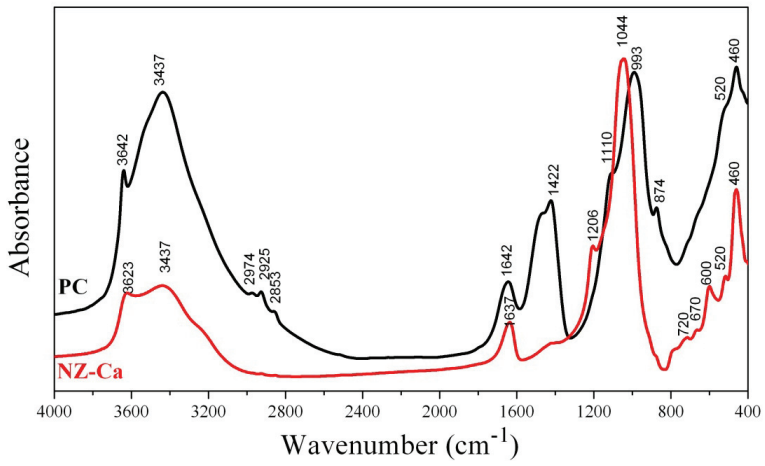

Figure 3. FTIR spectra of PC and NZ-Ca.

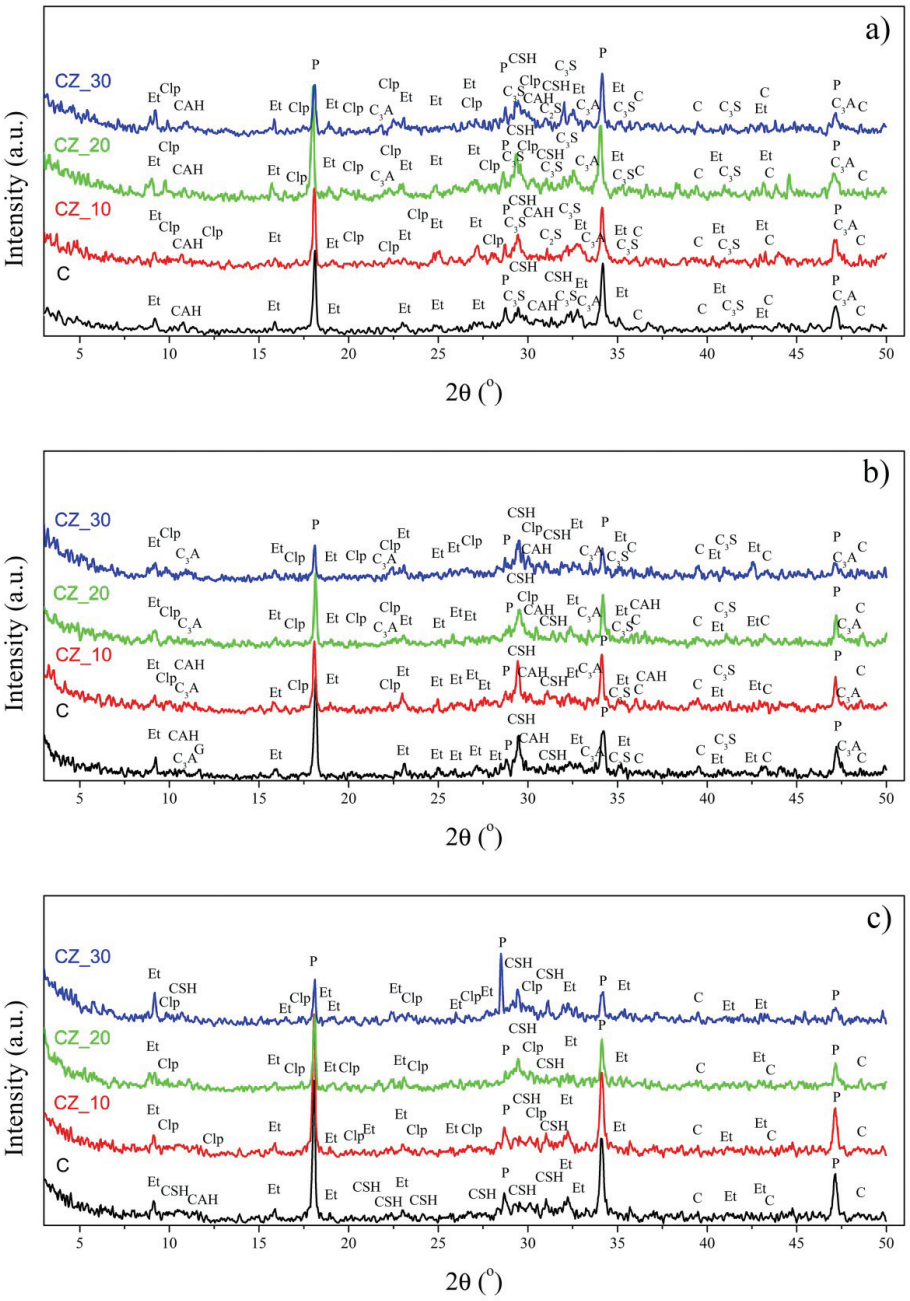

Figure 4. XRD diffractograms of reference and blended cement pastes exposed to deionised water, at the age of: a) 28, b) 60 and c) 180 days (P - portlandite, Et - ettringite, C-S-H - calcium silicate hydrate, C-A-H - calcium aluminium hydrate, Clp - clinoptilolite, C - calcite, C_3S - alite, C_3A - calcium aluminate (JCPDS: 38-1429)).

Besides the C-S-H phase, the presence of alite (JCPDS: 49-0442) and calcium aluminate (JCPDS: 38-1429) was confirmed up to 28 days of hydration, suggesting the existence of non-reacted cement grains. Moreover, a distinguished occurrence of ettringite (Et) (JCPDS: 41-1451) up to the age of 180 days and exposure to deionised water could be clearly noticed, Figure 4. According to Duchesne and Bertron [29], ettringite is unstable under pH value of 10.7. Its presence up to 180 days indicates that the exposure to deionised water as a leaching medium did not reduce pore solution pH value under the above-mentioned value. The presence of ettringite could also be explained by the availability of sulphate ions due to the specific zeolite feature to absorb SO_3 through alumina in zeolite structure [43]. Additionally, the occurrence of calcium carbonate (JCPDS: 01--0837) suggests the carbonation process took place during the manipulation with specimen in the course of its preparation.

FTIR spectra

The information acquired by XRD analysis was complemented with FTIR analysis, Figure 5. In order to obtain an integral view of the structural changes and the formation of the reaction products during hydration process and exposure to deionised water, it was most important to monitor the intensity decrease of the main absorption peak at 1044 cm^{-1} caused by Ca clinoptilolite decomposition and the changes in the position and the intensity of FTIR bands at around 970 cm^{-1} assigned to C-S-H gels [44]. Unfortunately, the peak at 1044 cm^{-1} was not distinguished mainly because of the overlapping with the peaks related to the formation of C-S-H gel. Changes of a very complex C-S-H gel structure with a variable Ca/Si ratio can be tracked through the shifting of wavelength value in comparison to bands centered at ~970 cm^{-1}. Bulatovic *et al.* [45] obtained band value at ~969 cm^{-1} for the curing process up to 180 days in tap water for the same type of cement supplied by the same producer. This value changes to lower wavelength values when the Ca/Si ratio increases, indicating depolymerisation or, in this test, a rise of Ca^{2+} in C-S-H gel structure. On the other hand, a decrease in Ca/Si ratio is assigned to the wavelength values higher than the main position, indicating polymerisation [46,47]. The exposure to leaching conditions leads to the reduction of Ca/Si ratio [29].

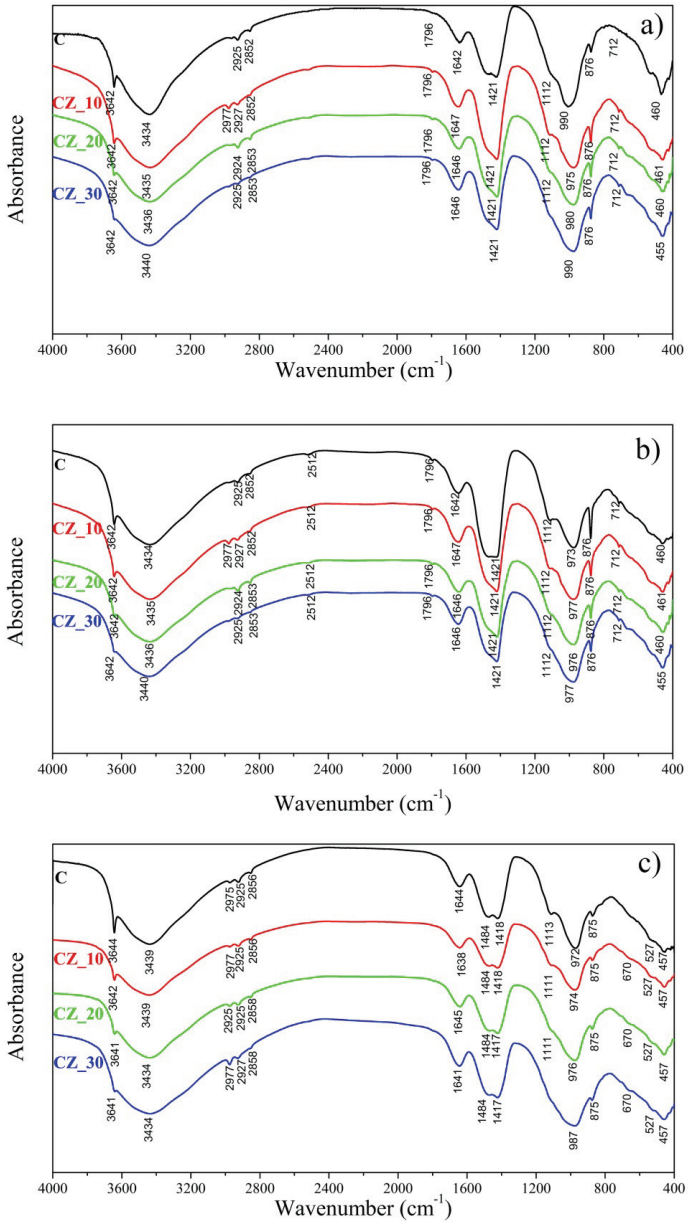

Figure 5. FTIR spectra of reference and blended cement pastes exposed to deionised water, at the age of: a) 28, b) 60 and c) 180 days.

The obtained value of the absorption band at ~990 cm^{-1} for reference paste (C) at the age of 28 days and the exposure to deionised water, Table 5, Figure 5, had higher wavenumbers in comparison to 970 cm^{-1} at later ages, implying leaching and, consequently, a decrease in Ca/Si ratio. Gained wavelength values for blended cement paste CZ 10 were more stable than the reference and other blended pastes up to the age of 180 days and exposure to deionised water, Table 5, implying that Ca^{2+} originating from NZ-Ca, succeeded to keep the pore solution buffered by calcium hydroxide during leaching. The observed shifting in band position at ~970 cm^{-1} had the highest peak value obtained for CZ 30 28 (990 cm^{-1}) indicating a greater level of polymerisation/leaching, *i.e.*, lower Ca/Si value in C-S-H gel structure. CZ 20 28 (981 cm^{-1}) and CZ 10 28 (974 cm^{-1}) displayed lower values than C 28 (990 cm^{-1}), pointing to a higher Ca/Si ratio value in C-S-H gel. The shift of absorption peak position to lower values for C 60 (973 cm^{-1}) indicated that C-S-H structure was less affected by leaching and a new equilibrium was established between pore solution and solid phase [26]. These processes lead to the dissolution of NZ and precipitation of products reflecting Ca/Si ratio in C-S-H gel structure. A similar direction of changes was obtained for CZ 30 pastes at the age of 60 and 180 days in comparison to CZ 30 28, Table 5.

Table 5. Changes of C-S-H absorption peak values (cm^{-1}) with time

Paste type	Age (days)		
	28	60	180
C	990	973	972
CZ 10	974	977	974
CZ 20	981	976	976
CZ 30	990	977	987

The absorption bands at ~3640, ~3435 and ~1646 cm^{-1} were ascribed to different vibrational modes of the O-H molecular group. The stretching vibrations of Ca-OH from portlandite were indicated due to the absorption band at ~3640 cm^{-1}, while the absorption bands at ~3435 cm^{-1} and ~1646 cm^{-1} were associated to the presence of hydrogen-bonded OH^- group. Özen *et al.* [48] assigned absorption bands at ~3435 and ~1646 cm^{-1} to bending and stretching deformation of zeolitic water.

Distinctive ettringite bands are generally assigned to 1100 and 610 cm^{-1}. The presence of a weak shoulder, Figure 5, at ~1111 cm^{-1} could be assigned to ettringite or gypsum [49]. The presence of carbonates was noted due to the occurrence of the absorption bands at ~1421, ~876 and ~711 cm^{-1} [47]. The intensity of the peaks at ~1421 and ~876 cm^{-1} was the highest at the age of 60 days and exposure to deionised water.

The effect of leaching on compressive strength of pastes

The optimal replacement ratio of cement by NZ-Ca is defined depending on desired properties. Namely, in this investigation the criteria to achieve the resistance to leaching in deionised water is maintaining: *i*) the unchanged Ca/Si ratio in C-S-H gel and *ii*) the stability of C-S-H gel and ettringite. Heukamp *et al.* [50] indicated that decalcification of C-S-H gel to low Ca/Si ratio leads to a decrease in the cohesion of pastes, while decomposition of ettringite leads to an increase in porosity.

The optimal replacement ratio estimated following these criteria does not have to counterpart to the one obtained for the best compressive strength, as a traditional criterion of acceptance for concrete [51].

The average compressive strengths of cement pastes containing 0, 10, 20 and 30% of NZ-Ca as an SCM, exposed to deionised water in various time periods, are presented in Figure 6.

By analysing the presented results, the following findings have emerged:

- The pastes containing 10% of NZ-Ca had the highest compressive strength values, while the pastes with 30% of NZ-Ca had the lowest ones;
- The increase in the compressive strength of blended cement pastes was less prominent up to the exposure of 60 days, while later it was more pronounced, especially for CZ 10 and CZ 30 pastes. On the other hand, the reference cement paste, C, did not show a significant increase in compressive strength in the time period after 60 days;
- The compressive strengths of CZ 10 were almost always higher than the corresponding values of the reference paste. At the age of 90 and 180 days compressive strengths of CZ 10 increased by 9 and 12%, respectively, when compared to their corresponding reference values, Figure 6b;
- The compressive strengths of CZ 20 were very close to their corresponding reference values for all ages and periods of exposure to deionised water, Figure 6b. Although the compressive strengths of CZ 30 paste were always lower than their corresponding reference values, an upward trend over time could be noticed; *i.e.*, the difference between compressive strength and corresponding reference value decreased by 16 and 10% at the age of 90 and 180, respectively.

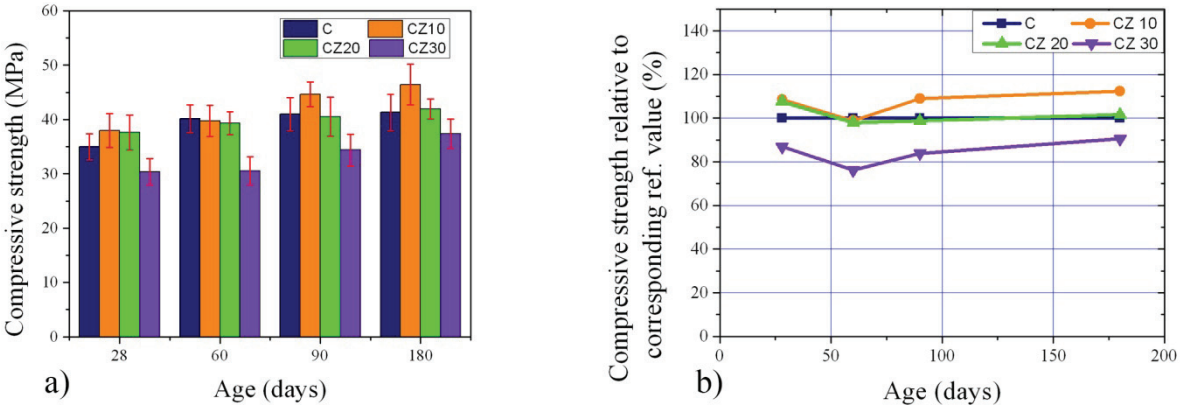

Figure 6. Average compressive strengths of pastes: a) versus time and b) relative to corresponding reference value, versus time.

Given that leaching is a very slow process that starts from the surface in contact with deionised water, the abrupt decrease of compressive strength for 60 days of exposure to deionised water, for all levels of cement replacement, could not be dominantly assigned to leaching. Due to a prolonged pozzolanic reaction of NZ-Ca, the appearance of these features could be related to the continuous expansion of the mean NZ-Ca cell volume causing a lower density of hydrated products and, consequently, compressive strength decrease. Bish [52] reported that the mean Ca-clinoptilolite cell volume continuously expanded resulting in lower density of pastes, while examining the dissolution process of 6 natural and 3 cation-exchanged (Ca, K, Na) clinoptilolites in pozzolanic reactions. Therefore, a decline in pastes density will impact a drop in compressive strength of zeolite blended cements. The density of zeolite blended cement pastes declined as the dosage of NZ rose. In addition, the contribution of the type of smectite clay determined by XRD analysis as a component of NZ-Ca was not clarified.

The effect of NZ-Ca pozzolanic reaction was noticeable at the age of 90 days, when the compressive strength of CZ 10 paste exceeded the reference value.

Good compressive strength results obtained for CZ 10 specimens along with their XRD and FTIR results indicate the importance of avoiding a fall in Ca^{2+} concentration in the pore solution. The very existence of ettringite and portlandite mineral phases after 180 days of examination points to a structural stability of investigated paste samples during leaching in deionised water. Their presence in these specimens indicates that a high pH value (above 11.5) of pore solution will not drop within the test conditions. Furthermore, the constant Ca/Si ratio of C-S-H gel - being observed as almost not altered values of wavelength numbers (around 970 cm^{-1}, Table 5) and attributed to the presence of C-S-H gel (specifically for CZ 10 pastes) - implies that the effect of C-S-H gel decalcification was negligible during the exposure to deionised water. In addition, the compressive strength for CZ 10 was the highest.

The statements discussed in the paper as the results of the investigation suggest that the structural stability of cement-based material with NZ-Ca as an SCM after the exposure to deionised water is most likely caused by the existence of sufficient buffering capacity, regardless of the observed diffusion and leaching of Ca^{2+} from paste specimens to deionised water.

CONCLUSION

Based on the presented results, the following conclusions can be drawn:

- Natural Ca-exchanged clinoptilolite containing smectite as a secondary component can be classified as a pozzolanic material, type II addition;
- The presence of portlandite and ettringite in paste at the age of 180 days and the exposure to the deionised water was identified by XRD and FTIR analyses, indicating that pH value in that moment was not lower than 10.7. This implies that leaching in deionised water did not influence the stability of the hydration products. The results of the FTIR analysis confirmed that up to 180 days of exposure, the blend containing 10% Ca-exchanged clinoptilolite had an almost constant Ca/Si ratio value, thus confirming a buffering effect of calcium ions.
- The paste specimens showed the compressive strength of blended cement pastes was less prominent up to 60 days of exposure to deionised water, while it was more pronounced later in comparison to reference specimens. The replacement level of Ca-exchanged clinoptilolite in cement pastes up to 20% did not cause the reduction of compressive

strength. Even more, with the replacement level up to 10% of natural zeolite, compressive strengths were higher than in the reference cement pastes.

Acknowledgment

This research has been supported by the Ministry of Education, Science and Technological Development of the Republic of Serbia through the project No. 451-03-68/2020-14/200156: "Innovative scientific and artistic research from the FTS domain".

REFERENCES

[1] M. Najimi, J. Sobhani, B. Ahmadi, M. Shekarchi, Constr. Build. Mater. 35 (2012) 1023-1033

[2] M.C.G. Juenger, R. Snellings, S.A. Bernal, Cem. Concr. Res. 122 (2019) 257-273

[3] G. Mertens, R. Snellings, K.V. Balen, B. Bicer-Simsir, P. Verlooy, J. Elsen, Cem. Concr. Res. 39 (2009) 233-240

[4] V.D. Kasić, V. Simić, D. Životić, A.S. Radosavljević--Mihajlović, J.N. Stojanović, Hem.Ind. 71 (2017) 49-60

[5] B. Ahmadi, M. Shekarchi, Cem. Concr. Compos. 32 (2010) 134-141

[6] J. Małolepszya, E. Grabowska, Procedia Eng. 108 (2015) 170-176

[7] C. Bilim, Constr. Build. Mater. 25 (2011) 3175-3180

[8] P. Krolo, R. Krstulović, P. Dabić, A. Bubić, Ceram.-Silik. 49 (2005) 213-219

[9] M. Vyšvaril, P. Bayer, Procedia Eng. 151 (2016) 162-169

[10] C. Napia, T. Sinsiri, C. Jaturapitakkul, P. Chindaprasirt, Waste Manage. 32 (2012) 1459-1467

[11] I. Plecas, S. Dimovic, I. Smiciklas, Prog. Nucl. Energy 48 (2006) 495-503

[12] M. Otieno, M. Alexander, J. du Plessis, J. S. Afr. Inst. Civ. Eng. 59 (2017) 57-67

[13] B. Anand, S.N. Sharma, in Recent Advancements in Mineral and Water Resources, R.N. Tiwari Ed., Excellent Publishers, New Delhi, 2016, p. 155

[14] G. Vu, T. Iskhakov, J.J. Timothy, C. Schulte-Schrepping, R. Breitenbücher, G. Meschke, Materials 13 (2020) 1-17

[15] N. Marinoni, A. Pavese, M. Voltolini, M. Merlini, Cem. Concr. Compos. 30 (2008) 700-705

[16] P. Faucon, P. Le Bescop, F. Adenot, P. Bonville, J.F. Jacquinot, F. Pineau, B. Felix, Cem. Concr. Res. 26 (1996) 1707-1715

[17] G. Kirov, L. Filizova, Geokhim. Mineral. Petrol. 49 (2012) 65-82

[18] B. Lothenbach, K. Scrivener, R.D. Hooton, Constr. Build. Mater. 41 (2011) 1244-1256

[19] J. Skibsted, R. Snellings, Cem. Concr. Res. 124 (2019), Paper 105799

[20] D. Caputo, B. Liguori, C. Colella, Cem. Concr. Compos. 30 (2008) 455-462

[21] R. Snellings, G. Mertens, J. Elsen, J. Therm. Anal. Calorim. 101 (2010) 97-105

[22] K.C. Newlands, D.E. Macphee, Adv. Appl. Ceram. 116 (2017) 216-224

[23] K.C. Newlands, M. Foss, T. Matchei, J. Skibsted, D.E. Macphee, J. Am. Ceram. Soc. 100 (2017) 1941-1955

[24] K. Luke, in Proceedins of 12th International Congress on the Chemistry of Cement, Montreal, Canada, 2007

[25] K.V. Ragnarsdóttir, Geochim. Cosmochim. Acta 57 (1993) 2439-2449

[26] C. Alonso, M. Castellote, I. Llorente, C. Andrade, Cem. Concr. Res. 36 (2006) 1583-1594

[27] W. Kunther, S. Ferreiro, J Skibsted, J. Mater. Chem., A 5 (2017) 17401-17412

[28] P. Feng, C. Miao, J.W. Bullard, Cement Concrete Comp. 49 (2014) 9-19

[29] J. Duchesne, A. Bertron, in Performance of Cement-Based Materials in Aggressive Aqueous Environments, State-of-the-Art Report, M. Alexander, A. Bertron, N. De Belie Eds., RILEM TC 211-PAE, 2013, pp. 91-112

[30] D. Vaičiukynienė, A. Kantautas, G. Krušinskas, A. Kielė, Ž. Rudžionis, Chem. Ind. Chem. Eng. Q. 22 (2016) 285-292

[31] J.K. Norvell, J.G. Stewart, M.C.G. Juenger, D.W. Fowler, J. Mater. Civ. Eng. 19 (2007) 1053-1059

[32] BS EN 197-1, Cement, Composition, specifications and conformity criteria for common cements, 2011

[33] BS EN 1097-7, Tests for mechanical and physical properties of aggregates, Part 7: Determination of the particle density of filler – Pycnometer method, 2008

[34] BS EN 196-6, Methods of testing cement, Part 6: Determination of fineness, 2010

[35] BS EN 451-2, Method of testing fly ash, Part 2: Determination of fineness by wet sieving, 1995

[36] BS EN 196-3, Methods of testing cement, Part 3: Determination of setting times and soundness, 2005

[37] BS EN 450-1, Fly ash for concrete, Part 1: Definition, specifications and conformity criteria, 2012

[38] F.A. Sabet, N.A. Libre, M. Shekarchi, Constr. Build. Mater. 44 (2013) 175-184

[39] BS EN 196-2, Methods of testing cement, Chemical analysis of cement, 2013

[40] I.E. Odom, Phil. Trans. R. Soc. Lond. A 311 (1984) 391--409

[41] M. Horgnies, J.J. Chen, C. Bouillon, in Proceedings of 6th International Conference on Computational Methods and Experiments in Materials Characterisation, Siena, Italy, 2013, p.251

[42] G. Rodriguez-Fuentes, A.R Ruiz-Salvador, M .Mir, O. Picazo, G. Quintana, Microporous Mesoporous Mater. 20 (1998) 269-281

[43] K. Sobol, T. Markiv, V. Terlyha, W. Franus, Pecularities, Bud-arch 14 (2015) 105-113

[44] F. Puertas, S. Goñi, M.S. Hernández, C. Varga, A. Guerrero, Cem. Concr. Compos. 34 (2012) 384-391

[45] V. Bulatović, M. Melešev, M. Radeka, V. Radonjanin, I. Lukić, Constr. Build. Mater. 152 (2017) 614-631

[46] P. Yu, R.J. Kirkpatrick, B. Poe, P.F. McMillan, X. Cong, J. Am. Ceram. Soc. 82 (1999) 742-748

[47] Y. Kocak, E. Tascı, U. Kaya, Constr. Build. Mater. 47 (2013) 720-727

[48] S. Özen, M.C. Göncüoglu, B. Liguori, B. de Gennaro, P. Cappelletti, G.D. Gatta, F. Iucolano, C. Colella, Constr. Build. Mater. 105 (2016) 46-61

[49] M.Y.A. Mollah, W. Yu, R. Schennach, D. L. Cocke, Cem. Concr. Res. 30 (2000) 267-273

[50] F.H. Heukamp, F.-J. Ulm, J.T. Germaine, Cem. Concr. Res. 33 (2003) 1155-1173

[51] A. Neville, Concrete: Neville's Insights and Issues, Thomas Telford Publishing, London, 2006, 75-78

[52] L.D. Bish, Clays Clay Miner. 32 (1984) 444-452.

TIANA MILOVIĆ[1]
OGNJEN RUDIĆ[2]
SAEEDA OMRAN FURGAN[1]
MIROSLAVA RADEKA[1]
MIRJANA MALEŠEV[1]
VLASTIMIR RADONJANIN[1]
SEBASTIAN BALOŠ[1]
MIRJANA LABAN[1]

[1]Fakultet tehničkih nauka, Univerzitet u Novom Sadu, Trg Dositeja Obradovića 6, 21000 Novi Sad, Srbija
[2] Institute of Technology and Testing of Building Materials (IMBT-TVFA), Graz University of Technology, Graz, Austria

NAUČNI RAD

UTICAJ DEJSTVA MEKE VODE NA PORTLAND CEMENT I MEŠAVINU PORTLAND CEMENTA I PRIRODNOG ZEOLITA

Trajnost infrastrukture spravljene od betona dovodi se u vezu sa svojstvima samog betona i uticajima koje agresivna spoljašnja sredina ima na njega. Kada je beton direktno izložen dejstvu meke vode, dolazi do ispiranja jona kalcijuma iz očvrsle cementne paste odnosno paste na bazi cementa, što dovodi do smanjenja čvrstoće i dalje devastacije strukture betona. U ovom radu su prikazani rezultati eksperimentalnog istraživanja uticaja dejstva meke vode na fazni sastav i čvrstoću pri pritisku pastā na bazi cementa, kada se cement supstituiše sa 0, 10, 20 i 30% prirodnog zeolita. Kako bi se simuliralo dejstvo meke vode u laboratorijskim uslovima, uzorci pastā su bili izloženi ispiranju u dejonizovanoj vodi u periodu od 180 dana. Procena promena faznog sastava (etringit, portlandit, kalcijum-siliko-hidratni gel) nastalih usled ispiranja jona kalcijuma urađena je na osnovu rezultata rendgenostrukturne analize, infracrvene spektroskopije i čvrstoće pri pritisku pasta. Prisustvo portlandita i etringita nakon 180 dana izlaganja dejstvu dejonizovane vode ukazuje da ispiranje nije uticalo na stabilnost produkata hidratacije u pastama na bazi cementa. Štaviše, cementna pasta sa 10% prirodnog zeolita imala je veću čvrstoću pri pritisku u odnosu na referentnu.

Ključne reči: Ca-klinoptilolit, čvrstoća pri pritisku, dejonizovana voda, FTIR spektroskopija, ispiranje, XRD analiza.

Journal of the
Association of Chemical Engineers of
Serbia, Belgrade, Serbia

Chemical Industry & Chemical Engineering Quarterly

CI&CEQ Vol. 27 Contents: Issues 1-4 YEAR 2021

No. 1

No. 2

No. 3

No. 4

Journal of the
Association of Chemical Engineers,
Belgrade, Serbia

Chemical Industry & Chemical Engineering Quarterly

CI&CEQ Vol. 27 Author Index YEAR 2021

A

B

C

D

Đ

E

F

G